الجمهورية الجزائرية الديمقراطية الشعبية
Democratic and Popular Republic of Algeria
وزارة التعليم العالي و البحث العلمي
Ministry of Higher Education and Scientific Research

Mohamed Khider University - BISKRA
Faculty of Exact Sciences and Science of Nature and Life
Department: Material sciences

جامعة محمد خيضر بسكرة
كلية العلوم الدقيقة وعلوم الطبيعة والحياة
قسم : علوم المادة

Thesis submitted for the award
of the diploma of

Doctor of Science in: Physics

Option : Semi-Conductors

Simulation of Quantum Infrared Photodetectors

Presented by:

Zoubir BECER

Publicly defended on: 21/02/2020

In front of the committee composed of:

A. BELGACHI	Prof.	Bechar University	Examiner
AF. MEFTAH	Prof.	Biskra University	President
A. BEGGAS	MCA.	Eloued University	Examiner
N. SENGOUGA	Prof.	Biskra University	Supervisor
A. BENNECER	DR.	Northampton University, UK	Co-Supervisor

I would like to dedicate this thesis to the soul of my father, loving mother, wife, sisters and brothers.

Acknowledgements

I am especially grateful to my supervisors, Abdeljalil Bennecer and Noureddine Sengouga, for their encouragement and confidence throughout this project. Their helpful comments and suggestions have contributed considerably to the improvement of this work. Thanks also go to my UK's friends with whom I had the pleasure to work with during these years: Reda, Said, Moussa, Nadim, Marwan, Ammar, Jonhson. Really it was a brotherhood friendship during my stay in UK. Special thanks go to my wife for her continuous encouragement, support and help throughout the very difficult period of writing up. Furthermore, I gratefully acknowledge the examination committee for accepting to be members of the committe. Thanks go to old friends Mostafa, Dahman, Rachid, Kamel and others for their helpfulness during these years. I also would like to thank Professor Phil Picton from University of Northampton, for his help with administration issue at the university.

Abstract

The topic of research is concerned with modelling and simulation of high temperature long wavelength infrared quantum photodetectors using advanced finite element methods. The aim is to devise novel designs based on quantum well structures to improve quantum efficiency, and operating temperature. These new designs rely on quantum confinement of electrons and holes inside a mixture of materials within which the energies of the carriers become discrete and differ from those observed in bulk materials. Type II InAs / GaSb superlattices is one of these meta–materials which offer a large flexibility in the design of infrared photodetectors, including the possibility to adjust the detected wavelength over a very wide range and to realize a suitable absobers' unipolar barriers to suppress dark current while maintaining a significant portion of photocurrent at high temperatures. In order to validate this interest, A set of rigorous modelling tools based on multi-band $\mathbf{k}\cdot\mathbf{p}$ band structure theory and Boltzmann transport theory has been developed, which provide a better understanding of the electronic structure and transport in these heterostructures. The framework takes into account in particular the effect of the intrinsic strained property of the unintentional interfaces on the electronic structure and the optical properties. First, the finite element method is used to solve 8×8 $\mathbf{k}\cdot\mathbf{p}$ Hamiltonians for InAs/GaSb superlattices with type II alignment to compute the optical and materials' characteristics. For InAs and AlAsSb and alloys based detectors, An optical material library has been developed to generate all the needed bulk material properties. Secondly, the transfer matrix method or the Beer-Lambert law is used to compute the optical generation profiles in the device. Finally, the the finite volume method has been employed to solve the transport equations to compute the dark- and photo- currents, quantum efficiency among other device properties. Using this tools, new structures based on nBn and nBp architectures have been designed, with optimized design, which contribute to the realization of mid- and long-wave infrared photodetector based on Type-II superlattices InAs / GaSb material system as well as InAs/AlAsSb alloy mterial system. The developed model allows to study the underlying physics of these devices and to explain the factors limiting the device performances.

Based on the simulation results, detectors involving absorbers with period composed of 14 Mono-Layer (ML) of InAs and 7 ML of GaSb was found to have a band gap wavelength close

to 11 μm and exhibit a lower dark current than those with period mainly composed of GaSb. The designed LWIR barrier device consists of a 4 μm thick p-type InAs-rich 14 ML InAs / 7ML GaSb LWIR T2SL absorber, a 200 nm thick p-type InAs/AlSb SL barrier and an n-type InAs-rich 14 ML InAs / 7ML GaSb LWIR T2SL contact layer. The 16.5ML InAs / 4ML AlSb superlattice of the BL is designed to give a smooth conduction band alignment and a large VBO of nearly 400 meV with the AL. The optimum doping level of absorber, barrier and contact layer are found to be $1 \times 10^{16} cm^3$, $5 \times 10^{15} cm^3$ and $1 \times 10^{16} cm^3$ respectively. This nBp detector design exhibits at 77 K a diffusion limited dark-current down to -300 mV with a dark-current level plateau as low as $8.5 \times 10^{-5} A/cm^2$ which is more than one order of magnitude lower compared to a similar PIN photodiode. Furthermore, this value is near the level of the MCT 'rule 07' demonstrating that InAs/GaSb SL detectors may provide new opportunities to replace the MCT technology in the LWIR spectral window given the MCT material instability problem at longer wavelengths. Moreover, we have demonstrated that the presence of the majority carriers' barrier improves the current performances and the operating temperature over the standard PIN device. A temperature improvement of 20 K was found for a given current density of $2x10^{-4}$ A$/cm^{-2}$ compared to a similar LWIR PIN device working at 60 K.

Keywords : Superlattice, Infrared, Photodetector, T2SL, nBn, nBp, Barrier, InAs/GaSb, LWIR

ملخص

يهتم موضوع البحث بنمذجة ومحاكاة أجهزة كشف الأشعة تحت الحمراء الطويلة الكمية عالية درجة الحرارة باستخدام طرق العناصر المحدودة المتقدمة. الهدف هو ابتكار تصميمات جديدة تستند إلى هياكل الآبار الكمية لتحسين الكفاءة الكمية ودرجة حرارة التشغيل. تعتمد هذه التصميمات الجديدة على الحصر الكمي للإلكترونات والثقوب الموجودة داخل خليط من المواد ، حيث تصبح طاقات الحاملات منفصلة ومختلفة عن تلك التي لوحظت في المواد السائبة. تعتبر الشبكات الفائقة InAs/GaSb من النوع الثاني إحدى هذه المواد الفوقية التي توفر مرونة كبيرة في تصميم أجهزة الكشف الضوئي بالأشعة تحت الحمراء، بما في ذلك إمكانية ضبط الطول الموجي المكتشف على نطاق واسع جدًا وتحقيق حواجز أحادية القطبية مناسبة لقمع تيار الظلام مع الحفاظ على جزء كبير من التيار الضوئي عند درجات حرارة عالية. من أجل التحقق من صحة هذا الاهتمام ، تم تطوير أدوات محاكاة دقيقة بناءً على نظرية بنية العصابات المتعدد $k \cdot p$ ونظرية النقل لبلتزمان والتي توفر فهمًا أفضل للبنية الإلكترونية والنقل في هذه الهياكل غير المتجانسة. يأخذ النموذج في الاعتبار على وجه الخصوص تأثير خاصية الاجهادات الذاتية للسطوح البينية غير المقصودة على البنية الإلكترونية والخصائص البصرية. بداية، استخدمت طريقة العناصر المحدودة لحل الهاملتون 8×8 $k \cdot p$ للشبكات الفائقة InAs/GaSb التي توفر محاذاة لحواف العصابات من النوع الثاني لحساب الخصائص البصرية والمادية. بالنسبة لأجهزة الكشف القائمة على سبائك InAs و AlAsSb ، تم تطوير مكتبة مواد بصرية لتوليد جميع خصائص المواد السائبة المطلوبة. ثانيًا ، يتم استخدام طريقة مصفوفة الانتقال أو قانون Beer-Lambert لحساب ملفات تعريف التوليد البصري في الجهاز. أخيرًا ، أستخدمت طريقة الحجوم المحدود لحل معادلات النقل لحساب التيارات المظلمة والضوئية ، والكفاءة الكمية بالاضافة لكميات اخرى للحكم على اداء الجهاز. باستخدام هذه الأدوات ، تم تصميم هياكل جديدة بناءً على بنية nBn ، مع تصميم محسّن ، مما يساهم في تحقيق كواشف ضوئية بالأشعة تحت الحمراء للموجات الطويلة والمتوسطة على أساس الشبكات الفائقة من النوع الثاني لنظام المواد InAs/GaSb ، وكذا سبائك نظام المواد InAs/AlAsSb . يسمح النموذج المطور بدراسة الفيزياء الأساسية لهذه الأجهزة وشرح العوامل التي تحد من أدائها. استنادًا إلى نتائج المحاكاة ، وجد أن الكواشف التي تشتمل على ممتصات ذات ادوار مؤلفة من 14 ML من InAs و 7 ML من GaSb لها طول موجة فجوة نطاق قريبة من $11\ \mu m$ وتظهر تيارًا مظلما أقل من نظيراتها التي تحتوي على ادوار تتكون أساسًا من GaSb. يتكون كاشف الاشعة الحمراء الطويلة المصمم ذو الحاجز من شبكة فائقة من النوع الثاني ممتصة غنية بمادة InAs سمكها $4\ \mu m$ وبدور من 14 ML InAs / 7 ML GaSb T2SL بتطعيم p ، وحاجز بتطعيم p بسماكة $200\ nm$ من 14 ML InAs-rich InAs / 7 ML SL و طبقة تلامس من نفس مادة الممتص تطعيمها n. تم تصميم الشبكة الفائقة 16.5 ML InAs / 4 ML AlSb لطبقة الحاجز لإعطاء محاذاة سلسة لحافة عصابة النقل وحاجز VBO كبير في حافة عصابة التكافؤ يبلغ حوالي 400 meV مع طبقة الممتص. تم العثور على مستوى التطعيم الأمثل للطبقة الماصة والحاجز والتلامس بـ $1 \times 10^{16} cm^3$ و $5 \times 10^{15} cm^3$ و $1 \times 10^{16} cm^3$ على التوالي. يعرض تصميم الكاشف nBp هذا عند 77 K تيار ظلام انتشاري الى غاية -300 mV بحد اقصى يصل إلى $8.5 \times 10^{-5} A/cm^2$ وهو اقل بمقدار او يزيد عن نظيره في ثنائي ضوئي PIN مماثل. علاوة على ذلك ، هذه القيمة قريبة من مستوى "القاعدة 07" MCT مما يدل على أن الكواشف المعتمدة على الشبكات الفوقية InAs/GaSb قد توفر فرصًا جديدة لاستبدال تقنية

MCT في النافذة الطيفية LWIR نظرًا لمشكلة عدم استقرار مادة MCT عند الاطوال الموجية الطويلة. كذلك، تم أثبات أن وجود حاجز لحوامل الشحنة الاغلبية يحسن الأداء الحالي ودرجة حرارة التشغيل مقارنة بجهاز PIN القياسي. تم تسجيل تحسن في درجة حرارة التشغيل بمقدار 20 K لكثافة تيار معينة تبلغ $2 \cdot 10^{-4} A/cm^{-2}$ مقارنة بجهاز PIN LWIR مماثل يعمل عند 60 K .

كلمات مفتاحية: بنى فائقة، تحت حمراء، كاشف ضوئي ،T2SL ،nBn ،nBp ،حاجز، InAs/GaSb ، LWIR .

Résumé

Le sujet de recherche concerne la modélisation et la simulation de photodétecteurs quantiques infrarouges à haute température et à longue longueur d'onde à l'aide de méthodes avancées d'éléments finis. L'objectif est de concevoir de nouvelles conceptions basées sur des structures de puits quantiques pour améliorer l'efficacité quantique et la température de fonctionnement. Ces nouvelles conceptions reposent sur le confinement quantique des électrons et des trous à l'intérieur d'un mélange de matériaux dans lequel les énergies des porteurs deviennent discrètes et différentes de celles observées dans les matériaux massifs. Les super-réseaux GaSb/InAs de type II sont l'un de ces méta-matériaux qui offrent une grande flexibilité dans la conception des photodétecteurs infrarouges, y compris la possibilité d'ajuster la longueur d'onde détectée sur une très large gamme et de réaliser des barrières uniplairs appropriées pour supprimer le courant d'obscurité tout en maintenant une partie importante du photocourant à des températures élevées. Afin de valider cet intérêt, Un ensemble d'outils de modélisation rigoureux basés sur la théorie de la structure des bandes $\mathbf{k} \cdot \mathbf{p}$ multi-bandes et la théorie du transport de Boltzmann a été développé, qui permettent de mieux comprendre la structure électronique et le transport dans ces hétérostructures. Le model prend en compte en particulier l'effet de la propriété de contrainte intrinsèque des interfaces non intentionnelles sur la structure électronique et les propriétés optiques. Premièrement, la méthode des éléments finis est utilisée pour résoudre les hamiltoniens $\mathbf{k} \cdot \mathbf{p}$ 8×8 pour les super-réseaux InAs/GaSb avec un alignement de type II pour calculer les caractéristiques optiques et matérielles. Pour les détecteurs à base d'InAs et AlAsSb et d'alliages, une bibliothèque de matériaux optiques a été développée pour générer toutes les propriétés de matériaux massifs nécessaires. Deuxièmement, la méthode de la matrice de transfert ou la loi de Beer-Lambert est utilisée pour calculer les profils de génération optique dans le dispositif. Enfin, la méthode des volumes finis a été utilisé pour résoudre les équations de transport afin de calculer les courants d'obscurité et photo-courants, l'efficacité quantique entre autres propriétés du dispositif. En utilisant ces outils, des nouvelles structures basées sur l'architecture nBn et nBp, ont été conçues avec une conception optimisée, qui contribuent à la réalisation de photodétecteurs infrarouges à ondes moyennes et longues basées sur les super-réseaux de Type II du système de matériaux GaSb/InAs ainsi que sur le système de l'alliage InAs/AlAsSb. Le modèle développé permet d'étudier la physique sous-jacente de ces dispositifs et d'expliquer les facteurs limitant leurs performances. Sur la base des résultats de la simulation, les détecteurs impliquant des absorbeurs avec une période composée de 14 Mono-Couche (ML) d'InAs et de 7 ML de GaSb se sont avérés avoir une longueur d'onde de bande interdite proche de $11\ \mu m$ et présenter un courant d'obscurité plus faible que ceux avec une

période principalement composé de GaSb. Le dispositif de barrière LWIR conçu se compose d'un absorbeur de type p de $4\,\mu m$ d'épaisseur riche en InAs du 14 ML InAs / 7ML GaSb LWIR T2SL, d'une barrière InAs / AlSb SL de type p de 200 nm d'épaisseur et d'une couche de contact de type n riche en InAs du 14 ML InAs / 7ML GaSb LWIR T2SL. Le super-réseau 16.5 ML InAs / 4 ML AlSb de la couche de barrière est conçu pour donner un alignement de bande de conduction lisse et une grande discontinuité de bande de valence VBO de près de 400 meV avec l'absorbeur. On trouve que le niveau de dopage optimal de l'absorbeur, de la barrière et de la couche de contact est de $1 \times 10^{16} cm^3$, $5 \times 10^{15} cm^3$ et $1 \times 10^{16} cm^3$ respectivement. Cette conception de détecteur nBp présente à 77 K un courant d'obscurité limité en diffusion jusqu'à -300 mV avec un plateau de niveau de courant d'obscurité aussi bas que $8.5 \times 10^{-5} A/cm^2$, ce qui est plus d'un ordre de grandeur inférieur à une photodiode PIN similaire. En outre, cette valeur est proche du niveau de la « règle 07» MCT démontrant que les détecteurs InAs / GaSb SL peuvent offrir de nouvelles opportunités pour remplacer la technologie MCT dans la fenêtre spectrale LWIR étant donné le problème d'instabilité du matériau MCT à des longueurs d'onde plus longues. De plus, il a été démontré que la présence de la barrière des porteurs majoritaires améliore les performances actuelles et la température de fonctionnement par rapport au dispositif PIN standard. Une amélioration de la température de 20 K a été trouvée pour une densité de courant donnée de $2x10^{-4}$ A$/cm^{-2}$ par rapport à un dispositif LWIR PIN similaire fonctionnant à 60 K.

Mots-clés : Super-réseau, Infrarouge, Photodétecteur, T2SL, nBn, nBp, Barrière, InAs/GaSb, LWIR

Table of contents

List of figures

List of tables

Acronyms

IR	Infrared Radiation
NIR	NearWave InfraRed
SWIR	ShortWave InfraRed
MWIR	MidWave InfraRed
LWIR	LongWave InfraRed
VLWIR	Very LongWave InfraRed
MQW	Mullti Quantum Wel
QWL	Quantum Well Lasers
QWIP	Quantum Well Infrared Photodetectors
QWIP	Quantum Well Infrared Photodetector
QCL	Quantum Cascade Lasers
ISB	Inter-SubBand Transitions
LO	Longitudinal-Optical
TECs	Thermo-Electric Coolers
SRH	Shockley-Read-Hall
RAD	Radiative
AUG	Auger
T2SLs	Type-II superlattices

T2SL	Type-II superlattice
ML	Mono-Layer
SCZ	Space Charge Zone
SE	Single Element
FPA	Focal Plane Array
VBO	Valence Band Offset
CBO	Conduction Band Offset
WL	Window Layer
BL	Barrier Layer
AL	Absorber Layer
CL	Contact Layer
SL	Super-Lattice
hB	hole Barrier
eB	electron Barrier
HgCdTe	Mercury Cadmium Telluride
MCT	Mercury Cadmium Telluride
EVS	Enhanced Vision System
FEM	Finite Element Method
FDM	Finite Difference Method
TMM	Transfer Matrix Method
G-R	generation-recombination
PDE	Partial Differential Equation
BTE	Boltzmann's Transport Equation

DD	Drift-Diffusion
FBZ	First Brillouin Zone
LPE	Liquid Phase Epitaxy
MBE	Molecular Beam Epitaxy
DOS	Density Of States
CQD	Center for Quantum Devices
CHTM	Center for High Technology Materials
AFRL	Air Force Research Laboratory
NARL	Nanoboyut Research Laboratory
NWU	Northwestern University
RVS	Raytheon Vision Systems
UCSB	University of California, Santa Barbara
Columbia	Columbia University
UIUC	University of Illinois, Urbana-Champaign
UNM	University of New Mexico
NRL	Naval Research Laboratory
MPI	Max Planck Institute
FIA	Fraunhofer-Institute for Applied Solid State Physics
JPL	Jet Propulsion Laboratory
IES	Institut dElectronique du Sud
SCD	SemiConductor Devices

Introduction

Nowadays, our smartphones have one or more built-in digital cameras which are able to capture photographs and often record video in visible light [6]. The development of these technologies has been made possible thanks to advances in microelectronics. In fact, these devices are built around a sensor - which is also called the Focal Plane Array (FPA) – made from a semiconductor material: silicon. The photons impinging on each diode of the focal plane are absorbed by exciting an electron from the valence band to the silicon conduction band. Similarly, it is possible to manufacture cameras that detect infrared radiation. This requires using a semiconductor material whose energy difference between the valence band and the conduction band (i.e. the gap) corresponds to the infrared spectral range. Examples of bulk materials meeting these requirements such as InSb or $Hg_xCd_{1-x}Te$ are commonly used. It is well known that these low band gap materials are more difficult to grow and process than large band gap semiconductors such as GaAs. These difficulties have motivated the exploration of utilizing the Inter-SubBand Transitions (ISB) in Mullti Quantum Wel (MQW) structures made of large band gap semiconductors. In fact, advances in growth techniques have allowed us to produce different forms of semiconductor nanostructures (wells, wires and quantum dots) so as to confine the carriers in one, two or three directions in space. These has led to clear illustrations of some concepts of quantum mechanics such as quantization of energy levels. The Inter-SubBand Transitions (ISB) in quantum wells are transitions between states created by quantum confinement in ultra-thin layers of semiconductors. Their unique physical properties, such as an atomic-like density of states, as well as the fact that they can be manufactured in a highly uniform and pure crystal layers on large substrate wafers, with a precise control of each layer thickness, makes them an attractive building block for mid-infrared optoelectronics. The $GaAs/Al_xGa_{1-x}As$ material system appears to be the material of choice and an excellent candidate for ISB applications since the quantum well shape can be adjusted over a range wide enough to enable theoretically light detection at any narrow wavelength range within $6-20\ \mu m$. Indeed, Quantum Well Infrared Photodetectors (QWIPs), and Quantum Well Laserss (QWLs) and Quantum Cascade Laserss (QCLs) and modulators were all demonstrated using this technology,

and are becoming mainstream devices for a new generation of optoelectronics for sensing and telecommunication applications.
However, many civil and military applications, such as space infrared detection, molecular spectroscopy of air pollutants and control of industrial processes, require the development of detectors and lasers operating at longer wavelengths, especially in the atmospheric transparency windows ($3-5\mu m$ and $8-13\mu m$). In addition, quantum well detectors based on intersubband transitions of GaAs/Al_xGa_{1-x}As material system , are restricted to the absorption of normal incident radiation due to the selection rules. Hence, these detectors require 45^o coupling or a corrugated surface (for grating coupling). Furthermore, quantum efficiency is greatly reduced due to the selection rule allowing only one polarization mode of the incident light. Moreover, they exhibit a low Longitudinal-Optical (LO)-phonon energy ($33meV$ in GaAs) or equivalently inherently short lifetimes (about 10^{11} s), resulting in low quantum efficiency and relatively poor performance at temperatures above $50K$. At these higher temperatures, the dark current dominates the photo-current, leading to a low signal-to-noise ratio. At longer wavelengths (small energy gap) the situation becomes worse since thermally stimulated carriers blind the photocurrent signal. For all those reasons, uncooled infrared detectors at different wavelengths are important owing to the necessity of such detectors in a wide range of applications: civil, industry, medicine, astronomy, and military. Attempts to use cryogenic cooling or high-power-consuming Thermo-Electric Coolers (TECs) would not be practical for most applications.

Since the 1990s, a strong research activity has been developing to explore new technologies using superlattice material systems such as antimonide/arsenide heterostructures. Type-II superlattices (T2SLs), based on III-V semiconductors, have emerged as a strong competitor of $Hg_xCd_{1-x}Te$ alloys, with the possibility of extending the detection/emission spectral ranges with performance comparable to Mercury Cadmium Telluride (HgCdTe). In addition, they allow the creation of non-cryogenic infrared detectors. In fact, the current performance of InSb detectors for detection in the 3-5 µm band deteriorates with the temperature due to the thermal activation of the carriers [3]. This property prevents the use of this material for thermal imaging at room temperature. It is however possible by using Type-II superlattices with and an optimized device design to significantly improve the detection properties at non-cryogenic temperature.

Type II GaSb/InAs superlattices have a large flexibility in their design, which first, allows in principle to obtain interband transitions over a very wide range of wavelengths (from 3 to 30 μm) by changing only the thickness of the wells, and secondly reducing Auger recombinations. However, several difficulties are associated with the epitaxial growth of these material system: a significant lattice mismatch exist between different materials, the control of mixed As/Sb

interfaces is particularly sensitive and difficulty to master the mechanisms by which different V elements are incorporated.

This work aims to contribute to the realization of mid- and long-wave infrared photodetector based on Type-II superlattices (T2SLs) material system such as the GaSb/InAs superlattices as well as InAs/AlASSb alloys. For this end, an important modeling work of band structure and transport in T2SLs material system is then carried out. The development of this model is the core of this thesis. This work has allowed us to improve our understanding of the electronic transitions and transport phenomena which led to the development of a quantum transport simulation tool. This tool has been then used to develop optimized structures responding to the application needs mentioned above.

It is worth mentioning that despite the development of numerous research works, and despite the deep knowledge of quantum well physics even today,, the modelling of transport of multiple quantum well structures remains difficult and it is a targeted research goal for the theoretical physicist.

Within this thesis we shall concentrate on the theory and modeling of electronic band structure and transport in GaSb/InAs T2SLs-based infrared photodetectors.

Outline of the Thesis

This thesis is divided into five chapters:

Chapter one, recalls the basic concepts of infrared detection and imaging. The definitions of black body, emissivity and atmospheric transmission windows will be detailed. Then, the various quantum infrared detectors are described, before presenting in more detail the operating principle of infrared photodetectors based on quantum wells and superlattices.

Chapter two, will present the state of the art of quantum infrared detectors in general and a more detail focus will be given for Type-II superlattices based devices in LWIR and MWIR windows. The main properties of GaSb/InAs superlattices technology and it's current needs, such as improving the intrinsic performance, increasing operating temperature and increasing the size of FPAs are presented.

Chapter three, presents in detail the modelling results of energy bands in different nano-structures configurations leading to the creation of complex coupled quantum wells. The nano-structures are mainly antimonide Type-II superlattices. The calculations are carried out by the modelling tools developed during this thesis work. Information about finite elements as

well as $\mathbf{k} \cdot \mathbf{p}$ method and 8x8 $\mathbf{k} \cdot \mathbf{p}$ Hamiltonian adapted to the particularities of superlattices with type II alignment are described. This chapter includes a discussion on the miniband dispersion. The calculation of absorption coefficient for LongWave InfraRed (LWIR) and MidWave InfraRed (MWIR) Type-II SLs samples will be presented. The effects of unintentional interface formation on optical properties of type II superlattices will be investigated. A study of the sensitivity of the energy bandgap as a function of various physical parameters will be presented and discussed. The calculated electronic parameters can then be used to design new superlattice structures with better performance, especially in LWIR, where InAs/GaSb SR could bring improvements to actual arrays of detectors in terms of sensitivity and uniformity.

Chapter four focuses on the transport modelling of IR detectors of different designs based on Type-2 SLs as well as on InAs/AlASSb alloys. In this chapter, the simulation is carried out using our second simulation tool devoted specifically to transport modelling. The main input for this tools comes from our first simulation tool presented in chapter 3. It is subdivided into three parts. The first describes the main theoretical platform of the physical transport model and its numerical counter part. This includes the Boltzman transport equation for electrons and holes and it's adaptation to super-lattices based devices. The second validates and then investigates in detail a bulk InAs/AlAsSb nBn detector photodetector. The investigations includes the influence of the doping profile, conduction and valance band offsets on the level of dark current. The rest of this chapter shows how this simulation tool can be used in more complex design than the bulk design. Specifically, detectors based on InAs-rich InAs/GaSb LWIR T2SL material will be designed and optimized in terms of composition, doping, thickness and dark-current. The simulation tools allowed me to draw optimized structures.

Finally, chapter five summarizes the work of this thesis and provides an outlook for future endeavours.

Chapter 1

Infrared Photodetectors

This chapter introduces our notation and the fundamental concepts underlying infrared detection and imaging. Famous monograph of Antoni Rogalski [7] on the topic covers extensively many of the concepts in details.

1.1 Infrared Radiation Fundamentals

Every body above absolute zero temperature (273° C or 0K) emits heat in the form of radiations, depending on its temperature. This energy is due to the vibration of all charged particles such as molecules and atoms, which depends on the temperature of the body. The motion of molecules is synonymous with motion of accelerated charges, which generate electromagnetic radiation (photons). These photons move at the speed of light and obey the established and known optical laws in the visible domain. It can be directed, focused with lenses, or reflected with mirrors. For medium and low temperatures, the spectrum of this radiation is located over a wavelength range between 0.7 and 1000 μm; it is therefore not normally visible to the human eye. This spectrum is located below (in energy) the red zone of visible light, hence the Latin nomination **infra** for the term **infrared**.

1.1.1 Planck's Model of Thermal Emission

Thermal emission emerges from every body above absolute zero temperature in the form of electromagnetic waves; likewise, every body also absorbs part of electromagnetic waves, which falls on it. The first correct description of this observation is given by Planck in 1900 [33], following the unsuccessful work of Wien, Rayleigh and Jeans based on a classical approach in studying the radiation of a blackbody. A blackbody is an idealised radiator which can absorb

and emit all radiation frequencies. Planck's law describes the distribution of electromagnetic energy (or the distribution of photon density) radiated by a black body at a given temperature, as a function of wavelength (or correspondingly any spectral variable such as frequency or wavenumber or their angular equivalents). Planck's law is presented in different variants, which use quantities such as intensity, flux density or spectral distribution. The flux of photons emitted by the surface of a blackbody at a given wavelength λ, per unit projected area of emitting surface, per unit solid angle, per unit wavelength, also called **spectral photon Luminance** or **spectral photon radiance** is given by Planck's radiation law:

$$L_{\Omega,\lambda}(\lambda,T) = \frac{2c}{\lambda^4} \cdot \frac{1}{exp\frac{hc}{\lambda k_B T} - 1} \qquad [photons.s^{-1}.m^{-2}.m^{-1}st^{-1}] \tag{1.1}$$

By integrating this spectral photon luminance in all directions of the hemisphere in which the studied surface element dA radiates, a **spectral photon emittance** or **spectral phtoton exitance** denoted $M_\lambda(\lambda,T)$ is obtained:

$$\begin{aligned} M_\lambda(\lambda,T)\mathrm{d}A\ \mathrm{d}\lambda &= \int_{\text{hemisphere}} L_{\Omega,\lambda}(\lambda,T)\cos(\beta)\mathrm{d}A\ \mathrm{d}\lambda\mathrm{d}\Omega \\ &= \int_{\phi=0}^{2\pi}\int_{\beta=0}^{\frac{\pi}{2}} L_{\Omega,\lambda}(\lambda,T)\cos(\beta)\mathrm{d}A\ \mathrm{d}\lambda\sin(\beta)\mathrm{d}\phi\mathrm{d}\beta \\ &= 2\pi L_{\Omega,\lambda}(\lambda,T)\mathrm{d}A\ \mathrm{d}\lambda\int_{\beta=0}^{\frac{\pi}{2}}\cos(\beta)\sin(\beta)\mathrm{d}\beta \\ &= \pi L_{\Omega,\lambda}(\lambda,T)\mathrm{d}A\ \mathrm{d}\lambda \end{aligned}$$

Thus

$$M_\lambda(\lambda,T) = \frac{2\pi c}{\lambda^4} \cdot \frac{1}{exp\frac{hc}{\lambda k_B T} - 1} \qquad [photons.s^{-1}.m^{-2}.m^{-1}] \tag{1.2}$$

where, h represents Planck's constant, c the velocity of light in a vacuum, k_B Boltzmann's constant, λ the wavelength in a vacuum, T the absolute temperature of the blackbody. The infinitesimal solid angle dΩ is bounded by the azimuthal angles ϕ and $\phi + \mathrm{d}\phi$ as well as the polar ascent angles β and $\beta + \mathrm{d}\beta$.

The energy counterpart of the spectral photon exitance is called **spectral energy exitance** or **spectral radiant exitance** and is given by:

$$\tilde{M}_\lambda(\lambda,T) = \frac{2\pi hc^2}{\lambda^5} \cdot \frac{1}{exp\frac{hc}{\lambda k_B T} - 1} \qquad [W.m^{-2}.m^{-1}] \tag{1.3}$$

Spectral phtoton exitance for a number of blackbody temperatures (150K, 298K, 311K and 1273K) are shown in Figure 1.1. These different curves are plotted from Planck's law Equation 1.2.

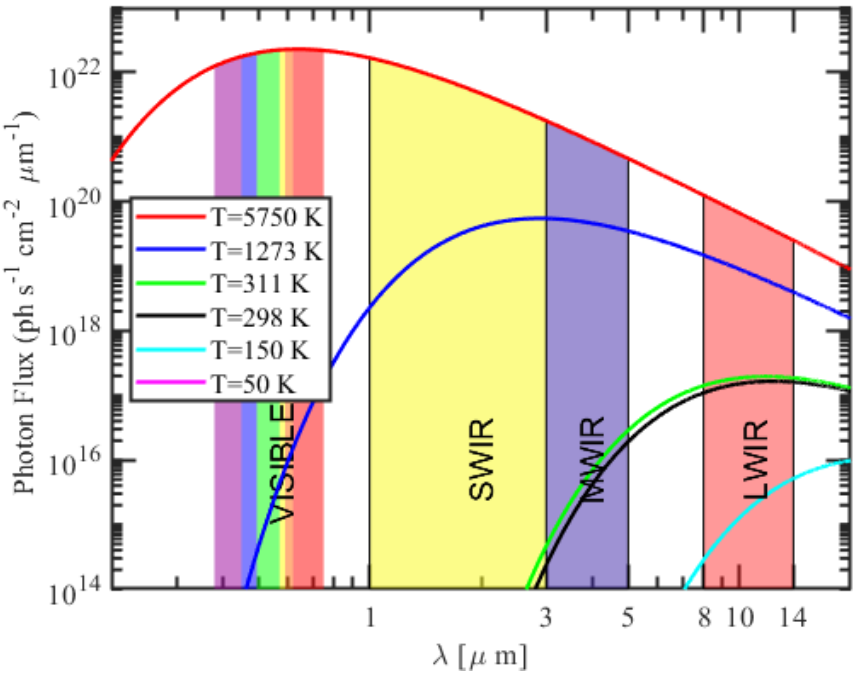

Figure. 1.1 Blackbody's spectral phtoton exitance for different temperatures.

Several observations can be drawn from Figure 1.1. Any body of non-zero temperature therefore emits electromagnetic radiation shifting towards short wavelengths as it heats up. This is indeed what can be observed every day when heating an object, red at the beginning and then white at high temperature, the white color being due to the superposition of all the wavelengths already emitted. This explains why the human eye can see very hot objects (temperatures above 900 K). This is the case for the sun, whose apparent temperature is around 5750K. At room temperature (i.e. 300K), the maximum radiation is located in the infrared and is therefore not visible to the naked eye. The invisible part of the spectrum, however, contains up to 100,000 times more energy (i.e. area under the curve). As the temperature increases, the amount of energy emitted at any wavelength increases while the wavelength of peak emission decreases.

Furthermore, Figure 1.1 shows two important things. First, because at each wavelength spectral phtoton exitance is an increasing function of temperature, curves at different temperatures never intersect. This point is important because it allows, from the spectral energy exitance of a blackbody at a given wavelength, to determine the apparent temperature of this body. In fact, as the temperature of the blackbody increases, the maximum of energy distribution moves towards

increasingly shorter wavelengths according to the law of displacement of Wien, obtained by derivation of the Equation 1.2:

$$\lambda_{max} = \frac{2898}{T}, \qquad [\mu m] \tag{1.4}$$

On the other hand, the importance of the blackbody radiation comes from the fact that objects of terrestrial temperature have a maximum emission in the infrared range. For example Figure 1.1 shows that an object at room temperature ($\sim 25^{\circ}C$) has its maximum emission located at $9.7\mu m$, a human body ($\sim 38^{\circ}C$): $9.3\mu m$, a wood fire ($\sim 1000^{\circ}C$): $2.9\mu m$, the sun ($5750K$): $504nm$. Also, from a detection point of view, lower temperature require measurement to longer wavelengths. In addition, vertical distance between the curves at a given wavelength is greater at short wavelengths ($2\mu m$) than longer wavelengths ($12\mu m$). This means radiation changes much more for a given temperature change at shorter wavelengths, making detectors that operate at such wavelengths more sensitive.

Finally, the total power emitted by a blackbody $P(T)$ or equivalently the **radian flux density** (i.e. integrated with respect to λ of Equation 1.3) only depends on its temperature and increases as the fourth power of the latter.

$$\begin{aligned} P(T)\mathrm{d}A &= \int_{\lambda=0}^{\infty} M_{\lambda}(\lambda, T)\mathrm{d}A \ \mathrm{d}\lambda \\ &= \sigma T^4 \mathrm{d}A \end{aligned}$$

Thus $P(T)$ reads:

$$P(T) = \sigma T^4, \qquad [W.m^{-2}] \tag{1.5}$$

where, $\sigma = \dfrac{2\pi^5 k_B^4}{15h^3c^2} \approx 5.670400 \cdot 10^{-8}$ $[W.m^{-2}.K^{-4}]$ is the Stefan-Boltzman constant. This relationship was discovered by Stefan and Boltzmann in 1879 and allows to determine the exact temperature based on the emitted signal.

1.1.2 Grey-Bodies and Emissivity

Objects that resemble perfectly the behaviour of black bodies are seldom to be found in reality. The ability to emit or absorb photons in a specific proportions depends on the intrinsic properties of each body. Objects that are not blackbodies i.e. greybodies emit only a fraction of blackbody radiation, and the remaining fraction is either transmitted or, for opaque objects, reflected.

For a blackbody the absorptance equals one. At a given wavelength the ratio of infrared energy radiated by an object at a given temperature to that emitted by a blackbody at the same temperature is termed as emissivity. This characteristic often depends on the wavelength. Gray bodies are object for which the emissivity does not depend on the wavelength.

1.1.3 Atmospheric Transmission and Absorption

An essential requirement for all infrared radiation terrestrial application is transmission through air. However, the processes of scattering and absorption attenuates the radiation. The absorption of an electromagnetic wave by the atmosphere is determined by various factors such as the wavelength, the constituents of the atmosphere (CO_2, H_2O in particular), the length of the path or even the climatic conditions. To illustrate this absorption phenomenon, Figure 1.2 shows the spectral transmission through 6000 ft of air (US Standard conditions).

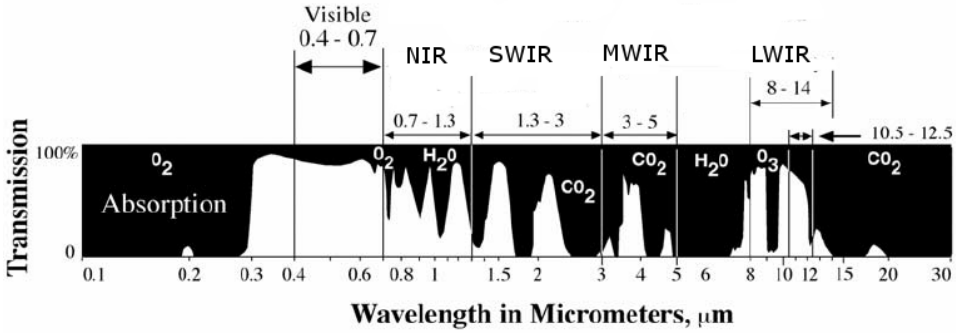

Figure. 1.2 Spectral transmission of the atmosphere under US Standard conditions.

Specific absorption bands of H_2O, CO_2 and O_2 appear clearly in this figure. Water vapor (H_2O) gives the highest infrared absorption. Carbon dioxide (CO_2) is also active, at $\lambda = 4\mu m$, but with less intensity. These atmospheric elements restricts atmospheric transmission mainly to two main windows at $3-5\mu m$ and $8-14\mu m$. Ozone, nitrous oxide, carbon monoxide and methane do absorb radiation but with less important strength. Between these absorption bands, there are spectral bands called atmospheric transmission windows (Figure 1.2). These bands directly specify the infrared detection domains as defined in Table 1.1.

These definitions are not standards, we can find slightly different nominations. In fact, the NearWave InfraRed (NIR) and the ShortWave InfraRed (SWIR) can be combined into one detection band, band I. MWIR (MidWave InfraRed) and LongWave InfraRed (LWIR) can be called band II and band III respectively. Among the different spectral infrared detection domains, the 8-12 μm window is particularly interesting because it covers the maximum emission of

Table 1.1 Spectral infrared detection windows.

Infrared Window	Wavelength [μm]
NearWave InfraRed (NIR)	0.7-1.5
ShortWave InfraRed (SWIR)	1.5-2.5
MidWave InfraRed (MWIR)	3-5
LongWave InfraRed (LWIR)	8-12
Very LongWave InfraRed (VLWIR)	13-20

blackbodies at room temperature (Figure 1.1). In addition, atmospheric transmission in this part of the spectrum is very important (Figure 1.2). This spectral detection range is thus optimal for imaging a scene at 293 K (room temperature). However, in the presence of fog, the atmospheric transmission could be weak at $10\mu m$ than at $4\mu m$, thus a $3-5\mu m$ detector is then possible. According to the blackbody law, this $3-5\mu m$ band is also interesting and more appropriate for detection of hotter objects (emission of carbon dioxide). Regarding Very LongWave InfraRed (VLWIR) band, from Figure 1.1, we can clearly see that the infrared detection at long wavelengths reveals cold bodies whereas, Figure 1.2 indicates poor transmission through the atmosphere for this range of λ. However, this observation is no longer true if we measure the exo-atmospheric transmission (i.e.: altitude> 20 km) of the radiation. VLWIR detection is then performed above the infrared radiation absorption layer. Applications such as astronomy or defence are then targeted.

For each application, it is therefore necessary to know the optimal wavelengths' range for detection. We notice from Figure 1.1 that the infrared detector should be adjusted over a spectral band as wide as possible in order to collect the maximum flux emitted by a given blackbody. However, to determine the temperature of a blackbody, it may instead require measurements at particular wavelengths. The flux received by the detector is also highly dependent on many factors such as weather which led to the use of very different detectors. Today, a new need for infrared detection has also emerged: the ability to detect several wavelengths simultaneously to perform "discrimination", i.e., to distinguish two objects by avoiding imaging them at a single wavelength, which can be confusing. We have thus seen in recent years the emergence of bi-spectral or multispectral detectors which make it possible to associate several spectral detection bands with the same detector [112, 101]. This fundamental information on infrared radiation together width atmospheric transmission requirements, led to the need for detectors sensitive to this radiation, namely infrared detectors.

1.1.4 Infrared Detection Applications

In this section, some applications of infrared detection will be given. Infrared is often limited to night vision, which allows many applications including military (aerial reconnaissance and piloting) and Civil (astronomy, meteorology, automation surveillance and agriculture) fields. However, it should not be forgotten that this spectral range has many other interests: thermal imaging (medical thermography and thermal insulation of housing, ect).

Medical Thermography

Medical thermography involves taking images of body at infrared wavelengths, thus recording thermal emission from the body and facilitating the detection of abnormalities and correlations with health issues (see Figure. 1.4) [bio]. The possibility of imaging minute differences in temperature (relative deviations of the order of one ten thousandth) of a scene makes it possible to clearly distinguish the vascularization of the body (see Figure. 1.4a), opening the way to research on blood flow (see Figure. 1.4c), arterial blockages in legs, some thyroid conditions (see Figure. 1.4b), diagnosis of severe burns or screening for early stage breast cancer (Figure 1.3). It is a non-invasive test that does not involve any harmful radiation [86].

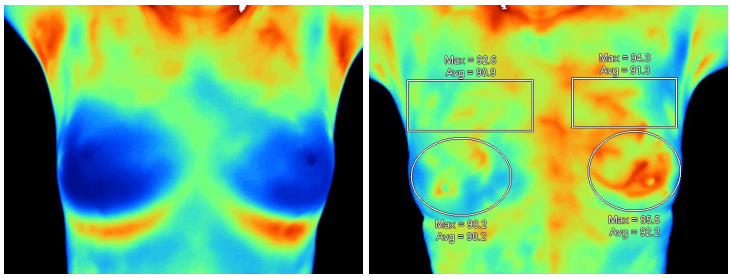

(a) Thermal image of healthy breasts

(b) Thermal image showing abnormalities in the left breast

Figure. 1.3 Benefits of Thermography for Breast Screening

Fire detection

Fires can cause damage to or lose of buildings, forests or facilities in an extremely short time. The value of property damaged in a fire can be considerable, while the death of a person represents an incalculable loss. With their contact-less temperature measurement method, thermography can help prevent fires by detecting early hot spots before they cause ignition. Thermal cameras with aid of a tracking and recognition software system can locate hot spots

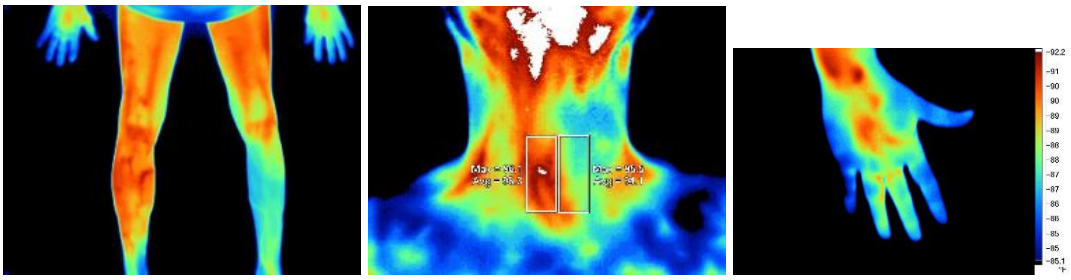

(a) Atrophy, right calf muscle (b) Thyroid Nodule (c) Vasculitis

Figure. 1.4 Some potential application of Clinical Thermography

and then initiate an automated firefighting response, including activating an extinguishing system or closing a system.

Thermal Balance

Infrared images are also a practical means of detecting heat leaks from buildings from a distance and can therefore contribute to their energy recovery. The infrared image reveals substantial, widespread heat loss due to inefficient insulation.

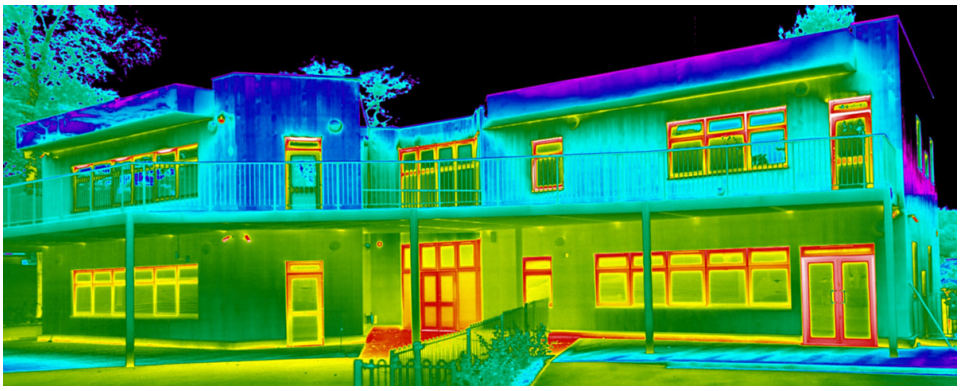

Figure. 1.5 Building Thermography and heat loss surveys.

Vision in foggy weather

Scattering by gas molecules is negligibly small for wavelengths longer than $2\mu m$. In addition, water does not absorb LWIR window which makes infrared vision possible through the foggy weather. This advantage can be exploited, among other things, to make landing aid devices for aviation known as Enhanced Vision System (EVS). EVS systems use an Infrared Radiation (IR)

camera mounted in the aircraft's nose to project a raster image on the head-up display (HUD) (see Fig. 1.6).

(a) Without Enhanced Vision System (b) With Enhanced Vision System

Figure. 1.6 Enhanced Vision System turns night into day and help piltos see through smoke, haze and foggy weather. The suspended water droplets that cause diffusion in the visible are transparent in the infrared.

1.2 Infrared Detector Fundamentals

Infrared detectors are transducers of infrared radiant energy emitted by objects into a measurable electrical signal. By detecting the infrared energy they offer the possibility of seeing in dark or through obscured conditions. The detected energy for each infrared wavelength is then converted to a digital image representing the energy differences between objects of the same scene. Hidden details under regular visible light reveals to the world through infrared lighting. Hot objects appears in a bright view from the typically cooler backgrounds. The visibility is improved in adverse weather conditions.

1.2.1 Classes of Infrared Detectors

The infrared detectors falls into two main classes which correspond to two different detection principles but with identical aim: convert the incident optical flux into a measurable form. The first class called thermal detectors, exploits the dependence of one of the physical properties of a material system on its temperature. Their operating principle is quite intuitive; upon heated by infrared flux their temperature changes which is then measured by any temperature-dependent properties, such as thermoelectric voltage, resistance, or pyroelectric voltage. This class of detectors were the first developed because of its simple principle. The second class is based on electronic transitions caused by the absorption of a photon, and are therefore called quantum detectors or photon detectors. This detector technology is based on the physics of semiconductors and therefore developed since the 1960s.

Thermal Detectors: Thermal detectors converts the infrared flux into heat by absorption. Measuring the thermal variation of a material parameter delivers the output signal. Examples mainly includes: microbolometers, pyroelectric detectors and thermoelectric

detectors. Microbolometers are thermal detectors in which the output signal is linked to the variation in the resistivity of the material as a function of its temperature. Usually, amorphous silicon (a-Si) and vanadium oxide (VOx) are the two most commonly used materials for microbolometers. Since the operation of such detectors involves a change in temperature which is relatively slow process, they have an inherently slow response time (5 à 15 ms) and a relatively low sensitivity compared to quantum detectors. In addition, the output signal does not have a spectral dependence as it does on the incident radian power. These detectors do not need to be cooled, unlike quantum detectors, which gives them a number of advantages due to the absence of a cryogenic coolers: they are lighter, less bulky, less expensive and have a longer service lifetime. The reader interested in a detailed presentation of these class of detectors can refer to the well known monograph of Antoni Rogalski [7]. For applications requiring very short response times, quantum detectors are the first choice.

Quantum Detectors: In this class of detectors, the semiconductor materials respond to infrared radiation by photoexciting electrons between two groups of quantum levels; one conducting and the other non-conducting. The conducting group is usually the conduction band of a semiconductor whereas the later can be a full valence band, a blocking potential barrier (e.g. Schottky barrier) or a quantum bound states (e.g. levels of impurity atoms or artificial quantum well). The observed electrical output signal results from a change in conductivity, voltage or current. The spectral response of quantum detectors exhibit a selective wavelength dependence as well as a very fast response. However they require to be cooled down to cryogenic temperatures to lower thermal generation of charge carriers which compete with their optical counterpart. If the absorbing zone of a quantum detector is unintentionally doped, we speak of an intrinsic detector. On the contrary, if this zone is doped we speak of an extrinsic detector. We go more precisely into the details of the physics of these detectors in the following section.

1.2.2 Quantum Infrared Detectors

1.2.2.1 Different Operating Principles

Quantum detectors are generally classified into two distinct subgroups depending on the electrical measurement to be performed. These are photovoltaic and photoconductive detectors.

a) Photovoltaic Detectors: A photovoltaic (PV) detector relies on the working principle of a **pn** junction inside an inhomogeneous semiconductor, which generates a potential barrier

where a strong electric field is generated and from which the charge carriers are depleted. If the detector is reverse biased, it operates as a photodiode. When photons of sufficient energy propagate through the semiconductor, they can create excess photocarriers in the material (electron-hole pairs). The electron-hole pairs created results in the circulation in the external circuit of a photocurrent. An alternative to the **pn** junction is the **pin** structure shown in Figure. 1.7a. If the reverse bias of the structure is sufficient, a strong electric field exists throughout the intrinsic region, the photocarriers quickly reach their speed limit. This results in very fast photodiodes. In addition, the electric field in the depletion region prevents recombination of carriers, which makes the photodiode very sensitive.

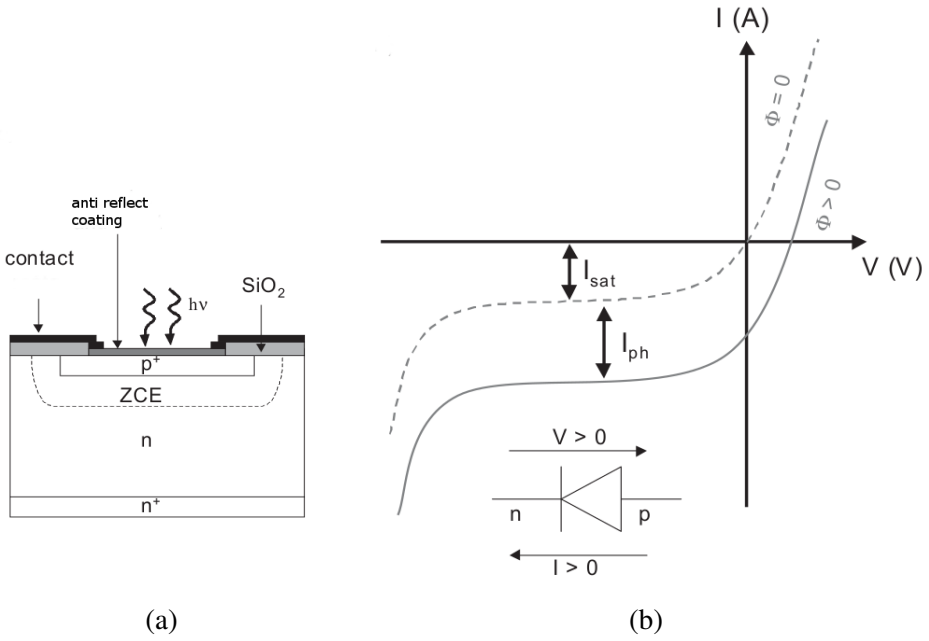

(a) (b)

Figure. 1.7 a) Typical configuration of a photovoltaic detector. b) Current-voltage characteristic of a photovoltaic detector under light and dark conditions.

Figure. 1.7b shows the current-voltage characteristic of a photovoltaic detector (photocurrent operation). This changes when the detector is subjected to a photon flux. We then observe an increase in the current with an excess ΔI representing the photocurrent I_{ph}.

b) Photoconductive Detectors: The photoconductive detector is essentially a homogeneous semiconductor slab either doped or not, with two electrodes attached to the ends. These electrodes are used to apply an electric field across the slab, to collect electrons from one side and to re-inject as much on the other side to ensure the electrical neutrality of the

material. If a photon of energy $h\nu$ greater than the gap energy is absorbed, then a electron-hole pairs are created, thereby increasing the conductivity of the material: this is the photoconduction mechanism. A photoconductive detector is in fact a radiation-sensitive resistor which varies under illumination. An external bias is required to measures this resistance change. So, if the photoconductive detector is biased, the variation in conductivity induced by the illumination results in a current variation $\Delta I = I_{ph}$, see Figure. 1.8. For example, the detectors using Si:Ga are p-type extrinsic photoconductive detectors because of the acceptor type Ga atoms for silicon; i.e. the electronic transition takes place between the valence band and an energy level of an impurity and not over the band gap of the host material. Detectors using multiple quantum wells states are classified under photoconductive detectors in the sense that it is necessary to apply a voltage bias across the sample to extract a signal, in contrast to photovoltaic detectors which have an internal electric field which deliver a current for a zero voltage bias. However, unlike photoconductive detectors, the active layer of a multiple quantum wells detector is made of semiconductors heterostructures.

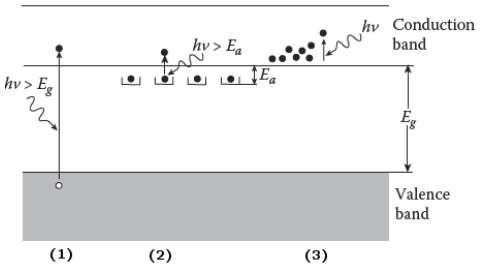

(a) (1) intrinsic (2) extrinsic (3) free.

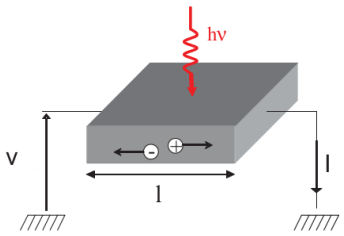

(b)

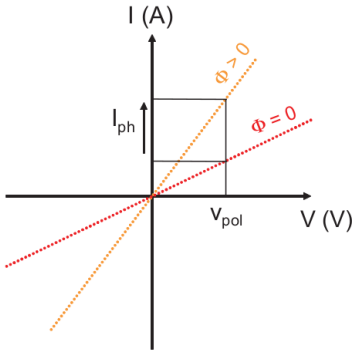

(c)

Figure. 1.8 a) Fundamental optical absorption process in semiconductors. b) Principle of operation of a photoconductive detector. c) Current-voltage characteristic.

1.2.3 Operating temperature problem

The most glaring difference between thermal and quantum infrared detectors is the temperature at which they operate. Unlike quantum detectors, thermal detectors are not sensitive to thermally activated processes such as generation-recombination of carriers. This is the reason why they can operate at room temperature. Their sensitivity therefore depends on the capacity of the absorbent material to modify one of its properties like resistivity under the effect of a photonic flux.

On the other hand, for a quantum detector at room temperature, thermal fluctuation offers the electrons present in the material sufficient energy to cross the gap energy by themselves. Therefore, when it is not exposed to a photonic flux, the detector still presents an output signal known as **dark current**. This current and the associated dark noise limits the operating temperature by degrading the signal-to-noise ratio (SNR). This implies in other words that a detector operating at room temperature "dazzles" itself. The higher the cut-off wavelength λ_C, the lower this temperature must be. The orders of magnitude are between $200K$ and $300K$ for the SWIR, $80K$ to $150K$ for the MWIR and below $80K$ for the LWIR. It is therefore necessary to cool the quantum detectors to cryogenic temperatures ($< 150K$) in order to address the longest wavelengths in MWIR and LWIR. Cooling mechanism is either a cryogen or refrigerant. Cooling the detector requires encapsulation within a vacuum tight enclosure that serves the twin purposes of avoiding condensation and solidification on the detector and prevents cryogen from boiling off too rapidly by convection.

The outside wall of the detector block adds other constraints: being at room temperature, it therefore also emits infrared radiation according to Planck's law (Equation 1.1). In Figure 1.1, we notice that a wall at 300K will thus emit in both the MWIR and the LWIR while a wall at $200K$ will emit only in the LWIR but not the MWIR. It is thus clear that there is also a need to cool the environment of the detector to a temperature which depends on the addressed detection window. This is why in cooled detectors, a cold screen is implemented in order to limit extraneous radiation coming from elsewhere rather than the scene. Figure 1.9 shows the interior of a detector block (which becomes a camera when an optic is added in front of it), evacuated in order to optimize the cooling of the FPA and the cold screen.

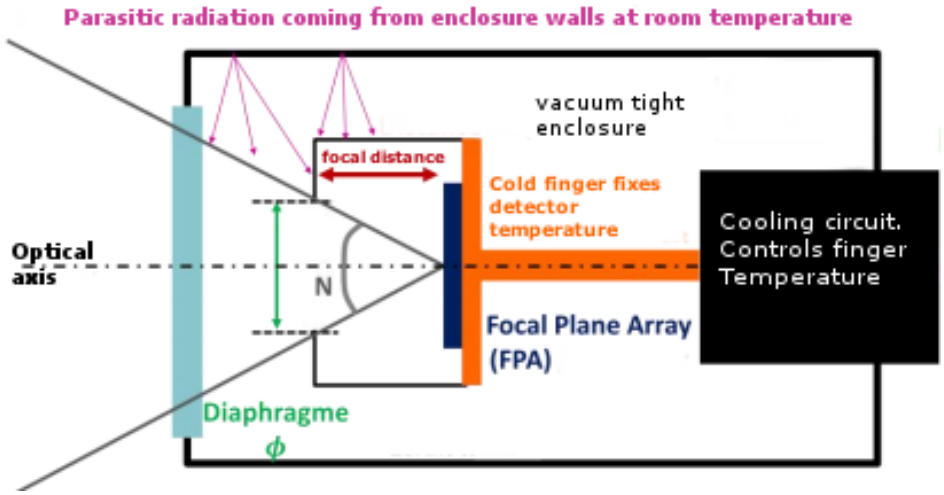

Figure. 1.9 Diagram of a detector block. Elements in direct contact with the cold finger are the FPA and the cold screen.

1.2.4 Quntum Infrared Detectors' Material systems

Various materials and their compositions have been used for infrared detection. The most commonly used material systems are:

1. Direct bandgap semiconductors
    - Binary alloys: InSb, InAs
    - Ternary alloys: HgCdTe, InGaAs
    - Type II, III superlattices: InAs/GaSb, InAs/GaInSb, HgTe/CdTe
2. Extrinsic semiconductors
    - Si:As, Si:Ga, Si:Sb
    - Ge:Hg, Ge:Ga
3. Type I superlattices
    - GaAs/AlGaAs quantum well detectors
4. Silicon Schottky barrier
    - PtSi, IrSi

InSb, GaAs/AlGaAs, HgCdTe and type II superlattices (InAs/GaSb) are amongst the most frequently used material for such systems. For all the material systems mentioned above except the fist, the majority carriers are usually involved by detection. Detectors based on the direct band gap semiconductors list exploit minority carriers.

The manufacturing of optoelectronic components is based on the growth of these semiconductor materials. The main growth techniques used for the fabrication of infrared detectors are chemical vapor deposition from metal-organic compounds (MOCVD: Metal Organic Chemical Vapor Deposition) and epitaxy. The latter involves growing a monocrystalline material on the surface of another monocrystalline material with the same crystal structure and typically the same lattice constant. There are several types of epitaxy such as Liquid Phase Epitaxy (LPE) or Molecular Beam Epitaxy (MBE). In order to be able to grow one semiconductor over another, the materials must have similar lattice constants. If this condition is not fulfilled, growth is accompanied by the development of strain (tensile or compressive), which is usually one of the reasons for poor crystal quality. Figure. 1.10 shows the lattice constant and the corresponding band gap energy for column IV semiconductors and for III-V and II-VI compounds. We note immediately that some materials have similar lattice constants, while having very different electronic properties; this is the case for example with the group (Ga, Al, As), or even (Cd, Te, Hg). The crystalline property is particularly interesting since it ensures the possibility of epitaxially growing ternary alloys (AlGaAs or HgCdTe) on GaAs or CdTe substrate respectively.

For the heterostructure $Al_xGa_{1-x}As$ we note a difference of 0.16 % in lattice constant between GaAs ($a = 5.653$) and AlAs ($a = 5.662$). This crystallographic similarity ensures the growth of alternating layers (superlattice) of GaAs and $Al_xGa_{1-x}As$ with no structural defects and regardless of the Al composition x. A closer look at the electronic properties of GaAs and AlAs materials, reveals a clear difference in the value of E_g. The gap of $Al_xGa_{1-x}As$ then varies between the gap of GaAs (1.42 eV) and that of AlAs (2.3 eV) in proportion to the concentration x of aluminum (for $x < 0.45$).

The ternary material system $Hg_{1-x}Cd_xTe$ (Mercury,Cadmium Tellurium) is an alloy between CdTe and HgTe. These two binary compounds crystallize in a face-centred cubic structure with very similar lattices constants (6.4815 and 6.46152 respectively). In fact, the difference in lattice constants between these two binary materials is very small, of the order of 0.3%. By controlling the proportions x of cadmium and $1-x$ of mercury, we obtain the semiconductor material $Hg_{1-x}Cd_xTe$ with the possibility of changing the band gap between the two binary original materials. This alloy allowed the band gap and hence the spectral response range to be tailored for specific applications.

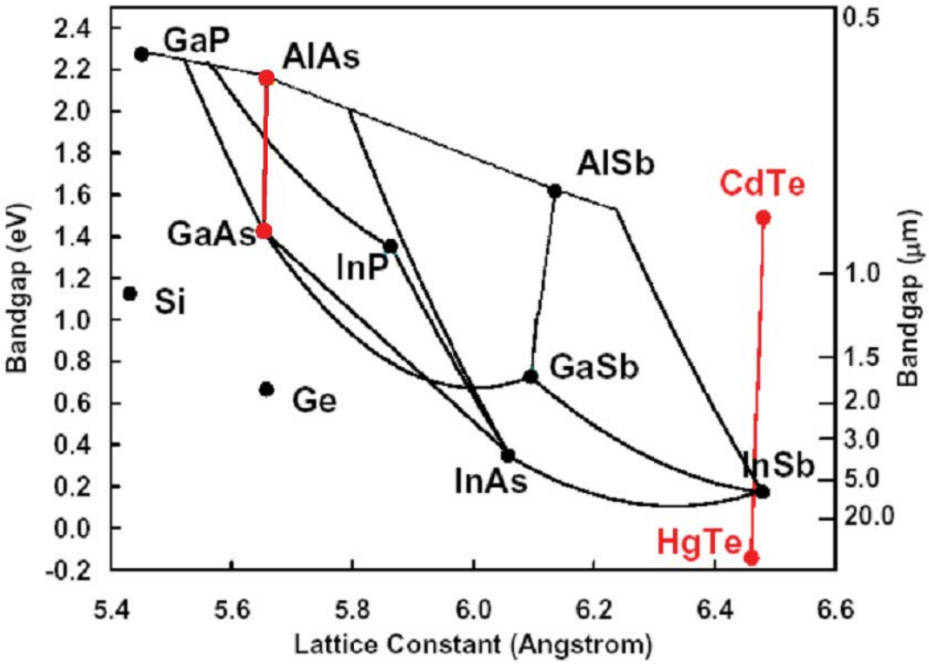

Figure. 1.10 Band gap plot of common semiconductor materials versus crystal lattice constant.

Type II Superlattice (T2SL: Type-II Superlattice) are metamaterials, whose valence and conduction bands are artificially created by the stacking of thin layers of $In_xGa_{1-x}As_ySb_{1-y}$, on GaSb substrates. The hybridization of the electronic states of the heterostructure is such that mini-bands are created for the holes and the electrons. The engineering of the bands allows the variation of the gap of the metamaterial. Importantly, The $Hg_{1-x}Cd_xTe$, $Al_xGa_{1-x}As$ and $In_xGa_{1-x}As_ySb_{1-y}$ heterostructures are of particular interest because they demonstrated the most successful realization of infrared quantum detectors during the last two decades.

1.2.5 Detection Arrays and Readout Circuit

Thermal image is a temperature-difference representation of the scene obtained by scanning an optically focused image of the later over a number of infrared detectors: single element detectors, linear arrays or two dimensional (2D) focal plane arrays (FPAs). This scan is made either mechanically or electronically and then the output of detectors is converted into a visual image. The resolution of the thermal image is mainly determined by the size of the detector array (the number of picture elements -pixels-). Currently, the infrared FPAs are designed according to a hybrid architecture of the type presented in Figure. 1.11. They are composed of two main parts, namely the NxM detector array which absorbs and converts the photons flux into electrons and the Silicon readout integrated circuits (ROIC) which reads and processes the

signal from each detector to convert it into an electronic measurable form (by amplification or digital filtering). Hybrid architecture means that the detector array and the ROIC are not technologically compatible. This architecture provides two advantages. First, it allows use of the material best suited for the detection while benefiting from the maturity of silicon technology in the field of signal processing (CMOS technology). Secondly, it allows us to reach optical fill factors as high as hundred percent (fraction of the detector's surface effectively dedicated to detecting IR photons).

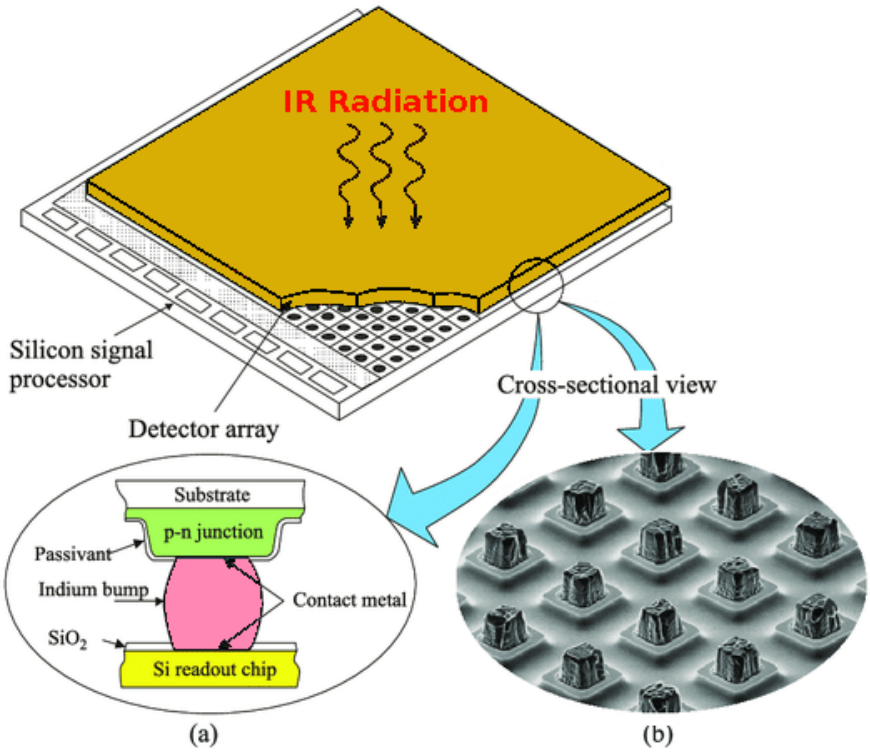

Figure. 1.11 Schematic representation of a hybrid array detector. (a) Indium bump technique, (b) SEM micrograph shows mesa photodiode array with Indium bumps after adaptation from [110]

The most common technique used to connect each detector-array element to its respective signal path on the ROIC uses indium bumps interconnections. This technique is known as the flip chip technology which is the most used architecture in the hybrid array technology. A high optical fill factor is easily obtained with this technique [97]. Note that the ROIC is an essential element of the FPA which strongly influences its performance. Thus, to meet the increasing demanding needs in term of uniformity, sensitivity and reliability , circuit designers'

imagination have led to a more sophisticated ROICs. In fact, ROICs have been loaded with functions comprising noise reduction or with analog-digital conversion functions [85].

Different technological steps required for manufacturing of detector arrays are shown in Figure. 1.12. Building FPAs with hybrid architecture is part of a long cycle ranging typically from several months to a year.

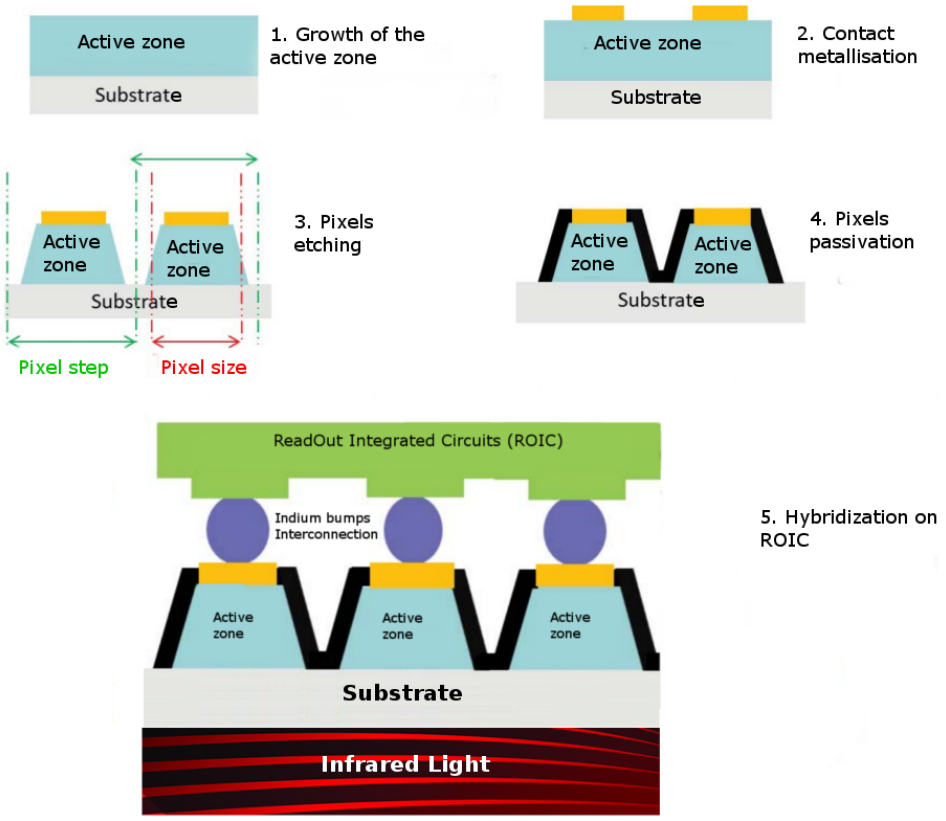

Figure. 1.12 Schematic representation of the main fabrication steps of an infrared FPA detector.

1.2.6 Quantum Infrared Detector Figures of Merits

We have mentioned in Section 1.1.3 that each object has its own thermal "identity" or thermal signature, not only due to infrared radiation it emits, but also to the phenomena of reflection and scattering on its surface. In addition, informations on how to choose a spectral band for detection as a function of the observed scene has been given. The differences in thermal signatures of objects has led to the development of different kind of quantum detectors targeted to specific application. Bearing this in mind, we consider how to determine the most suitable detector for a particular application. This choice is often difficult because it depends on a

large number of parameters often referred to as **Figures of merit**. The latter have been defined which allow to characterize the performance of quantum detectors. The manufacturers usually describe the performance of their detectors in these terms. In the following, the most used figures of merit will be presented in brief.

1.2.6.1 Dark Current

The dark current corresponds to the current flowing in a biased detector in the absence of a light source: it is an offset which is added to the signal current (this being linked to the flux coming from the scene).

$$\mathrm{J_{dark}} = \frac{\mathrm{I_{dark}}}{\mathrm{S}} \quad \left(\mathrm{A/cm^2}\right) \tag{1.6}$$

Where I_{dark} is the dark current and S is the surface area of the detector. The dark current density is generally measured as a function of the bias voltage applied to the detector, and as a function of its operating temperature, for a given detector size. The analysis of these current measurements allow us to identify the volume and / or surface origins of the dark current. This gives valuable information to manufactures to improve the various stages of production from epitaxial growth of layers up to the detector final product.

The infrared community often uses Rule07 [129, 130, 94] presented in Figure. 1.13 and Figure. 1.14 to compare, in terms of dark current, the performance of the technological design of detectors to that of the MCT empirical benchmark. This is an empirical law (established in 2007) extracted from I_{dark} measurements of MCT photodiodes. Its range of validity is for $I_{det} > 77K$ and the product $\lambda_c I_{det}$ between 400 and 1700 µm K. There are two common ways to represent the Rule07. The first, shown in Figure. 1.13, compares dark current densities as a function of wavelength at a given operating temperature. The second represents this same current density as a function of the inverse of the product of the operating temperature and the cut-off wavelength of the detector (as can be seen in Figure. 1.14). The advantage of this representation is that it allows more detectors to be incorporated for inter-design comparison, with different choices of operating temperatures (which impacts the dark current density).

1.2.6.2 $\mathrm{R_0A}$

In addition, since the dark current density is dependent on the voltage applied to the diode, it is possible to use another widely used figure of merit known as R_0A, defined as follows:

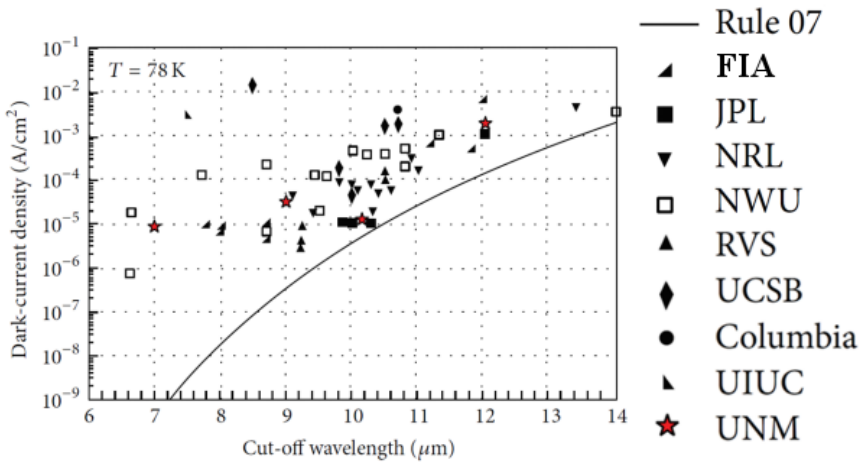

Figure. 1.13 Dark-current density of T2SL detectors compared with Rule 07 [102]. Abbreviations for the different institution working on T2SL detectors: FIA, JPL, NRL, NWU, RVS, UCSB, Columbia, UIUC, and UNM.

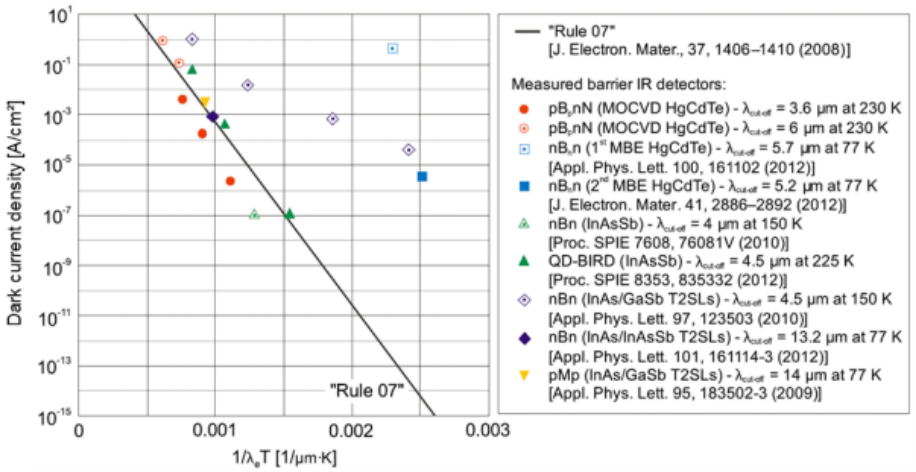

Figure. 1.14 Dark current density as a function of the inverse of the product of the operating temperature and the cut-off wavelength of the detector from a given technology and design [63]. This compares to MCT's state of the art in terms of dark current density.

$$\mathrm{R_0A} = \left(\frac{\partial \mathrm{J_{dark}}}{\partial \mathrm{V}}\right)^{-1}_{\mathrm{V=0}} \quad \left(\Omega/\mathrm{cm}^2\right) \tag{1.7}$$

Where V is the applied potential. So we look to maximize R_0A. This figure of merit allows us to account for the detector noise in dark conditions.

1.2.6.3 Quantum efficiency

Another common figure of merit for optical detectors is the quantum efficiency. Quantum efficiency is the ratio between the number of hole-electron pairs collected and the number of photons received by the structure, quantifying the ability of the detector to convert a photon into an hole-electron pair. If, over a period of time, 100,000 photons are incident on the detector and 10,000 hole-electron pairs are produced, the quantum efficiency is 10%. A low Quantum efficiency can be due to a low absorption in the material, or poor collection of photogenerated carriers. The experimental study of the spectral quantum efficiency thus allows to optimize the absorption zone and the overall structure of the detector. For example, by changing the doping type (N or P), we change the nature of the minority carriers which contribute to the quantum efficiency. The quantum efficiency η may be related to the responsivity R by the equation:

$$R(\lambda) = \eta(\lambda) \times \frac{q\lambda}{hc}. \tag{1.8}$$

with q the elementary charge, h the Planck constant, c the speed of light in a vacuum. This corresponds to the detector output per unit of input power. The units of responsivity are either Amperes/Watt (alternatively milliamperes/milliwatt or microamperes/microwatt, which are numerically the same) or Volts/Watt, depending on whether the output is an electric current or a voltage. The responsivity is an important parameter that is usually specified by the manufacturer. Knowledge of the responsivity allows the user to determine how much detector signal will be available for a specific application.

1.2.6.4 Specific Detectivity

Specific detectivity is the figure of merit which explains the signal-to-noise ratio and which is therefore used for IR detectors.

$$D^*(\lambda) = \frac{q\lambda}{hc}\eta\sqrt{A_{\mathrm{det}}\frac{\Delta f}{\sigma_{\mathrm{tot}}}} \tag{1.9}$$

with λ the wavelength, η the quantum efficiency, σ_{tot} the total noise, f the bandwidth of the amplifier (which is part of the reading circuit), A_{det} the detector surface, h the Planck constant, c the speed of light in a vacuum. The unit of specific detectivity is the **Jones** ($\text{cmHz}^{1/2}\text{W}^{-1}$). The more efficient the detector, the higher this merit function.

1.2.6.5 Noise Equivalent Temperature Difference: NETD

Finally, a figure of merit generally used to characterize cameras (FPAs), is employed which is sometimes used by extension for single detectors. It corresponds to the smallest temperature difference ΔT (expressed in Kelvin) that the detector is able to detect. The NETD, in other words is the difference in temperature of the black body used as the incident signal in such a way that the signal to noise ratio is equal to 1. The lower the NEDT the greater the sensitivity of the detector, but carries the disadvantage of being very dependent on the measurement conditions (opening of the cold screen, integration time, etc.).

In summary, if the detector shows higher performance as measured in terms of the above figures of merit as a single element, we switch to focal plane arrays. It is then necessary to undertake again the work carried out in single element in order to make sure that the properties highlighted previously remain valid where the FPAs are concerned.

Chapter 2

Quantum Infrared Detectors: A literature survey

In the present chapter we review the state of the art of most successful quantum infrared detectors technologies namely HgCdTe, GaAs/AlGaAs Multiple Quantum Wells and Type-II superlattices (T2SLs) Photodetectors. The limiting performances' factors are addresed and discussed.

2.1 Inroduction

The history of the infrared detection probably begins with the discovery of infrared radiation by Herschel in 1800. Since then, many detectors have been designed and investigated in order to observe and exploit infrared radiations. Figure. 2.1 shows the developmental history of the technology of infrared detectors over four generations: first generation (scanning systems which does not include multiplexing functions), second generation (staring systems-electronically scanned), third generation (staring systems with large numbers of pixels and two-color functionality), and fourth generation (staring systems with a very large number of pixels, multi-color functionality and other on-chip functions, e.g. better radiation/pixel coupling, avalanche multiplication in pixels, polarization/phase sensitivity) [113].

At present three main detectors' technologies are competing: Mercury Cadmium Telluride (HgCdTe) or (Mercury Cadmium Telluride (MCT)) Photodetectors, GaAs/AlGaAs based Multiple Quantum Well Infrared Photodetectors (QWIPs) and the relatively new emerging Type-II superlattices (T2SLs) Photodetectors based on III-V semiconductors. However, there are other quantum detectors worth mentioning such as Quantum Cascade Detectors (QCD), Quantum Dot Infrared Photodetector (QDIP) and Dot-in-a-Well (DWELL).

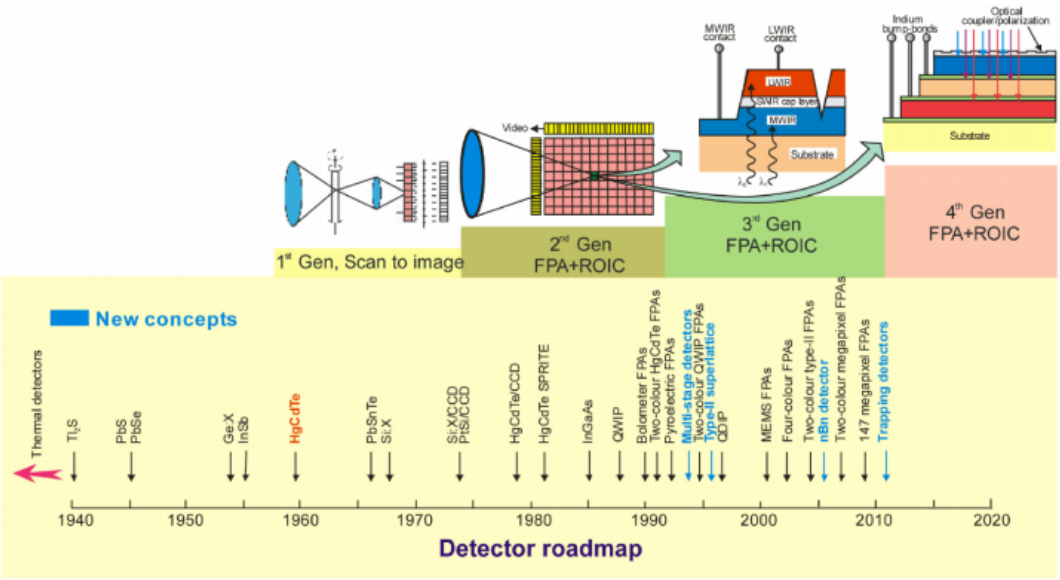

Figure. 2.1 Developmental history of the technology of infrared photodetector: first generation (scanning systems), second generation (staring systems, electronically scanned), third generation (staring systems with large numbers of pixels and two color functionality), and fourth generation (staring systems with a very large number of pixels, multi-color functionality and other on-chip functions).

2.2 HgCdTe Technology

The MCT quantum detectors belong to the class of photovoltaic detectors whose operating principle is described in Section 1.2.2.1. The electronic transition within this detector takes place between valence band and conduction bands (Figure. 2.2). The absorbed photons give rise to electron-hole pairs in a Space Charge Zone (SCZ). This technology offers many advantages; mainly wavelength tunability and multicolor capabilities. In in particular, one can tune the cut-off wavelength as a function of the mercury composition. In addition, it has a high absorption coefficient and low recombination rates, making it a very good detector.

In fact, the MCT stands out from other technologies through its presence in SWIR, MWIR and LWIR (80% for $T = 210K$ in SWIR [28], 70% for $T = 150K$ in MWIR [128] and 70% for $T = 81K$ in LWIR [3]) at a competitive quantum efficiency. Therefore, this technology covers a wide range of applications including multi–spectral detection needs, as far as efforts are made to increase its operating temperature. However, the main motivations to replace MCT detector are technological problems of HgCdTe material. One of them is a weak Hg-Te bond, which results in bulk, surface and interface instabilities. Moreover, uniformity and yield are still issues, especially in the VLWIR window. Finally, surface passivation must be well

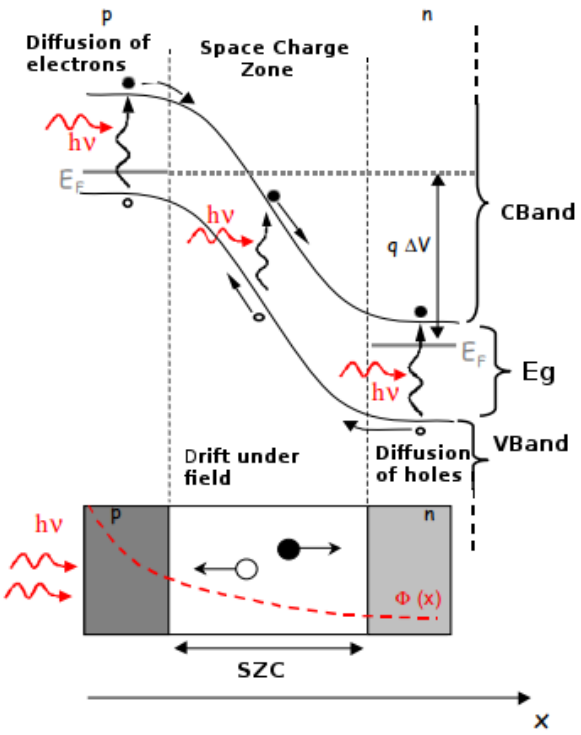

Figure. 2.2 Principle of operation of an HgCdTe quantum detector. SCZ : Space Charge Zone; E_F: Fermi level; $\phi(x)$: photon flux crossing the material ; ΔV: potential difference applied to the detector.

controlled in order to limit leakage currents. There is a wide variety of FPAs formats and pixels pitchs, with a trend to increase the size formats while decreasing the pixel pitch length. The state of the art corresponds to FPAs of: 4096×4096 size with pitchs of $18\mu m$ in the SWIR ($\lambda_c = 2.5\mu m$, $T = 80K$) [127], 2096×2096 size with pitchs of $10\mu m$ in the MWIR ($\lambda_c = 5.3\mu m$, $T = 37K$) [Teledyne] and 1024×768 size with pitchs of $16\mu m$ in the LWIR ($\lambda_c = 10m$, $T = 90K$) [Leonardocompany].

2.3 QWIPs Technology

Quantum Wells based Infrared Photodetectors relay on Inter-SubBand Transitions (ISB) in quantum wells or intersublevel in quantum dots are considered extrinsic in the sense that quantum wells replace impurity atoms in conventional extrinsic photoconductor. In such photodetectors, free carriers excited from doped quantum wells by infrared light provide the output signal. These free carriers are initially brought to the quantum wells by adding dopants to the active layer. Among the intersubband detectors, the QWIP: Quantum Well Infrared Photodetector, is the most widespread technology. The absorption takes place between two sub-bands of a quantum well: i.e between the fundamental sub-band and an exited sub-band most often in resonance with the barrier hight of the well (resonant absorption Figure. 2.3).

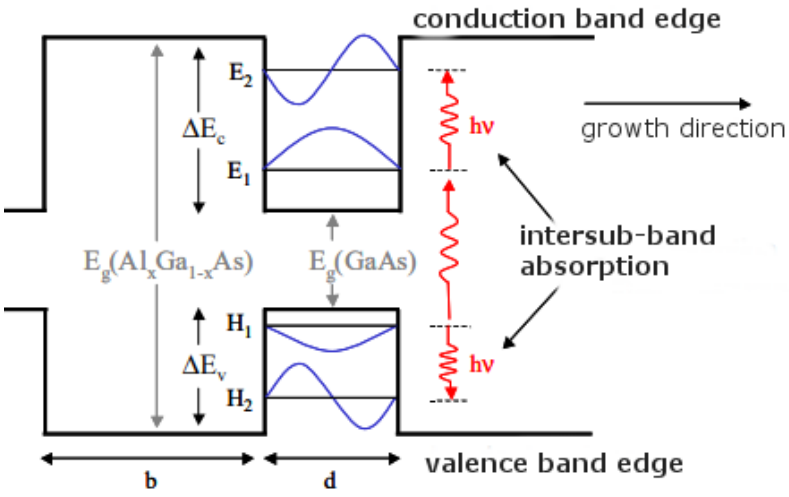

Figure. 2.3 Band diagram of a quantum well. Intersubband transitions between the energy levels of the conduction band or the valence band.

This unlike bulk detectors, makes QWIPs unipolar devices in which electronic transitions involve only a single type of charge carrier, electron or hole within the conduction or valence band. Another fundamental difference is that they allow for transitions with photon energies

lower than the band gap energy of the well material. Therefore, detection of long wavelengths is possible. The quantum well is created by surrounding on both sides a thin layer of lower band gap material by a material of a larger band gap (the barrier). When the width of the well is sufficiently small, the motion of the electrons in the well is restricted and thus quantized in the direction of growth of the materials. On the other hand, the transversal motion of the electrons remain free in the two other directions. The absorption will then be possible if and only if the incident electromagnetic electric field has a none null component in this direction. The QWIPs detectors consist of a number of identical quantum wells, each with a well of width d and a barrier of width b larger than the well width. To create a photocurrent, the excited electron must cross the absorption zone toward ohmic contacts placed on both sides of the structure. This transport is carried out by drift above the potential barrier using an applied bias on the contacts. The structure of quantum well detectors is shown in Figure. 2.4. Increasing the number of quantum wells serves to increases the total absorption and quantum efficiency of the device.

An important property of the QWIPs is the ability to vary the binding energy of electrons to match the desired IR response by changing quantum well depth and width. Therefore, they are naturally adapted to multi-color applications from MWIR to VLWIR windows. QWIPs based on GaAs/ AIGaAs material system also benefit from the mature III-V semiconductor technology which offer high quality, excellent uniformity, large formats, high yield and thus low cost, more thermal stability, and extrinsic radiation hardness [69]. Another feature of these detectors are their narrow spectral response. It then becomes preferable to compare QWIPs in terms of peak wavelength $_{pic}$ (commercially adjustable up to 11 μm [Irnova]) and spectral width $\Delta\lambda$. However, QWIP detectors have low quantum efficiency and low operating temperature. Quantum efficiency is limited by a number of factors. Because the dopant concentrations of each well are limited by the epitaxial growth processes, then each well contains few electrons which results in a weak absorption cross-sections. In addition, the Quantum efficiency of QWIPs is limited by the fact that free carriers are recaptured before travelling the full width of the stack due to inherently short intersubband lifetimes of carriers τ $10^{-11}s$. The minority carrier lifetime in HgCdTe materials is much longer, typically τ $10^{-6}s$. Quantum mechanical selection rules limit infrared absorption to radiation with electric field polarized perpendicular to the quantum well. QWIPs use an optical coupling structure (in general, a 2D diffraction grating) to allow absorption at normal incidence. Despite this, their quantum efficiency remains poor compared to other technologies operating in the same spectral band [70]. Compared to intrinsic photo conductors and bolometers, QWIPs have a higher thermionic emission rate (thermally stimulated carriers from the QW), which results in high dark currents. Therefore, their operating temperature are lower then 60k. The largest FPA format was produced by the

JPL [120]. It is a bispectral QWIP ($4-5\mu m$ and $8-9\mu m$ windows) in 1024×1024 format with $30\mu m$ pitchs operating at $60K$. However, the largest FPA commercially available is in 640×512 format with a $15\mu m$ pitch [48] ($\lambda_C = 8.5\mu m$, $\Delta\lambda = 1\mu m$, $T = 70K$).

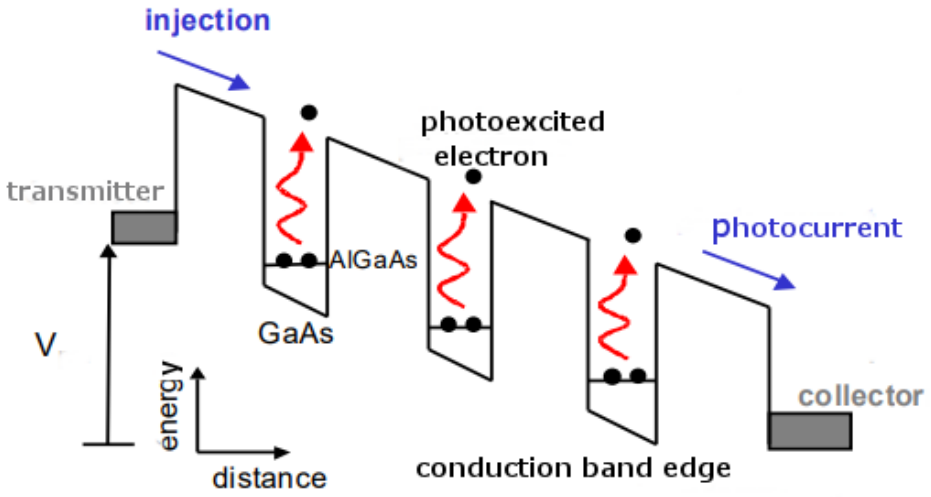

Figure. 2.4 Schematic representation the conduction band edge of a QWIPs under an applied bias. The absorbed photons promotes electrons to the excited level (conduction band), where they are swept away by an applied electric field to produce the photocurrent.

2.4 Type-II SuperLattice Technology

Finally, the InAs/GaSb superlattice technology, also known as Type-II superlattices (T2SLs). This is a relatively new emerging technology which aims to compete with the MCT, both in terms of performance and spectral ranges. The work in this these is mainly focuced on Type-II superlattice (T2SL) detector technology. Type-II superlattices (T2SLs) infrared photodetectors, based on III-V semiconductors, are grown by mature growth and fabrication technologies and favorable spatial uniformity over large areas. In addition, they have great potential for LWIR/VLWIR spectral ranges with performance comparable to HgCdTe with the same cutoff wavelength. Section 2.5 review T2SL technology in more detail. The current formats are 640x512 pixels with 15 μm pitchs in MWIR ($\lambda_c = 5.2\mu m$, $T = 140K$) [38] and 640×512 pixels with 15 μm pitch in LWIR($\lambda_c = 9.5\mu m$, $T = 77K$) [57].

2.5 Type-II Superlattices

Proposed in 1980s [117, 25, 121], the InAs/$Ga_{1-x}In_xSb$ (InAs/GaInSb) T2SL are still gaining a lot of interest regarding infrared (IR) detection applications. InAs/AlSb superlattices, GaSb/AlSb superlattices or any combination of these compounds are other examples of such classes of superlattices. This kind of superlattices are made using a periodic stack of heterojunctions between InAs layers and one of the two antimonides layers GaSb and AlSb or the ternary strained compound GaInSb. The stacking of a large number of these heterojunctions allows the creation of as many coupled quantum wells on account of different band alignment among the constituent materials. All the three binary semiconductors InAs, GaSb and AlSb are approximately lattice-matched around 6.1 Å. Their heterostructures offers band alignment that are drastically different from those of the more widely studied GaAs/AlGaAs material system. Figure. 2.5 shows the three possible types of band alignment: Type-I nested, Type-II staggered and Type-II broken gap (also known as type-III). In type-I nested superlattices such as GaSb/AlSb or GaAs/AlGaAs (not shown in Figure) superlattices, the electrons and holes are both confined within the same layers. In Type-II staggered superlattices like InAs/AlSb superlattices, the conduction band of InAs is slightly above the valence band of AlSb.

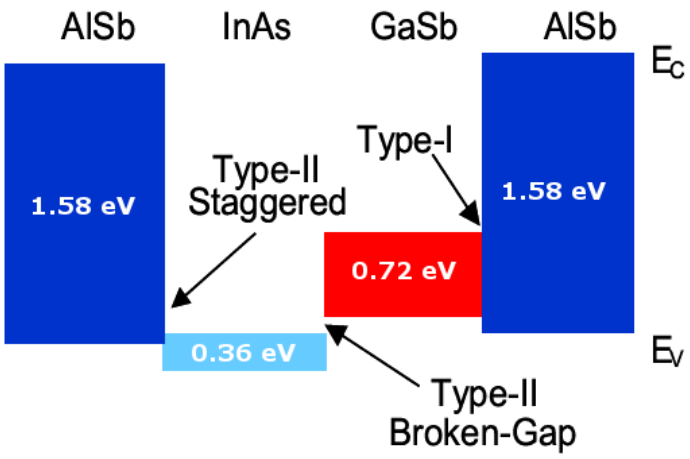

Figure. 2.5 Schematic representation of the band alignments in the nearly matched InAs/GaSb/AlSb material system. The solid rectangles indicate the relative position of energy gaps and band edges of the different materials among each other.

The most exotic alignment is that of InAs/GaSb heterojunctions with a **broken gap type II** alignment in which the conduction band edge of InAs lines up at a lower energy than the top of the valence band of GaSb. In such a heterostructure, the wave function of lowest InAs conduction subband and the highest GaSb valence subband are spatially delocalized in two different quantum wells formed on both sides of the heterointerface. Furthermore, these

wave functions are overlapping since there is either only a very small energy gap between the electrons in one layer and the holes in another layer or none at all. This overlap of electron (hole) wave functions between adjacent InAs (GaSb) layers leads to the formation of an electron (hole) minibands in the conduction (valence) band shown in Figure. 2.6 . This results in an unusual tunnelling-assisted radiative recombination transitions and novel transport properties. Optical transition in InAs/GaInSb T2SLs based detectors, takes place between the highest hole (heavy-hole) and the lowest conduction minibands.

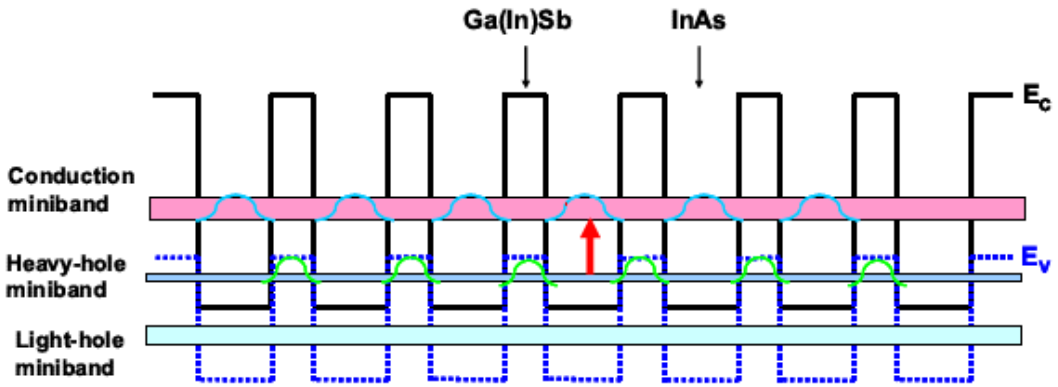

Figure. 2.6 Shematic energy band diagram of broken gap InAs/GaInSb T2SL. The effective gap of the structure is defined between the top of the first heavy holes (HH1) miniband and the bottom of the electrons miniband. The vertical arrow indicate the infrared transition.

Owing to many optical and electronic properties, InAs/GaInSb T2SL are being investigated as an alternative to the HgCdTe IR material systems. In this system, the effective band gap can be varied continuously by varying the thickness of one or two T2SL constituent layers. Therefore, the corresponding detection wavelength of the T2SLs can be tuned between 3 µm to 32 µm. Figure. 2.7 shows an example of the wide tunability of the T2SL.

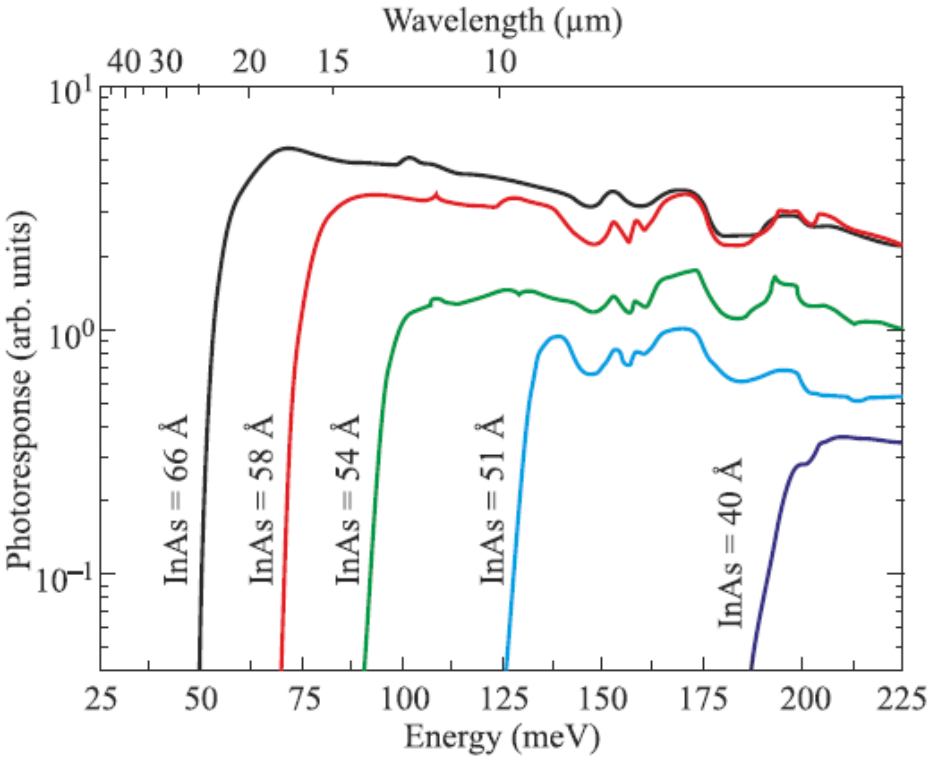

Figure. 2.7 Experimental cutoff wavelengths of InAs/GaInSb T2SL as a function of InAs thickness while GaSb is fixed at 40 Å. [111]

The electron effective mass for a 12 μm cutoff InAs/GaInSb T2SL is within the range (0.02–0.03) m_0 which is larger compared to 0.009 m_0 in HgCdTe alloy with comparable cutoff wavelength. This effective mass is large enough to reduce band-to-band tunnelling currents (being inversely proportional to the effective mass) in the T2SL and still small enough to ensure good mobility. Since the SL effective mass depends on the layers' material properties, sequences and thicknesses, a compromise is therefore to be found in the SL design according to the target application. Despite the small Oscillator strength of InAs/GaInSb T2SL, its absorption coefficient is comparable to that of MCT due to the higher joint density of states.

In addition, InGaSb layers of InAs/GaInSb T2SL are subjected to biaxial compression strain causing splitting of heavy-hole (HH) and light-hole (LH) minibands which with the effective mass being enhanced, reduces the Auger recombination rate and thereby enhances carriers lifetime which in turn reduces dark current (being inversely proportional to carriers lifetime) [131, 133]. It is worth mentioning that both InAs/GaSb and InAs/GaInSb superlattices are sometimes referred to them as strained superlattices in literature. This is true, because for InAs/GaSb SLs, the slight lattice mismatch (0.7%) between InAs and GaSb can lead to sufficient strain build-up to affect material quality in thick SLs. For InAs/GaSb SLs grown

on GaSb substrate, an InSb-like interfaces can be formed intentionally or unintentionally to provide strain balance. The InAs/GaInSb SLs which uses the ternary material GaInSb is intentionally strained for the purpose of increasing the Oscillator strength. The InAs/GaSb SLs minimally strained may have material quality advantages compared to its strained counterpart InAs/GaInSb SLs.

Indeed, all these properties including lower leakage currents and greater uniformity make InAs/GaInSb superlattices an attractive material system for infrared detection. However, they have not yet exceeded the performance of HgCdTe detectors because of a high level of dark current. Figure. 2.8 compares the darkcurrent in different infrared photodetectors with various absorber materials.

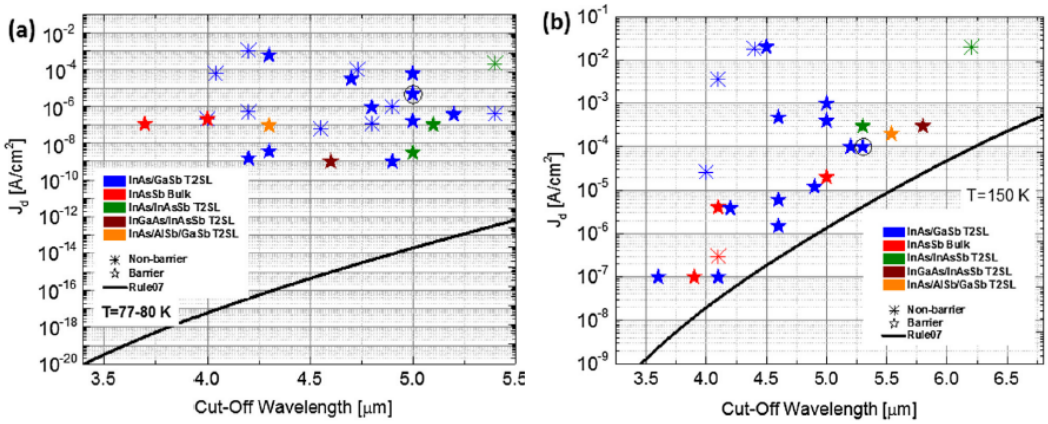

Figure. 2.8 Experimental dark current density of InAs/GaInSb T2SL MWIR detectors at (a) 80 and (b) 150 K. The Rule07, MCT dark current density is shown with solid black lines [49].

The high dark current exhibited by InAs/GaInSb T2SL is attributed to short carrier lifetimes limited by Shockley-Read-Hall (SRH) centers. At present, the measured carrier lifetime is below 150 ns in both MWIR and LWIR designs [131, 125]. It has been suggested that native defects associated with GaSb are responsible for the SRH-limited minority carrier lifetimes observed in InAs/GaSb T2SLs [123]. The promise of Auger suppression has not yet been observed in practical device material. These drawbacks are attributed to problems in material growth, processing, substrate preparation, and device passivation.

More recently, the InAs/InAs$_{1x}$Sb$_x$ (T2SL) also known as "Ga-free" InAs/InAsSb T2SL has been shown to be a potential alternative comparable to the InAs/GaInSb T2SL for infrared photodetectors due to their much enhanced recombination lifetimes in both the MWIR and LWIR spectral range [122, 90]. It is clear that the minority carrier lifetime is a crucial factor for the IR detector performance which reflects the quality of the infrared absorbing material and improves the device performances. Therefore, an understanding of the link between

material properties, device properties, and device performance opens up potential avenues for improving T2SL performance. Some of the fundamental investigations that are important for the development of this technology includes the theoretical calculation of InAs/GaSb superlattice optical properties via realistic band structure modelling, effect of interface types and the cross-sectional scanning electron imaging. Such investigations are still in continuous development and are the subject of many studies including the work presented in this thesis.

2.6 Detector Designs based on type II Superlattices

Despite the enormous efforts devoted to improve infrared photodetectors performances in terms of the absorber fundamental material properties, their performances remains relatively modest. The operating temperatures of photodetectors based on the traditional homojunction designs is still much lower than 300 K [80, 132]. During the last two decades, there has been considerable progress towards detector design innovations for further performance enhancement. In particular, developed **unipolar barrier** device architecture such as the **nBn** [78, 93], the **XBn** [56], and **CBIRD** the Complementary Barrier Infrared Detector [135, 137, 133] have provided an effective means for addressing low operating temperature problems. In the following we briefly review high-performance unipolar barrier infrared detectors based on T2SL absorbers.

2.6.1 Uniplor Barrier Detector Architecture

Historically, the idea of barrier detector was first proposed by Anthony White in a patent in 1983 as a high impedance HgCdTe photoconductor [2]. Later on, Gary Wicks and Shimon Maimon in 2006, proposed AlAsSb unipolar barrier of type nBn for bulk InAs absorber [78]. It has been demonstrated in InAs, InAsSb, InAs/GaSb typeII superlattices (T2SLs) [136] and in HgCdTe ternary alloy [43]. The “unipolar barriers” are designed to block the motion of one carrier type but allows the unimpeded flow of the other by incorporating a large bandgap thin layer(see Figure. 2.9). In general, the barrier detector architectures serves to suppress SRH generation-recombination and surface leakage dark currents [78, 93, 135, 137, 133], which are the two main dark current mechanisms that have plagued III-V semiconductor infrared detectors. Among different types of barrier detectors, the nBn type is the most famous one which serves to blocks majority but not minority carriers without impending photocurrent. The band edge structure of a detector implemented with nBn barrier is shown in Figure. 2.9b.

The nBn detector is composed of an ntype narrow bandgap absorption zone, separated from the n-type contact layer by a material with a bandgap energy much higher than that of

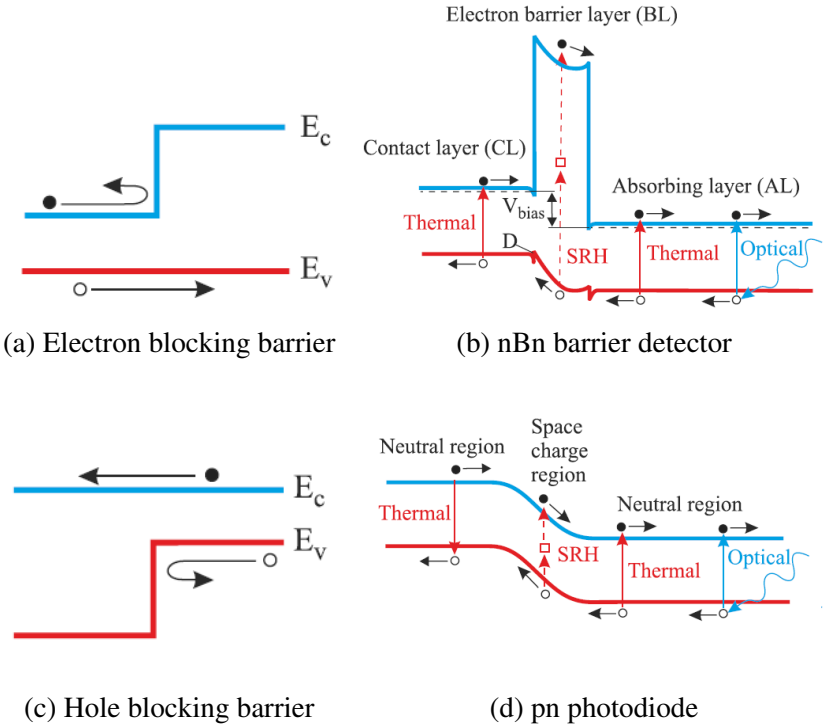

(a) Electron blocking barrier (b) nBn barrier detector

(c) Hole blocking barrier (d) pn photodiode

Figure. 2.9 Schematic illustrations of (a) electron blocking barrier,(c) hole blocking barrier, (b) band edge diagram of nBn barrier detector and (d) band edge diagram of pn photodiode. All the band offsets are explicitly shown.

the absorption zone which serves as a barrier for electrons. In this structure configuration the nBn detector is a hybrid device between photoconductor and photodiode. In this respect, it resembles a photoconductor with unity gain, due to the absence of majority carrier flow, while it is similar to a p-n photodiode in which the space charge region is replaced by an electron blocking unipolar barrier, and the pcontact is replaced by an ncontact. Implementing unipolar barriers for detectors is not readily achievable because of the lattice matching requirements for both the absorbers and barriers with the available substrates. In addition, a proper Valence Band Offset (VBO) and Conduction Band Offset (CBO) must exit between the absorber and the barrier. Ideally, one of the band offsets is required to be zeros between the absorber and the barrier to allow for an unimpeded flow of minority carriers. The nearly lattice matched 6.1 ÅIII-V material system InAs, GaSb and AlSb which can be grown on GaSb and InAs substrates is well suited for implementing unipolar barriers. It offers a high flexibility in forming different alloys and superlattices in building absorber/unipolar barriers for photodetectors. Importantly, type-II broken gap InAs/GaInSb SLs absorbors can be implemented with unipolar barriers to design high performance infrared detectors due to the ability to tune the positions of the conduction and valence band edges independently. Other barriers based designs improvements, includes absorber/barrier doping profile and barrier position within the design. Properly chosen doping profile near the unipolar barrier/absorber heterojunction can be used to reduce G-R dark current [137], for instance, the same doping type in the barrier and absorber is a key to maintaining low, diffusion limited dark current. The barrier should be placed near the minority carrier collector and away from the region of optical absorption.

In order to determine whether the diffusion mechanism or the generation-recombination mechanism is the dominant source of dark current in a particular device, it is a common practice to plot the dark current density as a function of inverse temperature. The diffusion dark current component typically varies as $T^3 exp(-E_g/k_B T)$ whereas generationrecombination component varies as $T^{3/2} exp(-E_g/2k_B T)$ and is dominant by SRH process in the depletion region. A fit to the last formulas is carried to determine the dominant regime. Figure. 2.10 shows a typical plots of the logarithm of the dark current vs. the reciprocal of the temperature in a conventional diode and in nBn detector. The steeper part of curve is Diffusion limited dark current and the less steep part is generationrecombination limited. The absence of a depletion region in nBn detector, leads to a total suppression of the generationrecombination dark current contribution from the photonabsorbing region. The red dashed line (nBn) curve is an extension of the high temperature diffusion limited region to temperatures below T_C. T_C is the crossover temperature at which the diffusion and generationrecombination currents are equal. In a lowtemperature region, nBn detector offers two important advantages. First, it

should exhibit a higher signaltonoise ratio than a conventional diode operating at the same temperature. Second, it will operate at a higher temperature than a conventional diode with the same dark current. This is depicted by a horizontal green dashed line in Figure. 2.10.

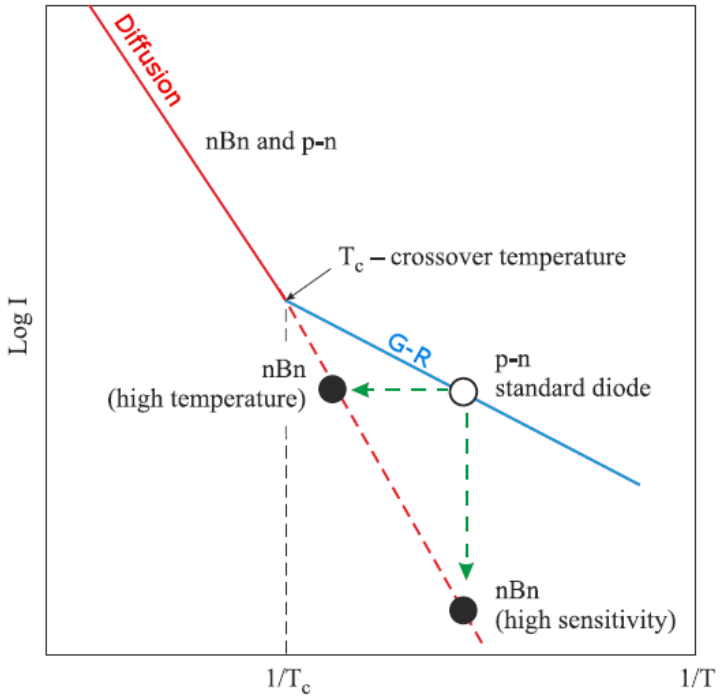

Figure. 2.10 Schematic Arrhenius plot of the dark current in a standard diode and in nBn device. The diffusion and G–R limited portions of curves are labeled.

Wide variation of barrier detector design has been considered in the literature including nBn, pBn and pBn, are shown in Figure. 2.11. The pBn or nBp design variants are a photovoltaic devices with a built-in voltage between the p and n region that falls across the barrier layer [56, 54]. The operation principle of pBn device is different from other two variations, nBn and pBp. In the latter, the operation is similar to a photoconductor that requires an applied bias whereas a device based pBn design is an actual photodiode with a built-in potential that can operate with zero applied bias. In the pBn structure, a wide band gap layer is inserted between the p^+ contact layer and the lightly doped n-type absorber region. This facilitates a drop of the electric field mostly across the wide band gap layer, rather than across the narrow-gap absorber region, and hence reducing SRH dark currents and tunneling currents. The barrier layer also prevents the diffusion of minority carrier electrons from the p^+ contact layer into the absorber region and hence further reducing the dark current.

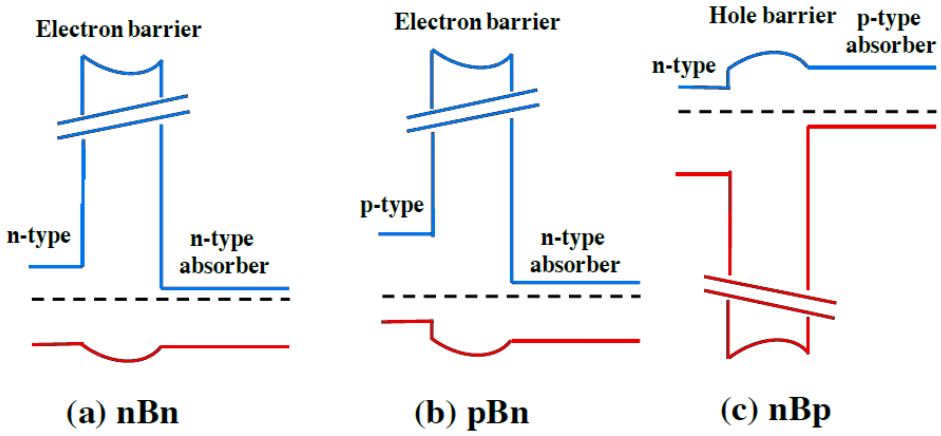

Figure. 2.11 Schematic band edges of barrier structures: (a) nBn, (b) pBn, and (c) nBp.

The CBIRD detector is an other important design that implements a pair of complementary barriers, namely, an electron barrier and a hole barrier formed at different depths in the growth sequence. Such structure is known as complementary barrier infrared device (CBIRD) and was invented by Ting et al at JPL [135]. This device consists of a lightly ptype InAs/GaSb SL absorber sandwiched between an ntype InAs/AlSb hole Barrier (hB) SL and wider gap InAs/GaSb electron Barrier (eB). The barriers are designed in such a way as to have approximately zero conduction and valence band offset with respect to SL absorber. A heavily doped ntype InAsSb layer adjacent to the eB SL acts as the bottom contact layer. The np junction between the hB InAs/AlSb SL and the absorber SL reduces SRHrelated dark current and trapassisted tunnelling. The LWIR CBIRD superlattice detector performance is closer to the "Rule 07" trend line.

Moreover, the M-structure superlattice [89] is an alternative design based on the 6.1 Å semiconductor material's family. It is obtained by the sequence: AlSb/GaSb/InAs/GaSb/AlSb, as shown in Figure 2.12, with color region indicating the prohibited band gap of each material. The structure is named by the letter M reflecting the shape of the band alignment of the constituent materials. This design shows potential advantages including higher carrier effective mass, tunable valence energies, and compatible growth conditions with standard type II InAs/GaSb superlattice. The AlSb layer in one period of the M design, having a wider energy gap, which blocks the interaction between electrons in the two adjacent InAs wells, thus, reducing the tunneling probability and increasing the electron effective mass. At the same time, the AlSb layer also acts as a barrier for holes and reshapes the GaSb hole-quantum well into a double quantum well. The effective well width is reduced, and the hole's energy level becomes sensitive to the well dimension.

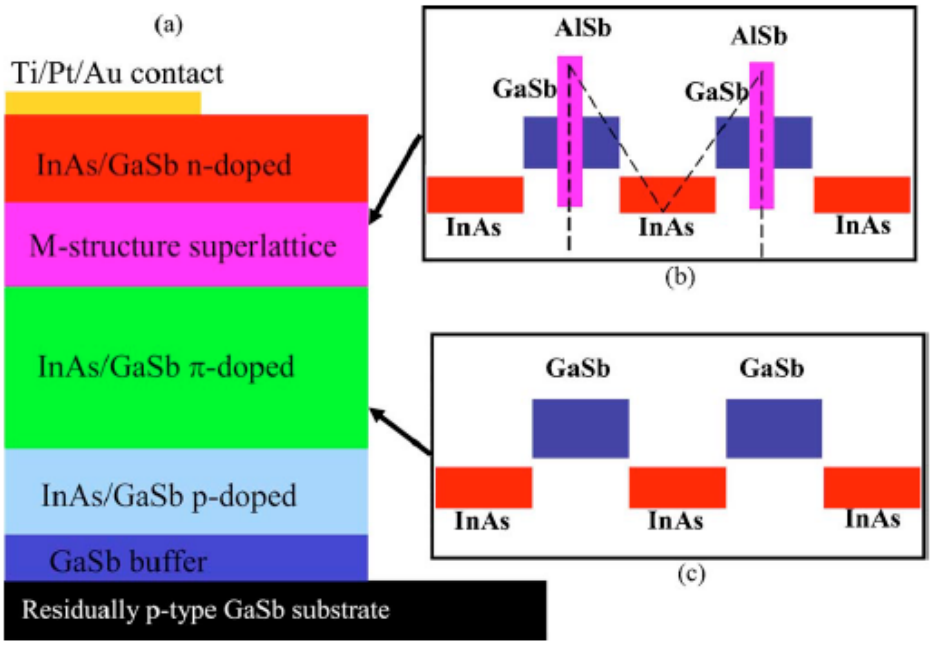

Figure. 2.12 (a) Schematic diagram of a p- π -M- n superlattice photodiode design, (b) The band alignments of M–superlattice design; the dash line shows the letter M shape of the band alignment, (c) Band alignment of standard type II superlattice.

Tables 2.1, Table 2.2 and Table 2.3, list the demonstrated performance levels of different detectors design based on InAs/GaSb T2SLs across different wavelength regimes. Presently, commercially available MWIR detectors and focal plane arrays (FPAs) are predominantly based on pin design. The best results are obtained by the CQD group (Center for Quantum Devices) which uses the M structure design. They notably produce 320 × 256 InAs/GaSb T2SL matrices operating at high temperatures (150 K) with a quantum efficiency of 67%. For LWIR window, ultimately, a megapixel arrays have been produced by the CQD and JPL groups with a quantum efficiency as high as 78% and with an NETD of 23.6 mK. However, this high reported result, given the lack of any precise indication, it may be presumed that, unlike the other measurements shown in Tables 2.1, 2.2 and 2.3, the measurements to obtain this result were carried out on an array with an anti-reflective treatment and in double pass, which undoubtedly explains the record. The VLWIR spectral window is also addressed by InAs/GaSb T2SL. Results on a photodiode (single element) based on InAs/InAsSb for detection in VLWIR has been reported by the CQD group [37]. No results have yet been published for VLWIR InAs/GaSb T2SL arrays. However, reservations have been expressed regarding the use of this

type of SLs structure due to low recovery of wave functions [57] and the use of InAs/InAsSb T2SLs is still the subject of debate.

Table 2.1 Demonstrated performance metrics for MWIR detector based on InAs/GaSb T2SL. SE stands for Single Element detector.

Groupe	**ref**	**Structure**	**Design**	λ_c	**T**	**QE**	**R_0A**	D*	NETD
				(μ m)	(K)	(%)	(Ω cm^2)	(Jones)	(mK)
CQD	[144]	InAs/GaSb 8/11 SE on GaSb	pin	5	300	25	$1.5{\cdot}10^2$	10^9	–
CQD	[95]	InAs/GaSb SE and FPA on GaSb	pMp	4.2	150	60	$5{\cdot}10^2$	$1.05\cdot10^{12}$	–
CQD	[17]	InAs/GaSb 320 × 256 FPA on GaSb	pMp	4.9	150	67	–	$1.2\cdot10^{12}$	11
FIA	[142]	InAs/GaSb 9.5/12 SE on GaSb	pin	5.4	77	30	$4{\cdot}10^5$	–	–
FIA	[116]	InAs/GaSb 384 × 288	pin	3-4	77	–	–	–	17.9
		bispectrale FPA on GaSb		4-5	77				9.9
CHTM	[108, 53]	InAs/GaSb 8/8 SE,FPA on GaSb	nBn	4.2	300	18	–	$1\cdot10^9$	–
SCD	[58]	InAs/GaSb 8.6/13.5 SE on GaSb	nBn	4.4	80	–	–	–	–
IES	[32]	InAs/GaSb 7/4 320x256 FPA SE on GaSb	pin	5	80	82	–	–	–
CQD	[87]	InAs/GaSb 8.6/13.5 SE on GaSb	pMp	4.4	150	44	–	–	$8\cdot10^{11}$
CHTM	[118]	InAs/InAsSb SE on GaSb	pin	5	80	24.1	–	–	–
AFRL	[10]	InAs/InAsSb SE on GaSb	pin	3.4	180	27	–	–	–
CHTM	[119]	InAs/InAsSb SE on GaSb	pin	5.4	77	20	–	–	–
SCD	[59]	InAsSb/AlSbAs 640 × 512 FPA on GaSb	XBn	4.2	150	–	–	–	–
CHTM	[19]	InAs/InAsSb SE on Si	nBn	5.5	200	25.6	–	–	$1.5\cdot10^{10}$
AFRL	[8]	InAs/InAsSb 320×256 FPA SE on GaSb	nBn	5.5	160	56	–	–	10 @80K
NARL, MPI	[64]	InAs/GaSb SE on GaSb	pin	3.7	80	–	–	$4.7\cdot10^{10}$	–
NARL, MPI	[64]	InAs/GaSb SE on GaAs	pin	3.7	80	–	–	$2.34\cdot10^{10}$	–
CQD	[145]	InAs/InAsSb SE on GaSb	pBn	4.7	300	39	–	$2\cdot10^9$	–

Table 2.2 Demonstrated performance metrics for LWIR detector based on InAs/GaSb T2SL. SE stands for Single Element detector.

Groupe	**ref**	**Structure**	**Design**	λ_c (μ m)	**T** (K)	**QE** (%)	**R$_0$A** (Ω cm^2)	D* (Jones)	NETD (mK)
CQD	[88]	InAs/GaSb 13/7 SE on GaSb	pMp	11	77	54	100	$2.2 \cdot 10^{11}$	–
CQD	[18]	InAs/GaSb 13/7 320 ×256FPA*onGaSb*	pin	12	150	31	13	$2 \cdot 10^{11}$	340
CQD	[79]	InAs/GaSb 13/7 320×256FPA*onGaSb*	M	11	77	78	166	$6 \cdot 10^{11}$	23.6
JPL	[79]	InAs/GaSb 14.5/7 1024 ×1024FPA*onGaSb*	CBIRD	11.5	80	21	–	–	53
SCD	[60]	InAs/GaSb 640 ×512FPA*onGaSb*	XBp	9.3	77	50	–	–	15

Table 2.3 Demonstrated performance metrics for VLWIR detector based on InAs/GaSb T2SL. SE stands for Single Element detector.

Groupe	**ref**	**Structure**	**Design**	λ_c (μ m)	**T** (K)	**QE** (%)	**R$_0$A** (Ω cm^2)	D* (Jones)	NETD (mK)
CQD	[143]	InAs/GaSb 17/7 SE on GaSb	pin	18.8	80	40	0.55	$4.5 \cdot 10^{10}$	–
CQD	[40]	InAs/GaSb 14/5 SE on GaSb	pin	17	77	30	0.08	$7.63 \cdot 10^{9}$	–
CQD	[37]	InAs/InAsSb SE on GaSb	pin	14.6	77	46	–	$1.4 \cdot 10^{10}$	–

The group abbreviations in Table 2.1, Table 2.2 and 2.3 stands fort:

- CQD: Center for Quantum Devices, Northwestern University, Evanston, Illinois, USA.
- CHTM: Center for High Technology Materials New Mexico, Albuquerque, USA.
- AFRL: Air Force Research Laboratory, Wright-Patterson Air Force Base, Ohio, USA.
- NARL: Nanoboyut Research Laboratory, Anadolu University, Department of Physics, Eskisehir, Turkey.

- MPI: Max Planck Institute for Solid State Research, Stuttgart, Germany.
- FIA: Fraunhofer-Institute for Applied Solid State Physics, Germany.
- JPL: Jet Propulsion Laboratory, California Institute of Technology, Pasadena, California, USA.
- IES: Institut d'Electronique du Sud, UMR-CNRS 5214, Universite Montpellier 2, Montpellier, France.
- SCD: SemiConductor Devices, Haifa.

In summary, although, the IR detection technology based on InAs/GaSb T2SL has now reached a certain technological maturity in various American laboratories, allowing for industrial development, the performance of these detectors is still below theoretical limits. This led several groups to develop modelling tools to understand the physics limits of InAs/GaSb T2SL detectors.

Chapter 3

Modeling Electronic and Optical Properties of Type II Superlattices

3.1 Introduction

In recent years, developments in crystal growth techniques and in semiconductor device technology has resulted in the fabrication of complicated nano-heterostructures with interesting physical phenomena and promising device applications. Thus, new methods and tools are required for the simulation and analysis of such nanostructures [4]. Among these nanostructures, Antimony-based type-II superlattices (T2SLs) have gained a lot of attention in the field of infrared detectors and lasers due to their high operating temperature. T2SLs combined with unipolar barrier architectures [133, 78] have been recently demonstrated to operate at room temperature in infrared photodetectors [72] and interband cascade lasers [51]. Another interesting property of T2SLs is the ability to tune an effective band gap over a wide range by varying layer thicknesses instead of mole compositions [114, 96].

However, they have not yet achieved their predicted functionality in practice, due to their low lifetime and high level of dark current attributed to the presence of generation-recombination (G-R) centers, which is associated with native defects and residual impurities[13]. The physical information of all of these effects can be found in the band structure and the band topologies of superlattices. Therefore, precise knowledge of the electronic properties of narrow band gap T2SLs is necessary for a proper device analysis.

This chapter deals with calculation of band structure and the optical properties of type II InAs/GaSb superlattice using 8×8 $\mathbf{k}\cdot\mathbf{p}$ theory. The Luttinger–Kohn Hamiltonian is chosen and its formulation is presented using $\mathbf{k}\cdot\mathbf{p}$ theory taking into account strain effects and the coupling between conduction and valence bands. This formulation is adapted to heterostructures

by using the envelope function approximation (EFA). Then, the finite element discretization scheme for the $\mathbf{k}\cdot\mathbf{p}$ Hamiltonian is presented by applying the variational principle [147] to the multiband Hamiltonian, which leads to an equivalent eigenvalue matrix representation of the problem. Moreover our simulation tool is presented and its accuracy is validated using energy-dependent effective mass non-parabolic model on a structure of a single quantum wells using Finite Element Method (FEM), Finite Difference Method (FDM), and the Transfer Matrix Method (TMM). Furthermore, the tools are applied to calculate the bulk dispersion of InAs material under compressive strain. The main focus is devoted to the calculation of miniband dispersions and absorption coefficients of the active region of an infrared photodetector based on type-II InAs/GaSb superlattices operating at room temperature.

3.2 Band Structure Theory

Band structure or equivalently electronic structure express the arrangement of energy states of crystal's electrons into allowed and forbidden bands. This emerges as a direct consequences of the lattice periodicity and symmetry of crystalline solids. The band structure has a particular importance for semiconductors as many properties of semiconductors are obtained by only a limited number of these bands. The optical properties of semiconductors and their nano-structures are intimately connected to the electronic states and hence to the structure of the bands. The bulk semiconductors bands structure varies continuously within each band n relating the crystal momentum $\mathbf{k}$ of an electron to its energy $E_n(\mathbf{k})$. In nano-structures being combining different materials, the translational symmetry of the crystal is broken which leads to a change in the electronic properties from their bulk properties. These alteration have a pronounced impact on the electronic and optical properties of nanostructures.

3.2.1 Crystal structure and Brillouin zone

Semiconductors are crystalline solids. The III-V binary compound semiconductors composed of elements from the group III (Al, Ga, In, . . .) and the group V (N, P, As, Sb . . .) of the periodic table of elements shows great technological potentials. In their bulk, arsenides, phosphides and antiminides are arranged in a Zinc-Blend ZB crystal structure with cubic symmetry, where the atoms of group III -cations (Ga or In) and V -anions (As or P) are located at the nodes of two face centred cubic lattice shifted to each other by a quarter of the diagonal. Figure 3.1 shows the conventional and primitive unit cell of ZB crystal structure with a constant lattice a_0 . The First Brillouin Zone (FBZ) is shown in Figure 3.1.

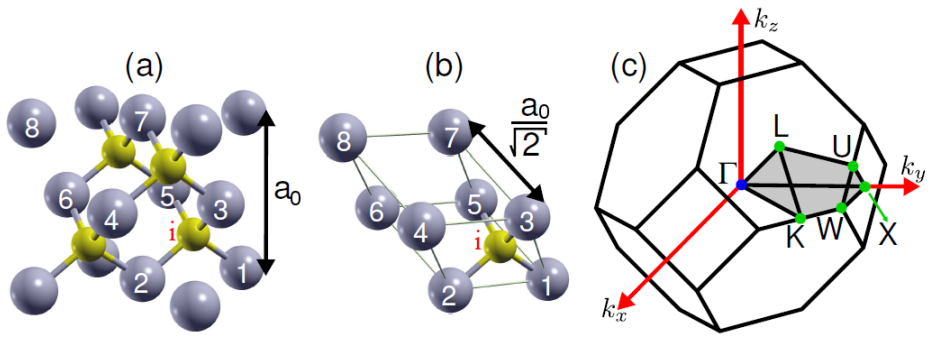

Figure. 3.1 ZB Conventional unit cell (a), ZB primitive unit cell and (c) the corresponding First Brillouin Zone (FBZ). The atoms are numbered using Roman and Arabic to help differentiate between different atoms. In the FBZ, the nominated points are the poits of hight symmetry.

3.2.2 Crystal Schrödinger Hamiltonian

In order to find the bands structures and related quantities one should start ideally from the whole Crystal Hamiltonian Equation including all the interaction among all the involved particles: electrons i, j and atoms cores I, J of the system. This equation in the absence of any external electro-magnetic fields dreads:

$$H = \underbrace{\sum_i \frac{\mathbf{p}_i^2}{2m_0}}_{T_e} + \underbrace{\sum_I \frac{\mathbf{p}_I^2}{2m_I}}_{T_a} + \underbrace{\frac{1}{2}\sum_{i,j} \frac{e^2}{4\pi\varepsilon_0 |\mathbf{x}_i - \mathbf{x}_j|}}_{V_{ee}} + \underbrace{\frac{1}{2}\sum_{I,J} \frac{e^2 z_I z_J}{4\pi\varepsilon_0 |\mathbf{x}_I - \mathbf{x}_J|}}_{V_{aa}} - \underbrace{\frac{1}{2}\sum_{i,J} \frac{e^2 z_J}{4\pi\varepsilon_0 |\mathbf{x}_i - \mathbf{x}_J|}}_{V_{ae}} \tag{3.1}$$

Where e is the elementary charge, z the charge of the particle, $\mathbf{p}$ is the momentum and $\mathbf{x}$ the position of the particle. This is a complex problem that, in reality, is impossible to be solved directly because of the huge number of particles involved $\left(10^{22} - 10^{23} \text{ atoms } /\text{cm}^3\right)$ and, therefore, approximations are required. Under the Born-Openheimer approximation [148, 23] the motion of electrons and atoms cores can be separated due to the much higher mass of the latter than the former. The light-mass electrons respond instantaneously to the motion of atoms' cores. This leads to the following crystal electron Hamiltonian in which the electrons feel an average potential $U(\mathbf{x}_i)$:

$$H = \sum_i \left(\frac{\mathbf{p}_i^2}{2m_0} + U(\mathbf{x}_i) \right) + \underbrace{\frac{1}{2} \sum_{i,j} \frac{e^2}{4\pi\varepsilon_0 \left| \mathbf{x}_i - \mathbf{x}_j \right|}}_{V_{\text{ee}}} \tag{3.2}$$

Moreover, a single electron approximation also known as mean field approximation is performed by assuming that the electron-electron interaction V_{ee} with the core- and valence electrons can also be cast into an additional effective potential. Then, the lest equation reduces to a single electron Hamiltonian equation, in which an electron experiences a global effective potential $U(\mathbf{x})$:

$$H = \frac{\mathbf{p}^2}{2m_0} + U(\mathbf{x}) \tag{3.3}$$

In the last two equations we have already made the assumption that electrons interact with a frozen atomic cores lattice. Switching on this interaction again can be made using phonons theory[30], however this is out the scope of the thesis.

3.3 Computational Methods

The accurate determination of the overall band structure and wave functions of nanostructures is very complicated to tackle analytically except for a few special cases. Therefore, numerical calculations are required to handle complex designs. Among the difficulties of calculating the full band structure for heterostructures is the sensitivity of modeling tools and techniques to the input parameters, namely effective masses, band gap energies, and Valence Band Offset (VBO), especially for structures made of narrow gap materials such as InAs and InSb [96]. Importantly, the exact VBO values are crucial for modeling heterostructures, yet they are very sensitive to the heterointerface imperfections and even a small shift leads to erroneous results. The choice of the modeling technique often comprises a trade-off between accuracy and computational load.

Generally, the approaches used for the overall band structure calculation fall into two categories: first principle calculations (i.e., ab initio) [92, 44] and empirical methods [148, 50, 23]. Ab initio calculations such as density functional theory and the quantum Monte Carlo start from atomistic values where information about atomic orbitals and atoms' positions are required without the need of any fitting and/or empirical parameters [92, 44]. Although these methods yield highly accurate results, they require considerably long execution time and hence they are limited to systems of a small number of atoms. In contrast, empirical methods are usually used for band structures calculation of large semiconductor heterostructures where some

properties are approximated using experimentally fitted parameters. These fitting parameters give a tremendous reduction to the computational cost. One of the most used empirical methods for the band structure calculation is the $\mathbf{k}\cdot\mathbf{p}$ method, which treats heterostructures as a stack of bulk materials. The method is convenient to model large complex designs due to its highly computational efficiency and good accuracy, despite the hidden atomic scene. The aim of this work is to develop rigorous modeling tools for calculating the band structure of nanostructures using the $\mathbf{k}\cdot\mathbf{p}$ approach. Since this method is sensitive to variations of input parameters across the heterointerface, the Finite Element Method (FEM) is chosen as a numerical technique to discretize the $\mathbf{k}\cdot\mathbf{p}$ Hamiltonians. The finite element method has been applied to many quantum mechanical problems ranging from simple isolated systems such as the hydrogen atom [11, 99, 34] and the single quantum well [83, 98] to more complex problems such as the periodic potential [27] and shown to give very precise numerical results in calculating the energies of the system. However, due to the complexity of the FEM and the complicated formulation of the variational functional for a given multiband $\mathbf{k}\cdot\mathbf{p}$ Hamiltonian, Finite Difference Method (FDM) is usually favored over FEM. Despite FEM accuracy, its application or use remains limited. In FEM, a non-uniform mesh as well as high order Lagrange/Hermit basis functions can be utilized [91], hence the band structure and wavefunctions for heterostructures with layers of arbitrary thicknesses can be calculated accurately with a smoothed mesh the near heterointerface edges.

In the following two sections, we address the formalism of the $\mathbf{k}\cdot\mathbf{p}$ method for bulk materials and nano–structures.

3.4 k.p Method for Bulk Materials

A pure bulk material is characterized by an invariant properties throughout its space. These properties are described by a periodic replication of unit cells in all space using the lattice translation vector $\mathbf{R}$. To develop the $\mathbf{k}\cdot\mathbf{p}$ method for such materials, let's start with the time independent single electron Schrödinger equation assuming no external field:

$$H_0\varphi = \left(-\frac{\hbar^2}{2m_0}\nabla^2 + U(\mathbf{x})\right)\varphi = E\varphi \tag{3.4}$$

The potential $U(\mathbf{x})$ is periodic within the lattice and obeys its translational symmetry so that, the translational invariance:

$$U(\mathbf{x}+\mathbf{R}) = U(\mathbf{x}) \tag{3.5}$$

holds for all lattice vectors **R** mapping the infinite crystal lattice to itself. As a consequence, the wavefunction $\varphi_{n\mathbf{k}}$ obey Bloch's theorem which states that the wavefunction soultion to Equation 3.4 can be expressed as the product of a plane wave $\mathbf{exp}(i\mathbf{k}\cdot\mathbf{x})$ and a Bloch factor $u_{n\mathbf{k}}$:

$$\varphi_{n\mathbf{k}}(\mathbf{x}) = u_{n\mathbf{k}}(\mathbf{x})e^{i\mathbf{k}\cdot\mathbf{x}} \tag{3.6}$$

Here, the $u_{n\mathbf{k}}(\mathbf{x})$ denotes the lattice periodic part with

$$u_{n\mathbf{k}}(\mathbf{x}+\mathbf{R}) = u_{n\mathbf{k}}(\mathbf{x}) \tag{3.7}$$

and the plane wave is the slowly modulating envelope. The $n\mathbf{k}$ are the quantum numbers indexing the solutions.

The spin-orbit interaction quite generally have a notable effects on the band structure, and therefore should be included in the Hamiltonian:

$$H = H_0 + \frac{\hbar}{4m_0^2c^2}(\sigma\times\nabla U)\cdot\mathbf{p}. \tag{3.8}$$

where c is the speed of light in vacuum and σ denotes the Pauli spin matrix vector $\sigma = (\sigma_1,\sigma_2,\sigma_3)^T$:

$$\sigma_x = \begin{pmatrix} 0 & 1 \\ 1 & 0 \end{pmatrix}, \quad \sigma_y = \begin{pmatrix} 0 & -i \\ i & 0 \end{pmatrix}, \quad \sigma_z = \begin{pmatrix} 1 & 0 \\ 0 & -1 \end{pmatrix}. \tag{3.9}$$

By inserting Equation 3.6 into Equation 3.4 and then applying the differential operators to the plane wave and multiplying the equation on both sides from the left with $\mathbf{exp}(-i\mathbf{k}\cdot\mathbf{x})$ the following equation for the periodic part of the Bloch function $u_{n\mathbf{k}}$ is obtained:

$$\left[\underbrace{\frac{\mathbf{p}^2}{2m_0}+U(\mathbf{x})}_{\mathrm{H_0}} + \underbrace{\frac{\hbar}{4m_0^2c^2}(\sigma\times\nabla U)\cdot\mathbf{p}}_{\mathrm{H_{SO}}} + \underbrace{\frac{\hbar}{4m_0^2c^2}(\sigma\times\nabla U)\cdot\mathbf{k}}_{\mathrm{H_{kSO}}} + \underbrace{\frac{\hbar^2k^2}{2m_0}}_{\mathrm{H_{k2}}} + \underbrace{\frac{\hbar}{m_0}\mathbf{k}\cdot\mathbf{p}}_{\mathrm{H_{kp}}}\right] u_{n\mathbf{k}}(\mathbf{x}) = E_n(\mathbf{k})u_{n\mathbf{k}}(\mathbf{x}) \tag{3.10}$$

with the different terms indicated to further reference.

It has the form of the Schrödinger equation, but contains **k**-dependent terms. Because of the **k**· **p** term, it is called the **k**· **p equation**. The $\mathrm{kH_{SO}}$ term is often neglected, because the velocity

of the electron in its atomic orbit is very much greater than the velocity of a wave packet made up of wave vectors in the neighborhood of $\mathbf{k}$ [47]. An important consequence of the Bloch theorem is the fact that wavefunctions with different $\mathbf{k}$ values are not coupled together (due to the slowly varying plane wave) and therefore Equation 3.10 has a parametric dependence on the crystal momentum $\mathbf{k}$. For each integer band index n, the eigenenergies $E_n(\mathbf{k})$ depend continuously on the vector $\mathbf{k}$ in reciprocal space.

The main idea behind the $\mathbf{k}\cdot\mathbf{p}$ theory used to solve Equation 3.10, is based on expanding $u_{n\mathbf{k}}(\mathbf{x})$ around a point in the reciprocal space with high symmetry of the band structure, usually the Γ point at $\mathbf{k}_0 = 0$:

$$u_{m\mathbf{k}}(\mathbf{x}) = \sum_{n'} a_{m\mathbf{k},n'} u_{n'\mathbf{0}}(\mathbf{x}) \tag{3.11}$$

where the solutions $u_{n\mathbf{0}}(\mathbf{x})$ known as zone-center functions obey the Equation 3.10 at $\mathbf{k} = 0$:

$$\left(-\frac{\hbar^2}{2m_0}\nabla^2 + U(\mathbf{x})\right) u_{n\mathbf{0}} = E_n(\mathbf{0}) u_{n\mathbf{0}}(\mathbf{x}) \tag{3.12}$$

To obtain the coefficients $a_{m\mathbf{k},n'}$, the Equation 3.11 is substituted in Equation 3.10 multiplied from the left by $u_{n\mathbf{0}}(\mathbf{x})$ and integrated over the crystal cell leads to the matrix eigenvalue problem for the expansion coefficients $a_{m\mathbf{k},n'}$:

$$E_m(\mathbf{k}) a_{m\mathbf{k},n} = \sum_{n'} H_{nn'}(\mathbf{k}) a_{m\mathbf{k},n'} \tag{3.13}$$

and the Hamiltonian is represented by the following infinite dimensional matrix

$$H_{nn'} = \left\{ E_{n'}(0) + \frac{\hbar^2 k^2}{2m_0} \right\} \delta_{nn'} + \frac{\hbar}{m_0}\mathbf{k}\cdot\mathbf{p}_{nn'} + \mathrm{H}_{\mathrm{SOnn'}} + \mathrm{H}_{\mathrm{kSOnn'}} \tag{3.14}$$

that couples all energy bands by means of the matrix elements $\mathbf{p}_{nn'}$, $\mathrm{H}_{\mathrm{SOnn'}}$ and $\mathrm{H}_{\mathrm{kSOnn'}}$ between the respective Bloch factors at the zone centre,

$$\mathbf{p}_{nn'} = \int u^*_{n0}(\mathbf{x}) \mathbf{p} u_{n'0}(\mathbf{x}) \mathrm{d}\mathbf{x}. \tag{3.15}$$

$$\mathrm{H}_{\mathrm{SOnn'}} = \int u^*_{n0}(\mathbf{x}) \mathrm{H}_{\mathrm{SO}} u_{n'0}(\mathbf{x}) \mathrm{d}\mathbf{x}. \tag{3.16}$$

$$\mathrm{H}_{\mathrm{kSOnn'}} = \int u^*_{n0}(\mathbf{x}) \mathrm{H}_{\mathrm{kSO}} u_{n'0}(\mathbf{x}) \mathrm{d}\mathbf{x}. \tag{3.17}$$

The first and last matrix elements can be cast into one generalized matrix element using the the notation,

$$\pi = \mathbf{p} + \frac{\hbar}{4m_0c^2}(\sigma \times \nabla U). \tag{3.18}$$

therefore Equation 3.14 becomes,

$$H_{nn'} = \left\{ E_{n'}(0) + \frac{\hbar^2 k^2}{2m_0} \right\} \delta_{nn'} + \frac{\hbar}{m_0}\mathbf{k} \cdot \pi_{nn'} + \mathrm{H}_{\mathrm{SOnn'}}. \tag{3.19}$$

The diagonalization of the **k** dependent, infinite matrix would lead to the exact coefficients and energies $E_m(\mathbf{k})$. As the matrix is continuous in **k**, it is clear that the dispersion $E_m(\mathbf{k})$ will also be continuous as we have already mentioned. However, diagonalizing an infinite matrix is not possible, instead extracting and diagonalizing a finite size Hamiltonian matrix from Equation 3.14 using Löwdin's perturbation method [74] is possible. This is justified for many optoelectronic devices as only a small number of energy bands are important, namely the lowest conduction and highest valence bands around the Γ point. Other bands can be regarded as being remote, so the interaction in–between these important bands can be considered to dominate for the band structure of interest.

In Löwdin perturbation approach the energy bands are classified in two classes S and R. Bands in class S are the bands we want to describe and consequently their number defines the size of the finite Hamiltonian matrix. The bands R are considered being remote and include all the other energy bands of the system. It is desirable that class S bands to be close in energy and interact strongly with each other but weakly with bands in class R. Furthermore, the interaction among energy bands of class R is neglected and their effect on the class S bands are accounted for perturbatively. Away from the expansion point, the energy bands in class S and R can happen to interact more strongly which means that the **k**· **p** method is reaching it's limits. When this happens we either modify the class S by including more important bands of class R or simply discard the calculation before this interacting region.

The expansion of the periodic functions into classes S and R is written as:

$$u_{m\mathbf{k}}(\mathbf{x}) = \sum_{n'}^{S} a_{m\mathbf{k},n'} u_{n'\mathbf{0}}(\mathbf{x}) + \sum_{n}^{R} a_{m\mathbf{k},n} u_{n\mathbf{0}}(\mathbf{x}) \tag{3.20}$$

again with the assumption that the periodic functions $u_{n\mathbf{0}}(\mathbf{x})$ are the solutions for the unperturbed Hamiltonian term H_0 in Equation 3.10. Therefore the perturbed Hamiltonian term ΔH

$$\Delta \mathrm{H} = \mathrm{H_{kp}} + \mathrm{H_{k2}} + \mathrm{H_{SO}} + \mathrm{H_{kSO}} \tag{3.21}$$

within Löwdin approch we can calculate several order of perturbation for the different Hamiltonian terms in equation Equation 3.21. To include the effects of the energy bands in class R we must consider at least the second order contribution. Usually, perturbation corrections up to second order terms are considered where the first order matrix elements are given by

$$\Delta H^{(1)}_{f,g}\left(s,s'\right) = \left\langle s\left|\mathbf{H_f}\right|s'\right\rangle \tag{3.22}$$

while the second matrix elements reads

$$\Delta H^{(2)}_{f,g}\left(s,s'\right) = \sum_{s}^{R} \frac{\left\langle s\left|\mathbf{H_f}\right|r\right\rangle \left\langle r\left|\mathbf{H_g}\right|s'\right\rangle}{E_{ss'} - E_r}, \tag{3.23}$$

where **f** and **g** being any of the terms identified in the Hamiltonian Equation 3.21 and the Dirac notation has been used for periodic functions: $\langle \mathbf{x}|\,\alpha\rangle = u_{\alpha\mathbf{0}}(\mathbf{x})$ with $\alpha = \{s,s'\}$ in class S and $\alpha = \{r\}$ in class R.

Applying Löwdin theory reduces the infinite dimensional Hamiltonian matrix in Equation 3.14 to the following finite dimensional $\mathbf{k}\cdot\,\mathbf{p}$ Hamiltonian matrix:

$$H_{nn'} = \left\{E_{n'}(0) + \frac{\hbar^2 k^2}{2m_0}\right\}\delta_{nn'} + \frac{\hbar}{m_0}\mathbf{k}\cdot\pi_{nn'} + \mathrm{H_{SOnn'}} + \sum_{\alpha\in R}\frac{H_{n\alpha}(\mathbf{k})H_{\alpha n'}(\mathbf{k})}{E_n(0) - E_\alpha(0)} \tag{3.24}$$

where now the indices n and n' run only over the number of bands in class S.

However, how can we proceed with the construction of this matrix without knowing neither the effective potential nor the zone centre functions?. In fact Equation 3.12 is not solved explicitly and no closed expression for $u_{n\mathbf{0}}(\mathbf{x})$ is needed. Instead, the matrix Equation 3.14 is constructed by using group theory to derive symmetry properties of the zone center functions $u_{n\mathbf{0}}(\mathbf{x})$. Using these symmetry properties, similarities and equivalences for the momentum matrix elements $\mathbf{p}_{nn'}$ can be deduced. The topic of the group theory is beyond the current scope. It can be found in [148] and [14]. Therefore, within the framework of group theory it is possible to calculate non zero matrix elements used in Equations 3.22 and 3.23 and construct the sub matrix that when diagonalized provide the energy band structure. The momentum matrix elements $\mathbf{p}_{nn'}$ are usually used as fitting parameters to match experimentally obtained results. In addition, many of the momentum matrix elements vanish due to symmetry. By

increasing the number of bands in class S more accurate results can be obtained, but with a trade off of more complex modelling.

Depending on the number of bands in class S different $\mathbf{k}\cdot\mathbf{p}$ models have been developed and the resulting Hamiltonians are given specific names based on the their size. This also includes the effective mass approximation where only a single band is considered. Common multi band $\mathbf{k}\cdot\mathbf{p}$ models are the 4 band and 6 band Luttinger − Kohn Hamiltonians models that includes only valence bands, and the 8 band and 14 band models that include valence as well as conduction bands. In the following, we will present the details of the effective mass approximation model, the 6 band, and the 8 band model used in this work. All these models are for the zinc blend crystal structure and are implemented in our tools.

3.4.1 The single band effective mass model

The Effective Mass Model (EMM) is the simplest model that can be derived from the $\mathbf{k}\cdot\mathbf{p}$ theory in which only a single band in class S weakly interacting with all other bands R is considered. In this case the perturbation theory and Lowdin's method give the same results. Thus Equation 3.24 for the $\mathbf{k}\cdot\mathbf{p}$ Hamiltonian matrix becomes a simple scalar function

$$E_n(\mathbf{k}) = E_n(0) + \frac{\hbar^2 k^2}{2m_0} + \frac{\hbar}{m_0}\mathbf{k}\cdot\langle n|\mathbf{p}|n\rangle + \frac{\hbar^2}{m_0^2}\sum_{l\neq n}\frac{|\mathbf{k}\cdot\langle n|\pi|l\rangle|^2}{E_n(0)-E_l(0)} \tag{3.25}$$

Note here that we have neglected the spin orbit terms. Since the energy band has an extremum at $\mathbf{k}=0$, the term linear in $\mathbf{k}$ is zero because of $\mathbf{p}_{nn'}=0$.

Rewriting the last equation by introducing the Cartesian indices α,β $= x, y, z$, and assume Einstein's summation convention for these indices we obtain,

$$E_n(\mathbf{k}) = E_n(0) + \frac{\hbar^2 k^2}{2m_0} + \frac{\hbar^2}{m_0^2}k_\alpha k_\beta \sum_{l\neq n}\frac{\langle n|\mathbf{p}_\alpha|l\rangle\langle l|\mathbf{p}_\beta|n\rangle}{E_n(0)-E_l(0)}. \tag{3.26}$$

$$= E_n(0) + \frac{\hbar^2}{2}k_\alpha k_\beta \left(\frac{1}{m_n^*}\right)_{\alpha,\beta}. \tag{3.27}$$

$$= E_n(0) + \frac{\hbar^2}{2}\mathbf{k}^T\frac{1}{\mathbf{m}_n^*}\mathbf{k}. \tag{3.28}$$

where the symmetric 3×3 matrix $\mathbf{m}_n^*$ called the effective mass tensor is given by,

$$\left(\frac{1}{m_n^*}\right)_{\alpha,\beta} = \left(\frac{1}{m_0}\right)\delta_{\alpha,\beta} + \frac{2}{m_0^2}\sum_{l\neq n}\frac{\langle n|\mathbf{p}_\alpha|l\rangle\langle l|\mathbf{p}_\beta|n\rangle}{E_n(0)-E_l(0)}. \tag{3.29}$$

The single band effective mass model is usually adopted to compute the conduction band dispersion in direct semiconductors. The accuracy of the model depends on the difference between the actual band edge and other zone centre energies; ie the denominators in Equation 3.25. The higher this difference as it is the case for wide bandgap materials the higher the accuracy of the model. This accuracy could be increased by adjusting the effective mass tensor elements from experiment measurements. This is useful because the zone centre functions are not well known as well as the matrix elements based on these states.

Let's estimate the conduction band electron effective m_c^* from Equation 3.29. Symmetry arguments from group theory indicate that the main contribution for the last term stem from the matrix elements between the lowest zone center conduction band state Γ_{1c} with symmetry $|s\rangle$ and the highest valence band state Γ_{4v} consisted of three degenerate states with symmetry $|p_x\rangle$,$|p_y\rangle$ and $|p_z\rangle$. The separation between these two energy states is just the direct band gap E_g, therefore the effective mass m_c^* can be approximated by

$$\frac{1}{m_c^*} = \frac{1}{m_0} + \frac{2}{m_0^2}\frac{\langle 1c|\mathbf{p}_\alpha|4v\rangle\langle 4v|\mathbf{p}_\beta|1c\rangle}{E_g}. \tag{3.30}$$

Using symmetry arguments it can be shown that $\langle p_\alpha|\mathbf{p}_\beta|s\rangle = P\delta_{\alpha,\beta}$, thus Equation 3.30 reduces to:

$$\frac{m_0}{m_c^*} = 1 + \frac{2P^2}{m_0 E_g}. \tag{3.31}$$

The last approximation in Equation 3.31 comes from the fact that $2P^2/m_0E_g \gg 1$ where a rough estimate using nearly free electron wave functions indicate that $2P^2/m_0 \approx 20eV$. Table 3.1 compares the values of m_c^* estimated from Equation 3.31 with their experimental values [148] for different semiconductors in zinc blende structure.

Table 3.1 Theoretical estimation of conduction band effective masses for zinc blende semiconductors and compared with experimental values. The values of E_g are obtained from experiment.

Material	Ge	GaN	GaAs	GaSb	InP	InAs	ZnS	ZnSe	ZnTe	CdTe
E_g[eV]	0.89	3.44	1.55	0.81	1.34	0.45	3.80	2.82	2.39	1.59
m_c^*/m_0	0.04	0.17	0.078	0.04	0.067	0.023	0.16	0.14	0.12	0.08
m_c^*/m_0 (Exp)	0.041	0.17	0.067	0.047	0.073	0.026	0.20	0.134	0.124	0.093

The conduction band has multiple local minima at specific points in the Brillouin zone. For zinc blende crystal structure, these are the Γ point ($\mathbf{k}_0 = 0$), the X point ($\mathbf{k}_0 = \{100\}$), and the L point ($\mathbf{k}_0 = \{111\} / \sqrt{3}$).

The minima at the X point are 3 fold, the ones at the L point are 4 fold degenerate, as each is shared by two neighboring Brillouin zones. In silicon, there are no minima at the X point but along Δ, which is the connecting line between Γ and X. These minima are therefore 6 fold degenerate. At the Γ point of the bulk Brillouin zone the tensor $\mathbf{m}_n^*$ is isotropic

$$\mathbf{m}_n^* = m_n^* \mathbf{1}_{3\times 3} \tag{3.32}$$

due to symmetry reasons. The effective mass tensors at the X point, the Γ point and along Δ are characterized by a longitudinal effective mass m_{nl}^* and a transversal effective m_{nt}^*,

$$\mathbf{m}_n^* = (m_{nl}^* - m_{nt}^*)\,\hat{\mathbf{k}}_0 \hat{\mathbf{k}}_0^T + m_{nt}^* \mathbf{1}_{3\times 3} \tag{3.33}$$

and describe ellipsoids of revolution with the axis of symmetry pointing in the direction of $\mathbf{k}_0$.

3.4.2 The 3 x 3 Dresselhaus-Kip-Kittel valence band model

This was the first $\mathbf{k}\cdot\mathbf{p}$ model developed by Dresselhaus, Kip, and Kittel (DKK) [21] to describe the valence band structure without including spin orbit interaction H_{SO}. The valence bands wave functions being created by $p-$ like orbitals in most semiconductors they are thus threefold degenerate with energy $E_n(0) = E_v$. Therefore, the degenerate perturbation theory should be adopted in the $\mathbf{k}\cdot\mathbf{p}$ approach. In the DKK model, the zone center states in the valence band, are denoted by ε_s^+, $s = 1,2,3$ and belong to class S. These states being originated from the p_x, p_y, and p_z atomic orbitals they are also denoted respectively by $|yz\rangle$, $|zx\rangle$, and $|xy\rangle$, to refer to the directions along which they are even.

The first order contributions from degenerate perturbation theory are zero,

$$\left\langle \varepsilon_s^+ \left| p_\alpha \right| \varepsilon_r^+ \right\rangle = 0, \quad s,r \in \{1,2,3\}, \alpha \in \{x,y,z\} \tag{3.34}$$

because of equal parities of the zone center states. The second order contributions from degenerate perturbation theory are due to the matrix elements,

$$H_{rs} = \frac{\hbar^2}{m_0^2} \sum_{l\in R} \frac{\langle r|\mathbf{k}\cdot\mathbf{p}|l\rangle\langle l|\mathbf{k}\cdot\mathbf{p}|s\rangle}{E_n(0) - E_l(0)} = \frac{\hbar^2}{m_0^2} k_\alpha k_\beta \sum_{l\in R} \frac{\langle r|p_\alpha|l\rangle \langle l|p_\beta|s\rangle}{E_n(0) - E_l(0)} \tag{3.35}$$

where again the Einstein's summation convention over α and β is assumed. Equation 3.35 can be simplified by taking into account the particular symmetry of the zone center states. In fact, the following matrix elements hold,

$$\begin{gathered}\langle xy|p_z|n\rangle = \langle yz|p_x|n\rangle = \langle zx|p_y|n\rangle \\ \langle xy|p_x|n\rangle = \langle yz|p_y|n\rangle = \langle zx|p_z|n\rangle = \langle xy|p_y|n\rangle = \langle yz|p_z|n\rangle = \langle zx|p_x|n\rangle\end{gathered} \tag{3.36}$$

because of symmetry. The final result of applying degenerate perturbation theory leads to the following $\mathbf{k}\cdot\mathbf{p}$ Hamiltonian which when diagonalized give band structure dispersion:

$$\begin{aligned}H_{DKK}^{3\times3}(\mathbf{k}) &= \left(E_v + \frac{\hbar^2}{2m_0}\mathbf{k}^2\right)\mathbf{1}_{3\times3} + N\mathbf{k}\mathbf{k}^T + (L-N)\,\mathrm{diag}\left(k_x^2, k_y^2, k_z^2\right) \\ &\quad + M\,\mathrm{diag}\left(k_y^2+k_z^2, k_x^2+k_z^2, k_x^2+k_y^2\right) \\ &= \left(E_v + \frac{\hbar^2}{2m_0}\mathbf{k}^2\right)\mathbf{1}_{3\times3} + H_{DKK}\end{aligned} \tag{3.37}$$

where the Dresselhaus−Kip−Kittel Hamiltonian [21] is given by:

$$H_{DKK} = \begin{pmatrix} Lk_x^2 + M\left(k_y^2+k_z^2\right) & Nk_xk_y & Nk_xk_z \\ Nk_xk_y & Lk_y^2 + M\left(k_x^2+k_z^2\right) & Nk_yk_z \\ Nk_xk_z & Nk_yk_z & Lk_z^2 + M\left(k_x^2+k_y^2\right) \end{pmatrix} \tag{3.38}$$

The parameters L, M, N are called the Dresselhaus parameters [21] and depend on the momentum matrix elements p_{nl},

$$L = \frac{\hbar^2}{m_0^2}\sum_{l\in R}\frac{|\langle xy|p_z|l\rangle|^2}{E_n(0)-E_l(0)} \tag{3.39}$$

$$M = \frac{\hbar^2}{m_0^2}\sum_{l\in R}\frac{|\langle xy|p_x|l\rangle|^2}{E_n(0)-E_l(0)} \tag{3.40}$$

$$N = \frac{\hbar^2}{m_0^2}\sum_{l\in R}\frac{\langle xy|p_x|l\rangle\langle l|p_z|yz\rangle + \langle xy|p_z|l\rangle\langle l|p_x|xy\rangle}{E_n(0)-E_l(0)} \tag{3.41}$$

3.4.3 The 6 x 6 Luttinger-Kohn valence band model

The DKK model was subsequently extended by Luttinger and Kohn (LK), by including spin orbit interaction as in Equation 3.10. The spin−orbit interaction is a relativistic effect which

scales with the atomic number of the atom. Thus for semiconductors containing heavier elements, such as Ge, Ga, As, and Sb, one expects the spin−orbit coupling to be significant. By taking into account the spin-orbit interaction, the solutions of Equation 3.10 should be understood as a two component spinor. The three zone center valence band states are now doubly degenerate with their spin counterparts: $\varepsilon_1^+|\uparrow\rangle$, $\varepsilon_2^+|\uparrow\rangle$, $\varepsilon_3^+|\uparrow\rangle$, $\varepsilon_1^+|\downarrow\rangle$, $\varepsilon_2^+|\downarrow\rangle$, $\varepsilon_3^+|\downarrow\rangle$. However, Luttinger and Kohn changed the notation of these basis respectively to $|X\uparrow\rangle$, $|Y\uparrow\rangle$, $|Z\uparrow\rangle$, $|X\downarrow\rangle$, $|Y\downarrow\rangle$, $|Z\downarrow\rangle$, thereby referring to their symmetry axis. Furthermore, it was found convenient to choose the basis

$$\begin{aligned}
|1\rangle &= \left|\frac{3}{2},\frac{3}{2}\right\rangle = \frac{-1}{\sqrt{2}}|(X+iY)\uparrow\rangle \\
|2\rangle &= \left|\frac{3}{2},\frac{1}{2}\right\rangle = \frac{-1}{\sqrt{6}}|(X+\mathrm{i}Y)\downarrow\rangle + \sqrt{\frac{2}{3}}|Z\uparrow\rangle \\
|3\rangle &= \left|\frac{3}{2},\frac{-1}{2}\right\rangle = \frac{1}{\sqrt{6}}|(X-iY)\uparrow\rangle + \sqrt{\frac{2}{3}}|Z\downarrow\rangle \\
|4\rangle &= \left|\frac{3}{2},\frac{-3}{2}\right\rangle = \frac{1}{\sqrt{2}}|(X-iY)\downarrow\rangle \\
|5\rangle &= \left|\frac{1}{2},\frac{1}{2}\right\rangle = \frac{1}{\sqrt{3}}|(X+iY)\downarrow\rangle + \frac{1}{\sqrt{3}}|Z\uparrow\rangle \\
|6\rangle &= \left|\frac{1}{2},\frac{-1}{2}\right\rangle = \frac{1}{\sqrt{3}}|(X-iY)\uparrow\rangle - \frac{1}{\sqrt{3}}|Z\downarrow\rangle
\end{aligned} \tag{3.42}$$

These basis functions have the symmetry of the atomic $|j,m_j\rangle$ states, where j and m_j denote the quantum numbers of the total angular momentum J and its projection on the z axis J_z. Moreover, these basis exactly diagonalizes the $\mathrm{H_{SO}}$ Hamiltonian term and are used to classify the valence bands into heavy hole (HH), light hole (LH), and split-off hole (SO). Using these states with Lowdin's method, the finite sub Hamiltonian matrix in Equation 3.14 takes the form,

$$H_{nn'} = \left\{E_{n'}(0) + \frac{\hbar^2k^2}{2m_0}\right\}\delta_{nn'} + \frac{\hbar}{m_0} + \frac{\hbar^2}{m_0^2}k_\alpha k_\beta \sum_{l\in R}\frac{\langle n|p_\alpha|l\rangle\langle l|p_\beta|n\rangle}{E_n(0)-E_l(0)} \tag{3.43}$$

where we note that $\pi_{nn'} = 0$, for $n,n' \in S$ and $\pi_{nn'\alpha} \approx \langle n|p_\alpha|l\rangle$, for $n, \in S$ and $l \in R$.

The explicit expression for the $6\times6LK\mathbf{k}\cdot\mathbf{p}$ Hamiltonian in the JM_J basis 3.42 reads:

$$H_{LK}^{6\times6} = -\begin{bmatrix} P+Q & -S & R & 0 & -\frac{1}{\sqrt{2}}S & \sqrt{2}R \\ -S^{\dagger} & P-Q & 0 & R & -\sqrt{2}Q & \sqrt{\frac{3}{2}}S \\ R^{\dagger} & 0 & P-Q & S & \sqrt{\frac{3}{2}}S^{\dagger} & \sqrt{2}Q \\ 0 & R^{\dagger} & S^{\dagger} & P+Q & -\sqrt{2}R^{\dagger} & -\frac{1}{\sqrt{2}}S^{\dagger} \\ -\frac{1}{\sqrt{2}}S^{\dagger} & -\sqrt{2}Q & \sqrt{\frac{3}{2}}S & -\sqrt{2}R & P+\Delta & 0 \\ \sqrt{2}R^{\dagger} & \sqrt{\frac{3}{2}}S^{\dagger} & \sqrt{2}Q & -\frac{1}{\sqrt{2}}S & 0 & P+\Delta \end{bmatrix} \begin{matrix} \left|\frac{3}{2},\frac{3}{2}\right\rangle \\ \left|\frac{3}{2},\frac{1}{2}\right\rangle \\ \left|\frac{3}{2},-\frac{1}{2}\right\rangle \\ \left|\frac{3}{2},-\frac{3}{2}\right\rangle \\ \left|\frac{1}{2},\frac{1}{2}\right\rangle \\ \left|\frac{1}{2},-\frac{1}{2}\right\rangle \end{matrix} \tag{3.44}$$

where

$$\begin{aligned} P &= E_v + \left(\frac{\hbar^2}{2m_0}\right)\gamma_1\left(k_x^2+k_y^2+k_z^2\right) \\ Q &= \left(\frac{\hbar^2}{2m_0}\right)\gamma_2\left(k_x^2+k_y^2-2k_z^2\right) \\ R &= \left(\frac{\hbar^2}{2m_0}\right)\sqrt{3}\left[-\gamma_2\left(k_x^2-k_y^2\right)+2i\gamma_3 k_x k_y\right] \\ S &= \left(\frac{\hbar^2}{2m_0}\right)2\sqrt{3}\gamma_3\left(k_x-ik_y\right)k_z \end{aligned} \tag{3.45}$$

The Hamiltonian in Equation 3.44 is known as 6 band Luttinger−Kohn Hamiltonian. The parameters γ_1, γ_2, and γ_3 are called the Luttinger parameters and are related to the effective masses of the valence-band electrons along certain directions. Δ is spin-orbit split-off energy.

3.4.4 The 4 x 4 Luttinger-Kohn valence band model

For some semiconductors, the split-off bands are several hundred *meV* below the heavy and light hole bands. If the energy range of interest is restricted to several tens of *meV*, it is usual to assume that the split off bands can be safely ignored. In other words, the band structure of the heavy and light hole bands is approximately described by the 4 x 4 Hamiltonian obtained by eliminating the fifth and sixth columns and the corresponding rows from the 6 $\times$6H_{LK} Hamiltonian matrix,

$$H_{LK}^{4\times4} = -\begin{bmatrix} P+Q & -S & R & 0 \\ -S^{\dagger} & P-Q & 0 & R \\ R^{\dagger} & 0 & P-Q & S \\ 0 & R^{\dagger} & S^{\dagger} & P+Q \end{bmatrix} \begin{matrix} \left|\frac{3}{2},\frac{3}{2}\right\rangle \\ \left|\frac{3}{2},\frac{1}{2}\right\rangle \\ \left|\frac{3}{2},-\frac{1}{2}\right\rangle \\ \left|\frac{3}{2},-\frac{3}{2}\right\rangle \end{matrix} \tag{3.46}$$

The 4-band Luttinger-Kohn model could have limited accuracy when the spin-orbit split-off energy Δ is small. The entries remains the same as for the $6 \times 6\mathrm{H}_{LK}$ Hamiltonian matrix.

3.4.5 The 8 x 8 Luttinger-Kohn conduction-valence band model

An even more accurate results are obtained when also the conduction bands at the $\Gamma-$ point are included in the class S. Including the spin orbit effect, an appropriate basis to construct the zinc blende $8\times8\mathbf{k}\cdot\mathbf{p}$ Hamiltonian are:

$$
\begin{aligned}
|1\rangle &= |iS\uparrow\rangle \\
|2\rangle &= \frac{-1}{\sqrt{2}}|(X+iY)\uparrow\rangle = |\frac{3}{2},\frac{3}{2}\rangle \\
|3\rangle &= \frac{1}{\sqrt{6}}|-(X+iY)\downarrow+2Z\uparrow\rangle = |\frac{3}{2},\frac{1}{2}\rangle \\
|4\rangle &= \frac{1}{\sqrt{3}}|(X+iY)\downarrow+Z\uparrow\rangle = |\frac{1}{2},\frac{1}{2}\rangle \\
|5\rangle &= |iS\downarrow\rangle \\
|6\rangle &= \frac{1}{\sqrt{2}}|(X-iY)\downarrow\rangle = |\frac{3}{2},-\frac{3}{2}\rangle \\
|7\rangle &= \frac{1}{\sqrt{6}}|(X-iY)\downarrow+2Z\downarrow\rangle = |\frac{3}{2},-\frac{1}{2}\rangle \\
|8\rangle &= \frac{1}{\sqrt{3}}|(X-iY)\downarrow-Z\downarrow\rangle = |\frac{1}{2},-\frac{1}{2}\rangle
\end{aligned}
\tag{3.47}
$$

The resulting $8\times8\,\mathbf{k}\cdot\mathbf{p}$ Hamiltonian model then reads,

$$
H_{LK}^{8\times8} =
\begin{bmatrix}
E_c+A & -\sqrt{3}V & \sqrt{2}U & U & 0 & 0 & V^* & \sqrt{2}V^* \\
-\sqrt{3}V^* & E_v-P-Q & S & 1/\sqrt{2}S & 0 & 0 & -R & -\sqrt{2}R \\
\sqrt{2}U & S^* & E_v-P+Q & \sqrt{2}Q & -V^* & -R & 0 & -\sqrt{3/2}S \\
U & 1/\sqrt{2}S^* & \sqrt{2}Q & E_v-P-\Delta & \sqrt{2}V^* & \sqrt{2}R & -\sqrt{3/2}S & 0 \\
0 & 0 & -V & \sqrt{2}V & E_c+A & \sqrt{3}V^* & \sqrt{2}U & -U \\
0 & 0 & -R^* & \sqrt{2}R^* & \sqrt{3}V & E_v-P-Q & -S^* & 1/\sqrt{2}S^* \\
V & -R^* & 0 & -\sqrt{3/2}S^* & \sqrt{2}U & -S & E_v-P+Q & -\sqrt{2}Q \\
\sqrt{2}V & -\sqrt{2}R^* & -\sqrt{3/2}S^* & 0 & -U & 1/\sqrt{2}S & -\sqrt{2}Q & E_v-P-\Delta
\end{bmatrix}
\begin{matrix}
|1\rangle \\ |2\rangle \\ |3\rangle \\ |4\rangle \\ |5\rangle \\ |6\rangle \\ |7\rangle \\ |8\rangle
\end{matrix}
\tag{3.48}
$$

where

$$
\begin{aligned}
A &= \left(\frac{\hbar^2}{2m_e^*}\right)\left(k_t^2+k_z^2\right)\\
P &= \left(\frac{\hbar^2}{2m_0}\right)\gamma_1\left(k_t^2+k_z^2\right)\\
Q &= \left(\frac{\hbar^2}{2m_0}\right)\gamma_2\left(k_t^2-2k_z^2\right)\\
R &= \left(\frac{\hbar^2}{2m_0}\right)\sqrt{3}\left[-\gamma_2\left(k_x^2-k_y^2\right)+2i\gamma_3 k_x k_y\right]\\
S &= \left(\frac{\hbar^2}{2m_0}2\right)\sqrt{3}\gamma_3\left(k_x-ik_y\right)k_z\\
V &= \frac{1}{\sqrt{6}}P_{cv}\left(k_x+ik_y\right)\\
U &= \frac{1}{\sqrt{3}}P_{cv}k_z\\
P_{cv} &= \frac{\hbar}{m_0}\langle iS|\frac{\hbar}{i}\frac{\partial}{\partial x}|X\rangle = \sqrt{\left(\frac{\hbar^2}{2m_0}\right)E_p}
\end{aligned}
\tag{3.49}
$$

The shape of the Hamiltonian usually depends on the states and on the order of the basis states used for the construction.

3.5 k.p Method for Nanostructures

Within the previous sections, we showed the $\mathbf{k}\cdot\ \mathbf{p}$ formulation based on the translational invariance property of the Bravais lattice, in other words, the crystal was assumed to be homogeneous and infinitely extended. In nanostructures, this assumption is no longer valid and the translational symmetry is broken in certain directions. The broken symmetry may arise due to variations in material compositions, impurities or even from external applied electric field, magnetic field, or mechanical stress. In the case of a quantum well, the symmetry is broken by the atoms of the other species in one direction Figure() and the electrons find themselves confined within a lower-bandgap material, but still free to propagate within the translational invariant direction. The electrons in such systems are now subjected to an additional non-uniform perturbing potential $V(\mathbf{x})$. As a result, the Hamiltonian describing such systems is not translational invariant an the Bloch function is no longer valid and need to be revised according to:

$$
\varphi_{m\mathbf{k}_t}(\mathbf{r}_t,z) = \sum_{\mu} u_{\mu\mathbf{0}}(\mathbf{r}_t,z)e^{i\mathbf{k}_t\cdot\mathbf{r}_t}F_{\mu}^{m}(\mathbf{k}_t,z) \tag{3.50}
$$

and the Schrödinger equation need to be solved now reads,

$$H\varphi_{m\mathbf{k}_t}(\mathbf{r}_t,z)=\left(H_0+\frac{\hbar}{4m_0^2c^2}(\sigma\times\nabla U)\cdot\mathbf{p}+V(\mathbf{x})\right)\varphi_{m\mathbf{k}_t}(\mathbf{r}_t,z)=E_{m\mathbf{k}_t}\varphi_{m\mathbf{k}_t}(\mathbf{r}_t,z). \quad (3.51)$$

Here, $\mathbf{r}_t$ denotes the coordinate of translational invariant direction(s), z is the coordinate of the direction(s) where the crystal symmetry is broken and $u_{\mu\mathbf{0}}$ is a lattice–periodic function. The crystal momentum $\mathbf{k}$ is only defined within the translational invariant direction. The expression $F_\mu^m(\mathbf{k}_t,z)$ is referred to as **slowly–varying envelope** and denotes at every position in the symmetry broken direction z, how the lattice–periodic functions are mixed together. In the bulk crystal, the plane wave term decouples the wavefunctions with different crystal momenta $\mathbf{k}$. In a nanostructure, this decoupling is only true for the translational invariant direction, while in the symmetry broken direction, the states are now mixed together. As a consequence of the symmetry breaking, the energy bands are split into energy subbands, depending on the transversal crystal momentum $\mathbf{k}_t$.

The next step is to use the envelope function approximation (EFA) [100] and derive a proper equation to determine the envelope functions $F_\mu^m(\mathbf{k}_t,z)$. The role of EFA aims to adapt the Hamiltonian to be applied to heterostructures. In the EFA approach, the perturbing potential is assumed to be a slowly varying function on the scale of the lattice constant. To show the result of using the EFA, it is convenient to decompose the bulk Hamiltonians in Equations 3.25, 3.37, 3.44, 3.46 and 3.48 into six terms, each one being the coefficient of k_x^2, k_y^2, k_z^2, k_xk_y, k_xk_z, and k_yk_z terms:

$$H=\sum_{\alpha=x}^{z}\sum_{\beta=\alpha}^{z}H_{\alpha\beta}k_\alpha k_\beta \quad (3.52)$$

where the indices run over the coordinates x,y, and z. Then, if we consider the z-axis to be the quantization axis (along which crystal symmetry is broken), the adaption of the Hamiltonians includes replacing the wave vector component k_z by the corresponding operator $-\mathbf{i}\frac{\partial}{\partial z}$ where $\mathbf{i}=\sqrt{-1}$, thus the Hamiltonian takes the form:

$$\begin{aligned}H&=H_{zz}k_z^2+H_{xx}k_x^2+H_{yy}k_y^2\\&\quad+(H_{xz}k_x+H_{yz}k_y)k_z+H_{xy}k_xk_y\\&\equiv H_Ak_z^2+H_Bk_z+H_C\\&=-H_A\frac{\partial^2}{\partial z^2}-\mathbf{i}H_B\frac{\partial}{\partial z}+H_C.\end{aligned} \quad (3.53)$$

This, as shown shortly, turns the problem of solving the Schrödinger Equation 3.51 for band structure into a set of simultaneous differential equations for the eigen envelope functions and eigen energies. This formulation can be further extended to any size of Hamiltonian. In our case study, the size 8×8 is of main concern. To preserve hermiticity of the Hamiltonian, the resulting derivative operators in Equation 3.53 are ordered as follows:

$$H = -\frac{\partial}{\partial z} H_A \frac{\partial}{\partial z} - \mathbf{i}\frac{1}{2}\left(H_B \frac{\partial}{\partial z} + \frac{\partial}{\partial z} H_B \right) + H_C. \tag{3.54}$$

This reordering is known as the symmetrization rules [82] given by:

$$\begin{aligned} H(\mathbf{x})k_\alpha &\rightarrow \frac{1}{2}\left(H(\mathbf{x})k_\alpha + k_\alpha H(\mathbf{x})\right) \\ H(\mathbf{x})k_\alpha k_\beta &\rightarrow \frac{1}{2}\left(k_\alpha H(\mathbf{x})k_\beta + k_\beta H(\mathbf{x})k_\alpha\right) \\ \alpha, \beta &\in \{x, y, z\}. \end{aligned} \tag{3.55}$$

which ensure hermiticity of the Hamiltonian as well as the flux continuity across the heterointerface and is equivalent to the Ben–Daniel–Duke boundary conditions in the case of single band model. Within the context of EFA, the wave functions for 8×8 Hamiltonian are approximated in terms of 8 envelope functions F_μ and 8 basis states $|\mu\rangle$:

$$|\Psi_{n\mathbf{k}_t}(\mathbf{x})\rangle = \frac{1}{\sqrt{S}} \sum_{\mu=1}^{8} F_\mu^n(\mathbf{k}_t, z) e^{\mathbf{i}\mathbf{k}_t \cdot \mathbf{r}_t} |\mu\rangle. \tag{3.56}$$

where $\mathbf{k}_t = k_x\mathbf{e}_x + k_x\mathbf{e}_y$ and $\mathbf{r}_t = x\mathbf{e}_x + y\mathbf{e}_y$. S is a normalization area of the heterostructures. Thus, the final result of EFA is to solve the following multiband effective mass equation in which the Hamiltonian in Equation (3.54) acts on an eight-component envelop function vector called spinor $\mathbf{F}$:

$$\mathbf{F} = [F_1, F_2, F_3, F_4, F_5, F_6, F_7, F_8]^T \tag{3.57}$$

$$[H_{8\times 8} - E_{\mathbf{k}_t} I]\mathbf{F} = \mathbf{0} \tag{3.58}$$

Here, I is the identity matrix. $E_{\mathbf{k}_t}$ are the eigen energies of the multiband effective mass equation at in-plane vector $\mathbf{k}_t$. It is worth mentioning that, to reduce the size of the problem to be solved, the 8×8 Hamiltonian can be block–diagonalized into two 4×4 Hamiltonians

and the 6×6 into a 3×3 by choosing an appropriate transformation matrix based on a new set of basis states. More details can be found in [46]. However, the block–diagonalization is restricted to a single direction in the transversal k–space, while arbitrary directions require modifications of the basis used for the block-diagonalization.

3.6 Strained Nanostructures

Quite general, semiconductor's nanostructures materials are subjected to strain during the epitaxial growth of different materials on top of each other. The lattice constants mismatch, between the grown materials if exists, results in a displacement of the crystal's atoms from their original positions producing strain. Thereby the crystal bonds are stretched or compressed out of their equilibrium length, leading to strong forces seeking for a restoration of the initial configuration. Under the action of the strain, the periodic crystal is deformed, which certainly affects the electronic band structure. In the presence of an arbitrary strain, the periodicity of the crystal is lost and Bloch's theorem can not be applied. Therefore, the application of the $\mathbf{k}\cdot\mathbf{p}$ theory in an arbitrary strain field is questionable. However, in the presence of a uniform strain, i.e. a strain which is constant within the space, the crystal may preserve the periodic property with a new deformed elementary cell such that $\mathbf{k}\cdot\mathbf{p}$ theory can be applied to the strained crystal using the Bir–Pikus strain theory [14].

A precise description of deformation of the crystal bonds requires atomistic details, but the huge number of atoms favors the application of continuum–mechanical elasticity model to calculate these strain and its effect on band structure. The deformation of a solid exhibits in the formation of stresses σ (forces per unit area). Using Hooke's law, the relation between a small strain ε and the stress σ can then be expressed in terms of a fourth-rank tensor C_{ijkl}:

$$\sigma_{ij} = C_{ijkl}\varepsilon_{ij}\varepsilon_{kl} \tag{3.59}$$

where Einstein's summation conventions are assumed. In literature, the normal stress components are usually denoted as σ_{xx}, σ_{yy} and σ_{zz} and the shear stress components as σ_{xy}, σ_{yx}, σ_{xz} etc. The diagonal elements of the stress tensor are of special importance in applications. If only σ_{xx} is a non-zero stress component then the stress is said to be **uniaxial**, while if both σ_{xx} and σ_{yy} are not equal to zero the stress is defined as **biaxial**. The fourth rank tensor elements are called elastic constants or the elastic stiffness constants. Using general symmetry arguments, the 81 tensor elements C_{ijkl} can be reduced to 21 distinct values which in turn can further be reduced, depending on the symmetry of the given crystal structure.

Within the context of elasticity theory, a notation due to Voigt has been introduced to avoid dealing with the cumbersome second-rank ε_{ij} strain tensor and the fourth-rank C_{ijkl} tensor. Therefore, in Voigt's notation the strain tensor is represented as an independent six components vector

$$\varepsilon = (\varepsilon_{xx}, \varepsilon_{yy}, \varepsilon_{zz}, \varepsilon_{yz}, \varepsilon_{xz}, \varepsilon_{xy}) \tag{3.60}$$

and C_{ijkl} as a second rank tensor C_{ij}:

$$C_{ij}, \qquad i, j = 1, \ldots 6 \tag{3.61}$$

Using these notation, strain energy can simply be expressed as

$$W = \frac{1}{2} C_{ij} \varepsilon_i \varepsilon_j. \tag{3.62}$$

Using Voigt's notation, the relation between stress and strain for zinc–blende cubic crystals is given by:

$$\begin{bmatrix} \sigma_{xx} \\ \sigma_{yy} \\ \sigma_{zz} \\ \sigma_{yz} \\ \sigma_{xz} \\ \sigma_{xy} \end{bmatrix} = \begin{bmatrix} C_{11} & C_{12} & C_{12} & 0 & 0 & 0 \\ C_{12} & C_{11} & C_{12} & 0 & 0 & 0 \\ C_{12} & C_{12} & C_{11} & 0 & 0 & 0 \\ 0 & 0 & 0 & C_{44} & 0 & 0 \\ 0 & 0 & 0 & 0 & C_{44} & 0 \\ 0 & 0 & 0 & 0 & 0 & C_{44} \end{bmatrix} \begin{bmatrix} \varepsilon_{xx} \\ \varepsilon_{yy} \\ \varepsilon_{zz} \\ 2\varepsilon_{yz} \\ 2\varepsilon_{xz} \\ 2\varepsilon_{xy} \end{bmatrix} \tag{3.63}$$

To model the strain in a nanostructure, one assumes that there exists a bulk host substrate material with a given lattice constant. If a thin layer with different lattice constant is epitaxially grown on the top of this substrate, then the thin layer is forced to acquire the in-plane lattice constant of the substrate, while the perpendicular lattice constant is able to relax freely along the growth direction. As a result, the thin layer crystal lattice is under biaxial stress along the layer plan with only two diagonal components σ_{xx} and σ_{yy} while σ_{zz} and the shear components are zero. The biaxial stress is accompanied by an in-plane strain. If the lattice constant of strained epitaxial layer reaches the substrate lattice constant then the used growth is said to be pseudomorphic. In such cases, the in-plane strain can be easily calculated as:

$$\varepsilon_{\parallel} = \varepsilon_{xx} = \varepsilon_{yy} = \frac{a_{sub} - a}{a} \tag{3.64}$$

where a_{sub} and a are the lattice constant of the substrate and of any layer material within the heterostructures, respectively. The in-plane strain magnitude is usually of the order of 1% in quantum well systems e.g. for an AlN layer grown on a GaN substrate $|\varepsilon_{\parallel}| = 2\%$. However, materials with $|\varepsilon_{\parallel}| \leq 0.1\%$ such as the GaAs/AlGaAs system are considered as unstrained.

Depending on the sign of $\varepsilon_{\parallel}$, one can define a compressive ($\varepsilon_{\parallel} < 0$) or a tensile ($\varepsilon_{\parallel} > 0$) strain, respectively. A compressive strain will therefore force the lattice constant in the plane to shrink while conversely tensile strain will force it to expand. It is also reasonable to assume that the strain in the thin semiconductor layers is homogeneous and therefore constant throughout the layer.

Moreover, if the epitaxial layer width is larger than some critical thickness the layer have enough energy to resist the substrate force tending to unify its lattice constant. This reluctance for change results in a large number of defects and imperfections (cracks) in the growth surface. In terms of elastic energy, if for a specific layer width the strain energy of the strained layer exceeds the energy required for the generation of defects, then the layer system will tend to relax to a new state with lower strain energy forming imperfections in the growth plane. Therefore, pseudomorphic growth is a necessary condition for the fabrication of good quality layers with a small number of crystal defects.

Furthermore, despite $\sigma_{zz} = 0$, the vertical lattice constant is also exhibiting a strain ε_{zz} due to Poisson's effect. The so called Poisson's ratio ν is used to measures the strain in the vertical direction as function of in–plain strain: $\varepsilon_{zz} = -\nu\varepsilon_{xx}$.

The biaxial strain covers most of the important strained systems, namely a bulk semiconductor under an external uniaxial stress and a semiconductor strained-layer pseudomorphically grown on a (001) oriented substrate. For the commonly used zinc–blende semiconductor materials and assuming biaxial strain, the strains in the epitaxial layers are given as:

$$\begin{aligned} \varepsilon_{xx} &= \varepsilon_{yy} = \frac{a_{sub} - a}{a} \\ \varepsilon_{zz} &= -\frac{2C_{12}}{C_{11}}\varepsilon_{xx} \end{aligned} \tag{3.65}$$

where C_{11} and C_{12} are the elastic stiffness constants and the factor $\nu = -\frac{2C_{12}}{C_{11}}$ represents Poisson's ratio for zinc–blende semiconductors in the [001] direction. Its also possible to generate extrinsic strain as opposed to intrinsic strain mentioned above using an applied stress. For the case of an external uniaxial stress T along the directions [100], [110], and [001], the

generated strain contributes by [62]:

$$\begin{aligned}
&[100] : \varepsilon_{xx} = S_{11}T, \quad \varepsilon_{yy} = \varepsilon_{zz} = S_{12}T. \\
&[110] : \varepsilon_{xx} = \varepsilon_{yy} = \frac{1}{2}(S_{11} + S_{12})T, \quad \varepsilon_{zz} = S_{12}T, \quad \varepsilon_{xy} = \frac{1}{4}S_{44}T. \\
&[001] : \varepsilon_{xx} = \varepsilon_{yy}S_{12}T, \quad \varepsilon_{zz} = S_{11}T.
\end{aligned} \tag{3.66}$$

where S_{11}, S_{12}, and S_{44} are compliance constants related to the elastic stiffness constants.

3.6.1 Strained Hamiltonian

Strain has a noticeable effect on the electronic band structure. The presence of strain induces shifts in the band edges via the deformation potentials as described by Bir–Pikus strain theory. The idea behind this theory is to restore the crystal periodicity using a deformed coordinate transformation. The actual form of the deformation potential can be deduced using symmetry arguments. For the conduction band the strain results in a hydrostatic strain energy shift given by:

$$\Delta E_c = a_c(\varepsilon_{xx} + \varepsilon_{yy} + \varepsilon_{zz}) \tag{3.67}$$

The term hydrostatic reflects the fact that $(\varepsilon_{xx} + \varepsilon_{yy} + \varepsilon_{zz})$ represents the volume change of the crystal. For the valence bands, strain contribute by an additional term to the $\mathbf{k}\cdot\mathbf{p}$ Hamilton,

$$\begin{aligned}
\widetilde{S}(\varepsilon) = &\sqrt{3}d\varepsilon + (a_v + 2b - \sqrt{3}d)\,\mathrm{diag}(\varepsilon_{xx}, \varepsilon_{yy}, \varepsilon_{zz}) \\
&+ (a_v - b)\,\mathrm{diag}(\varepsilon_{yy} + \varepsilon_{zz}, \varepsilon_{xx} + \varepsilon_{zz}, \varepsilon_{xx} + \varepsilon_{yy})
\end{aligned} \tag{3.68}$$

The the parameters a_c,a_v and b, d define the Bir–Pikus hydrostatic and shear deformation potentials, respectively. The effect of strain in our tools is included in all the zinc–blende $\mathbf{k}\cdot\mathbf{p}$ models.

3.6.1.1 Strained 8 x 8 Luttinger-Kohn conduction-valence band model

Taking into account the strain effect the $8\times8 Luttinger-Kohn Hamiltonian model in Equation\ 3.48 reads$,

$$
H_{LK}^{8\times 8} =
\begin{bmatrix}
E_c+\mathscr{A} & -\sqrt{3}\mathscr{V} & \sqrt{2}\mathscr{U} & \mathscr{U} & 0 & 0 & \mathscr{V}^* & \sqrt{2}\mathscr{V}^* \\
-\sqrt{3}\mathscr{V}^* & E_v-\mathscr{P}-\mathscr{Q} & \mathscr{S} & 1/\sqrt{2}\mathscr{S} & 0 & 0 & -\mathscr{R} & -\sqrt{2}\mathscr{R} \\
\sqrt{2}\mathscr{U} & \mathscr{S}^* & E_v-\mathscr{P}+\mathscr{Q} & \sqrt{2}\mathscr{Q} & -\mathscr{V}^* & -\mathscr{R} & 0 & -\sqrt{3/2}\mathscr{S} \\
\mathscr{U} & 1/\sqrt{2}\mathscr{S}^* & \sqrt{2}\mathscr{Q} & E_v-\mathscr{P}-\Delta & \sqrt{2}\mathscr{V}^* & \sqrt{2}\mathscr{R} & -\sqrt{3/2}\mathscr{S} & 0 \\
0 & 0 & -\mathscr{V} & \sqrt{2}\mathscr{V} & E_c+\mathscr{A} & \sqrt{3}\mathscr{V}^* & \sqrt{2}\mathscr{U} & -\mathscr{U} \\
0 & 0 & -\mathscr{R}^* & \sqrt{2}\mathscr{R}^* & \sqrt{3}\mathscr{V} & E_v-\mathscr{P}-\mathscr{Q} & -\mathscr{S}^* & 1/\sqrt{2}\mathscr{S}^* \\
\mathscr{V} & -\mathscr{R}^* & 0 & -\sqrt{3/2}\mathscr{S}^* & \sqrt{2}\mathscr{U} & -\mathscr{S} & E_v-\mathscr{P}+\mathscr{Q} & -\sqrt{2}\mathscr{Q} \\
\sqrt{2}\mathscr{V} & -\sqrt{2}\mathscr{R}^* & -\sqrt{3/2}\mathscr{S}^* & 0 & -\mathscr{U} & 1/\sqrt{2}\mathscr{S} & -\sqrt{2}\mathscr{Q} & E_v-\mathscr{P}-\Delta
\end{bmatrix}
\begin{matrix}
|1\rangle \\ |2\rangle \\ |3\rangle \\ |4\rangle \\ |5\rangle \\ |6\rangle \\ |7\rangle \\ |8\rangle
\end{matrix}
\tag{3.69}
$$

where the entries in Equation 3.69 now reads,

$$
\begin{aligned}
\mathscr{A} &= A_k + A_\varepsilon \\
\mathscr{P} &= P_k + P_\varepsilon \\
\mathscr{Q} &= Q_k + Q_\varepsilon \\
A_k &= \left(\frac{\hbar^2}{2m_e^*}\right)\left(k_t^2+k_z^2\right) \\
P_k &= \left(\frac{\hbar^2}{2m_0}\right)\gamma_1\left(k_t^2+k_z^2\right) \\
Q_k &= \left(\frac{\hbar^2}{2m_0}\right)\gamma_2\left(k_t^2-2k_z^2\right) \\
\mathscr{R} &= \left(\frac{\hbar^2}{2m_0}\right)\sqrt{3}\left[-\gamma_2\left(k_x^2-k_y^2\right)+2i\gamma_3 k_x k_y\right] \\
\mathscr{S} &= \left(\frac{\hbar^2}{2m_0}\right)2\sqrt{3}\gamma_3\left(k_x-ik_y\right)k_z \\
\mathscr{V} &= \frac{1}{\sqrt{6}}P_{cv}\left(k_x+ik_y\right) \\
\mathscr{U} &= \frac{1}{\sqrt{3}}P_{cv}k_z \\
P_{cv} &= \frac{\hbar}{m_0}\left\langle iS\left|\frac{\hbar}{i}\frac{\partial}{\partial x}\right|X\right\rangle = \sqrt{\left(\hbar^2/2m_0\right)E_p} \\
A_\varepsilon &= a_c\left(\varepsilon_{xx}+\varepsilon_{yy}+\varepsilon_{zz}\right) \\
P_\varepsilon &= -a_v\left(\varepsilon_{xx}+\varepsilon_{yy}+\varepsilon_{zz}\right) \\
Q_\varepsilon &= -\frac{b}{2}\left(\varepsilon_{xx}+\varepsilon_{yy}-2\varepsilon_{zz}\right)
\end{aligned}
\tag{3.70}
$$

3.6.1.2 Non-Parabolic Single Band k.p Model

This model is a simplified version of the multiband model where only a single band is concerned. If one ignores the interaction between the conduction band and the valance bands, which is the case for most III–V direct gap semiconductors, then the conduction band can be described using the following single band parabolic Hamiltonian model [16]:

$$H(\mathbf{k}) = \frac{\hbar^2}{2}\left(\frac{k_x^2+k_y^2}{m_t^*}+\frac{k_z^2}{m_e^*}\right) + E_c + a_c\left(\varepsilon_{xx}+\varepsilon_{yy}+\varepsilon_{zz}\right) \tag{3.71}$$

where m_e^* is the electron effective mass along the growth direction and m_t^* the transverse one. E_c is the unstrained conduction band edge. The fact of using two different effective masses is to account for the anisotropy of the energy band. To increase the accuracy of this model Hamiltonian, the effect of non-parabolicity has to be accounted for, which includes the effect of remote bands in an indirect way without the need to solve the full multi–band Hamiltonian. To this end, an energy-dependent effective mass model has been proposed [84]:

$$m_e^*(E) = m_e^* \cdot \left(1+\frac{E-E_c}{E_g}\right) \tag{3.72}$$

where E_g is an effective energy gap and does not necessarily match with real energy gap. With this energy dependence, and under the effective mass approximation [12], the eigenvalue problem corresponding to the Hamiltonian in Equation 3.71 is quadratic and a nonlinear one in terms of energy [105]. To solve such a problem, an iterative algorithm should be invoked to avoid dealing with a fourth-order derivative when ensuring the continuity of probability current across heterointerfaces, which involves only the first derivative of the envelop function.

3.7 Finite Element Discretization of a k.p Hamiltonian

For bulk Hamiltonian, all its terms are position independent such as E_c and E_v. In addition, the wave vector components k_x, k_y, and k_z are input parameters and no space discretization is needed to calculate bulk dispersion. For bulk semiconductor, the overall band structure is determined by solving the following Schrodinger equation with a Hamiltonian using Equation 3.25, 3.37, 3.44, 3.46 or 3.48 in a compact form as:

$$H(\mathbf{k})|\varphi\rangle = E(\mathbf{k})|\varphi\rangle \tag{3.73}$$

where $|\varphi\rangle$ is a column vector for the basis used for the construction of the Hamiltonian and $\mathbf{k}$ is the wave vector. This gives the energy E versus $\mathbf{k}$ in different directions, namely k_x, k_y, and k_z.

With heterostructures, the band edges become position dependent, i.e. $E_c(\mathbf{x})$ and $E_c(\mathbf{x})$, and thus constitute the potential profile $V(\mathbf{x})$ of the heterostructure. Using the presented EMA theory in Section 3.5, the final form of the multiband effective mass equation for the eigen envelope functions $\mathbf{F}_{n\mathbf{k}_t} = [F_1, F_2, \ldots, F_M]^T$ is given by the second order coupled partial differential equations:

$$\mathbf{H}^{\mathbf{k}\cdot\mathbf{p}}_{M\times M}\mathbf{F}_{n\mathbf{k}_t}(z) = E\mathbf{F}_{n\mathbf{k}_t}(z) \tag{3.74}$$

where the $\mathbf{k}\cdot\mathbf{p}$ differential operator is given by:

$$\mathbf{H}^{\mathbf{k}\cdot\mathbf{p}}_{M\times M} = -\frac{\partial}{\partial z}H_A(\mathbf{k}_t,z)\frac{\partial}{\partial z} - \mathbf{i}\frac{1}{2}\left(H_B(\mathbf{k}_t,z)\frac{\partial}{\partial z} + \frac{\partial}{\partial z}H_B(\mathbf{k}_t,z)\right) + H_C(\mathbf{k}_t,z). \tag{3.75}$$

The equation (3.74) is applicable to all $\mathbf{k}\cdot\mathbf{p}$ models and forms an eigenvalue problem. z represents the quantized coordinates, while $\mathbf{k}_t$ denotes the transversal crystal momentum. The matrices H_A, H_B and H_C are parametrized in terms of the transversal $\mathbf{k}_t$ and are determined via Equations 3.25, 3.37, 3.44, 3.46 or 3.48 using the decomposition (3.53).

To use FEM analysis to solve the multiband effective mass in Equation (3.74), it is instructive to use either the Galerkin or variational approach, as both lead to the same final expression. In this work, the variational approach is adopted and briefly discussed, and more details can be found in [147]. The variational approach is based on seeking a variational expression corresponding to the set of differential equations to be solved. Following the steps in [147], we end up with the following variational expression:

$$\begin{aligned} V_{exp} = &\int\left\{\left(\frac{\partial}{\partial z}F^\dagger\right)H_A\left(\frac{\partial}{\partial z}F\right)\right\}dz \\ &+\mathbf{i}\frac{1}{2}\int\left\{\left(\frac{\partial}{\partial z}F^\dagger\right)H_BF - F^\dagger H_B\left(\frac{\partial}{\partial z}F\right)\right\}dz \\ &+\int\left\{F^\dagger(H_C-E)F\right\}dz. \end{aligned} \tag{3.76}$$

The next step is to minimize this functional using FEM to get the solution of the original problem in Equation (3.74). To achieve this, the envelop functions are approximated over each finite element as $\mathbf{F = N(z)}\cdot\widetilde{\mathbf{F}} = N_i\widetilde{F}_i$, where $\mathbf{N}$ is an interpolation shape function and $\widetilde{\mathbf{F}}$

is a nodal column vector with elements representing the values of the envelope function at the element nodal mesh points [83, 91]. Substituting **F** into Equation (3.74), we obtain the following matrix form to be minimized:

$$\begin{aligned} V_{exp} = \widetilde{F}^{\dagger} & \left[\int \left\{ \frac{\partial N^T}{\partial z} H_A \frac{\partial N}{\partial z} \right\} dz \right] \widetilde{F} \\ & + \mathbf{i} \frac{1}{2} \widetilde{F}^{\dagger} \left[\int \left\{ \frac{\partial N^T}{\partial z} H_B N - N^T H_B \frac{\partial N}{\partial z} \right\} dz \right] \widetilde{F} \\ & + \widetilde{F}^{\dagger} \left[\int N^T H_C N \, dz \right] \widetilde{F} \\ & - E \widetilde{F}^{\dagger} \left[\int N^T N \, dz \right] \widetilde{F}. \end{aligned} \tag{3.77}$$

which can be cast into a compact form as:

$$V_{exp} = \widetilde{F}^{\dagger} \widetilde{\mathbf{H}} \widetilde{F} - E \widetilde{F}^{\dagger} \widetilde{\mathbf{D}} \widetilde{F}. \tag{3.78}$$

where $\widetilde{\mathbf{H}}$ is a matrix arising from the first and the second terms, and $\widetilde{\mathbf{D}}$ is a matrix from the last term. Both matrices are of size $M \cdot n_s \times M \cdot n_s$ where n_s is the number of degrees of freedom used in the system. The minimization procedure with respect to the unknown nodal values of $\widetilde{\mathbf{F}}$ requires $\dfrac{\partial V_{exp}}{\partial F^{\dagger}} = 0$, which yields:

$$\widetilde{\mathbf{H}} \widetilde{F} = E \widetilde{\mathbf{D}} \widetilde{F}. \tag{3.79}$$

This is a generalized eigen value problem for the energies E and the representative nodal values of the envelope functions at the mesh points. In constructing the global matrix **H** and **D**, an element matrix overlay approach is usually used, which requires considerable care since we are dealing with up to eight simultaneous equations. The problem in Equation (3.79) can be efficiently solved using well-established algorithms devoted for large eigenvalue problem.

3.8 Simulation Results and Discussion

In this section, the electronic structure of semiconductor will be investigated using three applications: (1) the bound energies of a finite quantum well using the energy-dependent effective mass non-parabolic model; (2) the InAs bulk band structure; and (3) the electronic band structure for the absorber region of photodetectors based on a type-II InAs/GaSb superlattice at room temperature.

3.8.1 Electronic Structure of Finite Quantum Well

First, a case study was solved to validate the accuracy of the simulations to published results using an energy-dependent effective mass non-parabolic model on a structure of a single quantum well [105]. This is a 100 Å GaAs thin well layer surrounded by AlGaAs barrier layers. The barrier height was set to 0.276 eV and the effective masses of electrons at the band edges were taken to be $m_w/m_0 = 0.067$ in the well and $m_b/m_0 = 0.09$ in the barrier. Here, the subscripts w and b denote the well and barrier, respectively, and m_0 is the electron free mass. The in-plane wavevector components k_x and k_y were set to zero for the purpose of comparison. Using this model, Equations (3.71) and (3.72) under the EFA were solved repeatedly by updating the effective masses and eigen energies until their convergence. The results of the second-order Lagrange finite element method are shown in Table 3.2 along with the results of two other numerical methods, namely the Finite Difference Method (FDM) [13] and the Transfer Matrix Method (TMM) [45], which are also included in the simulation tools developed.

Table 3.2 Eigen energies of a single GaAs/AlGaAs quantum well (in meV). ΔE is the shift due to nonparabolicity. The FEM results are compared to the results from [105].

Well	Parabolic				Nonparabolic				ΔE			
Width	FDM	FEM	TMM	[?]	FDM	FEM	TMM	[?]	FDM	FEM	TMM	[?]
5 Å	267.48	267.48	265.40	267.51	267.51	267.51	265.42	267.53	+0.03	+0.03	+0.02	+0.02
20 Å	179.95	179.95	179.93	179.93	180.96	180.96	180.95	180.99	+1.01	+1.02	+1.01	+1.07
50 Å	79.56	79.58	79.58	79.54	81.03	81.05	81.05	81.07	+1.48	+1.47	+1.47	+1.53
	270.16	270.17	268.20	270.19	254.67	254.69	254.13	254.70	−15.49	−15.48	−14.08	−15.49
100 Å	31.48	31.49	31.49	31.48	32.18	32.19	32.19	32.20	+0.70	+0.70	+0.70	+0.72
	123.84	123.89	123.89	123.87	119.01	119.05	119.05	119.06	−4.83	−4.84	−4.84	−4.81
	258.34	258.40	257.83	258.42	234.89	234.95	234.84	234.96	−23.46	−23.45	−22.99	−23.46
200 Å	10.31	10.31	10.31	10.30	10.49	10.50	10.50	10.50	+0.18	+0.19	+0.19	+0.20
	41.13	41.15	41.15	41.14	40.88	40.90	40.90	40.91	−0.25	−0.25	−0.25	−0.23
	92.08	92.14	92.14	92.13	88.29	88.35	88.35	88.36	−3.79	−3.79	−3.79	−3.77
	161.91	162.08	162.08	162.07	148.78	148.92	148.92	148.93	−13.13	−13.16	−13.16	−13.14
	245.78	246.08	245.93	246.09	217.49	217.76	217.74	217.77	−28.29	−28.31	−28.19	−28.32

The calculation was carried for both the parabolic and non-parabolic case and the results are compared with Samir et al. [105]. Table 3.2 lists the confined eigen energies in quantum wells of different widths ranging from 5 Å to 200 Å. The results are in excellent agreement with the reported data. The results also clearly show that the single-band parabolic model leads

to energies slightly over estimated for higher lying states. Therefore, our results confirm the effects of including non-parabolicity, which shrinks the confined energy gaps with a noticeable shift in the higher energies.

An illustrative example for such effect is given in Figure 3.2, where the probability density of the first five states of a 100 Å GaAs quantum well embedded in AlGaAs is shown for the parabolic and non-parabolic case. In both panels, the energies E_n are indicated by the thin horizontal lines, and the probability densities $|\varphi(z)|^2$ by the shaded colored areas. There are only three confined states for electrons. The tunneling of the eigenfunctions through the barriers is larger for states with high energies and decreases from the parabolic to non-parabolic.

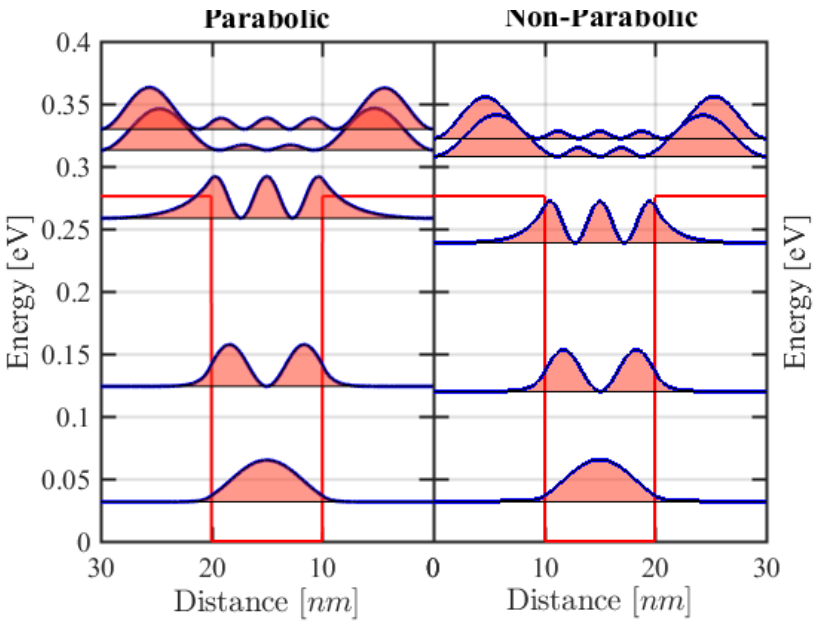

Figure. 3.2 The conduction band edge profile (red), first five electron eigenstates, and the corresponding probability densities for $k_t = 0$ in 100 Å GaAs/$Al_xGa_{l-x}As$ quantum well for $x = 0.3$: (**Right**) calculated using a parabolic single band model; and (**Left**) calculated using a non-parabolic single band model.

3.8.2 Bulk Band Structure of Strained InAs material

The second application that is investigated in this work deals with the calculation of the bulk band structure of InAs material strained by a GaAs substrate of 5.6533 Å lattice constant. Due to the lattice mismatch between these two material, the grown bulk layer experiences an intrinsic compressive strain of -7.09%. The value of strain used in this case is calculated using the formula $(a_{sub} - a)/a \times 100\%$ where a_{sub} and a are the lattice constant of the substrate and of InAs material. The overall conduction band and valence bands dispersion using the 8×8 $\mathbf{k}\cdot$

p Hamiltonian in Equation (3.69) is obtained by diagonalizing Equation (3.69) or equivalently by solving the following secular equation at each wavevector $\mathbf{k} \equiv \{k_x, k_y, k_z\}$:

$$det\left[H_{\alpha\beta}^{8\times 8}(\mathbf{k}) - \delta_{\alpha\beta}E(\mathbf{k})\right] = 0. \tag{3.80}$$

In Figure 3.3, the overall band structure curves of strained bulk InAs and unstrained standalone bulk InAs are shown along the k_x and k_z directions, respectively. These curves are dispersions for the conduction band (CB), Heavy Hole (HH), Light Hole (LH), and spin–orbit split-off (SO) valance bands. In Figure 3.3 (right), the 6×6 $\mathbf{k}\cdot\mathbf{p}$ Hamiltonian curves are shown. This 6×6 Hamiltonian couples only the three valance bands and ignores the coupling with conduction band, which is justified only in wide energy gap materials. Within this 6×6 Hamiltonian, the conduction-band states, which are not shown in this figure, can be treated separately using single-band model. In narrow energy gap materials such as InAs, the 6×6 Hamiltonian results show a discrepancy for higher in-plane wave vectors. Figure 3.4 shows the band structures of unstrained bulk InA along crystallographic directions pointing to high symmetry points. The Hamiltonian used is the 14×14 one from [104], which extends the interaction to more higher bands. The results confirm that including the conduction band into the Hamiltonian increases the conduction band for higher k_x values while pushing down LH and SO bands. This effect is negligible on HH band. In Figure 3.4 (left), the conduction band is parabolic in both directions k_x and k_z while the valence bands exhibit a non-parabolicity due to mixing effects. The strain lifts the HH and LH bands degeneracy at the zone center. The parabolic isotropy is in fact a reflection of the s-like character of conduction-band states in a bulk semiconductor. Table 3.3 lists the $\mathbf{k}\cdot\mathbf{p}$ band parameters used for the calculation [73, 96]. The script used to generate the dispersion curves is given in Figure 3.5. It should be noted that the $\mathbf{k}\cdot\mathbf{p}$ method results are sensitive to the input parameters.

Moreover, the $\mathbf{k}\cdot\mathbf{p}$ solutions are subject to a well-known problem of unphysical "spurious" solutions, especially with Hamiltonians that include more remote bands or when band parameters have large difference across layers' interfaces [46].

Table 3.3 **k**· **p** parameters used for the calculation [96, 73, 139].

Parameter	**Unit**	**InAs**	**GaSb**	**GaAs**	**InSb**
a	Å	6.0522	6.0854	5.6535	6.4794
C_{11}	10^{11} dyn/cm^2	8.33	8.842	12.21	6.67
C_{12}	10^{11} dyn/cm^2	4.526	4.026	5.66	3.65
a_c	eV	−5.08	−7.5	−7.17	−5.1
a_v	eV	1	0.8	−1.16	2.1
b	eV	−1.8	−2	−2	−2.0
E_g at 0K	eV	0.42	0.81	1.519	0.235
E_g at 77K	eV	0.407	0.8	1.43	0.227
E_p	eV	21.5	22.4	28.8	23.3
Δ	eV	0.38	0.81	0.341	0.81
m_c/m_0	–	0.0224	0.0412	0.0670	0.0135
γ_1	–	19.4	11.84	6.98	32.4
γ_2	–	8.545	4.25	2.06	13.3
γ_3	–	9.17	5.01	2.93	15.15
VBO	eV	−0.59	−0.03	−0.8	−0.03

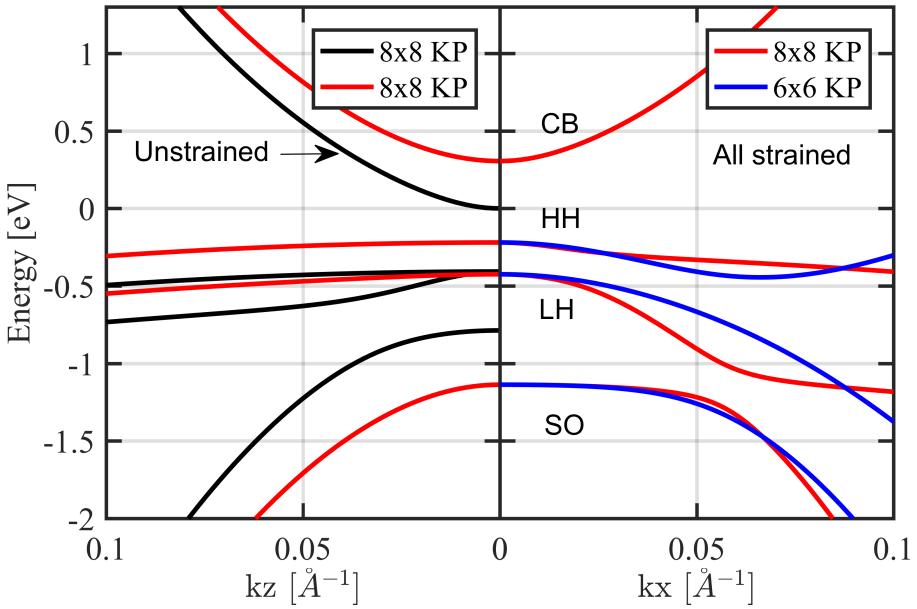

Figure. 3.3 (**Right**) The overall band dispersion of strained bulk InAs. The material is under intrinsic compressive strain of -7.09%. The red solid line is from the 8×8 Hamiltonian while the blue line is from the 6×6 Hamiltonian. (**Left**) The band dispersion of standalone bulk InAs against the strained one.

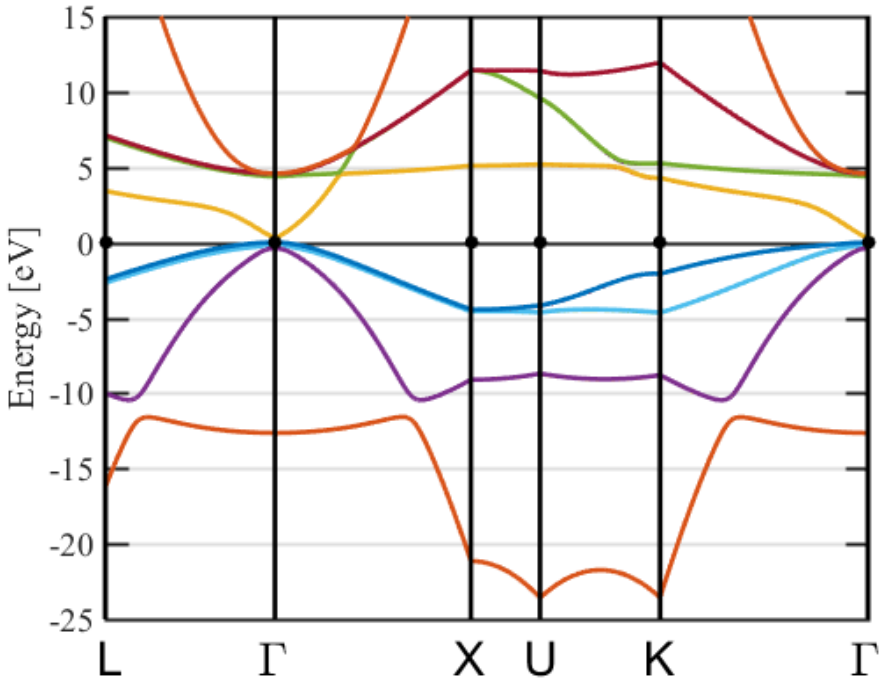

Figure. 3.4 The bulk band structure of unstrained InAs along different crystallographic directions. The vertical solid lines are the boundaries of the first Brillouin zone. Solid curves are from the 14×14 $\mathbf{k}\cdot\mathbf{p}$ Hamiltonian [104].

```
bulk.name='InAs';
bulk.substrate.name='GaAs';
bulk.direction=[1 0 0];
bulk.stress=0;
bulk.nKP=8;
bulk.model='Chaung';
bulk.SPscheme.s=0;
bulk.SPscheme.alfa=0;
bulk.SPscheme.model=0;
bulk=Setbulk(bulk);
a0=bulk.layer.a0;
kv=getKv('LGXUKG','line',nk,a0);
 for i=1:length(kv)
     kx=kv.kv(i,1);
     ky=kv.kv(i,2);
     kz=kv.kv(i,3);
    Ek(i,:)=BULK_KP(bulk,kx,ky,kz);
 end
PLOTBAND(kv,Ek,15,-25,'LGXUKG','nm')
```

Figure. 3.5 The compact script used to setup and calculate band dispersion of bulk InAs. The Strained 8×8 $\mathbf{k}\cdot\mathbf{p}$ Hamiltonian used is from Chuang et al [73].

Such unphysical solutions should be identified and removed from the region of interest. The spurious solutions arise from the incompleteness of the basis states used for the construction of the Hamiltonian [30]. This is still a standing problem; different approaches and models have been proposed to eliminate them but each approach has its drawbacks. Such solutions may appear as highly oscillatory or strongly localized wave functions within the band gap or dispersion curves bending in the wrong direction [24, 31, 22]. Three main reasons have been identified for the source of the spurious solutions. First, the input experimental parameters can trigger wing-band solutions within the band gap originating from second-order Hamiltonian's terms at large-$\mathbf{k}$ values [31, 61, 22]. These solutions can be avoided by parameter rescaling procedures [81, 138]. Second, the interface between two materials can be subject to localized spurious solutions due to improper boundary condition for the envelope function components. These solutions can be removed by a proper ordering of differential operators [106, 138]. Finally, the spurious solutions may also be triggered by the chosen discretization scheme

and the mesh width, and it was found to be related to the ill-representation of the first-order derivative terms of the Hamiltonian [75, 22].

In the developed simulation tools, two elimination models are implemented. The first one is based on adding a small correction to the off-diagonal elements of the Hamiltonian [61] to discard terms responsible for the spurious solutions and the second one modifies Kane's parameter P_{cv} [30, 31].

3.8.3 Electronic Band Structure of Type-II InAs/GaSb Superlattice

Finally, the last test case illustrates the ability of the tools to model a realistic optoelectronic device where the miniband dispersions of the active region of an infrared photodetectors based on type-II InAs/GaSb superlattices are calculated. The studied superlattice is mainly composed of nine InAs/GaSb periods with thicknesses around 44 Å/21 Å, respectively. The InAs layers are chosen to be thicker than GaSb layers to efficiently reduce the dark current [107]. This superlattice is designed to operate in a long wavelength infrared radiation (LWIR) 8–14 m atmospheric detection window. The potential profile $V(\mathbf{r})$ of this active region is periodic and this periodicity is handled using the Bloch theorem, which greatly simplifies the computational task. Within this theorem, the wave function in two adjacent superlattice periods differs only by a phase shift: $\varphi(z) = \varphi(z-p)e^{\mathbf{i}k_p \cdot p}$ where k_p is the Bloch wavenumber and p is the superlattice period. From a computational point of view, this boundary condition is implemented by overlaying the last element matrix onto the first one modulated by the factors $e^{\pm \mathbf{i}k_p \cdot p}$ in the global matrix system. The Dirichlet boundary condition is implemented by setting the envelope function to zero at the external borders of the structure. Type II InAs/GaSb superlattice is made of narrow energy gap materials in which the coupling between conduction bands and valance bands is strong; therefore, the 8×8 $\mathbf{k} \cdot \mathbf{p}$ Hamiltonian in Equation (3.69) should be used. To account for this strong interaction, the original electron effective mass m_e^* in the diagonal Hamiltonian matrix as well as the original Luttinger parameters γ_1, γ_2, and γ_3 should

be updated according to:

$$\frac{m_0}{m_e^*} = \frac{m_0}{m_c^*} - E_p \frac{E_g + 2\Delta/3}{E_g\,(E_g + \Delta)} \tag{3.81}$$

$$\begin{aligned} \gamma_1 &= \gamma_1^L - \frac{E_p}{3E_g + \Delta} \\ \gamma_2 &= \gamma_2^L - \frac{1}{2}\frac{E_p}{3E_g + \Delta} \\ \gamma_3 &= \gamma_3^L - \frac{1}{2}\frac{E_p}{3E_g + \Delta} \end{aligned} \tag{3.82}$$

where m_c^*, γ_1^L, γ_2^L, and γ_3^L are now the original effective mass and the original Luttinger parameters, respectively. These normalizations are only required with Hamiltonians of size greater than 8×8. This is because the strong interaction is explicitly included in the formulation of the eight-band model, whereas, in smaller size $\mathbf{k}\cdot\mathbf{p}$ models, the valence and conduction bands are decoupled and the Luttinger parameters are adjusted using Löwdin perturbation method [74]. Using the Löwdin perturbation, method, the Hamiltonian is reduced to a smaller number of relevant bands, including the effect of the remote bands perturbatively. In all calculations, the symmetrization rules given by Equation (3.55) are applied to taken into account the real space dependence of the bulk band parameters.

The band edge profile potential emanating from a structure of a nine-period InAs/GaSb44 Å/21 Å superlattice, simulated using our model is shown in Figure 3.6 (right). The corresponding miniband energy-dispersions versus in-plane wavevector k_t solved using Dirichlet boundary conditions are shown in Figure 3.6 (left). In this figure, the reference of energy is taken to be the unstrained conduction band edge of InAs layers with a VBO value of 560 meV. The formation of minibands confirms the quantum mechanical intuition that, since electrons and holes in InAs/GaSb Type II superlattice are separated in space, confined electrons in thin InAs layers form their mini-bands due to overlap of electron wave functions. Similarly, the interaction among holes in thin GaSb layers leads to hole minibands.

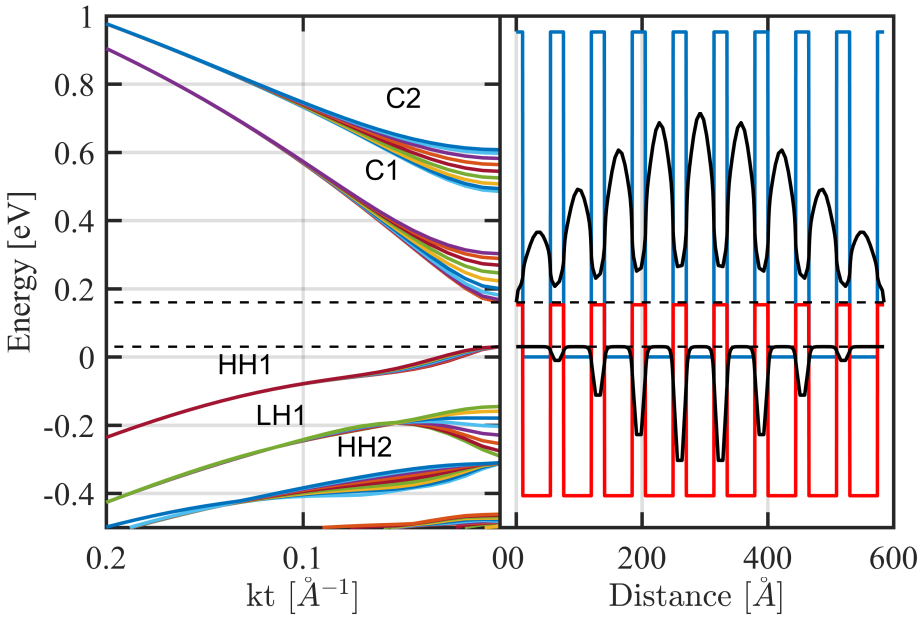

Figure. 3.6 (**Right**) Band edge profile E_c (in blue) and E_v (in red) of a nine-period InAs/GaSb 44 Å/21 Å grown on GaSb substrate. The fundamental electron and heavy-hole envelope-function component moduli squared are shown in black, respectively. (**Left**) The corresponding overall band dispersion as a function of the in-plane wavevector k_t where they have been calculated using full 8×8 Hamiltonian and Dirichlet boundary conditions. The black dashed horizontal lines indicate the effective bandgap. The reference of energies is the unstrained InAs conduction band edge with a VBO value of 560 meV.

The Hamiltonian used is the full 8×8 $\mathbf{k}\cdot\mathbf{p}$ model without block diagonalization. The fundamental electron and heavy-hole envelope-function component moduli squared for nine periods solved using Dirichlet boundary conditions are shown in Figure 3.6 (right). At $k_t = 0$, a classification of minibands states as heavy-hole, light-hole, and split-off states is possible, and are denoted by HHn, LHn, and SOn (n is the quantum number of the subband), respectively. The minibands nomination are assigned based on the dominance of envelope functions at the band edges [96], although this is usually not achievable with the eight band model and with all other higher multi-band $\mathbf{k}\cdot\mathbf{p}$ models exhibiting strong band mixing. The case is worse with narrow gap systems such as InAs/GaSb and type II heterostructures with a broken gap. The distribution of the eight components of the envelope function spinor $\langle F_\mu | F_\mu \rangle$ for the 21 eigenstates solution of Equation (3.79) near the effective gap is plotted in Figure 3.7. In this figure, the states numbered 4 and 20 have the largest components $\langle F_\mu | F_\mu \rangle$ among all other states. In addition, State 20 has the largest component $\langle F_1 | F_1 \rangle$ corresponding to $\langle S | S \rangle$, indicating a s-like character of conduction-band, while State 4 is mostly dominated by the two largest components $\langle F_2 | F_2 \rangle$ and $\langle F_6 | F_6 \rangle$, indicating a mixture of valence band character. Therefore,

these two states correspond, respectively, to the lowest state of a conduction miniband C1 and a highest state of a valence miniband HH1. The band dispersion of the SOn states are of less practical interest due to their lower energy range compared to the range of HHn and LHn states and therefore are not shown.

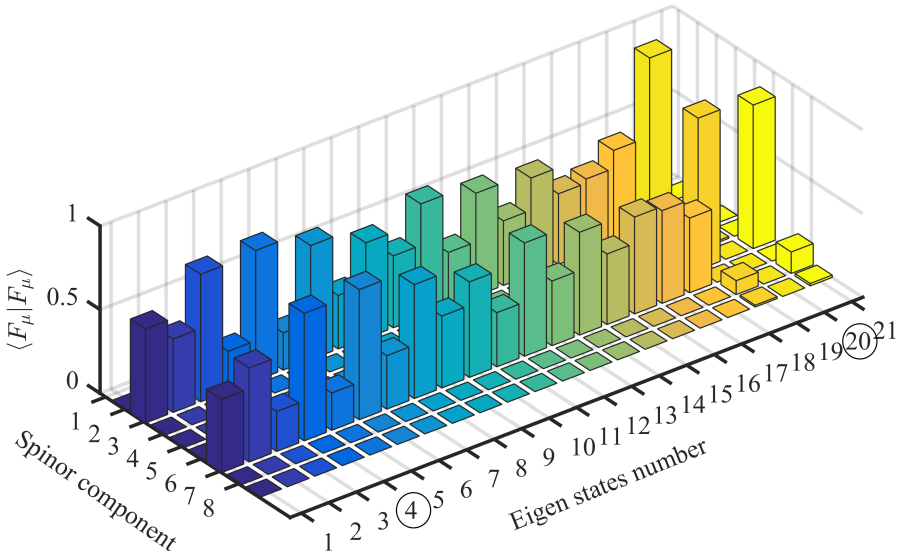

Figure. 3.7 Components of the envelope function spinor $\langle F_\mu | F_\mu \rangle$ of the eigenstates near the effective gap for 9 periods InAs/GaSb 44 Å/21 Å solved using Dirichlet boundary conditions.

The energy dispersion relations and the corresponding fundamental electron and heavy-hole envelope-function component moduli squared for a nine-period InAs/GaSb 44 Å/21 Å grown on GaSb substrate solved using Periodic boundary conditions are illustrated in Figure 3.8. Since there are nine degenerate set of subbands under Dirichlet boundary conditions, each of which belongs to one period, the strong interaction lifts the degeneracy into nine states for each subband, as shown in Figure 3.6. In general, each state splits into N_p states where N_p is the number of periods. Using periodic boundary conditions, because of the double degeneracy of $\pm k_p$ states, $E(+k_p) = E(-k_p)$, the degeneracy is lifted only into five states for each subband, as shown in Figure 3.8. For both cases of boundary conditions, the dispersion relations converge at higher in-plane wavevector k_t as the interaction becomes weaker. The time for the entire calculation in this case study using coarse meshing is 608.18 s. Obviously, the higher is the complexity of design, the longer is the execution time. This time increases with the increase

in the number of layers, the size of the Hamiltonian, and the number of in-plane wave vector sampling points. However, it could be optimized with the FEM approach where, for larger layers, one can use coarse mesh instead of fine mesh for thin layers. In fact, it could be further optimized by using Hermit shape functions.

The full form of the 8×8 Hamiltonian used in this work is reflected in the anisotropy of band structure. Figure 3.9 shows the fundamental heavy hole sub-band structure in polar coordinates for both full and block diagonalized Hamiltonian. The anisotropy is strong in the transversal [110] direction for the full form and is absent in the block diagonalized one, which yields unrealistic isotropic in-plane masses in the later case. This anisotropy is usually neglected in previous works where the axial approximation is usually used after block-diagonalization. The transversal directions along which the dispersion relations exhibit the largest difference are [100] and [110]. This anisotropy of the sub-band is estimated by the difference $E_{[100]}(\mathbf{k}_t) - E_{[110]}(\mathbf{k}_t)$. Between $(k_x = 1, k_y = 0)$ (Å^{-1}) and $(k_x = 1, k_y = 1)$ (Å^{-1}), it was found to be about -90 meV, which indicates that the effective mass is slightly larger along the [110] direction than the [100] direction. This observation confirms that the hole sub-bands are neither parabolic nor isotropic, as can be seen from the dispersion curves.

Figure. 3.8 (**Right**) Band edge profile E_c (in blue) and E_v (in red) of nine-period InAs/GaSb 44 Å/21 Å grown on GaSb substrate. The fundamental electron and heavy-hole envelope-function component moduli squared are shown in black, respectively. (**Left**) The corresponding overall band dispersion as a function of in-plane wave vector k_t where they have been calculated using the full 8×8 Hamiltonian and periodic boundary conditions. The black dashed horizontal lines indicate the effective bandgap. The reference of energy is the unstrained InAs conduction band edge with a VBO value of 560 meV.

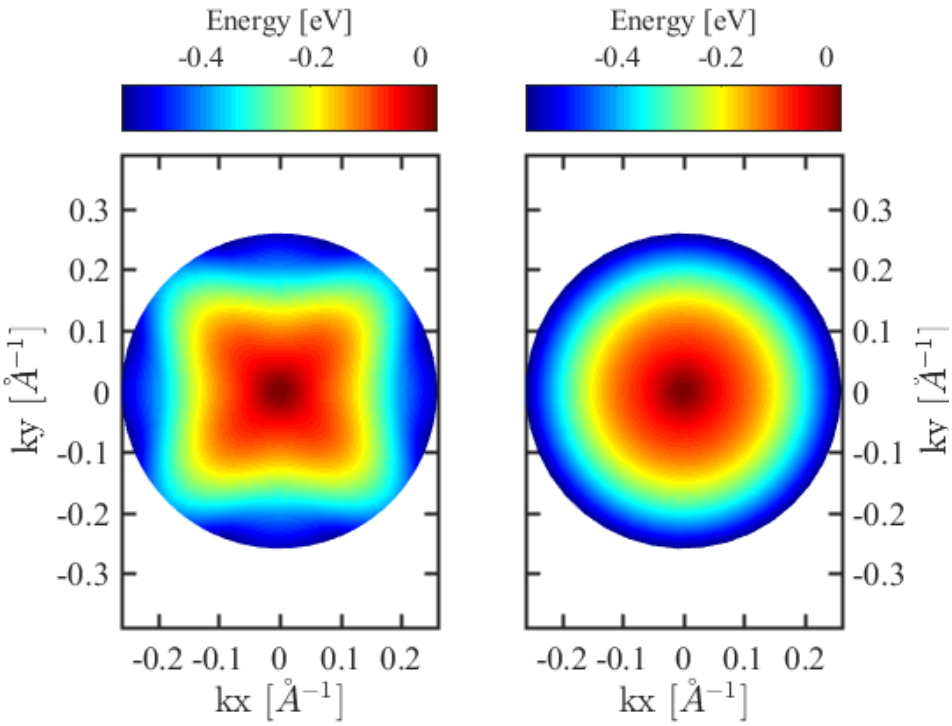

Figure. 3.9 Fundamental heavy hole sub-band structure: (**Right**) using full Hamiltonian; and (**Left**) using block diagonalized Hamiltonian.

Despite the difference between the two types of boundary conditions used, the effective band gaps and band edges at the zone center are expected to be comparable since there is no phase shift between the envelope functions at $k_p = 0$. As indicated in Figures 3.6 and 3.8, the effective bandgap is determined by the difference between the bottom of the lowest electron miniband (C1) and the top of the highest hole miniband (HH1) and it has the value of 0.13 eV, which is in excellent agreement with the one experimentally reported by [36] and theoretically with the absorption spectrum reported in Figure 3.11. This effective gap can be tuned by changing the layer thickness and is primarily determined by the position of the C1 bottom edge since the HH1 band width is less sensitive to layer thickness [9]. The HH1 band width is too small which might be interpreted as it experiences a balanced effect between higher and lower bands.

3.8.3.1 Density of States

The density of states counts the number of electronic states in the conduction or valence band at a given energy E. It is a physical quantity which immediately depends on the band structure of the material and is extremely important for the evaluation of a large number of macroscopic

properties related to carriers transport. The general formula for the density of states can be written as:

$$g(E) = \frac{N(E)}{\Omega} = \frac{1}{\Omega}\sum_{k'} \delta\left[E - E\left(\mathbf{k}'\right)\right]. \tag{3.83}$$

where $\Omega = L^3$ is the material's volume and $N(E)$ denotes the number of states at energy E. It is usually convenient to think of the $E(\mathrm{k})$ as a continuous function and to integrate rather than summing:

$$g(E) = N_k \int_{\mathbf{k}} \delta\left[E - E\left(\mathbf{k}'\right)\right] \mathrm{d}\mathbf{k}. \tag{3.84}$$

where N_k denotes the density of states in reciprocal **k**–space . As within nanostructures, carriers can be confined in quantum wells, where they are free to move only in two dimensions, or in quantum wires where they can only move in one dimension N_k have the general form:

$$N_k = 2 \times \frac{L^d}{(2\pi)^d}, \tag{3.85}$$

where L is the sample size, d the dimensionality (1, 2, or 3), and the factor of two accounts for spin degeneracy. The integrals are then carried out in one, two, or three dimensions. The integral given in Equation (3.84) can be solved analytically for some special cases. These include the case of the single band effective mass model with isotropic parabolic dispersion. For carriers in a bulk semiconductor (3D), $N_k = \frac{\Omega}{4\pi^3}$ and $g(E)$ per unit sample volume reads:

$$g(E)_{3D} = \frac{m^* \sqrt{2m^* E}}{\pi^2 \hbar^3}. \tag{3.86}$$

which goes as the square root of energy. For confined carriers, the density of states is altered. For quantum well, which is a two-dimensional structure (2D), with n bound states, the density of states shows a staircase form with height of the steps is a material constant but the their position depends on the position of the discrete energy level E_n:

$$g(E)_{2D} = \frac{m^*}{\pi\hbar^2}\sum_n \theta\left(E - E_n\right). \tag{3.87}$$

where $\theta(x)$ is the Heaviside function.

The density of states of a real band structure is very different from that obtained in the parabolic approximation. In most other cases, Equation (3.84) can only be calculated numerically. In particular, this includes the case of all multi-band $\mathbf{k}\cdot\mathbf{p}$ models. To do this, the band structure should be calculated first for each band not only in certain preferred directions, as for

drawing a band diagram, but in all the Brillouin zone. Then, for a given energy E, we search in $\mathbf{k}$ –space, the energies $E_{\mathbf{k}}$ of the band structure equal to E. To obtain a resolved density of states in energy space a high number of $\mathbf{k}$ points are required for the evaluation of $E_{\mathbf{k}}$. Therefore an interpolation schemes has been used to reduce the number of Brillouin zone points where $E_{\mathbf{k}}$ is evaluated. We obtain the density of states shown in Figure 3.10 by add contributions from all the available states of the band structure:

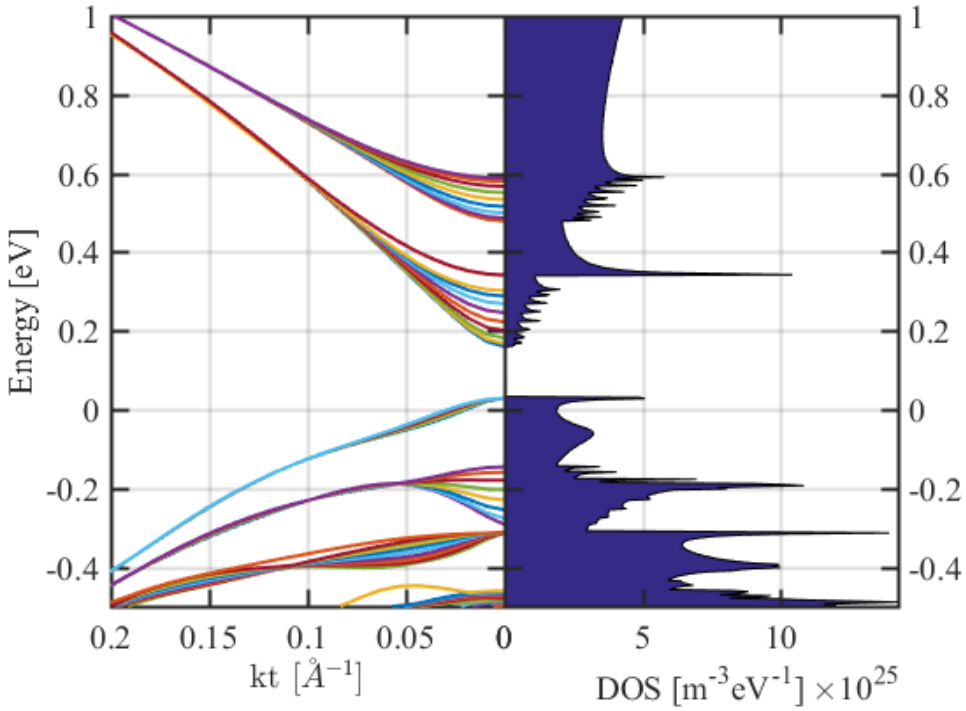

Figure. 3.10 (**Right**):Band dispersion of InAs/GaSb 44 Å/21 Å T2SL and (**Left**) the corresponding Density Of States (DOS) function.

The real DOS shows step-like behaviour at each miniband minima and sharp peaks at the miniband maxima due to the finite width of the minibands.

3.8.3.2 Absorption Spectrum

The absorption spectrum at photon energy $\hbar w$ is derived from Fermi's golden rule as:

$$\alpha(\hbar w) = \frac{4\pi^2 e^2}{n_r c \varepsilon_0 m_0^2 w L S} \sum_{n,m} \sum_{\mathbf{k}_t} |\langle \Psi_{n\mathbf{k}_t} | \hat{e} \cdot \mathbf{P} | \Psi_{m\mathbf{k}_t} \rangle|^2 \times [f_c^n(\mathbf{k}_t) - f_v^m(\mathbf{k}_t)] \times L(\mathbf{k}_t, \hbar w) \tag{3.88}$$

where ε_0 and C are the speed of light and permittivity in a vacuum, and n_r and L are the refractive index and the thickness of the superlattice, respectively. f_c^n and f_v^m are the Fermi functions for the mth valence sub-band with an energy E_v^m and the nth conduction sub-band with an energy E_c^n, respectively, given by:

$$f_c^n(\mathbf{k}_t) = \frac{1}{1 + exp\dfrac{E_c^n(\mathbf{k}_t) - F_n}{K_B T}} \tag{3.89}$$

$$f_v^m(\mathbf{k}_t) = \frac{1}{1 + exp\dfrac{E_v^m(\mathbf{k}_t) - F_m}{K_B T}} \tag{3.90}$$

To account for different scattering relaxations causing finite transition linewidth, a normalized Gaussian or Lorentzian $L(\mathbf{k}_t, \hbar w)$ distribution function with a broadening γ parameter can be chosen. The summation over $\mathbf{k}_t$ takes into account the spin degeneracy. The calculation of the optical transition matrix elements $\langle \Psi_{n\mathbf{k}_t} | \hat{e} \cdot \mathbf{P} | \Psi_{m\mathbf{k}_t} \rangle$ between the hole sub-bands and the electron subbands for TE ($e \perp \hat{z}$)- or TM ($e \parallel \hat{z}$)-polarized optical beams requires the evaluation of a dense 8×8 momentum matrix P:

$$\mathbf{P}_{8\times 8} = \frac{m_0}{\hbar} \nabla_{\mathbf{k}} H \tag{3.91}$$

Then, the final expression for the momentum matrix elements reads:

$$\langle \Psi_{n\mathbf{k}_t} | \hat{e} \cdot \mathbf{P} | \Psi_{m\mathbf{k}_t} \rangle = \hat{e} \cdot \sum_{\mu,\mu'} \int F_\mu^{n*}(\mathbf{k}_t, z) \left[\frac{m_0}{\hbar} \nabla_{\mathbf{k}} H_{\mu,\mu'} \right] F_{\mu'}^m(\mathbf{k}_t, z) dz \tag{3.92}$$

To accelerate the evaluation of these elements, the derivatives of the Hamiltonian elements are calculated explicitly in terms of spinor envelope components and are given in Appendix 5. Using Equations (13) and (14), the average time required to calculate the matrix element of a single transition at a given in-plane wavevector is reduced from 7 s to 0.7 s compared to the direct Hamiltonian derivation method. Figure 3.11 shows the total absorption spectrum for nine-period InAs/GaSb 44 Å/21 Å type II superlattice using both kind of boundary conditions. The cutoff energies for different types of interband transitions are consistent with the effective band gaps between different sub-bands predicted in Figures 3.6 and 3.8. The maxima observed in Figure 3.11 of around 550 meV indicate a large wavefunction overlap of around this energy value due to larger in-plane wavevector states' contributions, where the hole dispersions are neither parabolic nor isotropic. Figure 3.12 shows the largest envelope function spinor

component dependent on in-plane wavevectors near the LH1 miniband. Clearly, the in-plane states' contributions are high to produce the absorption maxima.

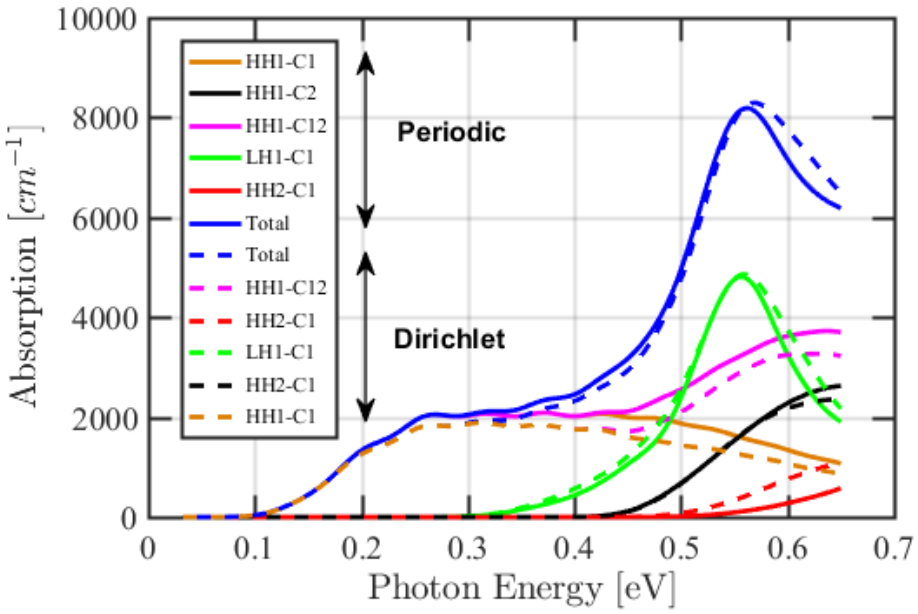

Figure. 3.11 The absorption spectrum for nine-period InAs/GaSb 44 Å/21 Å type II superlattice using both kind of boundary conditions at room temperature. The specific inter-miniband transitions contributing to the shown total absorption are explicitly indicated.

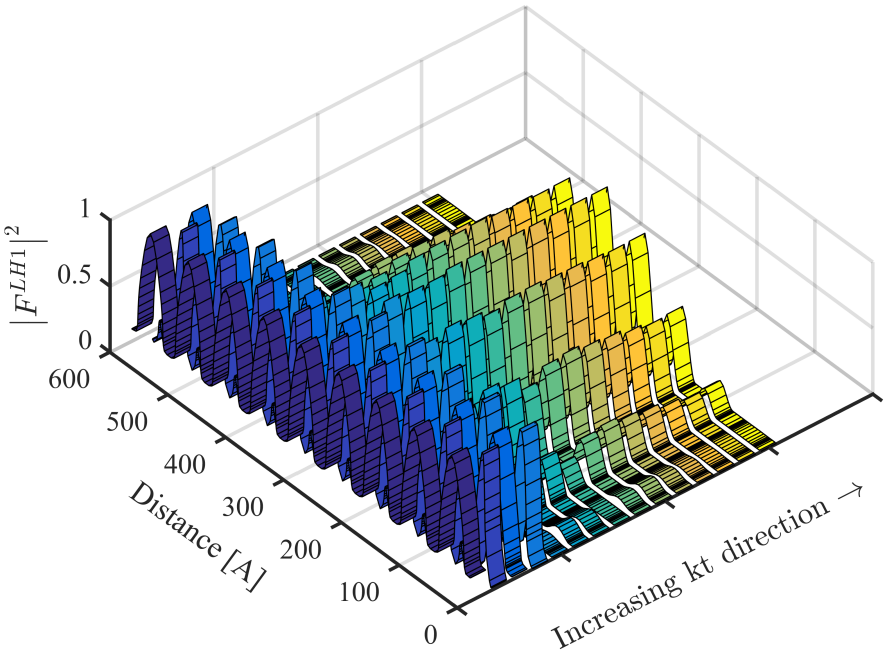

Figure. 3.12 The dependence of the light hole envelope function spinor component on in-plane wavevectors near the LH1 miniband for nine-period InAs/GaSb 44 Å/21 Å type II superlattice.

The strong coupling among the valance bands are indicated by the Spin orientation, i.e the spin expectation value $\langle\sigma\rangle$ for the Light–Hole band presented in Figure 3.13 for the k_xk_y plane.

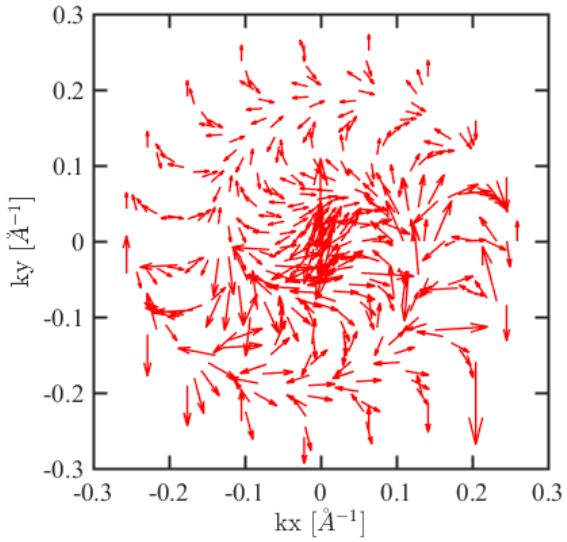

Figure. 3.13 The Spin Texture in the k_xk_y plane for the Light–Hole band in nine-period InAs/GaSb 48 Å/22 Å type II superlattice.

To clarify the sensitivity to the input parameters in Figure 3.14, the absorption spectrum for different Valence Band Offset (VBO) values is calculated. As could be inferred from Figure 3.14, an increase of InAs/GaSb superlattice's VBO from 510 meV to 575 meV leads to an increase of the absorption coefficient. Such a sensitivity indicates that the type II superlattice structure should be properly designed to achieve maximum quantum efficiency in real devices such as infrared detectors. In addition, for the LWIR window, a shift of nearly 1 m in the cutoff wavelength is due to 5 meV change in the VBO. Our calculations show that the LWIR cutoff wavelength is in a good agreement with the experimental data from reference [36].

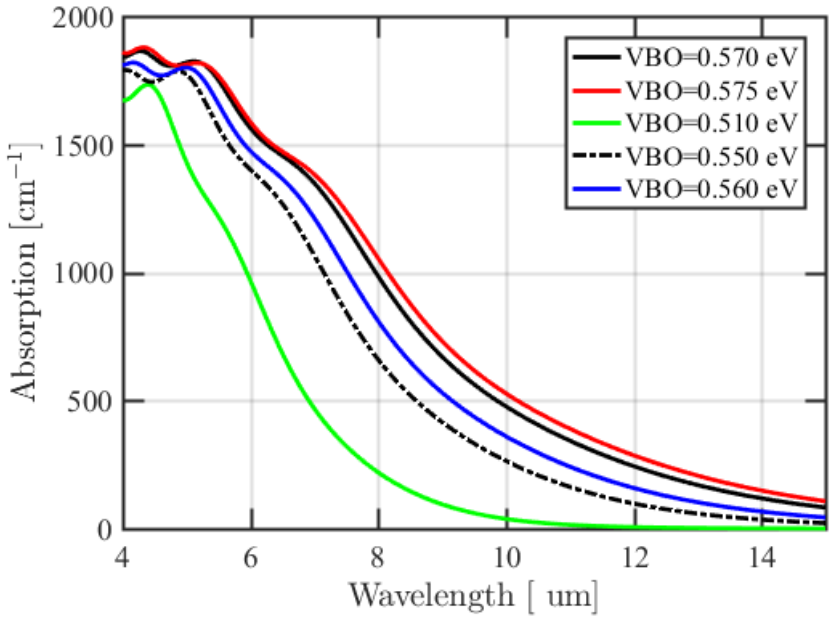

Figure. 3.14 Calculated total absorption spectrum for nine-period InAs/GaSb 48 Å/22 Å type II superlattice for different Valence Band Offset (VBO) values. The periodic boundary condition is used.

There exists a further complication with InAs/GaSb superlattices. Although the separation of the confined states and minibands can be tuned to a desired IR windows by adjusting the InAs and GaSb layer thicknesses, it was found that the physical and optical properties and device performance depend critically on the composition and structure of interfaces formed at the heterojunctions. Recent studies demonstrated that the interface InAs/GaSb is not always abrupt and in fact has chemical asymmetries in compositional profile due to segregation of Sb and In atoms at the interfaces [52, 76]. This segregation leads to the formation of unintentional interfaces (IFs) with different composition configurations. For InAs/GaSb SLs, IFs often turn out to be InSb-like or GaAs-like. Previous studies modeled IF's effect either by fine-tuning

the VBO values or the use of an interface potential profile (short-range delta function potentials centered at the interface [124] and graded or asymmetric interface [39, 66]). However, these approaches miss the effect of the intrinsic strained property of IFs on the electronic structure and the optical properties. The most successful approach is to insert InSb layers to account for large IFs lattice mismatch and the strain effect. A structure with an IF layer is obtained by introducing an interface InSb layer between InAs and GaSb on both sides, while the thickness of one superlattice period is kept fixed. The change in the fundamental effective gap as a function of the number of periods N are plotted in Figure 3.15 for InAs/GaSb 44 Å/21 Å SL without and with InSb IF layer forced at 1.2 Å.

For small number of periods, the effective gap exhibits a strong variation, which indicates the quantum mechanical interaction and the start of miniband formation, while, for a higher number of periods, the effective gap tends to converge to the fundamental minibands gap of the superlattice. For very small periods, the large scatter of eigen energies is a signature of the single quantum well confinement. The presence of InSb IF layer induces a decrease in the effective energy about 25%. This is because the valence band state energies are shifted upward due to the presence of hole states in InSb layer lying in a higher level than those in InAs and GaSb, whereas this effect is negligible with conduction band states since these states in InSb are in between the corresponding ones in InAs and GaSb. The overall effect of including IF layers on the HH miniband is minor with an upward shift less than 6 meV. It is suggested that this upward shift of HH miniband with respect to LH miniband, results in the reduction or suppression of the Auger recombination process. The absorption coefficients with effect of interfacial layers taken into account are shown in Figure 3.16 indicating an increasing shift in the cut-off wavelengths with IF layers thickness.

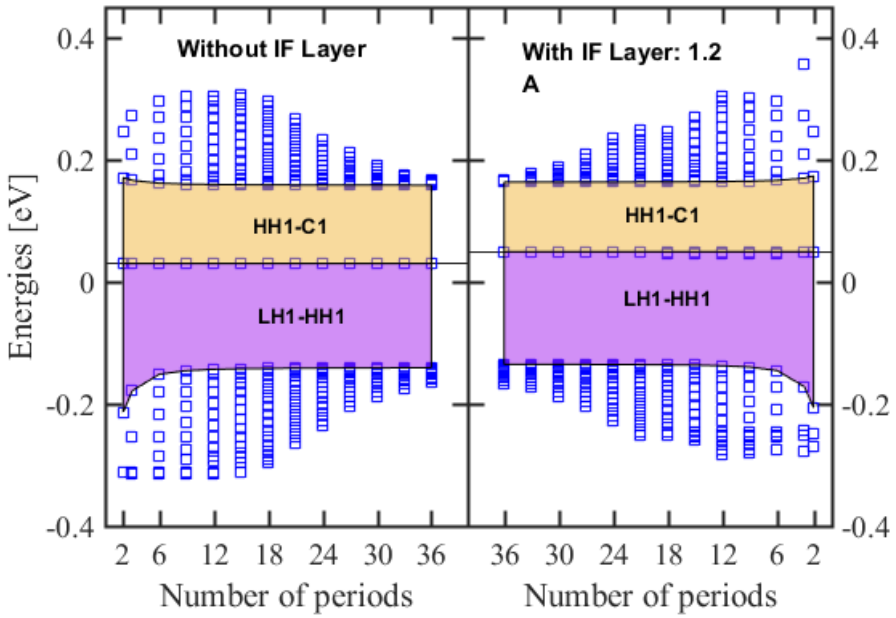

Figure. 3.15 Variation of the inter-miniband band transition energies at $k_x = k_y = 0$ with the number of periods for InAs/GaSb 44 Å/21 Å type II superlattice. The HH1-C1 and LH1-HH1 transitions are denoted by brown and mauve shaded zones, respectively. The effect of including InSb interfacial layers are also shown (**left**). The blue square markers are energies of states above the bottom of C1 miniband edge and below the top of LH1 miniband edge, while those at middle are for HH1 miniband. The value used for VBO is 560 meV.

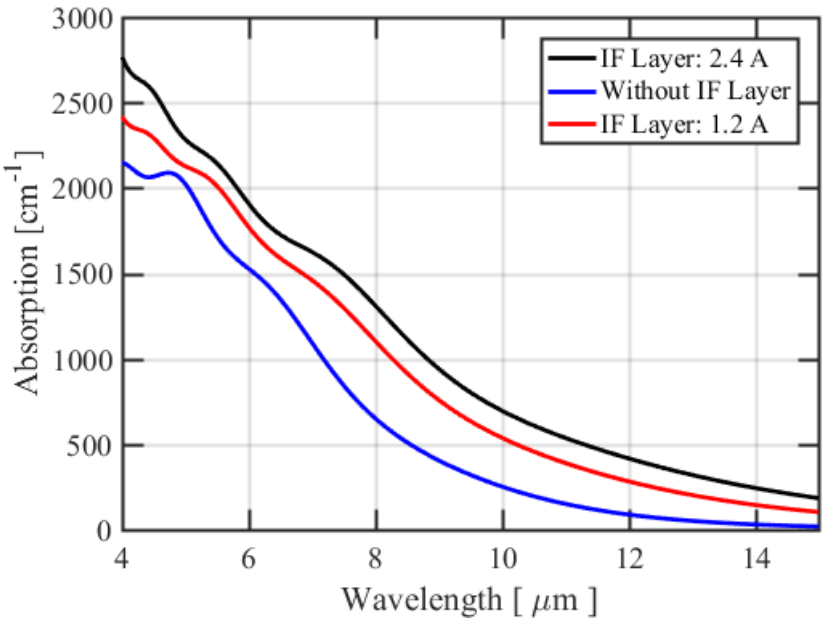

Figure. 3.16 Effect of InSb interfacial layers on the modeled total absorption spectrum for InAs/GaSb 44 Å/21 Å type II superlattice grown on GaSb substrate.

3.9 Summary

In this chapter, an efficient, accurate and rigorous model for the overall band structure calculation based on the $\mathbf{k}\cdot\mathbf{p}$ approach is presented and tested for cubic zincblende bulk semiconductor materials as well as for their quantum heterostructures. These modeling tools are useful for the design of optoelectronic devices and the estimation of their performance. The tools include different $\mathbf{k}\cdot\mathbf{p}$ Hamiltonian formulations namely: 14×14, 8×8, 6×6, 4×4, and single band non-parabolic model. These models take into account the strain effects and can be invoked easily within the modeling steps. The results of the using a non-parabolic model are in excellent agreement with published data. The predicted cutoff energies for different types of interband transitions are consistent with the calculated band dispersion curves of InAs/GaSb Type II broken gap superlattice and demonstrate excellent agreement with the experimental data reported in [36]. Our modeling shows that the IF's lattice mismatch and induced strain yields a significant increase in the absorption coefficient as well as in cut-off wavelengths. As a result, a wide tunable range of optical properties can be obtained with IF layers. Finally, the model can be extended easily to cover materials belonging to wurtzite crystal symmetry just by generating the correct Hamiltonian.

Chapter 4

Design and modelling of Barrier Infrared Detectors based InAs/GaSb type II superlattice

4.1 Introduction

Different semiconductor material systems are being invested into new quantum infrared photodetectors using different architectures. The material list includes bulk InAs, InSb, InAsSb, InGaAsSb, InAsPSb, and engineered materials HgCdTe (MCT), and InAs/GaSb, InAs/InAsSb, and InAsSb/InSb type-II superlattices. This investments has spurred by the limitation of the unmatched superior performance HgCdTe material: cryogenic operating temperature (less than 150 K for MWIR and 77 for LWIR), bulky and costly cryogenic coolers for high operating temperature, extremely expensive growing material processes and lack of native passivant oxide (CdTe for MCT). All of these new detector architectures being based on III-VI materials they can take benefit of existing III-VI processing techniques, utilizing inexpensive large diameter lattice matched substrates and as such are considerably cheaper than HgCdTe. Moreover, engineering the bandgap of these structures require the use of sophisticated MBE machines which delayed the development of these technologies until only within the last 15-25 years. Among these detector architectures, some have the potential to offer reduced dark current, higher operating temperature or multi-spectral detection.

The standard Infrared photodetectors technology is based on a conventional photodiode architecture in which an n-type absorber layer is surrounded by substrate from one side and by a p-type cap layer on the other side. Upon the absorption of a photon after passing through the

substrate into the n-type absorber layer a single electron-hole pair will be created. The electron will then drift under the effect of electric field to the n-contact and the hole will diffuse towards the cap layer where it will be collected by the p-contact. This process results in a measurable photocurrent. In fact, the contribution due to drift in the absorber region is significantly less than diffusion since all of the voltage is dropped across the depletion region.

Unfortunately, the photodiodes performance is notably inhibited by a relatively large dark current due to generation-recombination trap assisted current (G-R), diffusion current and surface leakage current. Fortunately, a very high quality HgCdTe lattice matched epitaxial layers can be engineered to significantly minimize G-R dark current component. The diffusion dark current component due to fundamental Auger and radiative recombination mechanisms can only be minimized through cooling to cryogenic temperatures as stated previously to subsequently improve the signal to noise ratio. The surface leakage current is minimized through properly passivating the detector surface though it is weakly temperature dependent. Nearly ideal performances with diffusion limited behaviour can be reached at cryogenic temperatures by HgCdTe photodiodes grown on lattice matched CdZnTe substrates and passivated with CdTe [67, 109]. InAsSb photodiodes with a 9% Antimony content is lattice matched to GaSb substrate face similar problems which also require cooling. However, at very low temperatures below 100 K they exhibit a strong dominant G-R current and there are no additional benefits from further cooling. Therefore, it is very desirable to devise a new detector architectures that allow for much higher operating temperatures ($\geq$ 140 K) while reducing the diffusion current and to avoid costly cryogenic cooling.

In the 2000s, (Klipstein, 2003 [55]; Maimon and Wicks, 2006 [78]) introduced a new type of quantum infrared photodetector with an aim to increase the operating temperatures and in some cases suppressing surface leakage dark current. This new type of detectors is now referred to in the literature as nBn [78], pBp [77], XBn [56] and CBIRD [135, 137] Barrier detectors. The original idea goes back to a patent in 1987 in which White [2] coined a method for improving photoconductor impedance without inhibiting quantum efficiency. This is accomplished by implementing into the device structure a thin wide bandgap barrier layer having ideally zero valance band offset with the absorber in order to impede the flow of majority carriers without blocking minority carriers. Due to the ability to block one carrier type while allowing the unimpeded flow of the other, this new type of detectors also coined the term unipolar barrier detector. Unipolar barrier infrared photodetectors have been implemented in a variety of semiconductor material systems including the list mentioned at beginning of this chapter. Among different type of Unipolar barrier-based devices, the nBn barrier detector is the most popular one which will be simulated in this work. This detector typically consists

of a narrow-gap n-type Absorber Layer (AL), a wide-gap depleted Barrier Layer (BL), and a narrow-gap n-type Contact Layer (CL). By blocking the electron flow by BL, the holes becomes the dominant source of current. Therefore, the nBn detector operates as a unipolar unity-gain minority carrier device. A key benefit of the nBn architecture is that, for a wide range of design parameters, there is no depletion region in the narrow-gap layers, thereby eliminating the space-charge G-R dark currents that have plagued conventional InAs and InAsSb homo-junction photodiodes and severely limited their applicability for high sensitivity requirements to lower temperatures. Another key benefit of the nBn architecture is self-passivation. Moreover, from experimental point of view, the III-VI nBn is considerably less expensive and much easier to fabricate than MWIR HgCdTe photodiodes.

Despite of the considerable experimental development effort invested into such new quantum infrared detectors, theoretical understanding of the physics underling this new devices and design guidelines is still lacking. In these respect, an accurate simulation of these engineered devices is an important requirement for the development process. Simulations can speed up design and optimization of the device structure without actually manufacturing each possible option. Moreover, the simulation results can be useful in elucidating underlying physical mechanisms and predicting device performance parameters which are not readily measurable. Consequently, I developed a second numerical modelling tool intended to study and analyze the operation of barrier detectors and to optimize their performance under dark and illumination conditions. The simulation model is dedicated to handle III–V materials and their combination. A number of free and commercial software packages have been developed and extensively used to simulate semiconductor devices. The free one-dimensional software usually lack advanced physical models encountered in engineered materials and most of them designed for homo-junction devices. Two-dimensional commercial software such as SILVACO ATLAS are less common, but are necessary for describing lateral effects. Silvaco ATLAS has been effectively used for the simulation of various types of devices based on traditional materials. However, it provides little built-in support for relatively new engineered material such as SLs due to a lack of proper understanding and availability of associated physical models and parameters. In this chapter, an effort is made to model and simulate the carriers transport within different infrared barrier detector using my second modelling tool and examine the effects of bias, contact doping, minority carrier lifetime, absorber doping and barrier doping on the dark current characteristics of barrier detectors

This chapter is organized as follows: Section 4.2 details the physical transport model implemented by the tool including the different current mechanisms affecting the operation of the device, the optical characteristics and the approach used to calculate some of infrared

detector figures of merits that should be given some specific care. Section 4.3 reviews the numerical model used to solve the equations of the transport model employing the required boundary conditions. This requires solving self-consistently the transport equations. The meshing techniques that ensures the convergence of the solution strategy is also presented. Section 4.4 focuses on the choice of material models used in this chapter. Section 4.5 validate the output of the developed tool with published results on GaAs/AlGaAs and Cds/CdTe heterostructurse based devices. Sections 4.6, 4.7 cover the numerical simulation of infrared detectors using the techniques outlined in section 4.2 and section 4.3. In section 4.6 the numerical simulation of InAs/InAsSb/AlAsSb nBn infrared detectors is performed to study the underlying physics including the factors that contribute to the dark current and quantum efficiency, as well as the effect of the doping in the wide-gap barrier layer. Finally, section 4.7 is devoted to design and theoretically evaluate the performances of InAs/GaSb T2SL barrier infrared detectors for LWIR spectral windows.

4.2 Physical Transport Model

As the quantum detectors studied in this work are mainly composed of strongly coupled superlattices, which results in miniband dispersion, a fully quantum transport modelling is ideally the best option to study carriers transport across the whole device. However, such a general theory is not available yet, only for simple case where the scattering of carriers are usually neglected though the involved calculations and the numerical computation remains quite tedious and time consuming [141, 140]. These simple quantum transport approach are derived using density-matrix theory [115] or nonequilibrium Green functions [65], the master-equation approach [29], or Wigner functions [15] under a large number of simplifying approximations: high temperature limit, neglecting broadening, low, medium, and high bias ect. Moreover the extension of these models to 2D or 3D adds another degree of complexity. A very elementary quantum transport theory has been provided by Esaki and Tsu in their pioneering paper [26] in which they derived a simplified version for the average drift velocity of carrier under an applied electric field. Furthermore, even if one starts from more advanced models, it remains extremely complicated to tackle the problem due to the complex band structure behaviour.

An alternative approach based on macroscopic description of semiconductors with nonuniform composition is available and known in the literature as Drift-Diffusion transport model (DD). This model is implemented in our tool and can be derived based on an approximate solution of the semi-classical Boltzmann's Transport Equation (BTE). A direct solution of the full BTE is challenging computationally, particularly when combined with applied fields.

Overall, the DD transport model still persistent to this date to be the only model able to simulate large structures and compute carrier transport in actual semiconductor devices (including solar cells, transistors, light-emitting diodes, or detectors) with a computational time compatible with optimization and design [71]. The formulation of the DD model describes heterostructures by conservation equations for the electric charge $\rho(\mathbf{x})$ and for the hole and electron concentrations, $p(\mathbf{x})$ and $n(\mathbf{x})$. These are the electron and hole continuity equations coupled with Poisson's equation to be solved in the DD analysis:

$$\nabla \cdot [\varepsilon \nabla \phi] = -\rho = q\left(p - n + N_{\mathrm{D}}^{+} - N_{\mathrm{A}}^{-} + \rho_{\mathrm{fix}}\right) \tag{4.1}$$

$$\frac{\partial n}{\partial t} = +\frac{1}{q}\nabla \cdot \mathbf{J}_n + G_n - R_n, \quad \mathbf{J}_n = +qD_n \nabla n - q\mu_n n \nabla \phi_n \tag{4.2}$$

$$\frac{\partial p}{\partial t} = -\frac{1}{q}\nabla \cdot \mathbf{J}_p + G_p - R_p, \quad \mathbf{J}_p = -qD_p \nabla p - q\mu_p p \nabla \phi_p \tag{4.3}$$

where

ε	:	position dependent dielectri constant	$[\mathrm{Fcm}^{-1}]$
ϕ	:	electrostatic potential	$[\mathrm{V}]$
q	:	elemental charge	$[\mathrm{C}]$
p	:	hole density	$[\mathrm{cm}^{-3}]$
n	:	electron density	$[\mathrm{cm}^{-3}]$
N_D^+	:	ionized donor density	$[\mathrm{cm}^{-3}]$
N_A^-	:	ionized acceptor density	$[\mathrm{cm}^{-3}]$
ρ_{fix}	:	charge density from traps and fixed charge density	$[\Omega cm^{-3}]$
$G_{n,p}$	:	electron/hole generation rate	$[\mathrm{cm}^3\mathrm{s}^{-1}]$
$R_{n,p}$	:	electron/hole recombination rate	$[\mathrm{cm}^{-3}\mathrm{s}^{-1}]$
$\mu_{n,p}$	:	electron/hole mobility	$[\mathrm{cm}^2\mathrm{V}^{-1}\mathrm{s}^{-1}]$
$D_{n,p}$	:	electron/hole diffusion constant	$[\mathrm{cm}^2\mathrm{s}^{-1}]$

(4.4)

4.2.1 Poisson's Equation

Poisson's equation relates the carrier concentrations to the electrostatic potential and counts for band bending due to the redistribution of charge carriers:

$$\nabla \cdot [\varepsilon(\mathbf{x}) \nabla \phi(\mathbf{x})] = -\rho(\mathbf{x}) \tag{4.5}$$

where $\phi(\mathbf{x})$ denotes the electrostatic potential, $\varepsilon(\mathbf{x})$ is the position dependent dielectric tensor which reflects nonuniform material composition, and $\rho(\mathbf{x})$ is the charge density. The charge density is consisted of holes $p(\mathbf{x})$, electrons $p(\mathbf{x})$, ionized donors $N_{\mathrm{D}}^{+}(\mathbf{x})$, ionized acceptors $N_{\mathrm{A}}^{-}(\mathbf{x})$, and fixed charges $\rho_{\mathrm{fix}}(\mathbf{x})$ as follow

$$\rho(\mathbf{x}) = e\left[p(\mathbf{x}) - n(\mathbf{x}) + N_{\mathrm{D}}^{+}(\mathbf{x}) - N_{\mathrm{A}}^{-}(\mathbf{x}) + \rho_{\mathrm{fix}}(\mathbf{x})\right] \tag{4.6}$$

Possible contributions to the fixed charges are due to fixed surface and volume trap charges as well as polarization charges $\rho_{\mathrm{pol}}(\mathbf{x})$ due to piezo– and pyroelectric polarizations thought our structures does not exhibit such charges. To obtain the unique solution of the Poisson equation external boundary conditions are required to be specified at the boundaries of simulation domain. In our structures these are provided by the top and bottom contacts. The application of the boundary conditions for the electrostatic potential will be discussed in the subsequent sections in combination with the boundary conditions for the charge density.

In the standard DD transport model, the charge carrier densities $n(\mathbf{x})$ and $p(\mathbf{x})$ are calculated according to Thomas-Fermi approximation by:

$$n(\mathbf{x}) = \sum_{i\in\mathrm{CB}} N_{\mathrm{c}}^{i}(T)\mathscr{F}_{1/2}\left(\left[-E_{\mathrm{c}}^{i}(\mathbf{x}) + q\phi(\mathbf{x}) + F_{\mathrm{n}}(\mathbf{x})\right]/k_B T\right) \tag{4.7}$$

$$p(\mathbf{x}) = \sum_{i\in\mathrm{VB}} N_{\mathrm{v}}^{i}(T)\mathscr{F}_{1/2}\left(\left[E_{\mathrm{v}}^{i}(\mathbf{x}) - q\phi(\mathbf{x}) - F_{\mathrm{p}}(\mathbf{x})\right]/k_B T\right) \tag{4.8}$$

The summations run over the included valence and conduction bands, respectively, however one band is usually chosen. Here, $E_{\mathrm{c}}^{i}(\mathbf{x})$ and $E_{\mathrm{v}}^{i}(\mathbf{x})$ denote the position dependent band edges, F_{n} and F_{p} are the quasi-Fermi levels for holes and electrons respectively, $\mathscr{F}_{1/2}$ denotes Fermi-Dirac integral of order $1/2$ which reduces to Boltzmann distribution for non-degenerate case, $N_{\mathrm{c}}^{i}(T)$ and $N_{\mathrm{v}}^{i}(T)$ are the equivalent densities of states at the valence and conduction band edges. They are given by

$$N_{\mathrm{c}}^{i}(T) = g_{\mathrm{c}}^{i}\left(\frac{m_{\mathrm{dos,e}}^{i}(\mathbf{x})k_B T}{2\pi\hbar^2}\right)^{3/2} \tag{4.9}$$

$$N_{\mathrm{v}}^{i}(T) = g_{\mathrm{v}}^{i}\left(\frac{m_{\mathrm{dos,h}}^{i}(\mathbf{x})k_B T}{2\pi\hbar^2}\right)^{3/2} \tag{4.10}$$

where $m^i_{\mathrm{dos,e}}(\mathbf{x})$ and $m^i_{\mathrm{dos,h}}(\mathbf{x})$ are the effective density-of-states masses for electrons and holes in the various valence and conduction bands. These density-of-states masses are calculated from the effective mass tensors $\underline{m}^{*i}_{\mathbf{e}}$ and $\underline{m}^{*i}_{\mathbf{h}}$ according to

$$m^i_{\mathrm{dos,e}}(\mathbf{x}) = (\det \underline{m}^{*i}_{\mathbf{e}})^{1/3} \tag{4.11}$$

$$m^i_{\mathrm{dos,h}}(\mathbf{x}) = (\det \underline{m}^{*i}_{\mathbf{h}})^{1/3} \tag{4.12}$$

Likewise, expressions for the densities of ionized impurities can be derived in the context of the Thomas-Fermi approximation. For the ionized donors and acceptors the resulting formulas are given by

$$N^+_{\mathrm{D}}(\mathbf{x}) = \sum_{i\in\mathrm{Donors}} \frac{N^i_{\mathrm{D}}(\mathbf{x})}{1 + g^i_{\mathrm{D}} \exp\left(+\left[F_{\mathrm{n}}(\mathbf{x}) - E^i_{\mathrm{D}}(\mathbf{x})\right]/k_B T\right)} \tag{4.13}$$

$$N^-_{\mathrm{A}}(\mathbf{x}) = \sum_{i\in\mathrm{Acceptors}} \frac{N^i_{\mathrm{A}}(\mathbf{x})}{1 + g^i_{\mathrm{A}} \exp\left(-\left[F_{\mathrm{p}}(\mathbf{x}) - E^i_{\mathrm{A}}(\mathbf{x})\right]/k_B T\right)} \tag{4.14}$$

where

$$E^i_{\mathrm{D}}(\mathbf{x}) = E_{\mathrm{c}}(\mathbf{x}) - q\phi - \Delta E^i_{\mathrm{D,ion}}(\mathbf{x}) \tag{4.15}$$

$$E^i_{\mathrm{A}}(\mathbf{x}) = E_{\mathrm{v}}(\mathbf{x}) - q\phi - \Delta E^i_{\mathrm{A,ion}}(\mathbf{x}) \tag{4.16}$$

The summation in Equations (4.13) and (4.14), runs over all different existing donors and acceptor levels. Each type of donors or acceptor is characterized by its ionization energy $\Delta E^i_{\mathrm{D,ion}}(\mathbf{x})$ or $\Delta E^i_{\mathrm{A,ion}}(\mathbf{x})$, degeneracy g^i_{D} or g^i_{A} respectively. The most accepted impurity degeneracies in literatures are $g_{\mathrm{D}} = 2$ for donors and $g_{\mathrm{A}} = 4$ for acceptors.

4.2.2 Current Continuity Equations

If an external bias is applied to the contacts of a device, the system is driven out of equilibrium and an electrical current may be generated between the contacts. In this situation charge distribution in general does not follow the Fermi-Dirac statistics. In the limit of semi-classical treatment, the non- equilibrium distribution function is obtained by solving the BTE. The BTE describes the space, phase and time evolution of a particle using a probability density function. It consists of terms due to drift, diffusion and scattering and is given by:

$$\frac{\partial f(\mathbf{x},\mathbf{k},t)}{\partial t}+\frac{\mathbf{F}_{\text{ext}}}{m}\cdot\nabla_v f(\mathbf{x},\mathbf{k},t)+\mathbf{v}\cdot\nabla_x f(\mathbf{x},\mathbf{k},t)=\left(\frac{\partial f(\mathbf{x},\mathbf{k},t)}{\partial t}\right)_{\text{collisions}} \tag{4.17}$$

where

$$\begin{aligned}
f(\mathbf{x},\mathbf{k},t) &: \text{non-equilibrium distribution function}\\
&\quad\ \text{depending on location, momentum, and time}\\
\mathbf{F}_{\text{ext}} &: \text{contribution of all external forces acting on the system}\\
(\mathbf{F}_{\text{ext}}/m)\cdot\nabla_v f(\mathbf{x},\mathbf{k},t) &: \text{contribution due to drift}\\
\mathbf{v}\cdot\nabla_x f(\mathbf{x},\mathbf{k},t) &: \text{contribution due to diffusion}\\
(\partial f(\mathbf{x},\mathbf{k},t)/\partial t)_{\text{collisions}} &: \text{contribution due to carrier scattering}
\end{aligned} \tag{4.18}$$

Note that $f(\mathbf{x},\mathbf{k},t)$ is simultaneously a function of both position and momentum. Therefore, (4.17) is strictly classical as it assumes position and momentum are simultaneously known, which violates the Heisenberg uncertainty principle. Therefore, the BTE cannot be used to described quantum mechanical effects and only provides a macroscopic view of the system. The semi-classical nomination mentioned earlier stem from the case when the collisions' term is evaluated quantum mechanically.

The DD current continuity equations can be derived by first approximating the BTE using the relaxation-time approximation in which the scattering term $(\partial f(\mathbf{x},\mathbf{k},t)/\partial t)_{\text{collisions}}$ is assumed to be inversely proportional to a characteristic time τ that characterizes the mean free time between collisions. Then equation (4.17) reduces to:

$$\frac{\partial f}{\partial t}+\frac{\mathbf{F}_{\text{ext}}}{m}\cdot\nabla_v f+\mathbf{v}\cdot\nabla_x f=-\frac{f-f_0}{\tau} \tag{4.19}$$

where f_0 is the equilibrium distribution function. The arguments from $f(\mathbf{x},\mathbf{k},t)$ are dropped for convenience. The time τ represents the average time in which the system, through collisions, relaxes from its non-equilibrium state to its equilibrium state. Secondly, by solving for the zeroth and first moments of Equation (4.19) the continuity equation and an expression for the current density can be obtained. Taking into account holes and electrons, the continuity equations at steady state are given by

$$-\frac{1}{q}\nabla\cdot\mathbf{J}_n(\mathbf{x}) = +U(\mathbf{x}) \tag{4.20}$$

$$-\frac{1}{q}\nabla\cdot\mathbf{J}_p(\mathbf{x}) = -U(\mathbf{x}) \tag{4.21}$$

where $\mathbf{J}_n(\mathbf{x})$ and $\mathbf{J}_p(\mathbf{x})$ are the current densities for holes and electrons, respectively. The two equations are coupled in terms of generation and recombination processes that are both included in $U(\mathbf{x}) = G(\mathbf{x}) - R(\mathbf{x})$. Depending on the sign of $U(\mathbf{x})$ either generation ($U(\mathbf{x}) < 0$) or recombination ($U(\mathbf{x}) > 0$) is dominant. The current densities that result from the first moment of the Boltzmann equation are given

$$\mathbf{J}_n(\mathbf{x}) = +qD_n(\mathbf{x})\nabla n(\mathbf{x}) - q\mu_n(\mathbf{x})n(\mathbf{x})\nabla\phi_n(\mathbf{x}) \tag{4.22}$$

$$\mathbf{J}_p(\mathbf{x}) = -qD_p(\mathbf{x})\nabla p(\mathbf{x}) - q\mu_p(\mathbf{x})p(\mathbf{x})\nabla\phi_p(\mathbf{x}) \tag{4.23}$$

The nonuniform material within these equations is described by the position-dependent band parameters V_n and V_p for conduction and valence bands respectively and are related to ϕ_n and ϕ_p by the electrostatic potential ϕ:

$$\phi_n = \phi + V_n \tag{4.24}$$

$$\phi_p = \phi - V_p \tag{4.25}$$

$$qV_n = \chi(\mathbf{x}) - \chi_r + k_BT\log\left[\frac{N_{\mathrm{c}}(\mathbf{x})}{N_{\mathrm{cr}}}\right] \tag{4.26}$$

$$qV_p = -(\chi(\mathbf{x}) - \chi_r) - (E_G(\mathbf{x}) - E_{Gr}) + k_BT\log\left[\frac{N_{\mathrm{v}}(\mathbf{x})}{N_{\mathrm{vr}}}\right] \tag{4.27}$$

where $N_{\mathrm{c}}(\mathbf{x})$ and $N_{\mathrm{v}}(\mathbf{x})$ are the position-dependent effective densities-of-states for conduction and valence bands respectively, and $E_G(\mathbf{x})$ is the bandgap. The parameter $\chi(\mathbf{x})$ (which may differ from the electron affinity is the difference between the conduction band edge and an internal reference energy. The subscript r refers to the values of the various parameters at a reference location within the heterostructure. It should be noted that in writing V_n and V_p Boltzmann statistics are assumed. When Fermi-Dirac statistics are employed, they also depend on the carrier concentrations $n(\mathbf{x})$ and $p(\mathbf{x})$ and need to be redefined.

4.2.3 SuperLattice in the DD Transport Model

Superlattices have been investigated in previous chapter in the context to tailor the absorption coefficient and band structure in quantum infrared photodetectors to their optimum values. In designing T2SL detectors, a band structure calculation is then performed first for calculating the conduction and valence band profiles for every SLs layer required to form detector structures. From the perspective of the DD transport model, the actual bandgap and electron affinity of each SL layer is not the same as for the bulk materials constituting the SL. Therefore to model T2SL detector structures, effective masses and bandgaps and other transport parameters for the superlattice regions are extracted from the band structure calculations described above. Device transport simulation is then performed by replacing the superlattices with effective bulk materials assigned these properties. The resulting band profiles used to solve the transport equations in a bulk-like fashion are shown in Figure 4.1 While for some extracted parameters there is an accepted agreement between the theoretical and experimental results, more feedback from the experimental results (if available) is always favourable for further improvements.

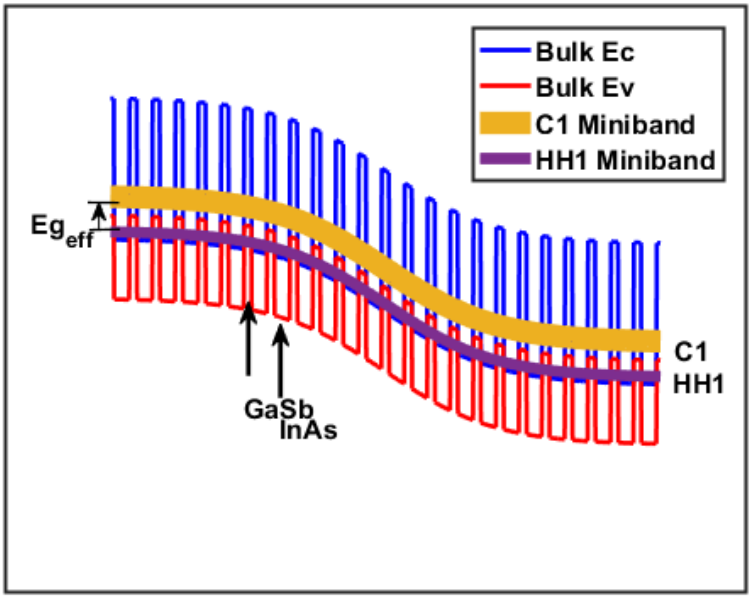

Figure. 4.1 Schematic view of the InAs/GaSb T2SL miniband edges illustrating the effective bulk material approach.

4.2.4 Boundary conditions

To complete the physical model description, boundary conditions on ϕ, n, and p need to be specified. The two most important types of boundary conditions are the Dirichlet and the Von Neumann boundary conditions. Generally, for a given domain Ω with boundary $\partial\Omega$, these are given by

$$\phi(\mathbf{x})|_{\mathbf{x}\in\partial\Omega} = f(\mathbf{x}) \quad \text{(Dirichlet boundary condition)} \tag{4.28}$$

and

$$\partial_{\mathbf{n}}\phi(\mathbf{x})|_{\mathbf{x}\in\partial\Omega} = g(\mathbf{x}) \quad \text{(Von Neumann boundary condition)} \tag{4.29}$$

where $\mathbf{n}$ denotes the normal to $\partial\Omega$ and $f(\mathbf{x})$ and $g(\mathbf{x})$ are given functions defined on $\partial\Omega$. For semiconductor devices simulation, Dirichlet boundary condition applies for Ohmic as well as for ideal Schottky contacts. In our work, the boundary condition are just two points: $\mathbf{x} = 0$ at the bottom contact and $\mathbf{x} = L$ at the top contact where L represent the thickness of the device. As default options, our tool uses ideal ohmic contacts for which we invoke space-charge neutrality and assume equilibrium which enables us to solve $\rho(x) = 0$ for ϕ^{eq} at $\mathbf{x} = 0$ and $\mathbf{x} = L$. The boundary conditions for p and n are then obtained from Equations (4.7) and (4.8),

$$\phi = \phi^{\text{eq}} \tag{4.30}$$

$$n = n^{\text{eq}} \tag{4.31}$$

$$p = p^{\text{eq}} \tag{4.32}$$

This in fact means that the contacts is at thermodynamic equilibrium with infinite surface recombination velocity. For Schottky barriers, the equilibrium contact potential is given by

$$q\phi^{\text{eq}} = -\phi_B - (\chi - \chi_r) + \frac{E_{gr}}{2} - \frac{k_B T}{2}\log\left(\frac{N_{cr}}{N_{cr}}\right) \tag{4.33}$$

where ϕ_B is the barrier height at the metal contact. If a contact is biased, then the applied voltage is added to it's equilibrium potential.

Our tool also has an option for Von Neumann boundary conditions for which the following formula is applied at a given contact:

$$\frac{d\phi}{dx} = 0 \tag{4.34}$$

$$J_n = 0 \tag{4.35}$$

$$J_p = 0 \tag{4.36}$$

In some cases it is desirable to simulate contacts with finite surface recombination velocities for electrons and holes denoted respectively by S_n and S_p. In such cases the last two boundary conditions are modified as follows,

$$J_n(0) = +qS_n^0(n(0) - n^{\text{eq}}(0)) \tag{4.37}$$

$$J_p(0) = -qS_p^0(p(0) - p^{\text{eq}}(0)) \tag{4.38}$$

$$J_n(L) = -qS_n^L(n(L) - n^{\text{eq}}(L)) \tag{4.39}$$

$$J_p(L) = +qS_p^L(p(L) - p^{\text{eq}}(L)) \tag{4.40}$$

4.3 Numerical model

The transport equations of the DD model give a quantitative description of the operation of most semiconductor devices. Those are a sets of coupled Partial Differential Equations (PDEs) in position space. The solution of these PDEs consists of computing the values $\phi(\mathbf{x})$, $n(\mathbf{x})$, and $p(\mathbf{x})$ that satisfy the DD equations. Due to the high non-linearity of the problem, a closed form solution does not exist only for simple and usually non-realistic situations. This immediately requires their discretization on a grid which in turn involve subdivision of the domain defined by the device into segments connecting nodes. This process is termed box integration finite differences scheme (or just box discretization) represent the first step in obtaining an approximate numerical solution to the problem. The following step consists of approximating in a suitable way the solution inside each segment of the grid. Next, the partial derivative operators in the system of PDEs are replaced by differential operators defined in terms of the nodal values of the unknowns. Finally, the resulting system of algebraic equations is solved for the nodal values of the unknowns. In this section I review the numerical techniques used by our tool and provide some details of their implementation in one-dimension.

4.3.1 Domain Box discretization

Box discretization belongs to a class of flux conservative schemes that are usually achieved by subdivision of the computational domain into boxes surrounding the mesh nodes (see Figure 4.2). As material discontinuities are naturally present in the simulation of nanostructures, then Box discretization scheme is systematically adopted for our work. After meshing the device domain, we integrate the DD PDEs over each box volume to obtain an integral equation that is then discretized using the finite differences scheme.

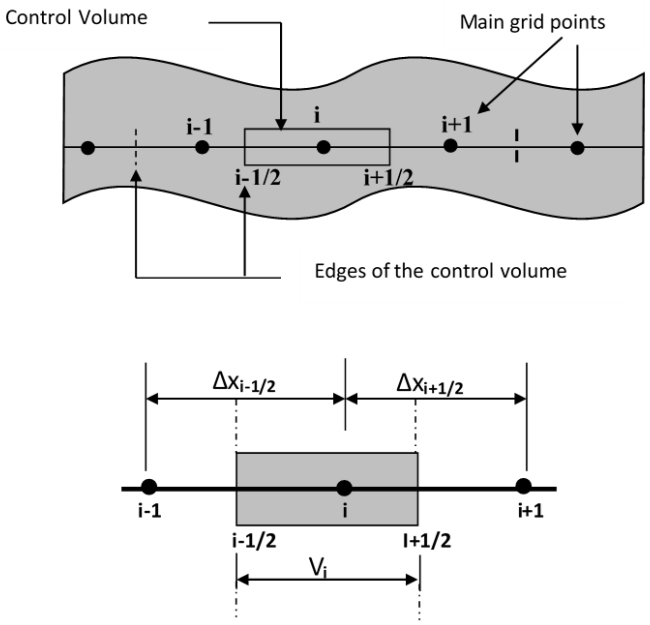

Figure. 4.2 Representation of non-uniform spatial discretization using Box meshing method.

4.3.2 Discretization of Poisson's Equation

The discretization of Poisson's equation will be illustrated here using one-dimensional grid shown in Figure 4.2. For this case, Poisson's equation in (4.5) reduces to:

$$\frac{\mathrm{d}}{\mathrm{dx}}\left(\varepsilon(\mathrm{x})\frac{\mathrm{d}\phi(\mathrm{x})}{\mathrm{dx}}\right) = -\rho(\mathrm{x}) \tag{4.41}$$

We want to find an approximate solution for the electrostatic potential $\phi(\mathbf{x})$ at the grid node x_i, where x_i is the ith element of the ordered set $\{x_1, x_2, \cdots, x_{N_{nodes}}\}$. For each is associated a control box $V_i = \left[x_{i-\frac{1}{2}}, x_{i+\frac{1}{2}}\right]$ where $x_{i+\frac{1}{2}} = (x_{i+1} + x_i)/2$. We further define grid spacings Δx_i between neighboring where $\Delta x_i = x_{i+1} - x_i$. To derive now a discretization for Equation

(4.41) we proceed as follows: For each grid node we integrate Equation (4.41) over the control volume $V_i = \frac{(\Delta x_i + \Delta x_{i-1})}{2} \times 1 \times 1$:

$$\int_{V_i} \frac{\mathrm{d}}{\mathrm{dx}} \left(\varepsilon(\mathrm{x}) \frac{\mathrm{d}\phi(\mathrm{x})}{\mathrm{dx}} \right) \mathrm{dx} = -\int_{V_i} \mathrm{dx} \rho(\mathrm{x}) \tag{4.42}$$

which gives

$$\left(\varepsilon(\mathrm{x}) \frac{\mathrm{d}\phi}{\mathrm{dx}} \right)_{x_{i+\frac{1}{2}}} - \left(\varepsilon(\mathrm{x}) \frac{\mathrm{d}\phi}{\mathrm{dx}} \right)_{\mathrm{x_{i-\frac{1}{2}}}} = -\int_{V_i} \mathrm{dx} \rho(\mathrm{x}) \tag{4.43}$$

In evaluating the RHS, the charge density $\rho(\mathrm{x})$ is assumed to be constant over the segment and equals the charge at node **i**. Similarly the dielectric constant $\varepsilon(\mathrm{x})$ is assumed constant and evaluated at the edges of the control volume. We now use finite differences to approximate the first-order derivatives at the edges of the box:

$$\left[\varepsilon_{i+\frac{1}{2}} \frac{\phi_{i+1} - \phi_i}{\Delta x_i} - \varepsilon_{i-\frac{1}{2}} \frac{\phi_i - \phi_{i-1}}{\Delta x_{i-1}} \right] = -\rho\left(x_i\right) \left[x_{i+\frac{1}{2}} - x_{i-\frac{1}{2}} \right] \tag{4.44}$$

Discretized Poisson's equation now can be rewritten in a form suitable for matrix implementation:

$$\frac{\varepsilon_{i+\frac{1}{2}}}{\Delta x_i} \phi_{i+1} - \left(\frac{\varepsilon_{i+\frac{1}{2}}}{\Delta x_i} + \frac{\varepsilon_{i-\frac{1}{2}}}{\Delta x_{i-1}} \right) \phi_i + \frac{\varepsilon_{i-\frac{1}{2}}}{\Delta x_{i-1}} \phi_{i-1} = -\rho_i V_i \tag{4.45}$$

4.3.3 Discretization of Continuity Equations

The continuity equation for electrons expressed in the form of (4.20) is simplified for the one-dimensional case as

$$-\frac{1}{q} \frac{d}{dx} J_n(x) = U(x) \tag{4.46}$$

Then, integrate over the control volume

$$-\frac{1}{q} \int_{V_i} \left(\frac{d}{dx} J_n(x) \right) dx = \int_{V_i} U(x) dx \tag{4.47}$$

which simplifies to

$$\left(J_n\right)_{i-\frac{1}{2}} - \left(J_n\right)_{i+\frac{1}{2}} = q U_i V_i \tag{4.48}$$

where $\left(J_n\right)_{i-\frac{1}{2}}$ and $\left(J_n\right)_{i+\frac{1}{2}}$ are the normal (outgoing) current density evaluated at the left and right edges of the box respectively. Defining the currents at the edges of boxes enforce current

flux conservation (the current exiting one box side is exactly equal to the current entering the neighboring box through the side in common).

Now we need a discretized expression for J_n. Recalling that

$$J_n(x) = +qD_n(x)\frac{dn(x)}{dx} - q\mu_n(x)n(x)\frac{d\phi_n(x)}{dx} \tag{4.49}$$

and assuming a Linearized interpolation schemes for the charge density between two nodes J_n can then be rewritten as

$$(J_n)_{i+\frac{1}{2}} = +qD_{n,i+\frac{1}{2}}\frac{n_{i+1}-n_i}{\Delta x_i} - q\mu_{n,i+\frac{1}{2}}n_{i+\frac{1}{2}}\frac{\phi_{i+1}-\phi_i}{\Delta x_i} \tag{4.50}$$

$$(J_n)_{i-\frac{1}{2}} = +qD_{n,i-\frac{1}{2}}\frac{n_i-n_{i-1}}{\Delta x_{i-1}} - q\mu_{n,i-\frac{1}{2}}n_{i-\frac{1}{2}}\frac{\phi_i-\phi_{i-1}}{\Delta x_{i-1}} \tag{4.51}$$

where n_i , ϕ_i, and n_{i+1} , ϕ_{i+1}, and n_{i-1}, ϕ_{i-1} are the electron density and electrostatic potential at the nodes i, $i+1$ and $i-1$ respectively. This scheme can lead to substantial errors in regions where the variation in the potential is high. An alternative famous approach known as the Scharfetter-Gummel scheme has provided an optimal solution to this problem. In this scheme the rapidly varying carrier concentrations are far better approximated with exponential functions rather than low order polynomial functions. Consequently, the possibility of obtaining non-physical negative carrier density is greatly reduced or totally eliminated with suitable mesh spacing. To derive the discretized form of J_n using Scharfetter-Gummel, begin by multiplying both terms of (**??**) by $exp(\frac{\phi(x)}{V_T})$ where $V_T = k_BT/q$ and the sub-index n of ϕ_n is dropped for convenience.

$$\begin{aligned} J_n \exp\left(-\frac{\phi(x)}{V_T}\right) &= qD_n\left[\exp\left(-\frac{\phi(x)}{V_T}\right)\frac{\partial n}{\partial x} - \frac{n}{V_T}\exp\left(-\frac{\phi(x)}{V_T}\right)\frac{\partial \phi}{\partial x}\right] \\ &= qD_n\left[\frac{\partial}{\partial x}\left(n\exp\left(-\frac{\phi(x)}{V_T}\right)\right)\right] \end{aligned} \tag{4.52}$$

Then, integrating between x_i and x_{i+1}

$$\begin{aligned} \int_{x_i}^{x_{i+1}} J_n \exp\left(-\frac{\phi(x)}{V_T}\right)dx &= qD_n\left[n\exp\left(-\frac{\phi(x)}{V_T}\right)\right]_{x_i}^{x_{i+1}} \\ &= qD_n\left[n_{i+1}\exp\left(-\frac{\phi_{i+1}}{V_T}\right) - n_i\exp\left(-\frac{\phi_i}{V_T}\right)\right] \end{aligned} \tag{4.53}$$

then by assuming J_n constant along the segment we find

$$J_n = qD_n \left[\frac{n_{i+1}}{\int_{x_i}^{x_{i+1}} \exp\left(\frac{\phi_{i+1}-\phi(x)}{V_T}\right) dx} - \frac{n_i}{\int_{x_i}^{x_{i+1}} \exp\left(\frac{\phi_i-\phi(x)}{V_T}\right) dx} \right] \tag{4.54}$$

Now we assume that ϕ varies linearly between mesh points,

$$\phi(x) = \frac{\phi_{i+1}-\phi_i}{(\Delta x_i)}(x-x_i) + \phi_i \tag{4.55}$$

$$\begin{aligned} J_n &= \frac{qD_n}{\Delta x_i} \left\{ n_{i+1} \frac{(\phi_i - \phi_{i+1})/V_T}{1-\exp\left[-\left(\frac{\phi_i-\phi_{i+1}}{V_T}\right)\right]} - n_i \frac{-(\phi_i-\phi_{i+1})/V_T}{1-\exp\left[+\left(\frac{\phi_i-\phi_{i+1}}{V_T}\right)\right]} \right\} \\ &= \frac{qD_n}{\Delta x_i} \left\{ n_i B(\Delta_{i,i+1}) - n_{i+1} B(-\Delta_{i,i+1}) \right\} \end{aligned} \tag{4.56}$$

where $\Delta_{i,i+1} = (\phi_i - \phi_{i+1})/V_T$ and

$$B(x) = \frac{x}{\exp(x)-1} \tag{4.57}$$

is the Bernoulli function. Similar expression can be found for the holes current equation,

$$J_p = -\frac{qD_p}{\Delta x_i} \left\{ p_i B(-\Delta_{i,i+1}) - p_{i+1} B(\Delta_{i,i+1}) \right\} \tag{4.58}$$

Finally, substitution of the discretized current equations for electrons (**??**) and holes (**??**) into their respective continuity equations yields the following discretized form of the later which must be solved together with discretized Poisson's equation at every node in the mesh by our tool

$$\begin{aligned} &\frac{1}{\Delta x_{i-1}} D_{n,i+\frac{1}{2}} B\left(\frac{\phi_{i+1}-\phi_i}{V_T}\right) n_{i+1} \\ &- \left[\frac{1}{\Delta x_{i-1}} D_{n,i-\frac{1}{2}} B\left(\frac{\phi_i-\phi_{i-1}}{V_T}\right) + \frac{1}{\Delta x_i} D_{n,i+\frac{1}{2}} B\left(\frac{\phi_i-\phi_{i+1}}{V_T}\right) \right] n_i \\ &+ \frac{1}{\Delta x_i} D_{n,i-\frac{1}{2}} B\left(\frac{\phi_{i-1}-\phi_i}{V_T}\right) n_{i-1} \\ &= U_i V_i \end{aligned} \tag{4.59}$$

Table 4.1 Normalisation constants used to renormalise equations and variables.

Quantity	Symbol	Expression	Unit
Density	C_0	10^{19}	cm^{-3}
Energy	V_T	k_BT	eV
Length	L_D	$\sqrt{\varepsilon_0 k_B T/(q^2 C_0)}$	cm
Mobility	μ_0	$\max \mu(\mathrm{x})$	$\mathrm{cm}^2/(\mathrm{V}\cdot\mathrm{s})$
Time	t_0	$\varepsilon_0/(q\mu_0 C_0)$	s
Gen. rate	G_0	$\mathrm{C}_0\mu_0\mathrm{k}_B T/\left(qL_D^2\right)$	$\mathrm{cm}^{-3}\cdot\mathrm{s}^{-1}$
Current	J_0	$\mu_0 C_0 k_B T/L_D$	$\mathrm{A/cm}^2$

$$
\begin{aligned}
&\frac{1}{\Delta x_{i-1}} D_{p,i+\frac{1}{2}} B\left(\frac{\phi_i-\phi_{i+1}}{V_T}\right) p_{i+1} \\
&-\left[\frac{1}{\Delta x_{i-1}} D_{p,i-\frac{1}{2}} B\left(\frac{\phi_{i-1}-\phi_i}{V_T}\right)+\frac{1}{\Delta x_i} D_{p,i+\frac{1}{2}} B\left(\frac{\phi_{i+1}-\phi_i}{V_T}\right)\right] p_i \\
&+\frac{1}{\Delta x_i} D_{p,i-\frac{1}{2}} B\left(\frac{\phi_i-\phi_{i-1}}{V_T}\right) p_{i-1} \\
&=U_i V_i
\end{aligned} \tag{4.60}
$$

Linear interpolation schemes is assumed to determine the edge point values for the diffusion coefficient or equivalently carrier mobility as they are related by Einstein's relation $D_{n,p} = k_BT\mu_{n,p}/q$ (as long as this relation is valid).

4.3.4 Numerical techniques

4.3.4.1 Renormalization Of Variables

Due to the limited precision of computers and hence to avoid underflow/overflow in numerical calculations, the descretized DD transport equation need to be renormalized using the normalisation constants listed in Table 4.1 before they are implemented in a computer code. In this respect, quantities such as carrier concentrations are renormalised by the intrinsic carrier concentration of a reference material or by relatively large value, the electrostatic potential ϕ is renormalised by the thermal voltage V_T and the electric field is renormalised by V_T/L_D , where L_D is the Debye length defined in Table 4.1. Then, after obtaining the desired solutions the real interested quantities are rescaled back to the original ones using the same normalisation constants.

4.3.4.2 Solution Methods

The first step to implement the descretized DD transport equations into a computer code after providing the input quantities, is to discretize the simulation domain into a grid of points or mesh. However there are limitations on the choice of mesh size which must be smaller than the Debye length where one has to resolve charge variations in space. Generally, in simulating planar heterostructures in the vertical direction, it is essential to mesh more finely at heterojunctions and doping boundaries in order to properly capture the physics of the device. Moreover, regions near contacts should be further refined to account for the perturbed carrier dynamics caused by the presence of these contacts.

The discretization of DD transport equations transforms each equation into a system of algebraic equations

$$\mathbf{A}\mathbf{x} = \mathbf{b} \tag{4.61}$$

for all nodes of the mesh, where $\mathbf{A}$ is a non-singular $N \times N$ matrix and $\mathbf{b}$ is a given right hand side $N \times 1$ column vector. These can also be written in residual form as,

$$F_i^{\phi}(\phi, n, p) = 0 \tag{4.62}$$

$$F_i^{n}(\phi, n, p) = 0 \tag{4.63}$$

$$F_i^{p}(\phi, n, p) = 0 \tag{4.64}$$

These system of equations are coupled in terms of fundamental variables ϕ, n and p and are nonlinear since the quantities ρ, J_n, J_p, and U involve nonlinear functions. Thus, it is not possible, quite generally, to obtain a solution directly in one step, but a nonlinear iteration method is required. The two famous schemes for solving these coupled set equations are the Gummel's iteration method and the Newton's method. It is not an easy task to determine an optimum strategy to find the solution, since this will depend on a number of details related to the particular device under investigation. In Gummel's iteration method, the equations are solved using a decoupled procedure, in which one system of equations say $F_i^{\phi}(\phi, n, p) = 0$ is solved first using a guess for the $\phi^0(\mathbf{x})$, $n^0(\mathbf{x})$ and $p^0(\mathbf{x})$, then the resulting potential $\phi^1(\mathbf{x})$ is used to solve electron and hole continuity equations to yields a new carrier distributions $n^1(\mathbf{x})$ and $p^1(\mathbf{x})$. These procedure is iterated many times until a converged values is obtained. To improve convergence, the nonlinear Poisson's equation is usually linearised in terms of ϕ_is and solved iteratively using Newton's method. The non-linearity arises here from the non-linear dependence of the density ρ on the electrostatic potential ϕ. In our tool, we adopted Newton's

method, therefore, equations (**??**), (**??**) and (**??**) are solved as a one block system of size $3N \times 3N$ employing the Newton-Raphson algorithm. In this sense, after writing the problem into that of finding the zero of a function $F(\phi, n, p) = 0$ as in (**??**), (**??**) and (**??**), I linearised the equations by Taylor expansion in fundamental variables ϕ, n and p to give,

$$\begin{bmatrix} \frac{\partial F^{\phi}}{\partial \phi} & \frac{\partial F^{\phi}}{\partial n} & \frac{\partial F^{\phi}}{\partial p} \\ \frac{\partial F^{n}}{\partial \phi} & \frac{\partial F^{n}}{\partial n} & \frac{\partial F^{n}}{\partial p} \\ \frac{\partial F^{p}}{\partial \phi} & \frac{\partial F^{p}}{\partial n} & \frac{\partial F^{p}}{\partial p} \end{bmatrix} \cdot \begin{bmatrix} \delta\phi \\ \delta n \\ \delta p \end{bmatrix} = \begin{bmatrix} F^{\phi} \\ F^{n} \\ F^{p} \end{bmatrix} \tag{4.65}$$

where the right hand side matrix is a short notation for a $3N \times 3N$ block tridiagonal matrix, ones solved for the corrections $(\delta\phi, \delta n, \delta p)^T$ starting from an initial guess, we can estimate an update values for the solutions ϕ, n and p,

$$\phi^{k+1} = \phi^{k} + \delta\phi \tag{4.66}$$

$$n^{k+1} = n^{k} + \delta n \tag{4.67}$$

$$p^{k+1} = p^{k} + \delta p \tag{4.68}$$

These operation is repeated many times until a converged solutions is obtained. The Newton's method offers advantages of fast convergence against high memory demand compared to relatively slow convergence against less memory demand for Gammel's method.

4.4 Extraction of parameters' values

The devices structures studied in this work are actually a stack of different layers combining bulk and SL materials. To conduct a successful modelling of these devices, precise material parameter values must be specified. For binary materials and ternary or quaternary alloys, the material properties are retrieved automatically from our tool's database. The main sources of database are from Vurgaftman's paper. The data parameters includes among other parameters, the energy bandgap, the electron and hole effective masses, the lattice constants and the elastic constants. For SLs, being a relatively novel materials, it's materials parameters are not readily available in the literature. In fact, it is not practical to draw up an exhaustive list of parameters values since the material properties might change with different superlattice designs. Therefore in this work the main parameters of the SLs based layers are calculated using $\mathbf{k}\cdot\mathbf{p}$ band modellings. This namely includes the bandgap, the effective electron and hole masses and absorption coefficient and minibands alignments (effective affinities). In case experimental

data are available, the bandgap is favourably determined from measured cut-off wavelength. The electron and Hole mobility, SRH lifetimes, radiative and Auger rates were determined following existing literature. Carriers mobilities and permittivity of superlattice structures were calculated as a weighted average of binary bulk materials values constituting the superlattice.

4.5 Validation of the Modelling Tool

We first check the output of our modelling tool with published results by presenting two illustrative applications. The first application simulates a simple p–GaAs/n–$Al_{0.25}Ga_{0.75}As$ abrupt heterostructure devices taken from [146] at different doping densities and bias. In the second application we consider a n^+CdS/p–CdTe heterojunction based prototype solar-cell by simulating it's quantum efficiency and band diagram. It is worth mentioning that sensible comparison to published experimental results is usually not feasible since the measured data depend strongly on the preparation of the devices and sometimes are intentionally hidden. If own experimental measurements can be performed, a 'calibration' of the modelling tool is needed by adjusting the process-dependent material parameters (within a plausible physical range) to reproduce the experimental results with the modelling tool. Therefore, a comparison to published simulation results may be more sensible but the complete device dimension, doping, etc are rarely given in full detail which, makes only a qualitative comparison sensible.

4.5.1 GaAs/AlGaAs Diode

The layers' sequences of this device as shown in Figure 4.3 is consisted of an p-doped GaAs layer with $N_{A1} = 10^{17} cm^{-3}$ followed by a n-type $Al_{0.25}Ga_{0.75}As$ layer at different doping density N_{D2}. For the present application, the temperature-dependent model for material parameters is taken into account for the energy bandgap, and electron and hole mobilities and are given by:

$$E_g = 1.519 - 5.405 \times 10^{-4} \frac{T^2}{(T+204)} \qquad [\text{eV}] \tag{4.69}$$

$$\mu_n = \frac{7200}{\left[1 + 5.51 \times 10^{-17} (N_D + N_A)\right]^{0.233}} \times \left(\frac{300}{T}\right)^{2.3} \qquad \left[\text{cm}^2\text{V}^{-1}\text{s}^{-1}\right] \tag{4.70}$$

$$\mu_p = \frac{380}{\left[1 + 3.17 \times 10^{-17} (N_D + N_A)\right]^{0.266}} \times \left(\frac{300}{T}\right)^{2.7} \qquad \left[\text{cm}^2\text{V}^{-1}\text{s}^{-1}\right] \tag{4.71}$$

Table 4.2 Material parameters used in the simulation of GaAs/AlGaAs diode.

Parameter	Symbol	Expression	Unit
Band gap	E_g	$E_{g\,GaAs} + 1.247x$	eV
Electron affinity	χ	$4.07 - 0.6\,[E_{g\,GaAs}(x) - E_{g\,GaAs}]$	eV
Electron effective mass	m_e^*	$(0.067 + 0.083x)$	m_0
Hole effective mass	m_h^*	$(0.48 + 0.31x)$	m_0
Dielectric constant	ε	$(13.1 - 3x)$	ε_0
Electron life time	τ_n	10^{-9}	s
Hole life time	τ_p	10^{-9}	s

The temperature-dependence bandgap model also applies for AlGaAs material, and the electron and hole mobilities are reduced by 12.7% and 6.7% per aluminium composition of 0.1 from the values in GaAs, respectively. The other material parameters used in this application are given in Table 4.2.

The recombination–generation model is swished on only for Shockley Read-Hall model with with single trap level at the middle of the gap. Furthermore, ideal Ohmic contacts are assumed for device which are described by an infinite recombination velocity by our tool. Moreover, the incomplete ionization of impurities is considered with acceptor ionization energy $\Delta E_{\mathrm{A}} = 0.026$ eV in GaAs and donor ionization energy $\Delta E_{\mathrm{D}} = 0.018$ eV in $Al_{0.25}Ga_{0.75}As$. A non-uniform mesh is adopted for the structure and refined with a logistic map function centrared at the junction interface as shown in Figure 4.3.

In the following the carrier transport across the heterojunction is investigated as a function of doping and bias. When the device is forward biased, the conduction band edge of AlGaAs is shifted upward (see Figure 4.4). With the decrease of energy barrier height, more electrons from AlGaAs jump over the barrier. However, under the reverse bias condition, the electrons injected from GaAs side see an abrupt energy barrier whose height is determined by the conduction band discontinuity.

Figure 4.5, shows the conduction band edge of the n–GaAs/n–$Al_{0.25}Ga_{0.75}As$ heterojunctions for different doping density of N_{D2}, at a reverse bias of -0.1 V. The shown electron quasi-Fermi level is for the case of $N_{D2} = 10^{16}\ cm^{-3}$. The figure indicates that at high doping concentration, the snick of the conduction band approaches the Fermi-level while the energy barrier width shrinks.

The current-voltage $J(V)$ characteristics of the p–GaAs/n–$Al_{0.25}Ga_{0.75}As$ heterojunction diode at $T = 300$ K is shown in Figure 4.6. At low applied forward-bias, the current is dominated by the space charge recombination (SRH) current $[J \propto \exp(qV_{\mathrm{Bias}}/2k_BT)]$. Under

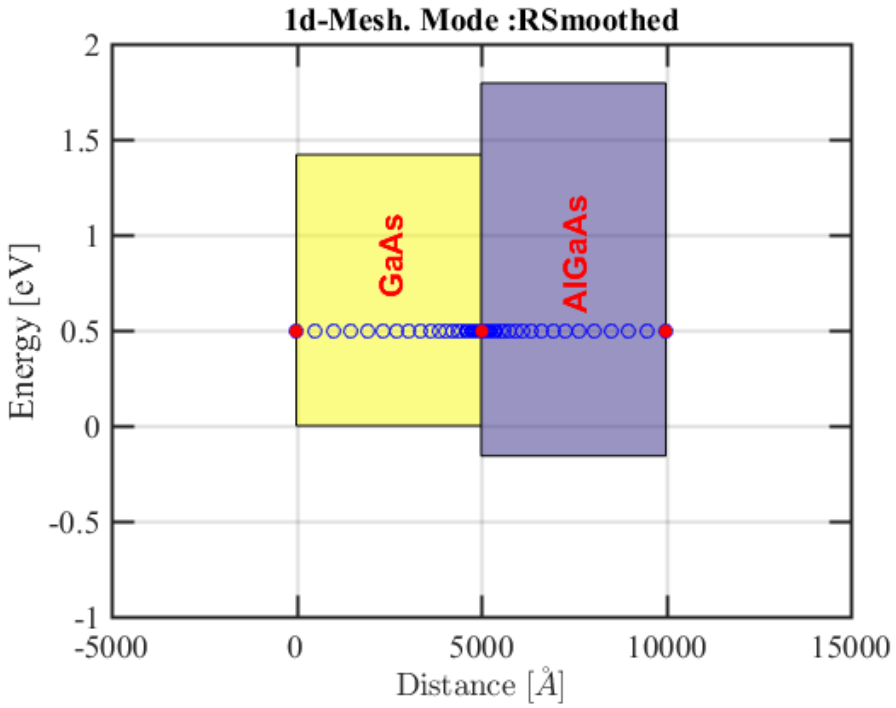

Figure. 4.3 The device structures used for the first application. The mesh is also shown using Right-Smoothed mesh mode at the junction interface. The doping density of the GaAs layer is kept fixed while the AlGaAs doping density is varied. The heights of the shaded boxes indicates the respective material bandgaps.

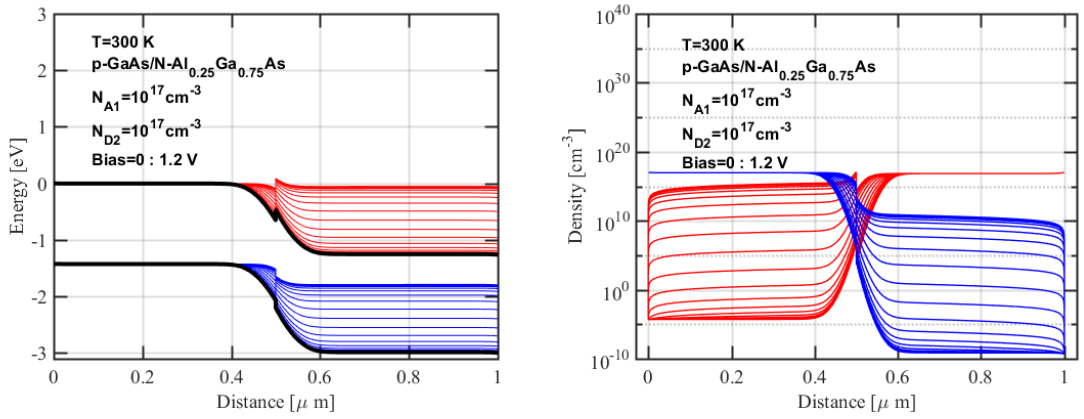

(a) Conduction band profiles at different Bias. Black curves is for $V_{Bias} = 0$.

(b) Charge density at different Bias. Red curves for electrons and blue curves for holes.

Figure. 4.4 Simulation results for p–GaAs/n–$Al_{0.25}Ga_{0.75}$ diode at different Bias.

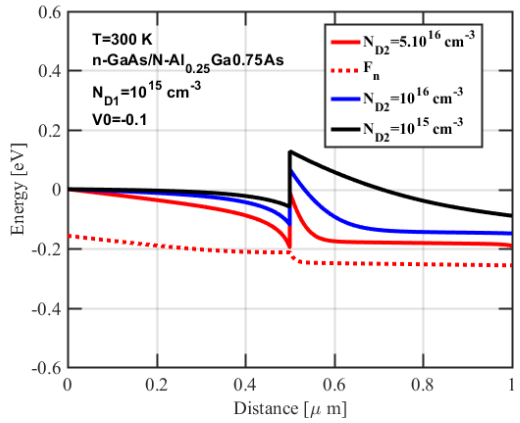

(a) Conduction band edges obtained by our tool.

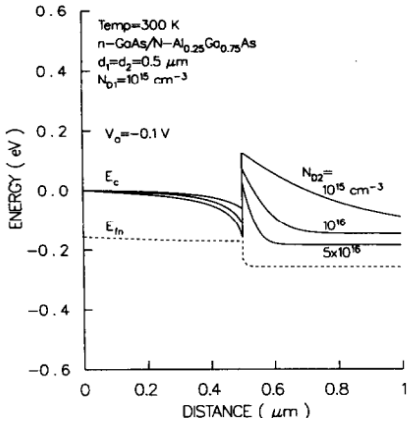

(b) After the original paper [].

Figure. 4.5 Calculated conduction band edges of the n–GaAs/n–$Al_{0.25}Ga_{0.75}As$ diode at different doping densities N_{D2} and under a Bias of -0.1 V.

reverse bias, the net flow across the junction is composed of a few minority carriers from each region. For negative voltages beyond a $-0.5\ V$, the $J(V)$ curves saturate, reminiscent of a reverse biased diode behaviour. However, we note a slightly increase in the revere bias current due to the expansion of the depletion region which is proportional to the magnitude of applied voltage.

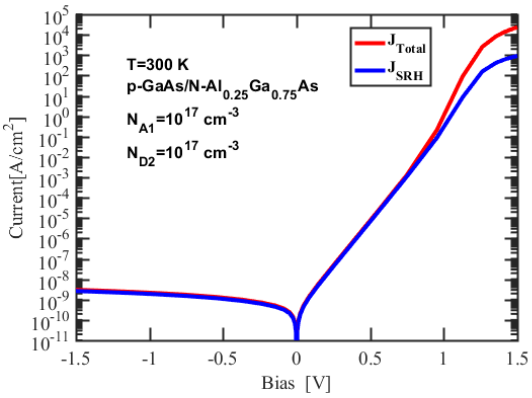

(a) $J(V)$ obtained by our tool.

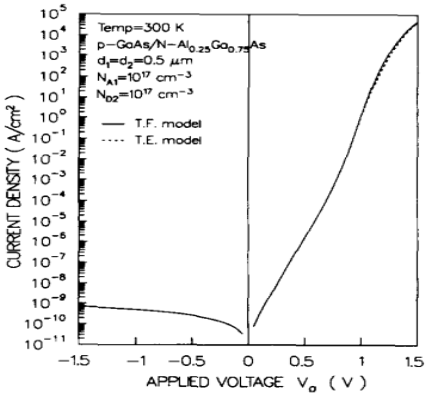

(b) $J(V)$ after the original paper [].

Figure. 4.6 Calculated $J(V)$ characteristics of a p–GaAs/n–$Al_{0.25}Ga_{0.75}As$ diode for $N_{A1} = 10^{17}$ cm^{-3} and $N_{D2} = 10^{17}$ cm^{-3} at $T = 300\ K$.

We conclude that the outputs of our modelling tool are in excellent agreement with the published results.

Table 4.3 Material parameters used in the simulation of CdS/CdTe Solor-Cell.

Parameter	Symbol	CdS	CdTe	Unit
Thickness	L	25	4000	nm
Band gap	E_g	2.4	1.5	eV
Electron affinity	χ	4.0	3.9	eV
Electron effective mass	m_e^*	0.02	0.3	m_0
Hole effective mass	m_h^*	0.06	0.29	m_0
Dielectric constant	ε	10	9.4	ε_0
Electron life time	τ_n	10	5	ns
Hole life time	τ_p	10^{-4}	5	ns
Electron mobility	μ_n	100	320	$cm^2/(V \cdot s)$
Hole mobility	μ_p	25	40	$cm^2/(V \cdot s)$

4.5.2 CdS/CdTe Solar-Cell

This is a simple heterojunction consisting of a thin n^+-doped layer of CdS and a p-type CdTe layer. The material parameters are shown in Table 4.3. The doping density was set to $10^{17}\ cm^{-3}$ for CdS layer and $10^{15}\ cm^{-3}$ for CdTe layer. For this example, we specify a finite recombination velocities for electrons and holes at left and right contacts to be both equal $10^7\ cm/s$. Our tool includes Shockley-Read-Hall, radiative, Auger, Band to Band, and Trap Assisted Tunnelling recombination mechanisms. Here only the Shockley-Read-Hall mechanism is considered. This application is choosen due to the similarity between detectors and solor-cells. The aim here is to show the capability of the tool in calculating the spectral response as function of bias.

The evaluation of the device is made under the standard solar spectrum: air mass 1.5 direct solar spectrum (AM1.5D). Figure 4.7 shows the computed band diagram at different bias and under dark conditions. The efficiency in CdTe/CdS solar cells mainly deteriorates due to optical, electrical and recombination losses. In actual CdTe/CdS solar cells, the solar radiation before reaching the photoelectrically active CdTe absorber layer passes through a glass plate, a transparent conducting oxide (TCO) and then CdS window layer. Obviously, each pass is accompanied by optical losses due to reflection at all interfaces. In this calculation, the transmission thought all interfaces before CdTe layer is assumed to be equal unity. Figure 4.8 shows the computed Quantum efficiency of CdS/CdTe solar cell at different applied voltages.

As expected, there is a reduction in quantum efficiency at higher voltages caused by the decrease of the depletion layer.

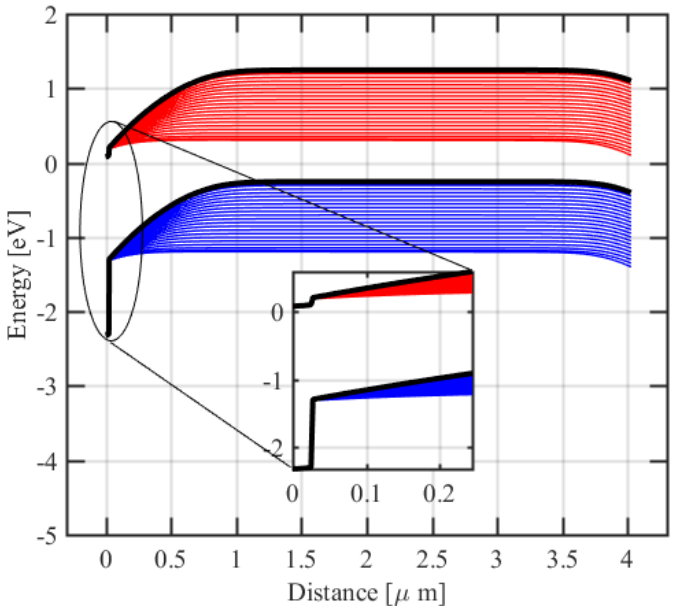

Figure. 4.7 Band diagram under dark conditions at different applied voltage for CdS/CdTe device.

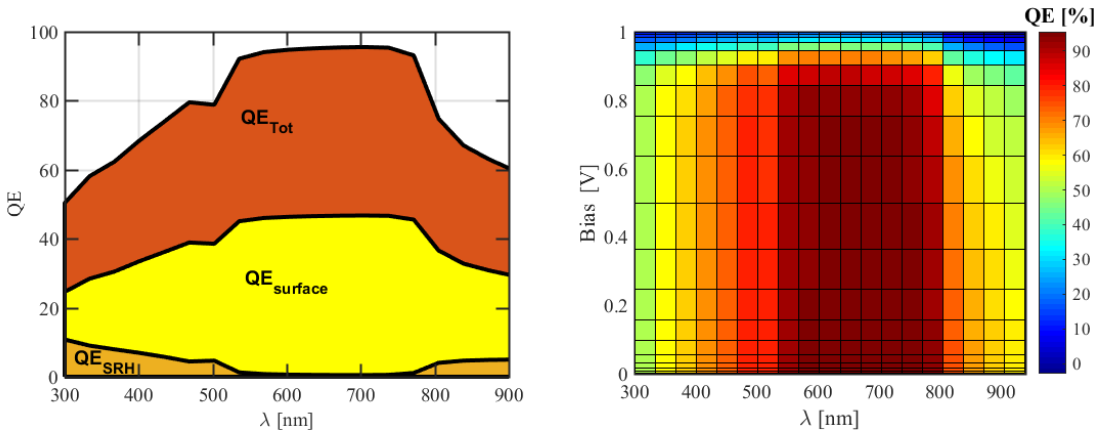

(a) QE at 0 V.

(b) QE at different bias.

Figure. 4.8 Quantum efficiency of CdS/CdTe solar device under solar spectrum AM1.5D at different Bias. The shaded zones at left shows together with the total QE, the different contributions to QE namely: SRH and surface recombination. The SRH component is rescaled to fit within the same figure.

4.6 Numerical Simulations of InAs nBn MWIR Detector

This section reports our initial results for the simulations of nBn MWIR detectors with an InAs absorber layer and an AlAsSb barrier layer using our tool. We theoretically investigate the effects of bias, temperature, contact doping, barrier doping and absorber doping on the dark current characteristics of these detectors. The results is proved to explain the behavior of the barrier detectors and their underlined physics. These investigations also includes photocurrent dependence of bias voltage for various illumination fluxes.

4.6.1 Detector's Structure and Model Specifications

The simulated structure is illustrated Figure 4.9. It consists of n–type GaSb-like substrate on which a $2\mu m$ thick and lightly n–doped InAs Absorber Layer (AL) is grown, followed by a 200 nm thick wide-gap $AlAs_{0.18}Sb_{0.82}$ barrier layer (BL) and finally terminated by a 100 nm thick InAs Contact Layer (CL). The contact and the absorber are lattice-matched to InAs. The GaSb-like substrate acts as a transparent Window Layer (WL) to the infrared radiation (IR) and has a larger bandgap than InAs to provide a valence band barrier for the minority carriers (holes) in the AL. This barrier prevent the hole collection at the back contact. The doping of the window layer, absorber layer, barrier layer, and contact layers are taken to be $1.2\times10^{16}\ cm^{-3}$, $1.2\times10^{16}\ cm^{-3}$, $1.8\times10^{15}\ cm^{-3}$, and $1.0\times10^{18}\ cm^{-3}$, respectively. On the WL, a transparent metallic contact is deposited and grounded at zero voltage during all the simulation. Similarly, on the top of structure, another metallic contact is placed to bias the device.

Table 4.4 provides more material specifications for each layer including expressions for the energy gap, recombination lifetimesn, electron affinity and effective masses. Due to the lack of a universal detailed parameters model for each material, a complete set of all of these parameters is not available in the open literature. Therefore, the material characteristics are gathered from multiple sources and in some instances are interpolated from the binary compounds. The Valence Band Offset (VBO) at the InAs/AlAsSb interface which is a key parameter for the energy band diagram construction, is assumed to be 19.8 meV at 200 K, where the InAs valence band edge line-up above the $AlAs_{0.18}Sb_{0.82}$ valence band edge. This line-up ensures for nBn detector that the valence band edges of the three layers are all aligned closely to allow hole transport between the absorber and collector layers. An accepted approach in constructing the line-ups between materials is based first on obtaining VBO for each material constituting the interface and then simply subtracting their individual values. For binary materials InAs, AlAs, and AlSb the VBO values are $-0.59eV$, $-1.33eV$, and $-0.41eV$ respectively, and are all relative to that for InSb taken from the review by Vurgaftman et al [139]. For $AlAs_xSb_{1-x}$, the

VBO value is obtained by linearly interpolating between the values for the binaries AlAs and AlSb which gives the value of $-0.5756eV$ for $x = 0.18$. Furthermore, because of the sensitivity of the band diagram to the band offset and the relatively high doping used in the CL, I have also activated the bandgap narrowing effect model in the CL according to:

$$\Delta E_g = 14.0 \times 10^{-9} N_d^{1/3} + 1.97 \times 10^{-7} N_d^{1/4} + 57.9 \times 10^{-12} N_d^{1/2} \tag{4.72}$$

where N_d is the electron dopant density.

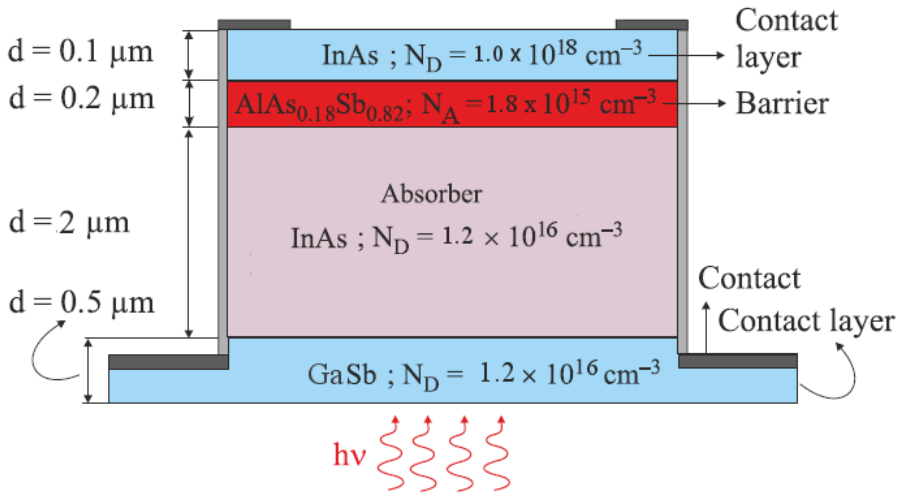

Figure. 4.9 Schematic illustration of layers' sequence of InAs nBn MWIR detector investigated in this work.

The physical transport model used here includes only radiative, Auger, and Shockley–Read–Hall mechanisms. The Absorber Layer (AL) SRH lifetime τ_{SRH} used in the simulations is $10\mu s$ for both electrons and holes. The carrier lifetimes are taken to be very long in the AlAsSb material so that very few carriers recombine there. The optical absorption coefficient of the AL can be fitted to the desired wavelength range according to the following expression:

$$\alpha(\hbar\omega) = \begin{cases} 948.23 \times \exp\left[170\left(\hbar\omega - E_0\right)\right], & \hbar\omega \leq E_g \\ \frac{K\left(\hbar\omega - E_g - c\right)\sqrt{\left(\hbar\omega - E_g - c\right)^2 - c^2}}{\hbar\omega} + 800, & \hbar\omega > E_g \end{cases} \tag{4.73}$$

where $E_0 = E_g + 0.001$, $K = 10000 + 20000E_g$, $\hbar\omega = hc/\lambda$ is the photon energy and λ is the wavelength. In fact, this expression depends on temperature as E_g does. The AL absorption coefficient as function of wavelength at $T = 200K$ is plotted in Figure 4.10. Because the BL material has a wide bandgap, the infrared radiation cannot be absorbed there, which allows to consider this layer to be completely transparent for IR radiation in this model.

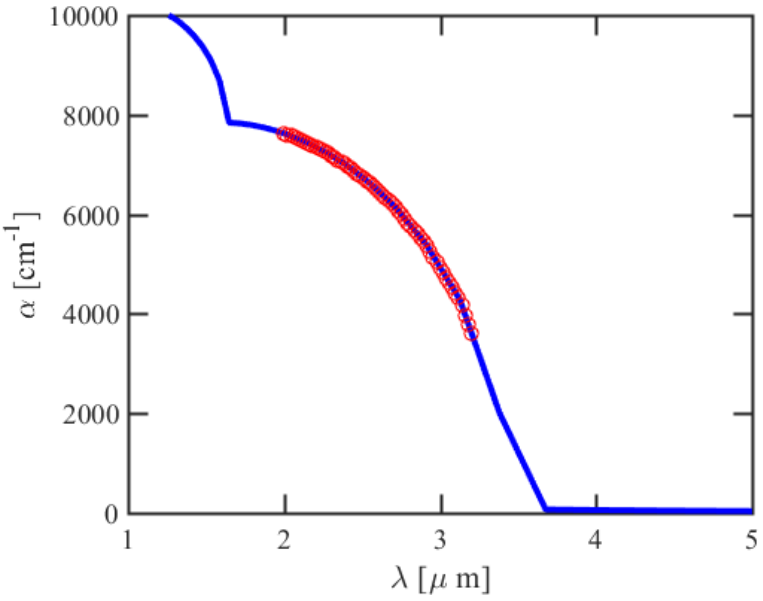

Figure. 4.10 Absorption coefficient of InAs as a function of wavelength at $T = 200K$. The red circles denoted the fitted absorption coefficient to a target wavelength range.

4.6.2 Energy Band and Hole Concentration Profiles

Several bias conditions illustrations of the calculated energy band diagrams for nBn detector is shown in Figure 4.11. Focusing on the barrier region, we observe a very small potential barrier in the valence band between InAs and AlAsSb, while a large barrier is present in the conduction band, creating a barrier for electrons. This barrier inhibits the flow of electrons from the AL to the CL, thus eliminating all electron currents. Additionally we observe at the neighbourhood of BL that band-bending slightly increases by increasing reverse bias which indicates that all the depletion region is located in the AlAsSb layer leading to a reduced dark current as a result of the suppressed SRH generation in the depleted region. In fact, it has already been shown that InAs nBn detectors exhibits lower dark current in several orders of magnitude compared to conventional InAs photodiode detectors. Because of the small VBO, the hole transport is not significantly affected by the barrier, making this a unipolar minority carrier device.

Furthermore, as it can be seen clearly from Figure 4.11, the reverse bias further reduces the valence band barrier and the electric field present in the barrier region sweeps holes out of the AL into the CL to be collected (Figure 4.12). Moreover, as the reverse bias is further increased, the depletion region at the interface between the AL and BL increases, leading to additional SRH generation, thus increasing the dark current. This effect can be reduced by properly choosing the doping concentration for the barrier layer.

Table 4.4 Material parameters specifications for each layer of nBn detector. The affinities χs are calculated with respect to affinity of InSb forced to be zero.

Parameter	WL	AL	BL	CL	Unit
Thickness	0.5	2	0.2	0.1	μm
E_g@0K	0.822	0.411	1.7526	0.411	eV
χ	0.415	0.415	-0.9266	0.415	eV
m_e^*	0.023	0.0254	0.0254	0.023	m_0
m_h^*	0.41	0.4159	0.4159	0.41	m_0
ε	15.15	15.3	13.36	15.15	ε_0
τ_n	10	10	100	10	μs
τ_p	10	10	100	10	μs
μ_n	4.15×10^4	4.15×10^4	3.01×10^3	4.15×10^4	$\mathrm{cm}^2/(\mathrm{V} \cdot s)$
μ_p	4.6×10^2	4.6×10^2	1.94×10^2	4.6×10^2	$\mathrm{cm}^2/(\mathrm{V} \cdot s)$
N_D	1.2×10^{16}	1.2×10^{16}	0	1×10^{18}	cm^{-3}
N_A	0	0	1.8×10^{15}	0	cm^{-3}
Varshni α	3.4×10^{-4}	3.4×10^{-4}	4.46×10^{-4}	3.4×10^{-4}	eV/K
Varshni β	210	210	210.2	210	K

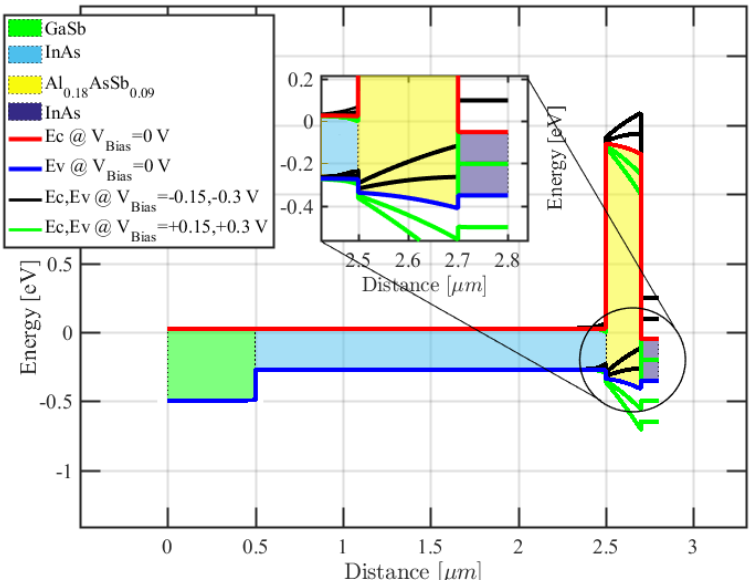

Figure. 4.11 Calculated energy band diagrams of the nBn device without incident light at 200 K under: zero bias, reverse bias and forward bias.

4.6.3 J(V) Characteristics: Dark- and Photo- Current

The calculated dark current density as a function of applied bias from $-0.3\ V$ to $0.3\ V$, for different temperatures between 120 K to 240 K is shown in Figure 4.13. The nearly saturated

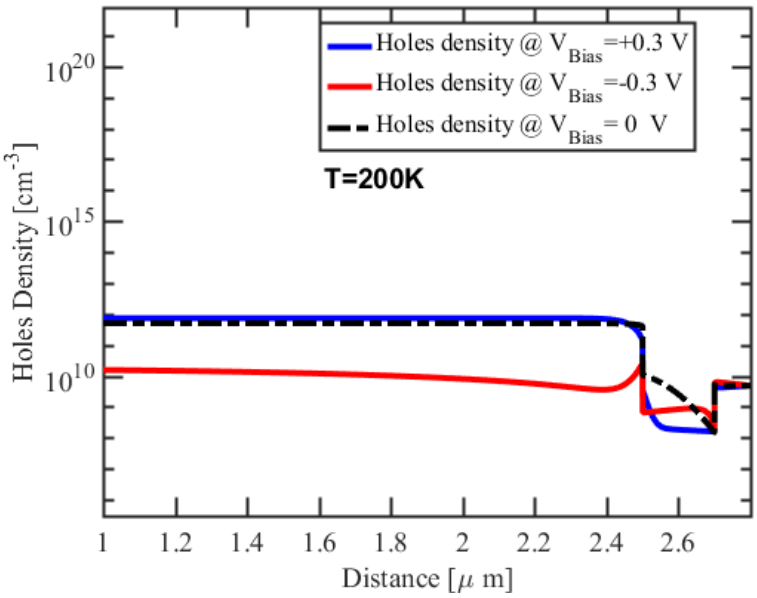

Figure. 4.12 Holes distributions for different bias values of the nBn device without incident light at 200 K.

behaviour of reverse dark current reflects a diffusion-limited behavior down to bias of -0.3 V before e SRH dark current starts to dominate at higher reverse bias. Figure 4.14 shows Arrhenius plots of dark current densities as a function of the reciprocal temperature for a set values of reverse applied bias between -0.03 V and -0.6 V.

Figure **??** indicates the dependence of the calculated photocurrent for various incident photon fluxes levels and applied bias at a temperature of 200 K for a fixed wavelength of $2.0\mu m$. We note that the detector has the following interesting features. First, even at zero applied bias, the device is out of equilibrium, due to the gradient in the hole density triggered by the optical illumination causing a net hole current flowing from the AL to the CL. Second, when a reverse bias is applied, a stronger electric field in the barrier compared with the values at equilibrium further enhances the hole collection in addition to collection by diffusion process. At forward bias, the applied voltage leads to an injection of holes from the CL to the AL. Third, the calculated photocurrent at forward bias voltages greater than 0.1 V is due to holes that are photogenerated in the CL by IR radiation that has travelled the AL and is absorbed in the CL. Last, the detector responses linearly to the increase of the incident optical fluxes up to 10^{18} photons cm^2s^{-1} and is operating under low-level injection conditions. Figure **??**(b) presents the Diffusion and drift photocurrent components.

The calculated photocurrent gives access to the evaluation of the spectral responses (QE) as function of lambda and bias at temperature of 200 K as shown in Figure 4.16. On the other

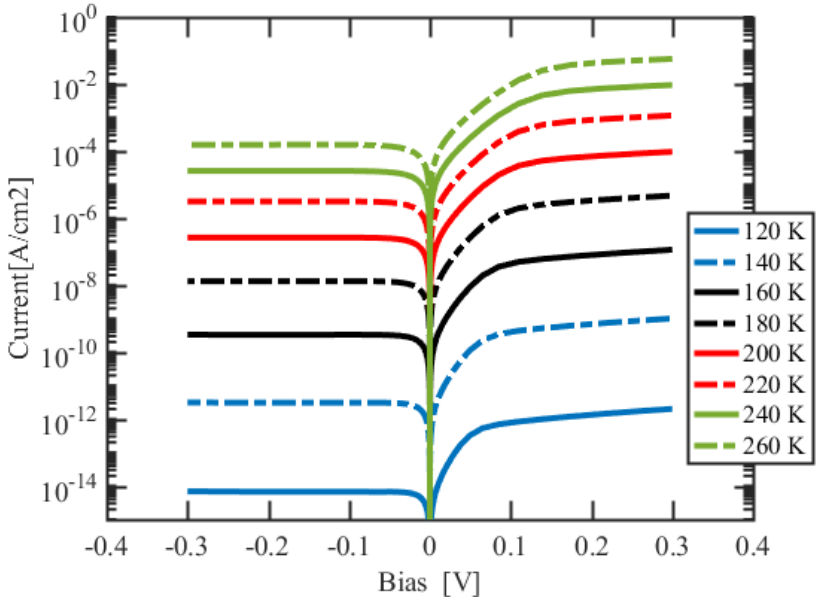

Figure. 4.13 Calculated darkcurrent versus bias voltage for various temperatures of InAs nBn detector.

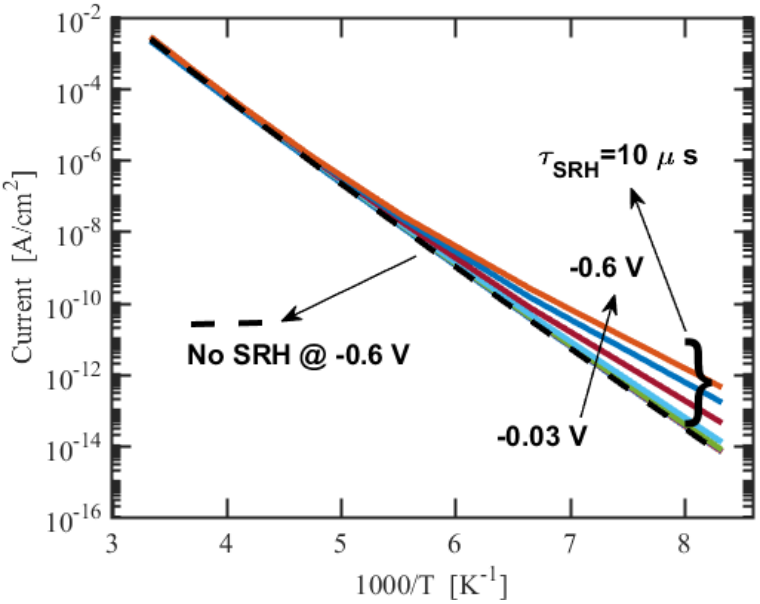

Figure. 4.14 Arrhenius plots of the dark current densities of InAs nBn detector under reverse bias voltages between -0.03 and $-0.6\,V$. Dash black curve calculated without SRH. Solid colored curves calculated including SRH with $\tau = 10\mu s$.

hand, the reflection losses at the WL is neglected. The calculation of QE is carried out using

the following method which assumes that over a small flux interval the quantum efficiency is constant:

$$QE = \frac{J_{Total}(\Phi + \Delta\Phi) - J_{Total}(\Phi)}{q}$$

where Φ and $\Delta\Phi$ is the incident photon flux and its increment respectively. This approach has been shown to give accurate results compared to the standard one of $QE = \frac{J - J_{Dark}}{q}$

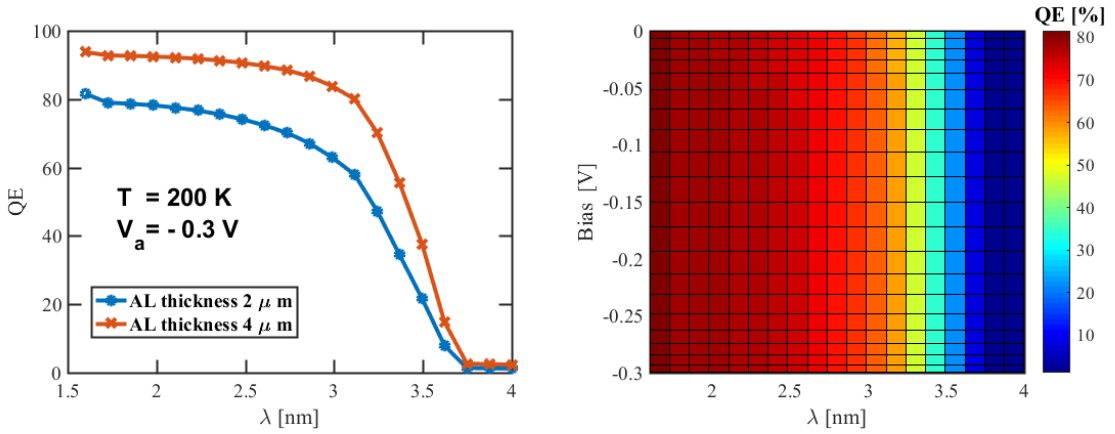

(a) @ $-0.3\,V$. (b) @ different bias: AL of $2\mu m$.

Figure. 4.16 Spectral responses of InAs nBn detector as function of bias under uniform illumination with an incident photon flux of 10^{17} photons $cm^{-2}s^{-1}$ at a temperature of 200 K.

4.7 Design and Simulation of InAs/GaSb T2SL Barrier Detectors

In this section, I design and theoretically evaluate, by using our modelling tools, the performances of T2SL LWIR barrier detectors. The material of choise is Type II InAs/GaSb superlattices thanks to its remarkable optical and hole transport properties [133, 59]. In fact, this engineered material offers many advantages for IR detection including a high effective mass, reduced Auger recombination rates, excellent material uniformity, normal incidence and the possibility to be engineered to a particular wavelength over a wide range of values while keeping the SL structure lattice matched to the GaSb substrate. Benefiting from the lattice-matched growth conditions and advances in the molecular beam epitaxy (MBE) technology, the type-II broken gap band alignment of this system enables an accurate control of energy

band structure and exhibits great flexibility in the design of detector devices without degrading the material quality. However, the reported short minority carrier lifetime (10 to 150 ns at 77 K) prevented this material system, in terms of dark currents, from reaching its theoretical limit nor to surpass MCT detectors. The main reason is due to a Shockley-Read-Hall (SRH) mechanism which limits the minority carrier lifetime of the SL, resulting in a higher dark currents than those of MCT. The poor carrier lifetimes in InAs/GaSb SL materials have been mainly attributed to native defects in the GaSb binary layer. Recently, the InAs/InAsSb SL (referred as the 'Ga-Free' SL) has been proposed as an alternative to the T2SL InAs/GaSb technology since a longer minority carrier lifetime has been reported both in the MWIR and LWIR spectral windows [90, 122, 35, 134]. Despite this fact and the initial made progress, Ga-Free detector performances have not proved to be superior than those of T2SL detectors and are still facing many challenges, especially for high temperature operation and/or LWIR spectral window. Therefore, InAs/GaSb SL remains the material of choice for LWIR detection supported by the growing interest in space applications such as Earth Observation missions.

The challenge for making high temperature LWIR photodetectors in InAs/GaSb SL material system is to reduce the dark current density in order to achieve a high signal-to noise ratio. The dark current is caused by the exponential decay of minority carriers through Shockley-Read-Hall (SRH), Radiative (RAD), and Auger (AUG) recombination, especially for the narrow bandgap absorbers. Increasing the operating temperature is highly desirable since it removes the burden of cryogenic cooling systems, and thus lower the cost of this technology. On the way of solving this problem, different types of barrier architectures have been proposed and implemented in phtodetectors for suppressing the dark current, which results in an increase in operating temperature in comparison with the p-i-n photodiodes. As has been mentioned in section 4.6, the nBn type barrier detector has received the most attention and development. However, the traditional nBn barrier detector requires bias to extract photocarriers and uses low mobility of minority carriers (holes) which reduce the device speed. For these reasons, the nBp barrier detector has been proposed, which has the advantages of zero bias operation and higher mobility minority electron leading to higher extraction efficiency. In the following, by means of our modelling tools, we present the design and the numerical simulation of LWIR InAs/GaSb T2SL nBp barrier photodetectors for high temperature operation. The composition, thickness and doping level of each of the device layers (absorbing, barrier and contact layers) are carefully chosen. The analysis of dark currents is made in term of the temperature of operation.

4.7.1 T2SL nBp Detector's Structure

The proposed nBp device architecture consists mainly of n-doped top Contact Layer (CL), a Barrier Layer (BL) with large Valence Band Offset (VBO) and minimal Conduction Band Offset (CBO), and a p-type LWIR superlattice Absorber Layer (AL). The full detector's structure is shown in Figure 4.17. In the following sections, when appropriate, the doping type of the barrier is denoted using a subscripts indicate the doping type, naimlly nB$_p$p or nB$_n$p.

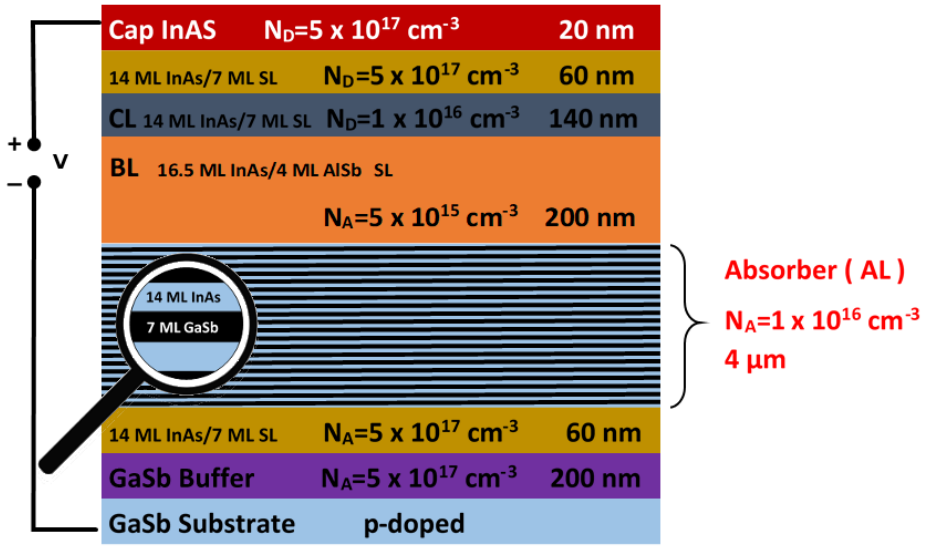

Figure. 4.17 Schematic illustration of InAs/GaSb T2SL nBp LWIR detector structure.

4.7.2 Absorber Layer Design

The first design requirement of an LWIR detector is to select an efficient absorber materials to achieve high quantum efficiency and low dark current density. In addition to the advantages mentioned above, InAs/GaSb T2SL offers also the possibility to choose different period compositions for a given wavelength. Indeed, the InAs/GaSb SL period thickness and composition have shown experimentally, strong effect on both material properties and PIN photodetector performances. T2SL absorbers with period mainly composed of InAs (referred to as the "InAs-rich SL"), exhibit a lower dark current than those with period mainly composed of GaSb (referred to as the GaSb-rich SL") having the same cut-off wavelength. Therefore, we propose and design a Type-II superlattice (T2SL) with 14 Mono-Layer (ML) of InAs and 7 ML of GaSb ($\sim 44 InAs/21 GaSb$), $per period as a material for the LWIR Absorber Layer (AL) with a band gap wavelength close t$

We will further support this choice with the arguments in the subsequent paragraphs. To get the desired band alignment, absorption coefficient and main effective material parameters for the Absorber Layer (AL), Barrier Layer (BL) and Contact Layer (CL), various T2SLs with different period compositions were simulated using our **k**· **p** tool developed in chapter 3. The conduction and valence band edge energies (E_c and E_V) and the corresponding effective band gap were calculated as a function of the SL's period compositions are shown in Figure 4.18 and Figure 4.19. In our **k**· **p** modelling, we compensate for the tensile strain of the InAs layer on GaSb layer ($\Delta a/a \sim -0.6\%$), by introducing an interface InSb layer between InAs and GaSb on both sides (see Figure 4.20). This interfacial effects has been investigated thoroughly in chapter 3 along with the absorption coefficient of the InAs-rich 14 ML InAs / 7ML GaSb LWIR T2SL.

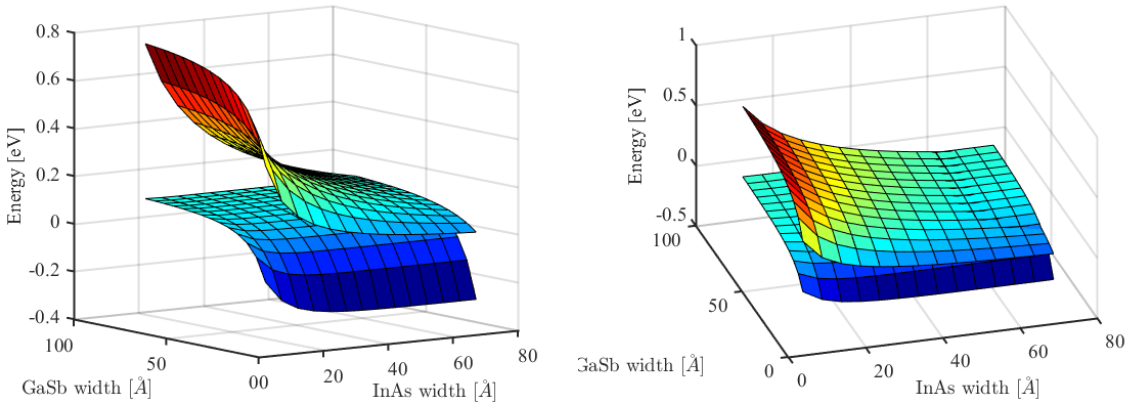

(a) At 77 K.

(b) At 300 K.

Figure. 4.18 Conduction band and valance band energies plotted as a function of period composition in a type II InAs/GaSb superlattice calculated with kp band calculation.

Figure 4.19 indicates that for increasing InAs quantum well thickness, the effective band gap decreases due to the strong localization of holes, while it slightly increases with increasing GaSb well thickness, which is due to quantum confinement effects as suggested by the electron-hole wavefunction profiles especially for thin InAs thickness. In addition, we can see that the InSb IF layer causes a decrease in the effective band gap energy where it is more pronounced for thicker InAs layer and fixed GaSb well thickness. This result indicates the importance of the IF layer consideration for band gap calculation which in turn impact on the absorption coefficient and cut-off wavelength as previously demonstrated in chapter 3. Furthermore, the splitting of the highest heave-hole band (HH1) and the highest light-hole band (LH1) responsible for the minimization/suppression of Auger recombination is more noticeable for InAs/GaSb T2SL with thinner GaSb layer.

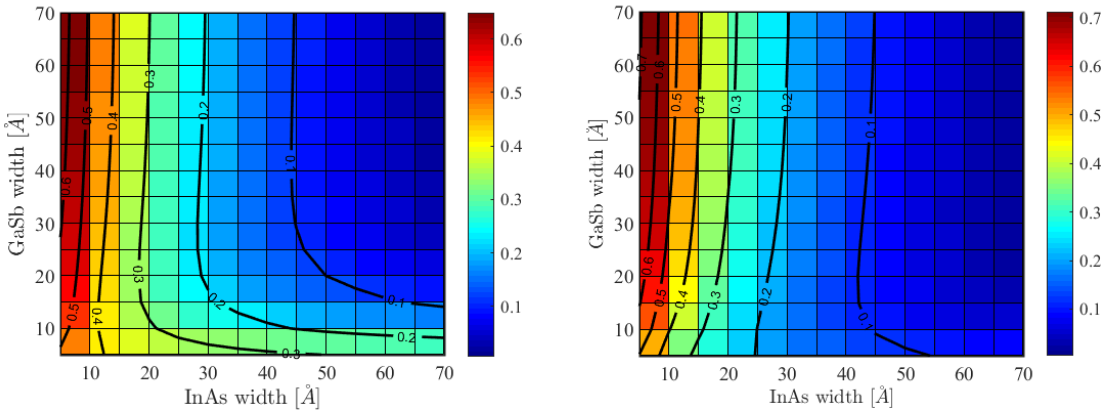

(a) Without the IF effect.

(b) With the IF effect of 2.4 Å.

Figure. 4.19 Effective Band gap energy Eg as a function of InAs layer width and GaSb layer width for a type II InAs/GaSb superlattice At 77 K including IF layer effect.

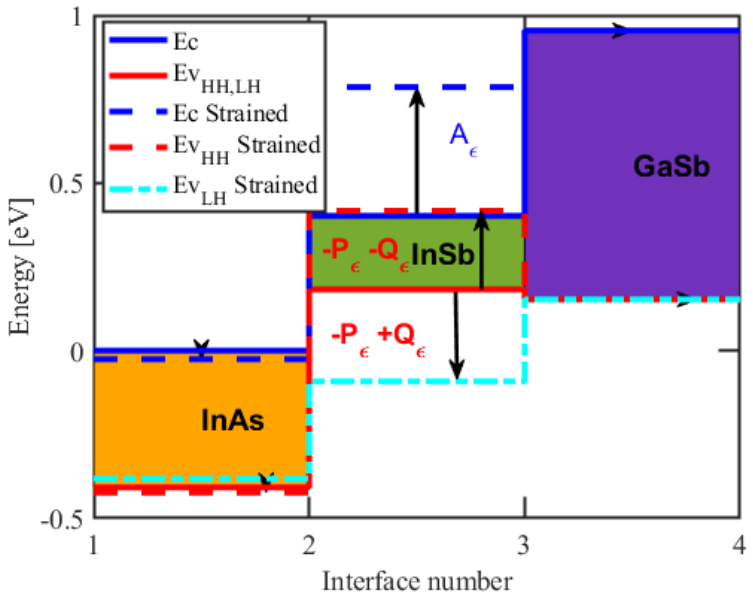

Figure. 4.20 The band edge profile at InAs/GaSb interface with forced InSb layer in between. The solid lines are unstrained band edges while the dashed blue, red and cyan lines denoted the strained conduction, heavy-hole and light-hole band edges respectively. The symbols are a Hamiltonian elements defined in chapter 3.

The electron and hole effective masses at the band edge in both directions: in-plane $m^*_{e,h,//}$ and perpendicular $m^*_{e,h,\perp}$ were also extracted from the calculated band structure $E_{\mathbf{k}}$ using $m^{*-1}_{e,h,//,\perp} = \hbar^{-2}\partial^2 E / \partial k^2_{//,\perp}\Big|_{\mathbf{k}=0}$. The effective mass is positive for a conduction-type band and negative for a valence-type band. Figure 4.21 shows the electron and hole effective masses

in color levels as a function of InAs and GaSb thicknesses. In the first chapter, I mentioned the importance of the high effective masses of T2SL in limiting the tunnelling dark currents. However, too large effective masses can also deteriorate the collection of carriers. It is therefore necessary to find a SL design having a good compromise between reducing the tunnelling current and the collection efficiency of photo-generated carriers. Overall, our calculation gives effective mass values higher than what would be expected by a simple interpolation of the two effective masses composing the period. In addition, we note a trend in Figure 4.21, as the thickness of InAs in the period decreases, the effective mass of the SL tends gradually to the bulk effective mass of GaSb material. The same trend holds also as we sweep the GaSb thickness interval while keeping InAs thickness fixed. Moreover, for a given band gap (or a cut-off wavelength), all the effective masses are accessible from 0.02 to 0.07 mainly by changing the thickness of GaSb layer. It's clear from Figure 4.22 that the InAs-rich 14 ML InAs / 7ML GaSb T2SL offers electron effective mass larger than the electron effective mass in the HgCdTe material which scales as $\sim 0.07 \times E_g$ [109]. Therefore, as the tunnelling probability is exponentially dependent on the effective mass, the 14 ML InAs / 7ML GaSb T2SL should exhibit lower tunnelling current than HgCdTe, especially in the LWIR range where the effective mass in HgCdTe is very small compared to the one in SL. Also, the collection efficiency is not affected too much by this choice of SL as an absorber since the effective mass is not too high. Furthermore, the flexibility of the InAs/GaSb SL material is reflected in the ability to achieve the same energy band gap with different SL design which have different electronic band structures which in turn can have an impact on the device operation.

Next in this parameters' investigations, the minority carrier lifetime and mobility should carefully be specified in order to conduct a successful carriers transport simulations as they determine the final device behaviour. The minority carrier lifetimes and mobilities are then selected from the existing literature on LWIR T2SL photodiodes [60]. The Varshni's parameters $E_g(0K)$, α and β accounting for temperature dependence of the bandgap were determined by fitting the energy band gap obtained from photo-luminescence (PL) measurements to the well-known Varshni's relation $E_g(T) = E_g(0K) - \frac{\alpha \cdot T^2}{\beta + T}$ [5, 20]. Some other physical parameters of the SL used in the simulation such as the permittivity were calculated as a weighted average of InAs and GaSb bulk values.

The quantum efficiency is a device-dependent property, which can be affected by many factors including doping level, AL thickness, minority carrier diffusion length. As a first attempt, the p-type active region is chosen to be $4\,\mu m$ thick and will be optimized later on. The detector can also be modelled with different p-doping conditions for the AL, however, an optimum value of $1 \times 10^{16} cm^{-3}$ is chosen as it is close enough to the range confirmed

Table 4.5 Material parameters used in the simulation for InAs-rich InAs/GaSb T2SL.

Parameter	Symbol	Value	Unit
Band gap	E_g@0K	0.111	eV
Trap energy	E_T	0	eV
Electron affinity	χ	4.76	eV
Electron effective mass calculated as: $m^*_{e,\perp}{}^{1/3} \times m^*_{e,//}{}^{2/3}$	m^*_e	0.025	m_0
Hole effective mass	m^*_h	0.309	m_0
Tunneling effective mass	m^*_t	0.025	m_0
Dielectric constant	ε	15.29	ε_0
Electron life time	τ_n	30	ns
Hole life time	τ_p	30	ns
Electron mobility	μ_n	2.6×10^4	$cm^2/(V \cdot s)$
Hole mobility	μ_p	680	$cm^2/(V \cdot s)$
Varshni parameter	α	1.9×10^{-5}	eV/K
Varshni parameter	β	270	K

from capacitance vs. voltage measurements on a similar SL structure [60, 20]. Finally, the material parameters chosen for our transport simulation of InAs-rich T2SL LWIR detector are summarized in Table 4.5.

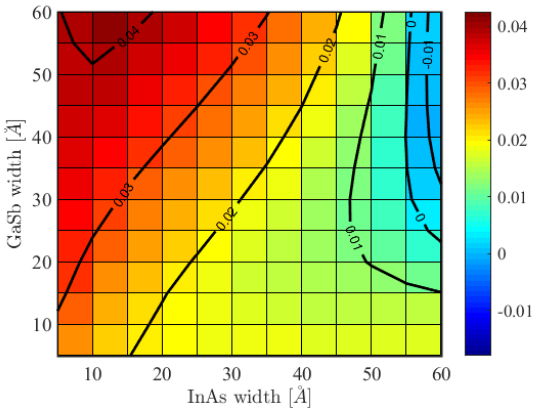

(a) In-plane $m^*_{e,x}$.

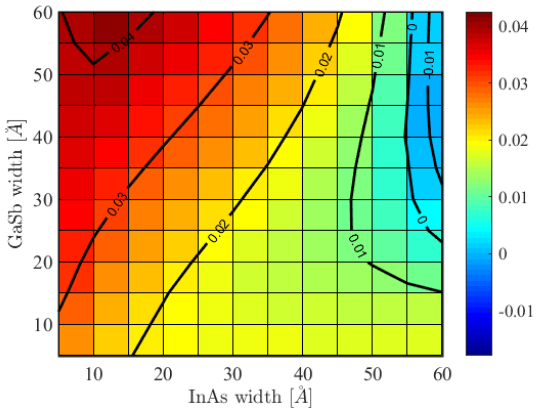

(b) In-plane $m^*_{e,y}$.

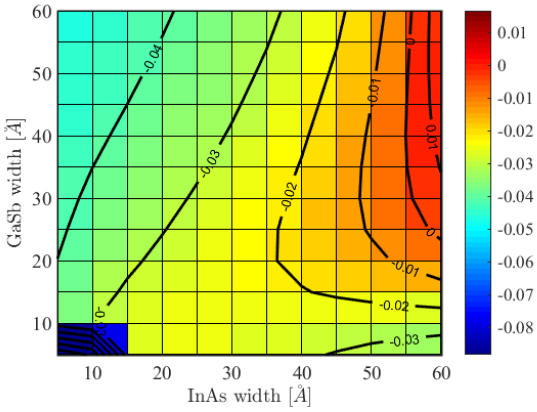

(c) In-plane $m^*_{hh,x}$.

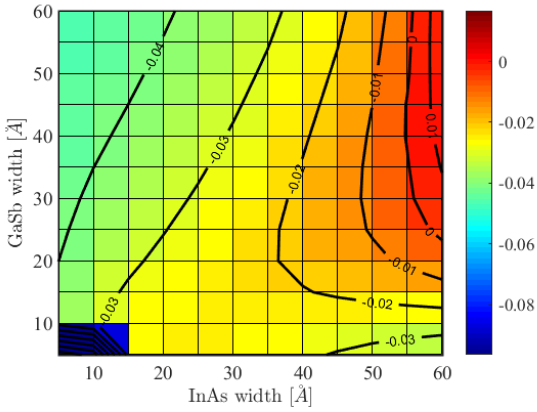

(d) In-plane $m^*_{hh,y}$.

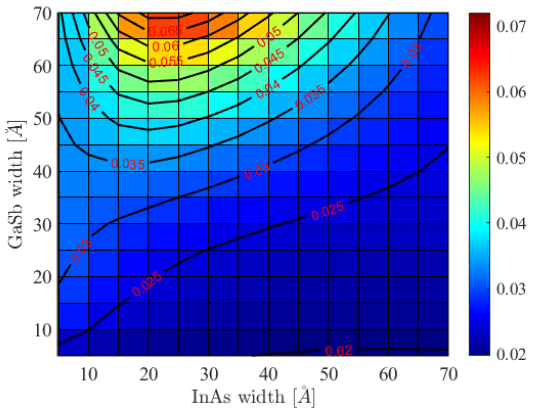

(e) Perpendicular $m^*_{e,z}$: No IF effect.

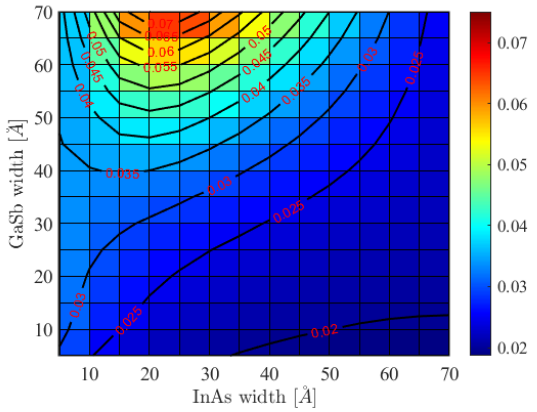

(f) Perpendicular $m^*_{e,z}$: IF effect of 2.4 Å.

Figure. 4.21 Effective masses as a function of InAs layer width and GaSb layer width for a type II InAs/GaSb superlattice At 77 K. The solid lines are the effective mass contour lines.

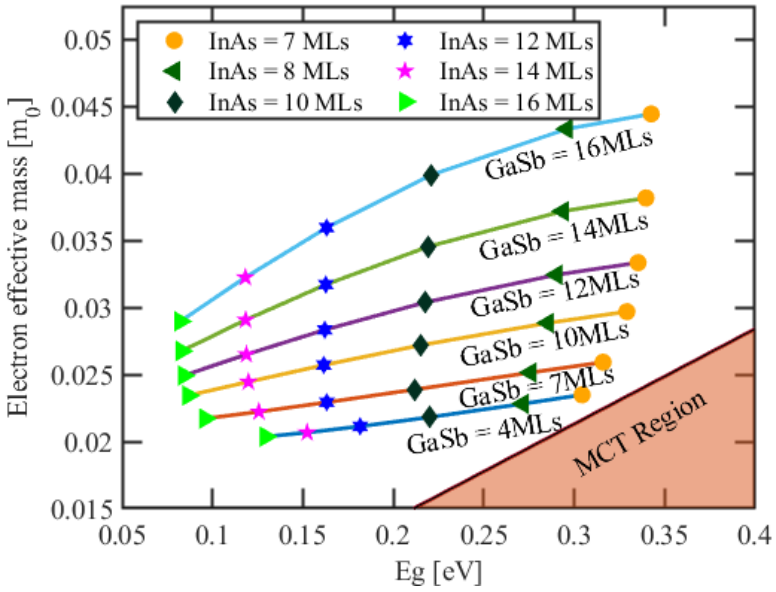

Figure. 4.22 Perpendicular electron effective mass for different period compositions of SL as a function of the energy band gap at 77K. Solid lines are for fixed GaSb layer thicknesses, while symbols are for fixed InAs layer thicknesses. Shaded zone shows the electron effective mass region in MCT material.

4.7.3 Barrier Layer Design

The second design requirement of an nBp LWIR detector is to select barrier materials for the chosen T2SL absorber such that the conduction band edge of the designed BL is smoothly aligned with the corresponding band edge of the AL, while it has a large VBO with respect to the AL. In this barrier design with a p-type doping for the CL, majority holes emanating by thermionic emission from the CL are blocked from reaching the AL essentially by the VBO potential barrier ΔE_V. This flux of carriers transfer over the barrier is proportional to $m_h^* T^2 \, exp(-\frac{\Delta E_V + E_F}{k_B T})$ and constitutes one of the dark currents components that should be minimized to ensure a diffusion limited behaviour. The thermionic current variation with the VBO at 77, 150 and 300 K is shown in Figure 4.23. The value of ΔE_V for which this thermionic flux equals the dark-current in a similar P-I-N device at 150 K was found to be 130 meV [20]. Therefore, a VBO value larger than 130 meV is required. Given that effective barrier $\Delta E_V + E_F$ for carriers depends on the doping level and the applied bias, the band bending may leads to a decrease in this effective barrier, thus a value larger than 300 meV has to be chosen for ΔE_V to be in the safe side in lowering the thermionic contribution at least by one order of magnitude than the diffusion dark-current. Similarly, a carriers' transfer through the barrier due to tunnelling is also possible

which may takes significant levels for very thin barriers. In our case, barrier thicknesses greater than a few hundred angstroms ensures that the tunnelling current is negligible.

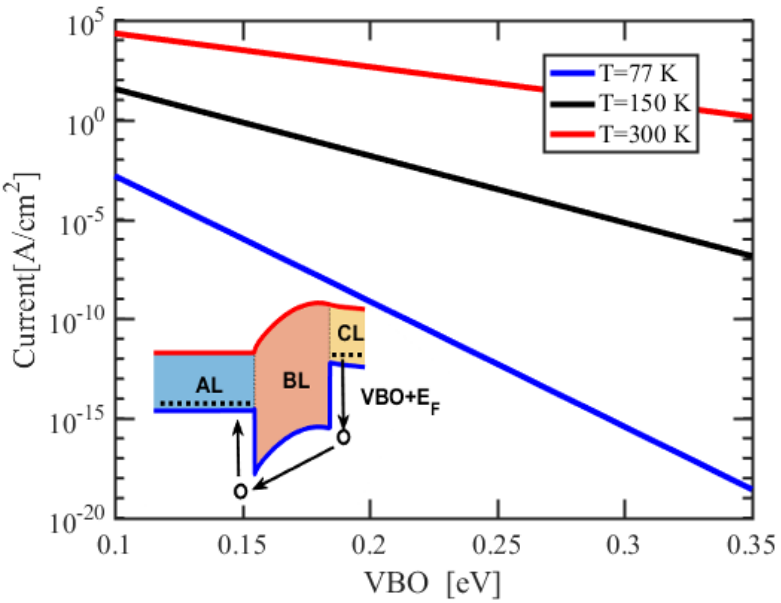

Figure. 4.23 Thermionic Emission current as a function of the VBO between contact and barrier at 77, 150 and 300 K. Inset shows the operating band edge profile of a pBp device.

Additionally, in order to allow for an impeded flow of photo-generated electron carriers when crossing the BL toward the CL where they will be collected, the BL needs to have ideally no barrier potential ΔE_C with respect to the AL. If this CBO has none negligible value, then a high reverse applied bias will be required to turn on the device by reducing the barrier ΔE_C. Usually this happen when the barrier, ΔE_C exceeds about $3k_BT_{op}$, where T_{op} is the operating temperature.

The material responding for the above barrier requirement is chosen to be made from InAs/AlSb SL with a composition of 16.5 MLs of InAs and 4 MLs of AlSb estimated by $\mathbf{k}\cdot\mathbf{p}$ treatments. The calculated band alignment between the AL and BL are shown in Figure 4.24. It can be seen that, the InAs/AlSb superlattice of the BL is designed to give a smooth conduction band alignment and a large VBO of nearly 400 meV with the AL. Note that in Figure 4.24, the CBO is defined as the energy difference between the bottom of the two electron mini-bands and the VBO as the energy difference between the top of the two hole mini-bands.

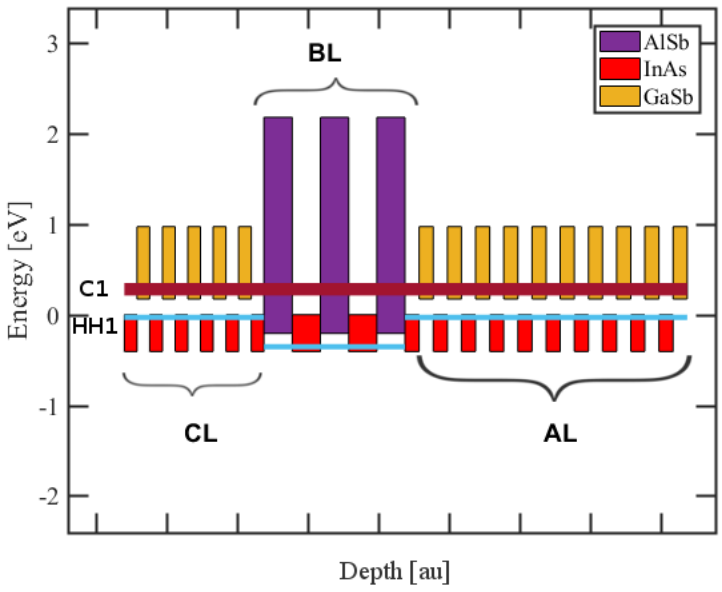

Figure. 4.24 Mini-bands alignment between the AL and BL of a T2SL based barrier device, superimposed on the individual alignment of the band gaps of InAs, GaSb and AlSb. The number of shown periods in each layer are in fact repeated many times in the real device and cannot to scale in one figure.

The doping type and level has an important effect on the device performance. In fact, when the BL doping is n-type and the AL p-type, in order to have the same Fermi level throughout the structure, the ionized electrons from donnor levels in the BL diffuse toward the AL and at the same time, the majority holes in AL defuse to BL until a PN junction is created at the interface BL/AL. As a result, the barrier is fully depleted because of its relatively small thickness and the donor states receive a positive charge as illustrated in Figure 4.25. In addition, the depletion zone extends into the AL where negative ionized acceptors are created. The pronounced extent of the depletion zone into the narrow band gap material of the AL, activates the contribution of G-R centres to the dark current even at very low bias. Therefore, the barrier layer cannot be n-type when the active zone is p-type to avoid the creation of an extended depletion zone at BL/AL interface.

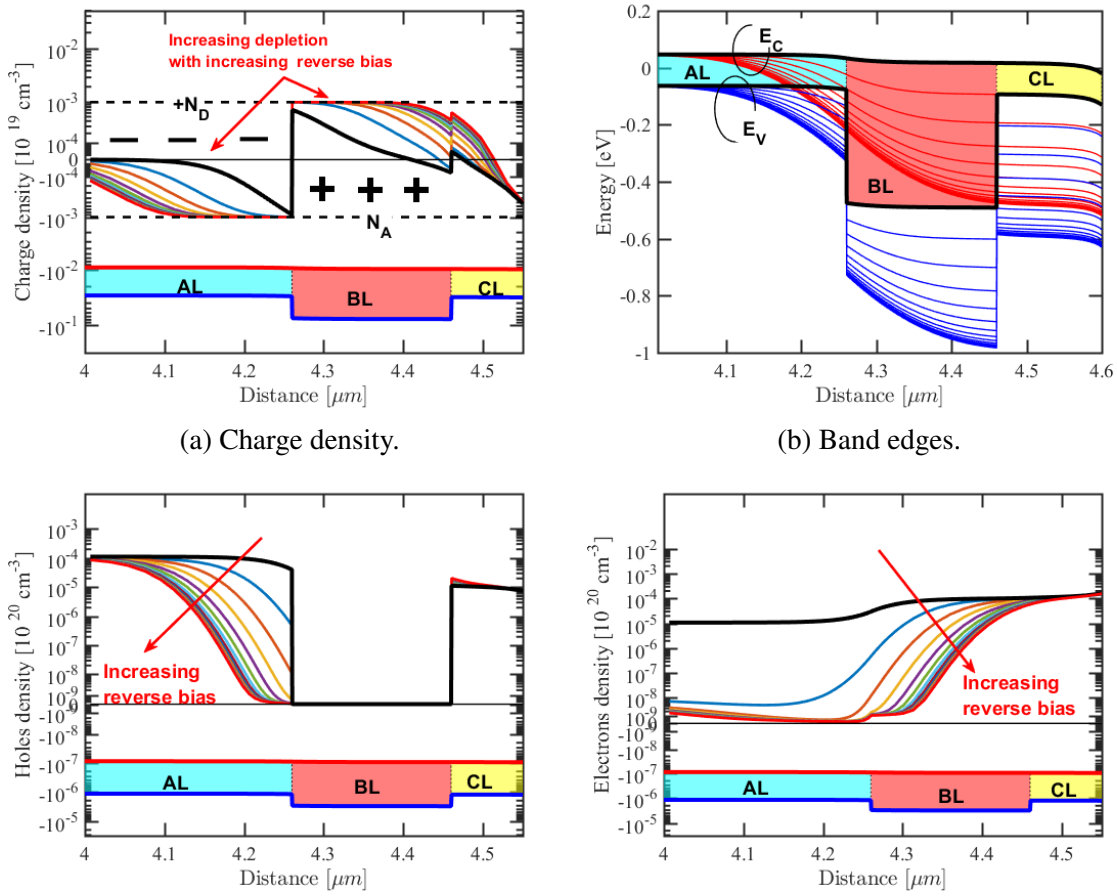

(a) Charge density.

(b) Band edges.

(c) Holes density.

(d) Electron density.

Figure. 4.25 Simulation results for the charge density, band edges, holes density and electron density around the barrier layer for a range of negative bias voltages for nB$_n$p structure at 77 K. The barrier doping level was fixed at $5 \times 10^{15} cm^3$. The black curves in each subfigure is for the equilibrium case.

Now, if the doping type of the BL is switched to p-type, the majority holes in the barrier reduce their energy substantially by diffusing to the AL to accumulate at the interface next to the barrier as shown in Figure 4.26. As a result, the acceptor states of the BL receive a negative charge and the barrier is fully depleted given its thickness. Since the extent of accumulation zone is usually narrow given the relatively low doping level, the depletion zone does not extends into the AL and remains confined into the BL, and so the electric field (see Figure 4.27a). The band bending under the effect of reverse bias leads to diminish this accumulation zone until its extinction at a maximum bias where the bands in the AL are totally flat. Beyond this bias, the depletion in the barrier layer will start to extend into the AL and the G-R contribution to the dark current will start to increase rapidly. The applied bias corresponds to the flat band

condition depends on the thickness and doping level of the BL. The effect of doping level will be investigated in following sections.

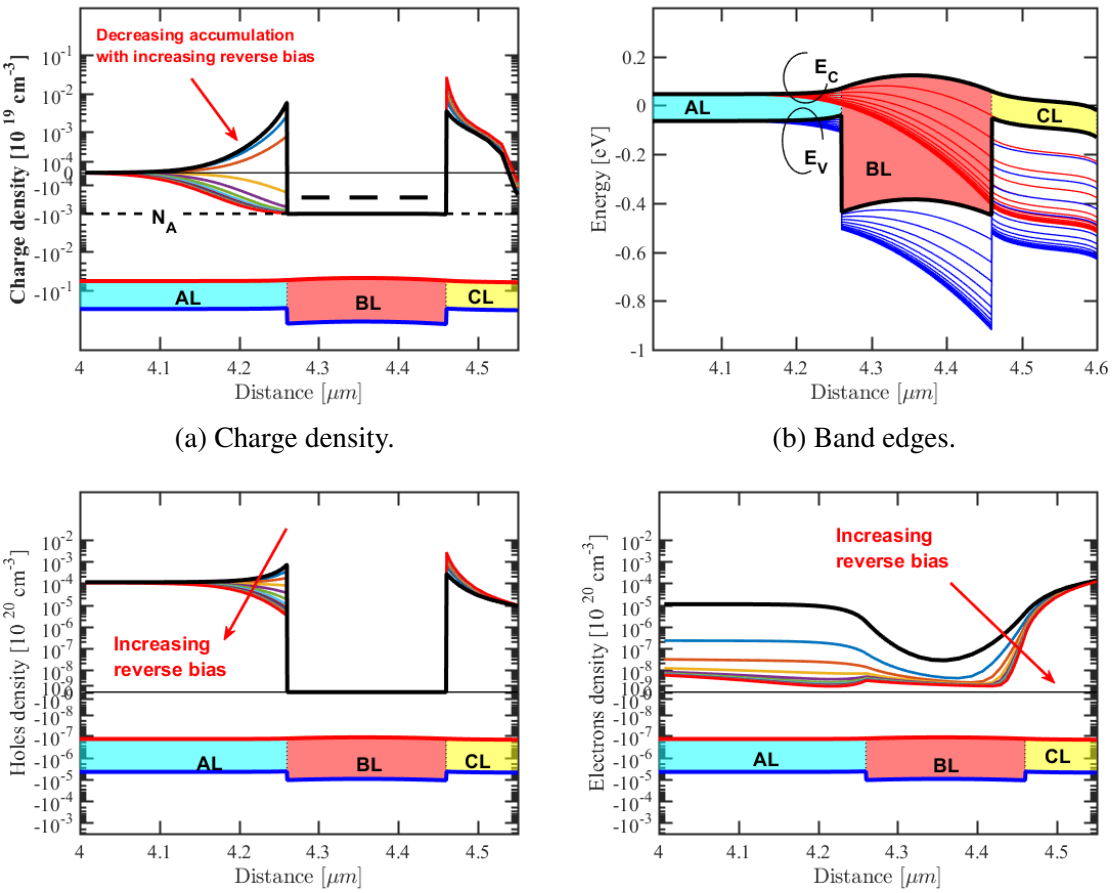

(a) Charge density.

(b) Band edges.

(c) Holes density.

(d) Electron density.

Figure. 4.26 Simulation results for the charge density, band edges, holes density and electron density around the barrier layer for a range of negative bias voltages for pB$_p$p structure at 77 K. The barrier doping level was fixed at $5 \times 10^{15} cm^3$. The black curves in each subfigure is for the equilibrium case.

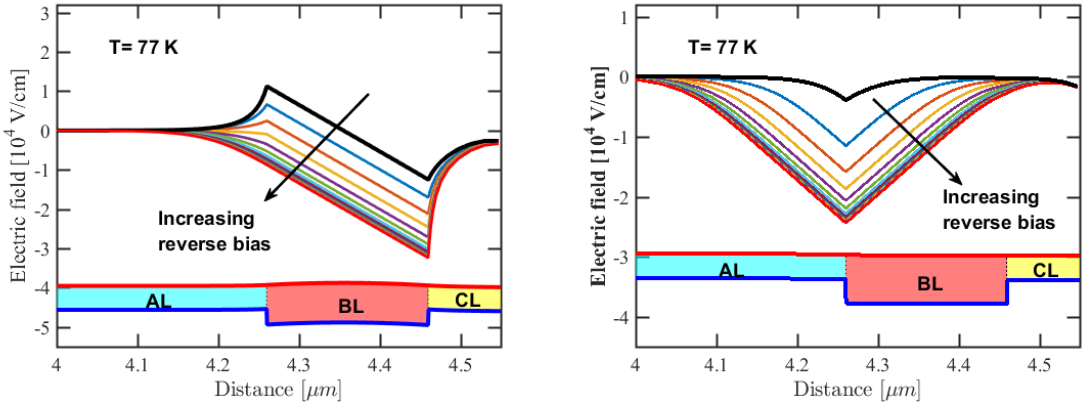

(a) Electric field in a nB$_p$p device.

(b) Electric field in a nB$_n$p device.

Figure. 4.27 Simulation results for the electric field in the space-charge and accumulation regions of the nB$_p$p and nB$_n$p detector around the barrier layer for a range of negative bias voltages. The barrier doping level was fixed at $5 \times 10^{15} cm^3$. The black curves in each subfigure is for the equilibrium case.

4.7.4 Contact Layer Design

The contact material can be made from the same or from a different material than the AL. In our case, the AL and the CL are both made from the InAs-rich T2SL with same composition. The only difference between the AL and CL is their thickness, which is not as critical for the contact as for the barrier or the absorber. However, the CL thickness is kept to be not too thick (typically less than 200 nm) to avoid its absorbing for IR radiation which deteriorates the quantum efficiency. The AL is always p-type as confirmed from the discussion above. The doping type in the CL can be either p-type or n-type to create pBp and nBp devices, respectively. In the beginning of designing our device, we have made the n-type choice for the CL, here, we confirm our choice by comparing in Figure 4.28 the band edges of a nBp and pBp designs with contact doping level of $10^{16} cm^{-3}$ at 77 K. As the band bending in nBp design pins the Fermi level close to the conduction band edge of CL, the thermionic current is therefore smaller than in the pBp design due to the reduction in the potential barrier in the valence band. In addition, the large band bending, in an n-type contact lowers the potential barrier in the conduction band for the minority electrons, thus reducing the turn on voltages compared to a pBp device. Finally, a n-type doping level of $10^{16} cm^{-3}$ is chosen for the CL of the nBp design since a narrow hole accumulation region is persistent to exist at the interface AL/BL which delays the formation of a depletion layer by confining the electric field into the BL.

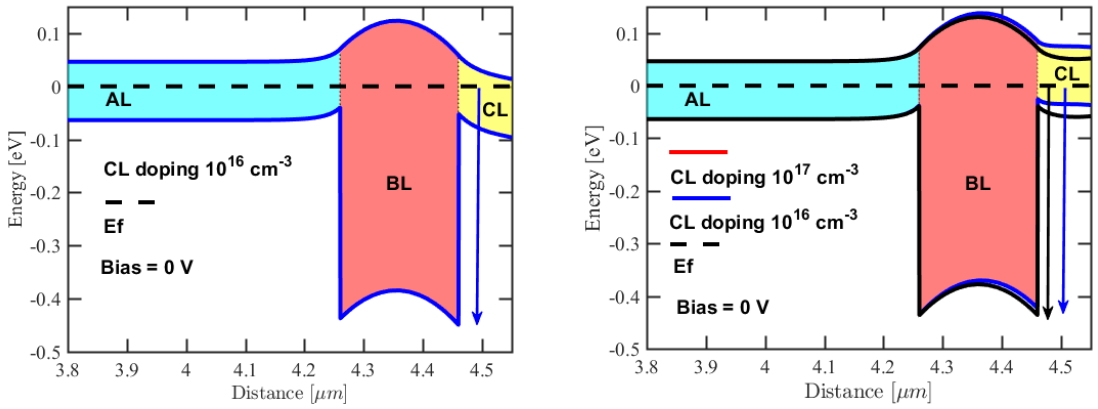

(a) Band edges of nB$_p$p.

(b) Band edges of pB$_p$p.

Figure. 4.28 Simulation results for band edges around the barrier layer at equilibrium for nB$_p$p and pB$_p$p structure. The barrier doping level was fixed at $5 \times 10^{15} cm^3$. The vertical arrows in each subfigure shows that the thermionic potential barrier is lower in nB$_p$p than in pB$_p$p device. Also the potential hump in the conduction band is lower for nB$_p$p case due to a larger band-bending.

Having established the initial design requirements for CL, BL and AL, now I will simulate and further analyse the design of the whole barrier detector.

4.7.5 Energy Band-Edge Profiles

The band edge profiles for the optimized nBp photodetector with a p-type barrier are shown in Figure 4.28 at a temperature of 77 K for equilibrium and for negative bias dark condition. The bias convention is shown in Figure 4.17. To enhance the collection of carrier, the top of the structure is terminated with a 60 nm thick n^+ doped InAs-rich T2SL followed by 20 thick n^+ doped InAs cap layer.

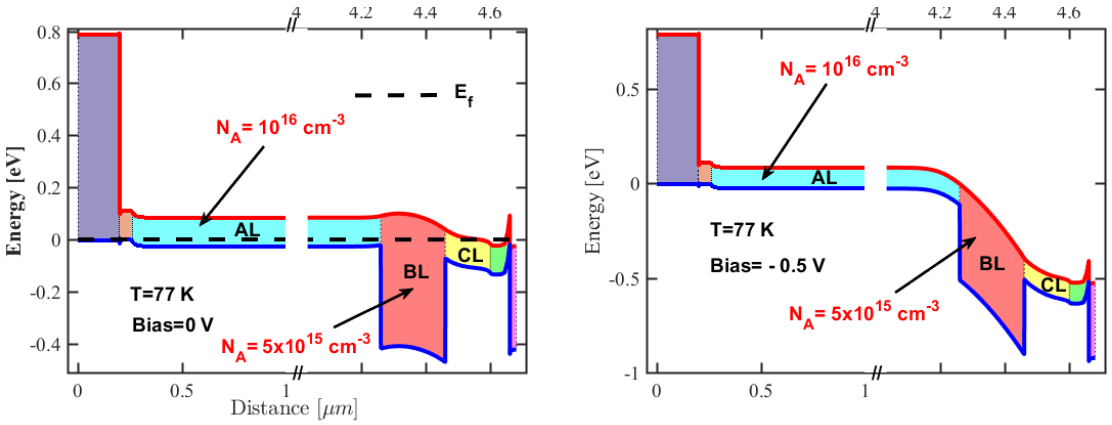

(a) Equilibrium.

(b) Reverse Biased.

Figure. 4.29 Band edge profiles for LWIR nB$_p$p detector with p-type barrier at dark condition and T=77 K: a) for equilibrium and b) for negative bias. The barrier doping level was fixed at $5 \times 10^{15} cm^3$.

The most notable feature of the band profiles is the presence of a large potential barrier in the BL. This large barrier blocks transfer of holes between the AL and the CL, for a large range of operating bias voltages. Additionally, the BL exhibits a smooth conduction band potential barrier which presents no impediment to the transport of minority electrons between the AL and the CL. The BL also has a valence band potential well for holes that forms due to its negatively charged acceptors. The presence of this potential well and its variation under the effect of band bending and the applied reverse bias does not affect the ability of the BL to block the majority holes. At negative bias, current is due to electrons that are thermally generated or photo-generated in the AL and that are subsequently driven from the AL to the CL by the strong electric field in the BL.

4.7.6 J(V) Characteristics of LWIR T2SL nBp Detector

The numerical simulations for the dark current density versus voltage relation $J(V)$ for a nBp LWIR photodetector at 77 K are presented in Figure 4.30. On the same figure is shown the dark current of an equivalent InAs-rich SL PIN detector. The dark current components accounted for in the numerical simulations are the Diffusion, Generation-Recombination, Trap-Assisted Tunneling (TAT) and the Band-to-Band (BTB) tunneling currents. The diffusion current component is generated due to diffusion of thermally generated minority carriers from the AL and are obtained by the Equation (4.22). The generation-recombination current component is triggered by the presence of traps within the forbidden gap and is obtained by integrating the well-known Shockley-Read-Hall (SRH) recombination rate equation:

$$J_{GR} = q \int R_{\text{SRH}} dz \tag{4.75}$$

where

$$R_{\text{SRH}} = \frac{pn - n_i^2}{\tau_p \left[n + n_i \exp\left(\frac{E_{trap}}{k_B T}\right)\right] + \tau_n \left[p + n_i \exp\left(\frac{-E_{trap}}{k_B T}\right)\right]} \tag{4.76}$$

where R_{SRH} is the Shockley-Read-Hall (SRH) recombination rate, and n, p and n_i are the electron, the hole and the intrinsic carrier concentration, respectively. E_{trap} is the difference between the trap energy level and the intrinsic Fermi level, k_B is the Boltzmann constant and T is the lattice temperature. τ_n and τ_p are the electron and hole carrier lifetimes.

The Trap-Assisted Tunneling current component is also modelled based on an approach developed by Hurkx [41]. This approach uses an effective lifetime by including a field effect factor in Equation (4.76). According to Hurkx the recombination rate expression becomes:

$$R_{\text{TAT}} = \frac{pn - n_i^2}{\frac{\tau_p}{1+\Gamma_p}\left(n + n_i e^{\frac{E_{trap}}{k_B T}}\right) + \frac{\tau_n}{1+\Gamma_n}\left(p + n_i e^{-\frac{E_{trap}}{k_B T}}\right)}. \tag{4.77}$$

where $\Gamma_{n,p}$ is the field-effect enhancement term given by

$$\Gamma_{n,p} = \frac{\Delta E_{n,p}}{k_B T} \int_0^1 \exp\left(\frac{\Delta E_{n,p}}{k_B T} u - K_{n,p} u^{\frac{3}{2}}\right) du \tag{4.78}$$

where $\Delta E_{n,p}$ is the energy interval in which the tunneling can occur for an electron or a hole, and u is the integration variable. $K_{n,p}$ is defined as:

$$K_{n,p} = \frac{4}{3} \frac{\sqrt{2 \cdot m_t \cdot \Delta E_{n,p}^3}}{q\hbar|E|} \tag{4.79}$$

with m_t the tunneling mass, E is the electric field and $\hbar$ the reduced Plank's constant. The combined SRH and TAT current density therefore becomes:

$$J_{SRH+TAT} = q \int R_{\text{TAT}} dz \tag{4.80}$$

For the band-to-band tunneling contribution, our tool implements a local model according to Hurkx [41] in which a recombination-generation rate R_{BTB} at each point in space is calculated

based solely on the value of the localized field at that point. Similarly, the BTB current density is then given by:

$$J_{BTB} = q \int R_{\mathrm{BTB}} dz. \tag{4.81}$$

As expected, the dark current of nBp design shows diffusion-limited behaviour down to 300 mV before other dark current components starts to dominate at higher reverse bias. On the other hand, the PIN device is not diffusion limited at small reverse bias. If we make a closer look at the absorber region adjacent to the barrier in Figure 4.29, we observe a less significant band-bending for nBp device than in pin device as shown in Figure 4.33. This in turn is confirmed in the Arrhenius plot of dark current density as function of temperature and bias in Figure 4.31. These plots shows diffusion-limited behaviour for the nBp device down to 77 K, while the PIN device is limited by other mechanisms at this temperature, with a dark current greater by more than many order of magnitude compared to the barrier device. In addition, at a given dark current in Figure 4.32, the presence of the barrier results in an increase in the operating temperature compared to PIN device. Specifically, for a current density $2x10^{-4}$ A/cm^{-2}, the operating temperature of the PIN device is nearly 60 K while for the nBp device it is close to 80 K with an improvement of 20 K. This difference in the operating temperature reduces the power consumption of the cooling system.

The diffusion plateau dark-current level reaches $8.5x10^{-5}$ A/cm^{-2} which is within one order of magnitude of MCT Rule-07 indicating that InAs/GaSb T2SL detectors may replace the MCT technology at longer wavelength. This claim might appear surprising since InAs/GaSb T2SL shows lower minority carrier lifetime τ than MCT material. However, as the diffusion current is inversely proportional to the $N_{dop} \times \tau$ product (with N_{dop} being the AL doping level) which must be kept at maximum without deteriorating the transport of carriers. Therefore, the short minority carrier lifetime effect can be compensated by a choosing a higher doping level for the the AL than in MCT. Moreover we enforce our claim by the fact that T2SL technology offers high operability, stability and durability of focal plane arrays [103].

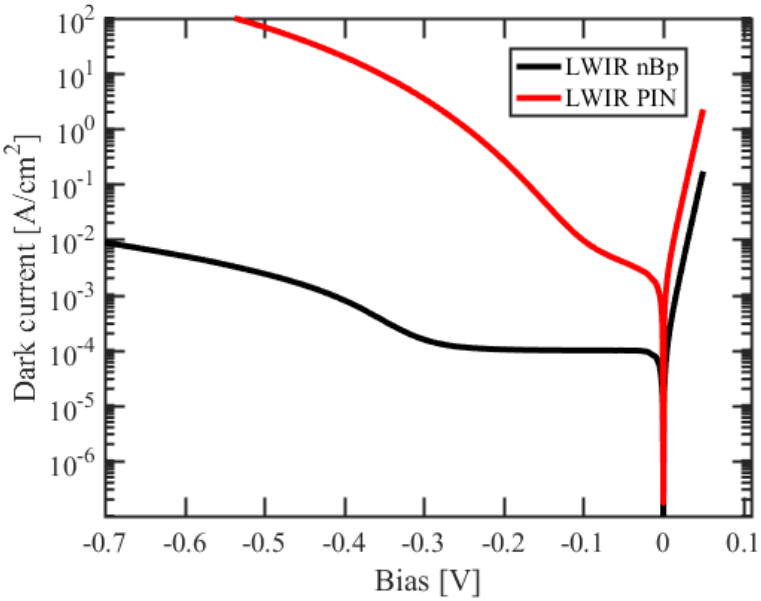

Figure. 4.30 The dark current density as a function of the applied bias voltage of the optimized LWIR T2SL based barrier detector and the corresponding dark current of its equivalent PIN detector at 77 K. Both devices have a p-type SL InAs/GaSb active layer with a bandgap wavelength close to 11 μm.

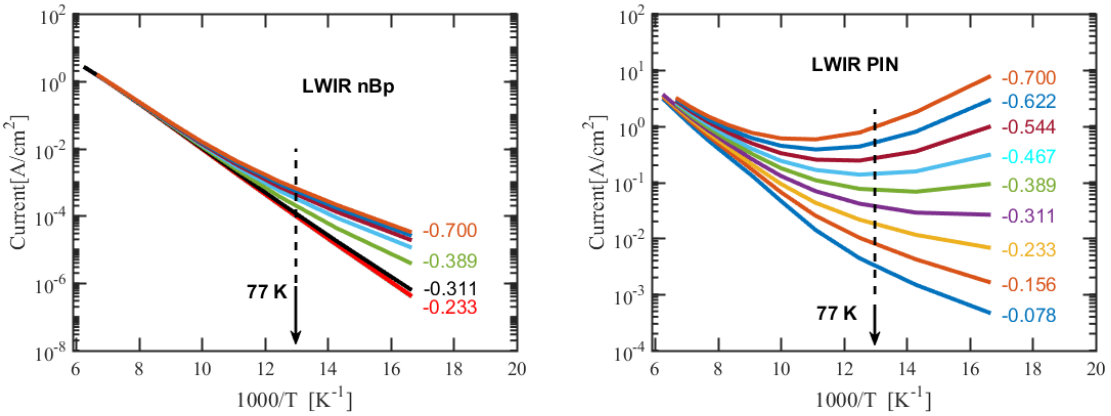

(a) LWIR nB$_p$p detector.

(b) Equivalent LWIR PIN detector.

Figure. 4.31 Arrenius plot of dark-current density of the LWIR nBp detector (a) and of the equivalent pin photodiode (b). The barrier doping level was fixed at $5x10^{15}$ cm^{-3}.

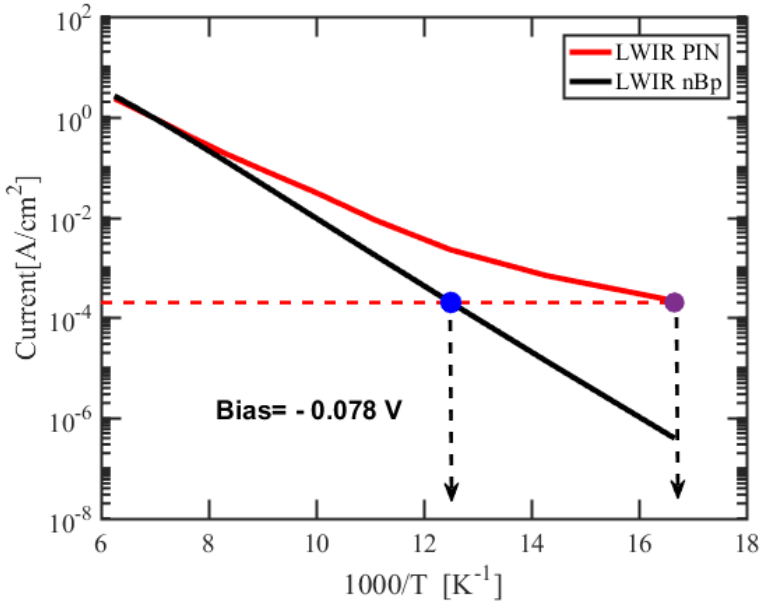

Figure. 4.32 The dark current density as a function of the temperature of the LWIR T2SL nBp detector and the corresponding dark current of its equivalent PIN detector at 75 mV. Solid points are for the temperatures for which both devices exhibit dark current density level of $2x10^{-4}$ A$/cm^{-2}$ indicated by horizontal red line.

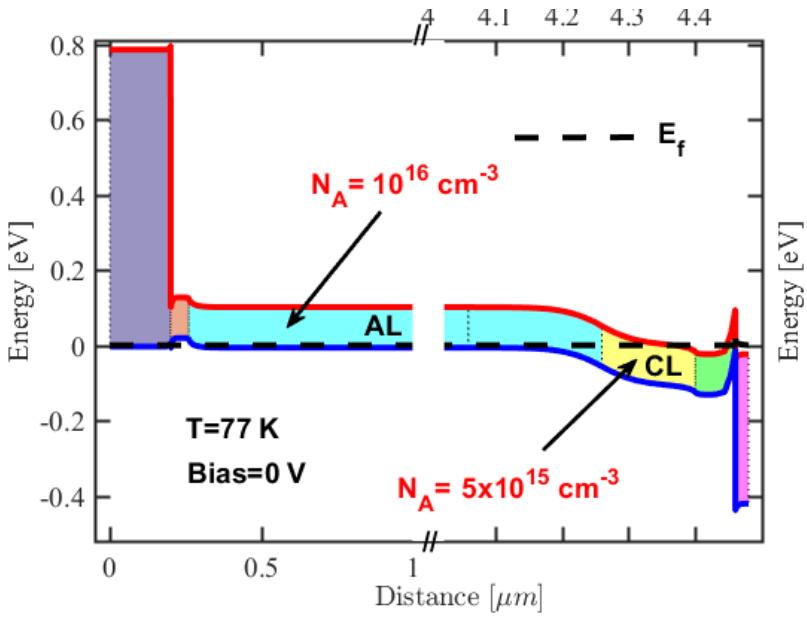

Figure. 4.33 Simulated band diagram of the T2SL pin structure at 77K and 0V. The structure here is the same as for the nBp structure except the barrier is excluded.

4.8 Summary

In this chapter, a physical transport model suitable for simulating different detector structures has been developed and validated. The numerical counterpart of this model has been implemented into our second modelling tool. The transport model is based on the adaptation of Boltzmann Transport Equation for electrons and holes inside minibands. Using our transport tool, the performance and physics of an nBn photodetector based on the InAs/AlAsSb material system is investigated. We have shown that, due to a small VBO, photogenerated minority carriers (holes) diffuse to the CL layer even without applied voltage indicating that the device is in an on state before applying any bias. Furthermore, by decreasing the reverse bias voltages down to 0.1 V and using CL with thickness greater than 3 μm, it is possible to push QE up 90%. We have also used our tool to design and simulate nBp barrier photodetector involving InAs-rich 14 ML InAs / 7ML GaSb LWIR T2SL for being used as an efficient absorber to achieve high operating temperature. By analysing band edge diagrams and the electro-optical properties, each layer of the barrier device has been optimized in terms of composition, doping and thickness. The designed barrier device consists of a 4 μm thick p-type InAs-rich 14 ML InAs / 7ML GaSb LWIR T2SL absorber, a 200 nm thick p-type InAs/AlSb SL barrier and an n-type InAs-rich 14 ML InAs / 7ML GaSb LWIR T2SL contact layer. The optimum doping level of absorber, barrier and contact layer are found to be $1 \times 10^{16} cm^3$, $5 \times 10^{15} cm^3$ and $1 \times 10^{16} cm^3$ respectively. The nBp photodetector based on this design exhibits a diffusion limited dark-current down to -300 mV with a dark-current level plateau as low as $8.5 \times 10^{-5} A/cm^2$ which is more than one order of magnitude lower compared to a similar PIN photodiode. Furthermore, this value is near the level of the MCT 'rule 07' demonstrating that InAs/GaSb SL detectors may provide new opportunities to replace the MCT technology in the LWIR spectral window given the MCT material instability problem at longer wavelengths. Moreover, we have demonstrated that the presence of the barrier allows improving the current performances and the operating temperature over the standard PIN device. In addition, as the surface leakage current, is more significant for LWIR absorbers, the barrier also plays the role of a passivation material.

Chapter 5

Conclusion

In this work, we have focused on exploring new designs for quantum infrared photodetectors to raise them to a new level of maturity. Specifically, the topic of research has been concerned with modelling and simulation of high temperature quantum infrared photodetectors using advanced finite element methods. The aim was to devise novel designs based on standard platforms to improve quantum efficiency, specific detectivity, conversion efficiency, and operating temperature. Based on the outcome of the literature survey, high temperature infrared photodetectors based on GaSb/InAs/AlSb heterostructures has been identified as an interesting and timely topic of research. In fact, these heterostructures cover a wide range of infrared spectrum and allow the use of type II band alignments, which provides great freedom in band gap engineering. Quantum infrared photodetectors are multidisciplinary devices: material science necessary for epitaxy, electronic band structure, carriers transport in these semiconductor layers, electromagnetic modeling of optical coupling. Therefore it is instructive to master each of these topics in order undestand how to find ways to increase the prformances of quantum infrared photodetectors. Towards this end, I have developed a robust numerical simulation tools for the simulation of IR detectors based on InAs/GaSb superlattices as well as InAs/AlAsSb alloys that takes into account the composition, doping and temperature dependence. The simulation is mainly mad through three process. First, I used finite element method to solve 8×8 $\mathbf{k} \cdot \mathbf{p}$ Hamiltonians for InAs/GaSb superlattices with type II alignment to compute the minibands alignments and optical and materials' characteristics. For InAs/AlAsSb alloys based detectors, I instead use the tool library to generates all the needed bulk material properties. Secondly, the transfer matrix method or the Beer-Lambert law is used to compute the optical generation profiles in the device. Finally, I employ the finite volume method to solve the transport equations to compute the dark- and photo- currents, quantum efficiency among other device properties.

Chapter one and two covered the context of this work and recalled the IR detection as well as the state of the art of the three main competing technologies namely HgCdTe, GaAs/AlGaAs Multiple Quantum Wells and Type-II superlattices (T2SLs) Photodetectors. More specifically, the main properties of GaSb/InAs superlattices technology and it's current needs, such as improving the intrinsic performance, increasing operating temperature and increasing the size of FPAs are presented. The InAs/GaSb superlattice meets these requirements. First, because the specific alignment between the InAs and the GaSb allows, by changing the thickness of the period, to address the detection wavelengths beween SWIR and LWIR. Secondally, the GaSb/InAs SL in the LWIR and VLWIR, offers effective masses higher than bulk materials with equivalent wavelength. This point is an advantage for detection, as these high masses limit the tunnel currents which are a major source of noise at high wavelengths. Moreover, theoretically the SL has a low Auger recombination rate, which improves the lifetime of the carriers. Finally, the use of III-V material assumes a uniformity in the growth of InAs/GaSb SLs, enabling the realization of large FPAs. For further improvements, the effect of incorporating unipolar barriers that could lead to higher performance infrared photodetectors where also investigated.

Next in chapter three, a significant effort has been devoted to the development of a quantum simulation tool to accurately characterize the different nano-structures in terms of band structure, density of states and absorption coefficient as well as interface configuration. The nano-structures are mainly antimonide Type-II superlattices and are described by an 8×8 $\mathbf{k} \cdot \mathbf{p}$ Hamiltonians that takes into account stain effects. Using this tool allows to predicted cutoff energies (band gaps) for different types of interband transitions and are consistent with the calculated band dispersion curves of InAs/GaSb Type II broken gap superlattice and demonstrate excellent agreement with the experimental data reported in [36]. In addition, the modelling results show that the Inter-Facial (IF's) lattice mismatch and induced strain yields a significant increase in the absorption coefficient as well as in cut-off wavelengths. As a result, a wide tunable range of optical properties can be obtained with IF layers.

Once the 8×8 $\mathbf{k} \cdot \mathbf{p}$ band structure tool model was validated, its output results were used in Chapter four as input parameters for the second tool devoted to study the transport characteristics of infrared barrier detectors based on InAs/GaSb superlattices. I first described and formulated the physical transport model using the Boltzman transport equation for electrons and holes. Then, I discussed the adaptation of the model to super-lattices based device. Next, I reviewed the numerical techniques required to solve the highly non-linear coupled transport equations. Subsequently, the validated numerical transport model on simple heterostructure devices, is used to investigate in detail a bulk InAs/AlAsSb nBn detector photodetector to explore some aspects of their operation. Being a new type of infrared detectors that implements a large

barrier for electrons in the conduction band, the nBn detector is a unipolar device. During the simulation and validation of a physical transport model for nBn detectors with InAs/AlAsSb structures, I fount it hard to retrieve a complete list of parameters for this material system due to a lack of information even thought it is a bulk alloy. Using these material models, I have performed a numerical simulation to study the underlying physics and assess the performance of InAs/ AlAsSb nBn detectors. I have shown that, even at zero bias voltage, a photo-current crosses the device due to the diffusion of photo-generated minority carriers (holes) to the CL layer that were not impeded by the small valence band offset. This diffusion current is triggered by the illumination that creates a non uniformity in the minority carriers' distribution in the AL. This observation is consistent with the demonstration reported by Klipstein et all [**?**]. Furthermore, I have shown that, a quantum efficiency as high as 90% is achievable by pushing the reverse bias down to $-0.3\ V$ and expanding the AL above 3.0 μm.

We have also shown that to enhance more in the suppression of SRH generation component from the dark current, a carefully chosen doping level in the AL and BL for a given bias voltage is advisable. For the first glance, it seems that a higher doping level would always lead to an increase in the signal-to-noise ratio because of no removal of electrons from the region near the AL/BL interface (small depletion region). In fact, the benefit of higher absorber doping in reducing diffusion and SRH generation dark currents, should be balanced against the possibility of reducing diffusion length due to shortened SRH lifetime. Clearly, there is an upper bound for the n-type doping level in the BL. While this is true for n-type BL, it's not the case for p-type BL where the AL doping should be kept relatively high. An optimized approach is to keep the n-type doping level in the AL relatively low, of the order of $10^{15}\ cm^{-3}$ while using an n-type doping barrier with similar doping level.

Finally in chapter four, we have also used our transport simulation tool to design and simulate nBp barrier photodetector involving InAs-rich 14 ML InAs / 7ML GaSb LWIR T2SL for being used as an efficient absorber to achieve high operating temperature. By analysing band edge diagrams and the electro-optical properties, each layer of the barrier device has been optimized in terms of composition, doping and thickness. The designed barrier device consists of a 4 $\mu\, m$ thick p-type InAs-rich 14 ML InAs / 7ML GaSb LWIR T2SL absorber, a 200 nm thick p-type InAs/AlSb SL barrier and an n-type InAs-rich 14 ML InAs / 7ML GaSb LWIR T2SL contact layer. The optimum doping level of absorber, barrier and contact layer are found to be $1 \times 10^{16} cm^3$, $5 \times 10^{15} cm^3$ and $1 \times 10^{16} cm^3$ respectively. The nBp photodetector based on this design shows a diffusion limited dark-current down to -300 mV with a dark-current density plateau as low as $5.5 \times 10^{-6} A/cm^2$ which is more than one order of magnitude lower compared to a similar PIN photodiode. Furthermore, this value is near the level of the MCT 'rule 07'

demonstrating that InAs/GaSb SL detectors may provide new opportunities to replace the MCT technology in the LWIR spectral window given the MCT material instability problem at longer wavelengths. Moreover, we have demonstrated that the presence of the barrier allows improving the current performances and the operating temperature over the standard PIN device.

Publications

The following publications are included in parts or in an extended version in this thesis:

- Becer, Z.; Bennecer, A.; Sengouga, N. Modeling Energy Bands in Type II Superlattices. Crystals 2019, 9, 629.
- Becer, Z.; Bennecer, A.; Sengouga, N. A Multiple Quantum Well Structure Simulator. In UKSim-AMSS 20th International Conference on Modelling & Simulation; IEEE: Cambridge, UK, 2018.
- Becer, Z.; Sengouga, N.; Medjouri, A. Optical and Electrical properties of mid-infrared InAs/GaSb superlattice photodetectors operating at room temperature. Conference International d'Optique, Photonique et leurs Application, ICOPA Algiers, 2013.

References

[bio] Clinical Thermography / Breast and Full-body Scans / Digital Infrared Thermal Imaging Explained.

[2] A. M. White (1983). Infrared detectors.

[3] Abedin, M. N., Mlynczak, M. G., and Refaat, T. F. (2010). Infrared detectors overview in the short-wave infrared to far-infrared for CLARREO mission. page 78080V.

[4] Agarwal, S., Balamukundhan, K., Neophytou, N., and Klimec, G. (2008). 1D heterostructure tool for atomistic simulation of nano-devices. *Proceedings of TECHCON 2008*.

[5] Alchaar, R., Rodriguez, J. B., Höglund, L., Naureen, S., and Christol, P. (2019). Characterization of an InAs/GaSb type-II superlattice barrier photodetector operating in the LWIR domain. *AIP Advances*, 9(5):055012.

[6] Anton, R. C., Dereniak, E. L., Garcia, and P., J. (1995). Characteristics of uncooled Indium Antimonide Photoconductors. In *Proc. SPIE*, page 2552.

[7] Antoni Rogalski (2015). *Infrared Detectors*, volume 1542.

[8] Ariyawansa, G., Duran, J., Reyner, C., and Scheihing, J. (2019). InAs/InAsSb strained-layer superlattice mid-wavelength infrared detector for high-temperature operation. *Micromachines*, 10(12).

[9] Ariyawansa, G., Grupen, M., Duran, J. M., Scheihing, J. E., Nelson, T. R., and Eismann, M. T. (2012). Design and modeling of InAs/GaSb type II superlattice based dual-band infrared detectors. *Journal of Applied Physics*, 111(7):073107.

[10] Ariyawansa, G., Reyner, C. J., Duran, J. M., Reding, J. D., Scheihing, J. E., and Steenbergen, E. H. (2016). Unipolar infrared detectors based on InGaAs/InAsSb ternary superlattices. *Applied Physics Letters*, 109(2):021112.

[11] Askar, A. (1975). Finite element method for bound state calculations in quantum mechanics. *The Journal of Chemical Physics*, 62(2):732.

[12] Bastard, G. (1981). Superlattice band structure in the envelope-function approximation. *Physical review B*, 24(10).

[13] Becer, Z., Bennecer, A., and Sengouga, N. (2018). A Multiple Quantum Well Structure Simulator. In *UKSim-AMSS 20th International Conference on Modelling & Simulation*, page 6, Cambridge UK. IEEE.

[14] Bir, G. L. and Pikus, G. E. (1974). *Symmetry and Strain-Induced Effects in Semiconductors*. John Wiley, New York.

[15] Bordone, P., Pascoli, M., Brunetti, R., Bertoni, A., Jacoboni, C., and Abramo, A. (1999). Quantum transport of electrons in open nanostructures with the Wigner-function formalism. *Physical Review B*, 59(4):3060–3069.

[16] Chang, C.-S. and Chuang, S. L. (1995). Modeling of Strained Quantum- Well Lasers with Spin-Orbit Coupling. *IEEE Journal of Selected Topics in Quantum Electronics*, I(2).

[17] Chen, G., Haddadi, A., Hoang, A.-M., Chevallier, R., and Razeghi, M. (2015). Demonstration of type-II superlattice MWIR minority carrier unipolar imager for high operation temperature application. *Optics Letters*, 40(1):45.

[18] Delaunay, P.-y., Nguyen, B. M., Hoffman, D., Huang, E. K.-w., Manurkar, P., Bogdanov, S., and Razeghi, M. (2009). Background limited performance of long wavelength infrared focal plane arrays fabricated from M-structure InAs / GaSb superlattices. In Razeghi, M., Sudharsanan, R., and Brown, G. J., editors, *Quantum Sensing and Nanophotonic Devices VI*, volume 7222, pages 284 – 293, Delaunay2009. SPIE.

[19] Delli, E., Letka, V., Hodgson, P. D., Repiso, E., Hayton, J. P., Craig, A. P., Lu, Q., Beanland, R., Krier, A., Marshall, A. R. J., and Carrington, P. J. (2019). Mid-Infrared InAs/InAsSb Superlattice nBn Photodetector Monolithically Integrated onto Silicon. *ACS Photonics*, 6(2):538–544.

[20] Delmas, M., Kwan, D. C. M., Debnath, M. C., Liang, B. L., and Huffaker, D. L. (2019). Flexibility of Ga-containing Type-II superlattice for long-wavelength infrared detection. *Journal of Physics D: Applied Physics*, 52(47):475102.

[21] Dresselhaus, G., Kip, A. F., and Kittel, C. (1955). Cyclotron Resonance of Electrons and Holes in Silicon and Germanium Crystals. *Physical Review*, 98(2):368–384.

[22] Eissfeller, T. and Vogl, P. (2011). Real-space multiband envelope-function approach without spurious solutions. *Physical Review B - Condensed Matter and Materials Physics*, 84(19).

[23] Enderlein, R. and Horing, N. J. (1997). *Fundamentals of Semiconductor Physics and Devices*. WORLD SCIENTIFIC, Singapore.

[24] Eppenga, R., Schuurmans, M. F. H., and Colak, S. (1987). New kp theory for GaAs/ Ga 1 x A 1 x As-type quantum wells. *Physical Review B*, 36(3):1554–1564.

[25] Esaki, L. (1981). InAs-GaSb superlattices-synthesized semiconductors and semimetals. *Journal of Crystal Growth*, 52:227–240.

[26] Esaki, L. and Tsu, R. (1970). Superlattice and Negative Differential Conductivity in Semiconductors. *IBM Journal of Research and Development*, 14(1):61–65.

[27] Ferrari, R. L. (1993). Electronic band structure for two-dimensional periodic lattice quantum configurations by the finite element method. *International Journal of Numerical Modelling: Electronic Networks, Devices and Fields*, 6(4):283–297.

[28] Figgemeier, H., Benecke, M., Hofmann, K., Oelmaier, R., Sieck, A., Wendler, J., and Ziegler, J. (2014). SWIR detectors for night vision at AIM. page 907008.

[29] Fischetti, M. V. (1999). Master-equation approach to the study of electronic transport in small semiconductor devices. *Physical Review B*, 59(7):4901–4917.

[30] Foreman, B. A. (1997). Elimination of spurious solutions from eight-band theory. *Physical Review B - Condensed Matter and Materials Physics*, 56(20):R12748–R12751.

[31] Foreman, B. A. (2007). Choosing a basis that eliminates spurious solutions in kp theory. *Physical Review B - Condensed Matter and Materials Physics*, 75(23).

[32] Giard, E., Ribet-Mohamed, I., Jaeck, J., Viale, T., Haïdar, R., Taalat, R., Delmas, M., Rodriguez, J. B., Steveler, E., Bardou, N., Boulard, F., and Christol, P. (2014). Quantum efficiency investigations of type-II InAs/GaSb midwave infrared superlattice photodetectors. *Journal of Applied Physics*, 116(4):1–7.

[33] Greiner, W. (2001). *Quantum Mechanics*. Springer Berlin Heidelberg, Berlin, Heidelberg.

[34] Guimarães, M. N. and Prudente, F. V. (2005). A study of the confined hydrogen atom using the finite element method. *Journal of Physics B: Atomic, Molecular and Optical Physics*, 38(15):2811–2825.

[35] Haddadi, A., Dehzangi, A., Adhikary, S., Chevallier, R., and Razeghi, M. (2017). Background–limited long wavelength infrared InAs/InAs 1 x Sb x type-II superlattice-based photodetectors operating at 110 K. *APL Materials*, 5(3):035502.

[36] Hill, C. J., Li, J. V., Mumolo, J. M., and Gunapala, S. D. (2007). MBE grown type-II MWIR and LWIR superlattice photodiodes. *Infrared Physics & Technology*, 50(2-3):187–190.

[37] Hoang, A. M., Chen, G., Chevallier, R., Haddadi, A., and Razeghi, M. (2014). High performance photodiodes based on InAs/InAsSb type-II superlattices for very long wavelength infrared detection. *Applied Physics Letters*, 104(25):251105.

[38] Höglund, L., Asplund, C., Marcks von Würtemberg, R., Gamfeldt, A., Kataria, H., Lantz, D., Smuk, S., Costard, E., and Martijn, H. (2016). Advantages of T2SL: results from production and new development at IRnova. page 98190Z.

[39] Hong, B. H., Rybchenko, S. I., Itskevich, I. E., Haywood, S. K., Intartaglia, R., Tasco, V., Rainò, G., and De Giorgi, M. (2009). Applicability of the <math display="inline"> <mrow> <mi mathvariant="bold">k</mi> <mo></mo> <mi mathvariant="bold">p</mi> </mrow> </math> method to modeling of InAs/GaSb short-period superlattices. *Physical Review B*, 79(16):165323.

[40] Hood, A., Razeghi, M., Aifer, E. H., and Brown, G. J. (2005). On[1] A. Hood, M. Razeghi, E. H. Aifer, and G. J. Brown, "On the performance and surface passivation of type II InAsGaSb superlattice photodiodes for the very-long-wavelength infrared," Appl. Phys. Lett., vol. 87, no. 15, p. 151113, Oct. 2005. the perfor. *Applied Physics Letters*, 87(15):151113.

[41] Hurkx, G. A., Klaassen, D. B., and Knuvers, M. P. (1992). A New Recombination Model for Device Simulation Including Tunneling. *IEEE Transactions on Electron Devices*, 39(2):331–338.

[Irnova] Irnova. No Title.

[43] Itsuno, A. M., Phillips, J. D., and Velicu, S. (2011). Design and Modeling of HgCdTe nBn Detectors. *Journal of Electronic Materials*, 40(8):1624–1629.

[44] Jacoboni, C. and Lugli, P. (1989). *The Monte Carlo Method for Semiconductor Device Simulation*. Springer Vienna, Vienna, Austria.

[45] Jirauschek, C. (2009). Accuracy of Transfer Matrix Approaches for Solving the Effective Mass SchrÖdinger Equation. *IEEE Journal of Quantum Electronics*, 45(9):1059–1067.

[46] Kaduki, K. A. and Batty, W. (2000). Envelope Function Approximation (EFA) Band-structure Calculations for III-V Non-square Stepped Alloy Quantum Wells Incorporating Ultra-narrow (˜5Å) Epitaxial Layers. *Physica Scripta*, 61(2):213–221.

[47] Kane, E. O. (1982). Handbook of Semiconductors. page Vol. 1. 193. North-Holland, Amsterdam, (edited by edition.

[48] Kataria, H., Asplund, C., Lindberg, A., Smuk, S., Alverbro, J., Evans, D., Sehlin, S., Becanovic, S., Tinghag, P., Höglund, L., Sjöström, F., and Costard, E. (2017). Novel high-resolution VGA QWIP detector. page 101772C.

[49] Kazemi, A., Myers, S., Taghipour, Z., Mathews, S., Schuler-Sandy, T., Lee, S., Cowan, V. M., Garduno, E., Steenbergen, E., Morath, C., Ariyawansa, G., Scheihing, J., and Krishna, S. (2018). Mid-wavelength infrared unipolar nBp superlattice photodetector. *Infrared Physics & Technology*, 88:114–118.

[50] Kelly, M. (1995). *Low-Dimensional Semiconductors: Materials, Physics, Technology, Devices*. Clarendon Press, Oxford, UK.

[51] Kim, C. S., Kim, M., Bewley, W. W., Lindle, J. R., Canedy, C. L., Abell, J., Vurgaftman, I., and Meyer, J. R. (2009). Corrugated-sidewall interband cascade lasers with single-mode midwave-infrared emission at room temperature. *Applied Physics Letters*, 95(23):231103.

[52] Kim, H., Meng, Y., Klem, J. F., Hawkins, S. D., Kim, J. K., and Zuo, J.-M. (2018). Sb-induced strain fluctuations in a strained layer superlattice of InAs/InAsSb. *Journal of Applied Physics*, 123(16):161521.

[53] Kim, H. S., Plis, E., Rodriguez, J. B., Bishop, G. D., Sharma, Y. D., Dawson, L. R., Krishna, S., Bundas, J., Cook, R., Burrows, D., Dennis, R., Patnaude, K., Reisinger, A., and Sundaram, M. (2008). Mid-IR focal plane array based on type-II InAsGaSb strain layer superlattice detector with nBn design. *Applied Physics Letters*, 92(18):183502.

[54] Klem, J. F., Kim, J. K., Cich, M. J., Hawkins, S. D., Fortune, T. R., and Rienstra, J. L. (2010). Comparison of nBn and nBp mid-wave barrier infrared photodetectors. page 76081P.

[55] Klipstein, P. (2003). Depletion-less photodiode with suppressed dark current and method for producing the same.

[56] Klipstein, P. (2008). "XB n " barrier photodetectors for high sensitivity and high operating temperature infrared sensors. page 69402U.

[57] Klipstein, P. (2015). XBnn and XBpp infrared detectors. *Journal of Crystal Growth*, 425:351–356.

[58] Klipstein, P., Aronov, D., Ezra, M. B., Barkai, I., Berkowicz, E., Brumer, M., Fraenkel, R., Glozman, A., Grossman, S., Jacobsohn, E., Klin, O., Lukomsky, I., Shkedy, L., Shtrichman, I., Snapi, N., Yassen, M., and Weiss, E. (2013). Recent progress in InSb based quantum detectors in Israel. *Infrared Physics and Technology*, 59:172–181.

[59] Klipstein, P. C., Avnon, E., Benny, Y., Berkowicz, E., Cohen, Y., Dobromislin, R., Fraenkel, R., Gershon, G., Glozman, A., Hojman, E., Ilan, E., Karni, Y., Klin, O., Kodriano, Y., Krasovitsky, L., Langof, L., Lukomsky, I., Nevo, I., Nitzani, M., Pivnik, I., Rappaport, N., Rosenberg, O., Shtrichman, I., Shkedy, L., Snapi, N., Talmor, R., Tessler, R., Weiss, E., and Tuito, A. (2017). Development and Production of Array Barrier Detectors at SCD. *Journal of Electronic Materials*, 46(9):5386–5393.

[60] Klipstein, P. C., Avnon, E., Benny, Y., Cohen, Y., Fraenkel, R., Gliksman, S., Glozman, A., Hojman, E., Klin, O., Krasovitsky, L., Langof, L., Lukomsky, I., Marderfeld, I., Yaron, N., Nitzani, M., Rappaport, N., Shtrichman, I., Snapi, N., and Weiss, E. (2018). Type II Superlattice Infrared Detector Technology at SCD. *Journal of Electronic Materials*, 47(10):5725–5729.

[61] Kolokolov, I., Li, J., and Ning, Z. (2003). Kp Hamiltonian without spurious-state solutions. *Physical Review B - Condensed Matter and Materials Physics*, 68(16):1–4.

[62] Kolokolov, K. I., Savin, A. M., Beneslavski, S. D., Minina, N. Y., and Hansen, O. P. (1999). Energy spectrum and topology evolution of the Fermi surface of two-dimensional holes in GaAs/AlGaAs heterostructures under uniaxial compression: Theory and experiment. *Physical Review B*, 59(11):7537–7545.

[63] Kopytko, M. and Rogalski, A. (2016). HgCdTe barrier infrared detectors. *Progress in Quantum Electronics*, 47:1–18.

[64] Korkmaz, M., Arikan, B., Suyolcu, Y. E., Aslan, B., and Serincan, U. (2018). Performance evaluation of InAs/GaSb superlattice photodetector grown on GaAs substrate using AlSb interfacial misfit array. *Semiconductor Science and Technology*, 33(3):035002.

[65] Lake, R., Klimeck, G., Bowen, R. C., and Jovanovic, D. (1997). Single and multiband modeling of quantum electron transport through layered semiconductor devices. *Journal of Applied Physics*, 81(12):7845–7869.

[66] Lau, W. H. and Flatté, M. E. (2002). Effect of interface structure on the optical properties of InAs/GaSb laser active regions. *Applied Physics Letters*, 80(10):1683–1685.

[67] Lei, W., Antoszewski, J., and Faraone, L. (2015). Progress, challenges, and opportunities for HgCdTe infrared materials and detectors. *Applied Physics Reviews*, 2(4):041303.

[Leonardocompany] Leonardocompany. Merlin LWIR Detector.

[69] Levine, B. F. (1993). Quantum-well infrared photodetectors. *Journal of Applied Physics*, 74(8).

[70] Lhuillier, E., Ribet-mohamed, I., Tauvy, M., Nedelcu, A., Berger, V., and Rosencher, E. (2009). Ultimate performance of quantum well infrared photodetectors in the tunneling regime. *Infrared Physics and Technology*, 52(4):132–137.

[71] Li, C.-K., Piccardo, M., Lu, L.-S., Mayboroda, S., Martinelli, L., Peretti, J., Speck, J. S., Weisbuch, C., Filoche, M., and Wu, Y.-R. (2017). Localization landscape theory of disorder in semiconductors. III. Application to carrier transport and recombination in light emitting diodes. *Physical Review B*, 95(14):144206.

[72] Li, J. V., Yang, R. Q., Hill, C. J., and Chuang, S. L. (2005). Interband cascade detectors with room temperature photovoltaic operation. *Applied Physics Letters*, 86(10):101102.

[73] Liu, G. and Chuang, S. L. (2002). Self-Consistent Model of Type-II Quantum-Cascade Lasers. 4646:60–69.

[74] Löwdin, P. (1951). A Note on the Quantum-Mechanical Perturbation Theory. *The Journal of Chemical Physics*, 19(11):1396–1401.

[75] Ma, X., Li, K., Zhang, Z., Jiang, Y., Xu, Y., and Song, G. (2014). Stable finite element method of eight-band k·p model without spurious solutions and numerical study of interfaces in heterostructures. *Journal of Applied Physics*, 116(23):235702.

[76] Magri, R. and Zunger, A. (2002). Effects of interfacial atomic segregation and intermixing on the electronic properties of InAs/GaSb superlattices. *Physical Review B*, 65(16):165302.

[77] Maimon, S. (2010). Reduced dark current photodetector.

[78] Maimon, S. and Wicks, G. W. (2006). nBn detector, an infrared detector with reduced dark current and higher operating temperature. *Applied Physics Letters*, 89(15):151109.

[79] Manurkar, P., Ramezani-Darvish, S., Nguyen, B.-M., Razeghi, M., and Hubbs, J. (2010). High performance long wavelength infrared mega-pixel focal plane array based on type-II superlattices. *Applied Physics Letters*, 97(19):193505.

[80] Martyniuk, P., Kopytko, M., and Rogalski, A. (2014). Barrier infrared detectors. *Opto-Electronics Review*, 22(2).

[81] Meney, A. T., Gonul, B., and O'Reilly, E. P. (1994). Evaluation of various approximations used in the envelope-function method. *Physical Review B*, 50(15):10893–10904.

[82] Morrow, R. A. and Brownstein, K. R. (1984). Model effective-mass Hamiltonians for abrupt heterojunctions and the associated wave-function-matching conditions. *Physical Review B*, 30(2):678–680.

[83] Nakamura, K., Shimizu, A., Koshiba, M., and Hayata, K. (1989). Finite-element analysis of quantum wells of arbitrary semiconductors with arbitrary potential profiles. *IEEE Journal of Quantum Electronics*, 25(5):889–895.

[84] Nelson, D. F., Miller, R. C., and Kleinman, D. A. (1987). Band nonparabolicity effects in semiconductor quantum wells. *Physical Review B*, 35(14):7770–7773.

[85] Nesher, O. and Klipstein, P. C. (2006). High-performance IR detectors at SCD present and future. *Opto-Electronics Review*, 14:59–68.

[86] Ng, E. Y. and Etehadtavakol, M., editors (2017). *Application of Infrared to Biomedical Sciences*. Series in BioEngineering. Springer Singapore, Singapore.

[87] Nguyen, B.-M., Chen, G., Hoang, A. M., Abdollahi Pour, S., Bogdanov, S., and Razeghi, M. (2011). Effect of contact doping in superlattice-based minority carrier unipolar detectors. *Applied Physics Letters*, 99(3):033501.

[88] Nguyen, B. M., Hoffman, D., Delaunay, P. Y., and Razeghi, M. (2007a). Dark current suppression in type II InAsGaSb superlattice long wavelength infrared photodiodes with M-structure barrier. *Applied Physics Letters*, 91(16).

[89] Nguyen, B.-M., Razeghi, M., Nathan, V., and Brown, G. J. (2007b). Type-II M structure photodiodes: an alternative material design for mid-wave to long wavelength infrared regimes. page 64790S.

[90] Olson, B. V., Shaner, E. A., Kim, J. K., Klem, J. F., Hawkins, S. D., Murray, L. M., Prineas, J. P., Flatté, M. E., and Boggess, T. F. (2012). Time-resolved optical measurements of minority carrier recombination in a mid-wave infrared InAsSb alloy and InAs/InAsSb superlattice. *Applied Physics Letters*, 101(9):092109.

[91] Park, S.-H., Ahn, D., and Lee, Y.-T. (2004). Finite element analysis of valence band structures in quantum wires. *Journal of Applied Physics*, 96(4):2055.

[92] Payne, M. C., Teter, M. P., Allan, D. C., Arias, T. A., and Joannopoulos, J. D. (1992). Iterative minimization techniques for ab initio total-energy calculations: molecular dynamics and conjugate gradients. *Reviews of Modern Physics*, 64(4):1045–1097.

[93] Pedrazzani, J., Maimon, S., and Wicks, G. (2008). Use of nBn structures to suppress surface leakage currents in unpassivated InAs infrared photodetectors. *Electronics Letters*, 44(25):1487.

[94] Plis, E. A. (2014). Review Article InAs / GaSb Type-II Superlattice Detectors. 2014.

[95] Pour, S. A., Huang, E. K., Chen, G., Haddadi, A., Nguyen, B.-M., and Razeghi, M. (2011). High operating temperature midwave infrared photodiodes and focal plane arrays based on type-II InAs/GaSb superlattices. *Applied Physics Letters*, 98(14):143501.

[96] Qiao, P.-F., Mou, S., and Chuang, S. L. (2012). Electronic band structures and optical properties of type-II superlattice photodetectors with interfacial effect. *Optics Express*, 20(3):2319.

[97] R, T. (1977). High Density Infrared Detector Arrays.

[98] Ram-Mohan, L. (2002). *Finite Element and Boundary Element Applications in Quantum Mechanics*. Oxford University Press, Oxford, UK.

[99] Ram-Mohan, L. R., Saigal, S., Dossa, D., and Shertzer, J. (1990). The finite-element method for energy eigenvalues of quantum mechanical systems. *Computers in Physics*, 4(1):50.

[100] Ram-Mohan, L. R., Yoo, K. H., and Aggarwal, R. L. (1988). Transfer-matrix algorithm for the calculation of the band structure of semiconductor superlattices. 38(9):6151–6159.

[101] Reisinger, A., Dennis, R., Patnaude, K., Burrows, D., Bundas, J., Beech, K., Faska, R., and Sundaram, M. (2013). Broadband QWIP FPAs for hyperspectral applications. *Infrared Physics and Technology*, 59:112–117.

[102] Rhiger, D. R. (2011). Performance Comparison of Long-Wavelength Infrared Type II Superlattice Devices with HgCdTe. *Journal of Electronic Materials*, 40(8):1815–1822.

[103] Ribet-Mohamed, I., Nghiem, J., Caes, M., Guénin, M., Höglund, L., Costard, E., Rodriguez, J., and Christol, P. (2019). Temporal stability and correctability of a MWIR T2SL focal plane array. *Infrared Physics & Technology*, 96:145–150.

[104] Ridene, S., Boujdaria, K., Bouchriha, H., and Fishman, G. (2001). Infrared absorption in Si/SiGe i/Si quantum wells. *Physical Review B*, 64(8):085329.

[105] Rihani, S., Page, H., Beere, H. E., Ritchie, D. A., and Pepper, M. (2009). Design and simulation of a THz QCL based on ??-X depopulation mechanism. *Physica E: Low-Dimensional Systems and Nanostructures*, 41(7):1240–1242.

[106] Rodina, A. V., Alekseev, A. Y., Efros, A. L., Rosen, M., and Meyer, B. K. (2002). General boundary conditions for the envelope function in the multiband kp model. *Physical Review B*, 65(12):125302.

[107] Rodriguez, J. B., Cervera, C., and Christol, P. (2010). A type-II superlattice period with a modified InAs to GaSb thickness ratio for midwavelength infrared photodiode performance improvement. *Applied Physics Letters*, 97(25):251113.

[108] Rodriguez, J. B., Plis, E., Bishop, G., Sharma, Y. D., Kim, H., Dawson, L. R., and Krishna, S. (2007). nBn structure based on InAsGaSb type-II strained layer superlattices. *Applied Physics Letters*, 91(4):043514.

[109] Rogalski, A. (2005). HgCdTe infrared detector material: history, status and outlook. *Reports on Progress in Physics*, 68(10):2267–2336.

[110] Rogalski, A. (2011). Recent progress in infrared detector technologies. *Infrared Physics and Technology*, 54(3):136–154.

[111] Rogalski, A. (2012). Progress in focal plane array technologies. *Progress in Quantum Electronics*, 36(2-3):342–473.

[112] Rogalski, A., Antoszewski, J., and Faraone, L. (2009). Third-generation infrared photodetector arrays. *Journal of Applied Physics*, 105(9):1–44.

[113] Rogalski, A., Martyniuk, P., and Kopytko, M. (2016). Challenges of small-pixel infrared detectors: a review. *Reports on Progress in Physics*, 79(4):046501.

[114] Rogalski, A., Martyniuk, P., and Kopytko, M. (2017). InAs/GaSb type-II superlattice infrared detectors: Future prospect. *Applied Physics Reviews*, 4(3):031304.

[115] Rossi, F., Di Carlo, A., and Lugli, P. (1998). Microscopic Theory of Quantum-Transport Phenomena in Mesoscopic Systems: A Monte Carlo Approach. *Physical Review Letters*, 80(15):3348–3351.

[116] Rutz, F., Rehm, R., Walther, M., Kirste, L., Masur, M., Wörl, A., Schmitz, J., Wauro, M., Niemasz, J., Scheibner, R., and Ziegler, J. (2011). Current developments for type-II superlattice imaging systems. page 80120U.

[117] Sai-Halasz, G. A., Tsu, R., and Esaki, L. (1977). A new semiconductor superlattice. *Applied Physics Letters*, 30(12):651–653.

[118] Schuler-Sandy, T., Klein, B., Casias, L., Mathews, S., Kadlec, C., Tian, Z., Plis, E., Myers, S., and Krishna, S. (2015). Growth of InAs–InAsSb SLS through the use of digital alloys. *Journal of Crystal Growth*, 425:29–32.

[119] Schuler-Sandy, T., Myers, S., Klein, B., Gautam, N., Ahirwar, P., Tian, Z.-B., Rotter, T., Balakrishnan, G., Plis, E., and Krishna, S. (2012). Gallium free type II InAs/InAsxSb1-x superlattice photodetectors. *Applied Physics Letters*, 101(7):071111.

[120] Simolon, B., Aziz, N., Cogan, S., Kurth, E., Lam, S., Petronio, S., Woolaway, J., Bandara, S., Gunapala, S., and Mumolo, J. (2009). High performance two-color one megapixel CMOS ROIC for QWIP detectors. *Infrared Physics & Technology*, 52(6):391–394.

[121] Smith, D. L. and Mailhiot, C. (1987). Proposal for strained type II superlattice infrared detectors. *Journal of Applied Physics*, 62(6):2545–2548.

[122] Steenbergen, E. H., Connelly, B. C., Metcalfe, G. D., Shen, H., Wraback, M., Lubyshev, D., Qiu, Y., Fastenau, J. M., Liu, A. W. K., Elhamri, S., Cellek, O. O., and Zhang, Y.-H. (2011). Significantly improved minority carrier lifetime observed in a long-wavelength infrared III-V type-II superlattice comprised of InAs/InAsSb. *Applied Physics Letters*, 99(25):251110.

[123] Svensson, S., Donetsky, D., Wang, D., Hier, H., Crowne, F., and Belenky, G. (2011). Growth of type II strained layer superlattice, bulk InAs and GaSb materials for minority lifetime characterization. *Journal of Crystal Growth*, 334(1):103–107.

[124] Szmulowicz, F., Haugan, H., and Brown, G. J. (2004). Effect of interfaces and the spin-orbit band on the band gaps of InAs/GaSb superlattices beyond the standard envelope-function approximation. *Physical Review B - Condensed Matter and Materials Physics*, 69(15):1–17.

[125] Taghipour, Z., Kazemi, A., Myers, S., Wijewarnasuriya, P. S., Mathews, S., Steenbergen, E., Morath, C. P., Cowan, V. M., Ariyawansa, G., Scheihing, J., and Krishna, S. (2017). Extraction of minority carrier diffusion length of MWIR Type-II superlattice nBp detector. 1040406(August):6.

[Teledyne] Teledyne. MCT HAWAII H2RG.

[127] Teledyne (2015). MCT HAWAII H4RG.

[128] Tennant, W. (2012). Interpreting mid-wave infrared MWIR HgCdTe photodetectors. *Progress in Quantum Electronics*, 36(2-3):273–292.

[129] Tennant, W., Lee, D., Zandian, M., Piquette, E., and Carmody, M. (2008). MBE HgCdTe Technology: A Very General Solution to IR Detection, Described by "Rule 07", a Very Convenient Heuristic. *Journal of Electronic Materials*, 37(9):1406–1410.

[130] Tennant, W. E. (2010). "Rule 07" Revisited: Still a Good Heuristic Predictor of p/n HgCdTe Photodiode Performance? *Journal of Electronic Materials*, 39(7):1030–1035.

[131] Ting, D. Z., Hill, C. J., Soibel, A., Nguyen, J., Keo, S. A., Lee, M. C., Mumolo, J. M., Liu, J. K., and Gunapala, S. D. (2010). Antimonide-based barrier infrared detectors. 7419:76601R.

[132] Ting, D. Z., Soibel, A., Höglund, L., Khoshakhlagh, A., Hill, C. J., Keo, S. A., Rafol, S. B., Fisher, A. M., Luong, E. M., Mumolo, J. M., Liu, J. K., Pepper, B. J., and Gunapala, S. D. (2016). Type-II Superlattice Unipolar Barrier Infrared Detectors. 1:466–467.

[133] Ting, D. Z., Soibel, A., Khoshakhlagh, A., Höglund, L., Keo, S. A., Rafol, S. B., Hill, C. J., Fisher, A. M., Luong, E. M., Nguyen, J., Liu, J. K., Mumolo, J. M., Pepper, B. J., and Gunapala, S. D. (2017). Antimonide type-II superlattice barrier infrared detectors. page 101770N.

[134] Ting, D. Z., Soibel, A., Khoshakhlagh, A., Rafol, S. B., Keo, S. A., Höglund, L., Fisher, A. M., Luong, E. M., and Gunapala, S. D. (2018). Mid-wavelength high operating temperature barrier infrared detector and focal plane array. *Applied Physics Letters*, 113(2):021101.

[135] Ting, D. Z.-Y., Hill, C. J., Soibel, A., Keo, S. A., Mumolo, J. M., Nguyen, J., and Gunapala, S. D. (2009). A high-performance long wavelength superlattice complementary barrier infrared detector. *Applied Physics Letters*, 95(2):023508.

[136] Ting, D. Z.-Y., Soibel, A., Höglund, L., Nguyen, J., Hill, C. J., Khoshakhlagh, A., and Gunapala, S. D. (2011). Type-II Superlattice Infrared Detectors. chapter 1, pages 1–57.

[137] Ting, D. Z.-Y., Soibel, A., Khoshakhlagh, A., Nguyen, J., Höglund, L., Keo, S. A., Mumolo, J. M., and Gunapala, S. D. (2013). Exclusion, extraction, and junction placement effects in the complementary barrier infrared detector. *Applied Physics Letters*, 102(12):121109.

[138] Veprek, R. G., Steiger, S., and Witzigmann, B. (2007). Ellipticity and the spurious solution problem of k.p envelope equations. *Physical Review B*, 76(16):165320.

[139] Vurgaftman, I. and Meyer, J. R. (2001). Band parameters for III – V compound semiconductors and their alloys. 89(11).

[140] Wacker, A. (2002). Semiconductor superlattices: A model system for nonlinear transport. *Physics Reports*, 357(1):1–111.

[141] Wacker, A. and Jauho, A.-p. (1998). Quantum Transport : The Link between Standard Approaches in Superlattices. *PHYSICAL REVIEW LETTERS*, pages 369–372.

[142] Walther, M., Schmitz, J., Rehm, R., Kopta, S., Fuchs, F., Fleißner, J., Cabanski, W., and Ziegler, J. (2005). Growth of InAs/GaSb short-period superlattices for high-resolution mid-wavelength infrared focal plane array detectors. *Journal of Crystal Growth*, 278(1-4):156–161.

[143] Wei, Y., Gin, A., Razeghi, M., and Brown, G. J. (2002). Advanced InAs/GaSb superlattice photovoltaic detectors for very long wavelength infrared applications. *Applied Physics Letters*, 80(18):3262–3264.

[144] Wei, Y., Hood, A., Yau, H., Gin, A., Razeghi, M., Tidrow, M. Z., and Nathan, V. (2005). Uncooled operation of type-II InAsGaSb superlattice photodiodes in the midwavelength infrared range. *Applied Physics Letters*, 86(23):233106.

[145] Wu, D., Li, J., Dehzangi, A., and Razeghi, M. (2020). Mid-wavelength infrared high operating temperature pBn photodetectors based on type-II InAs/InAsSb superlattice. *AIP Advances*, 10(2):025018.

[146] Yang, K., East, J. R., and Haddad, G. I. (1993). Numerical modeling of abrupt heterojunctions using a thermionic-field emission boundary condition. *Solid State Electronics*, 36(3):321–330.

[147] Yi, J. C. and Dagli, N. (1995). Finite-Element Analysis of Valence Band Structure and Optical Properties of Quantum-Wire Arrays on Vicinal Substrates. 31(2):208–218.

[148] YU, P. and Cardona, M. (2010). *Fundamentals of Semiconductors*. Springer: Berlin/Heidelberg, Germany, Germany.

Material Parameters

The simulation tools and implemented with different and flexible material system database to allow for simple and fast material setting. The database essentially includes parameters for elementary and binary materials such as Si, Ge, GaAs, AlAs, etc. Material parameters for ternary, or quaternary materials, such as $Al_xGa_{1-x}As$ or Al_xGa_{1-x} As_y Sb_{1-y} are determined from the material parameters of the binaries that they are composed of. For this, we use polynomial interpolation formulas. The simplest approach is linear interpolation by means of a convex combination. However, it turns out that for the calculation of some material properties of ternaries or quaternaries, a second order term should be included. This is widely known as bowing.

For the common material system $Al_xGa_{1-x}As$, the bowing parameter depends on the alloy composition x. We have developed consistent interpolation schemes for ternaries as well as quaternaries that also take such dependencies of the bowing parameter on the alloy composition into account in linear order. These schemes are presented in the following.

Binar Alloys of the form: $\mathbf{A}_x\mathbf{B}_{1-x}$

For alloys of this type (and also $A_xB_{1-x}H$ where H is an inert component) we can use linear interpolation:

$$Q^{(1)}(x) = xQ_A + (1-x)Q_B \tag{1}$$

to compute the material property Q as a function of the concentration x with

$$Q_A = Q(A), \quad Q_B = Q(B) \tag{2}$$

A second order interpolation scheme $Q^{(2)}(x)$ that is consistent to the components A and B can be obtained by adding a quadratic bowing parameter as

$$Q^{(2)}(x) = xQ_{\mathrm{A}} + (1-x)Q_{\mathrm{B}} + x(1-x)Q_{\mathrm{AB}} \tag{3}$$

Finally, a consistent third order interpolation is given by

$$\begin{aligned} Q^{(3)}(x) &= xQ_{\mathrm{A}} + (1-x)Q_{\mathrm{B}} + x(1-x)Q_{\mathrm{AB}}(x) \\ &= xQ_{\mathrm{A}} + (1-x)Q_{\mathrm{B}} + x(1-x)\left[xQ^{\mathrm{A}}_{\mathrm{AB}} + (1-x)Q^{\mathrm{B}}_{\mathrm{AB}}\right] \end{aligned} \tag{4}$$

where $Q_{AB}(x)$ is a bowing parameter that depends linearly on x.

Ternary Alloys of the form: $\mathbf{A}_x\mathbf{B}_y\mathbf{C}_{1-x-y}$

For alloys of this type (and also $\mathrm{A}_x\mathrm{B}_y\mathrm{C}_{1-x-y}\mathrm{H}$ where H is an inert component) we can use linear interpolation:

$$Q^{(1)}(x,y) = xQ_{\mathrm{A}} + yQ_{\mathrm{B}} + (1-x-y)Q_{\mathrm{C}} \tag{5}$$

to describe the material property Q as a function of the concentrations x and y with

$$Q_{\mathrm{A}} = Q(\mathrm{A}), \quad Q_{\mathrm{B}} = Q(\mathrm{B}), \quad Q_{\mathrm{C}} = Q(\mathrm{C}) \tag{6}$$

A second order interpolation scheme $Q^{(2)}(x)$ that is also consistent to the three limiting one parameter alloys $\mathrm{A}_z\mathrm{B}_{1-z}$, $\mathrm{A}_x\mathrm{C}_{1-x}$, and $\mathrm{B}_y\mathrm{C}_{1-y}$ is given by

$$Q^{(2)}(x,y) = xQ_{\mathrm{A}} + yQ_{\mathrm{B}} + (1-x-y)Q_{\mathrm{C}} + xyQ_{\mathrm{AB}} + x(1-x-y)Q_{\mathrm{AC}} + y(1-x-y)Q_{BC} \tag{7}$$

where Q_{AB}; Q_{AC}; and Q_{BC} are the bowing parameters for the limiting one-parameter alloys. Additional bowing that does not change the results for the limiting one-parameter cases can be achieved by adding a third order term as

$$\begin{aligned} Q^{(2.3)}(x,y) = {} & xQ_{\mathrm{A}} + yQ_{\mathrm{B}} + (1-x-y)Q_{\mathrm{C}} + xyQ_{\mathrm{AB}} + x(1-x-y)Q_{\mathrm{AC}} + y(1-x-y)Q_{\mathrm{BC}} \\ & + xy(1-x-y)Q_{\mathrm{ABC}} \end{aligned} \tag{8}$$

This extra term is also needed in order to achieve bowing on one of the three constraint surfaces

$$x = x_0, \quad y = y_0, \quad x+y = z_0. \tag{9}$$

But the most general third order interpolation scheme has 10 parameters. With

$$\begin{aligned} Q^{(3)}(x,y) = {} & xQ_{\mathrm{A}} + yQ_{\mathrm{B}} + (1-x-y)Q_{\mathrm{C}} + xy\left[xQ^{\mathrm{A}}_{\mathrm{AB}} + yQ^{\mathrm{B}}_{\mathrm{AB}}\right] \\ & + x(1-x-y)\left[xQ^{\mathrm{A}}_{\mathrm{AC}} + (1-x-y)Q^{\mathrm{C}}_{\mathrm{AC}}\right] \\ & + y(1-x-y)\left[yQ^{\mathrm{B}}_{\mathrm{BC}} + (1-x-y)Q^{\mathrm{C}}_{\mathrm{BC}}\right] \\ & + xy(1-x-y)Q_{\mathrm{ABC}} \end{aligned} \tag{10}$$

these parameters can again be chosen consistent to the three limiting one-parameter alloys.

Quaternary Alloys of the form: $\mathbf{A}_x\mathbf{B}_{1-x}\mathbf{C}_y D_{1-y}$

For alloys of this type (and also $\mathrm{A}_x\mathrm{B}_{1-x}\mathrm{C}_y D_{1-y}H$ where H is an inert component) we cannot use linear interpolation to describe a material property Q as a function of the concentrations x and y, since we need here at least four interpolation coefficients. For this reason, we add a quadratic term and use

$$Q^{(1.2)}(x,y) = xyQ_{\mathrm{AC}} + (1-x)yQ_{\mathrm{BC}} + x(1-y)Q_{\mathrm{AD}} + (1-x)(1-y)Q_{\mathrm{BD}} \tag{11}$$

to interpolate Q with

$$Q_{\mathrm{AC}} = Q(\mathrm{AC}), \quad Q_{\mathrm{BC}} = Q(\mathrm{BC}), \quad Q_{\mathrm{AD}} = f(\mathrm{AD}), \quad Q_{\mathrm{BD}} = Q(\mathrm{BD}) \tag{12}$$

Momentum Matrix Elements

We provide here the explicit derivation of matrix elements $nPm = \langle \Psi_{n\mathbf{k}_t} | (\hat{x} + \hat{y}) \cdot \mathbf{P} | \Psi_{m\mathbf{k}_t} \rangle$ corresponding to TE transition mode between the initial spinor $|\Psi_{m\mathbf{k}_t}\rangle$ and the final spinor $|\Psi_{n\mathbf{k}_t}\rangle$. These are for 8x8 KP Hamiltonian given by Equation (**??**) and are evaluated for any direction in transversal reciprocal $\mathbf{k}_t(k_x, k_y)$ space and in terms of spinor envelope components $|S_{m\mathbf{k}_t}\rangle$ from the initial vector state and $|F_{n\mathbf{k}_t}\rangle$ from the final vector state. In the following, the subscript $\mathbf{k}_t$ has been dropped for convenience.

$$
\begin{aligned}
nPm_x = \int dz \Bigg\{ & F_1^* \left(\frac{\hbar m_0}{m e^*} k_x S_1 + \frac{P_{cv} m_0}{\sqrt{6}\hbar} \left(-\sqrt{3} S_2 + S_7 + \sqrt{2} S_8 \right) \right) \\
& + F_2^* \left(-i \frac{P_{cv} m_0}{\sqrt{2}\hbar} S_1 - \hbar k_x (\gamma_1 + \gamma_2) S_2 + \sqrt{3} \hbar (\gamma_2 k_x - i \gamma_3 k_y) \left(S_7 + \sqrt{2} S_8 \right) - i \frac{3}{2} \gamma_3 \hbar \left(\frac{\partial}{\partial z} S_3 + \frac{\partial}{\partial z} S_4 \right) \right) \\
& + F_3^* \left(-\frac{P_{cv} m_0}{\sqrt{6}\hbar} S_5 - \hbar k_x (\gamma_1 - \gamma_2) S_3 + \sqrt{2} \gamma_2 \hbar k_x S_4 + \sqrt{3} \hbar (\gamma_2 k_x - i \gamma_3 k_y) S_6 + i \frac{\sqrt{3}}{2} \gamma_3 \hbar \left(\frac{\partial}{\partial z} S_2 + \frac{\sqrt{3}}{2} \frac{\partial}{\partial z} S_8 \right) \right) \\
& + F_4^* \left(\frac{P_{cv} m_0}{\sqrt{3}\hbar} S_5 + \hbar k_x \left(\sqrt{2} \gamma_2 S_3 - \gamma_1 S_4 \right) - \sqrt{6} \hbar (\gamma_2 k_x - i \gamma_3 k_y) S6 + i \frac{\sqrt{3}}{2\sqrt{2}} \gamma_3 \hbar \left(\frac{\partial}{\partial z} S_2 + \sqrt{3} \frac{\partial}{\partial z} S_7 \right) \right) \\
& + F_5^* \left(\frac{\hbar}{m e^*} k_x S_5 + \frac{P_{cv} m_0}{\sqrt{6}\hbar} \left(-S_3 + \sqrt{2} S_4 + \sqrt{3} S_6 \right) \right) \\
& + F_6^* \left(+ \frac{P_{cv} m_0}{\sqrt{2}\hbar} S_5 - \hbar k_x (\gamma_1 + \gamma_2) S_6 - \sqrt{3} \hbar (\gamma_2 k_x + i \gamma_3 k_y) \left(-S_3 + \sqrt{2} S_4 \right) - i \frac{3}{2} \gamma_3 \hbar \left(\frac{\partial}{\partial z} S_7 + \frac{1}{\sqrt{2}} \frac{\partial}{\partial z} S_8 \right) \right) \\
& + F_7^* \left(\frac{P_{cv} m_0}{\sqrt{6}\hbar} S_1 - \hbar k_x (\gamma_1 - \gamma_2) S_7 + \sqrt{3} \hbar (\gamma_2 k_x + i \gamma_3 k_y) S_2 - \sqrt{2} \gamma_2 \hbar k_x S_8 - i \frac{\sqrt{3}}{2} \gamma_3 \hbar \left(\frac{\sqrt{3}}{\sqrt{2}} \frac{\partial}{\partial z} S_4 - \frac{\partial}{\partial z} S_6 \right) \right) \\
& + F_8^* \left(\frac{P_{cv} m_0}{\sqrt{2}\hbar} S_1 - \sqrt{2} \gamma_2 \hbar k_x S_7 - \gamma_1 \hbar k_x S_8 + \sqrt{6} (\gamma_2 \hbar k_x + i \gamma_3 \hbar k_y) S_2 - i \frac{\sqrt{3}}{2} \gamma_3 \hbar \left(\frac{\sqrt{3}}{\sqrt{2}} \frac{\partial}{\partial z} S_3 + \frac{1}{\sqrt{2}} \frac{\partial}{\partial z} S_6 \right) \right) \\
& + i \frac{\sqrt{3} \gamma_3 \hbar}{2} \Bigg[\left(S_3 + \frac{1}{\sqrt{2}} S_4 \right) \frac{\partial}{\partial z} F_2^* - \left(S_2 + \frac{\sqrt{3}}{\sqrt{2}} S_8 \right) \frac{\partial}{\partial z} F_3^* - \left(\frac{\sqrt{3}}{\sqrt{2}} S_7 + \frac{1}{\sqrt{2}} S_2 \right) \frac{\partial}{\partial z} F_4^* \\
& \qquad + \left(S_7 - \frac{1}{\sqrt{2}} S_8 \right) \frac{\partial}{\partial z} F_6^* + \left(\frac{\sqrt{3}}{\sqrt{2}} S_4 - S_6 \right) \frac{\partial}{\partial z} F_7^* + \left(\frac{\sqrt{3}}{\sqrt{2}} S_3 - \frac{1}{\sqrt{2}} S_6 \right) \frac{\partial}{\partial z} F_8^* \Bigg] \Bigg\}. \qquad (13)
\end{aligned}
$$

$$
\begin{aligned}
nPm_y = \int dz \Bigg\{ & F_1^* \left(\frac{\hbar m_0}{m e^*} k_y S_1 - i \frac{P_{cv} m_0}{\sqrt{6}\hbar} \left(\sqrt{3} S_2 + S_7 + \sqrt{2} S_8 \right) \right) \\
& + F_2^* \left(i \frac{P_{cv} m_0}{\sqrt{2}\hbar} S_1 - hb k_y (\gamma_1 + \gamma_2) S_2 - \sqrt{3}\hbar (\gamma_2 k_y + i \gamma_3 k_x) \left(S_7 + \sqrt{2} S_8 \right) - \frac{\sqrt{3}}{2} \gamma_3 \hbar \left(\frac{\partial}{\partial z} S_3 + \frac{1}{2} \frac{\partial}{\partial z} S_4 \right) \right) \\
& + F_3^* \left(i \frac{P_{cv} m_0}{\sqrt{6}\hbar} S_5 - \sqrt{3}\hbar (\gamma_2 k_y + i \gamma_3 k_x) S_6 - \hbar k_y (\gamma_1 - \gamma_2) S_3 + \sqrt{2} \gamma_2 \hbar k_y S_4 - \frac{\sqrt{3}}{2} \gamma_3 \hbar \left(\frac{\partial}{\partial z} S_2 - \frac{\sqrt{3}}{2} \frac{\partial}{\partial z} S_8 \right) \right) \\
& + F_4^* \left(-i \frac{P_{cv} m_0}{\sqrt{3}\hbar} S_5 + \hbar k_y \left(\sqrt{2} \gamma_2 S_3 - \gamma_1 S_4 \right) + \sqrt{6}\hbar (\gamma_2 k_y + i \gamma_3 k_x) S_6 + \frac{\sqrt{3}}{2\sqrt{2}} \gamma_3 \hbar \left(-\frac{\partial}{\partial z} S_2 + \sqrt{3} \frac{\partial}{\partial z} S_7 \right) \right) \\
& + F_5^* \left(\frac{\hbar m_0}{m e^*} k_y S_5 - i \frac{P_{cv} m_0}{\sqrt{6}\hbar} \left(S_3 - \sqrt{2} S_4 + \sqrt{3} S_6 \right) \right) \\
& + F_6^* \left(i \frac{P_{cv} m_0}{\sqrt{2}\hbar} S_5 - \hbar k_y (\gamma_1 + \gamma_2) S_6 + \sqrt{3}\hbar (-\gamma_2 k_y + i \gamma_3 k_x) \left(S_3 - \sqrt{2} S_4 \right) + \frac{\sqrt{3}}{2} \gamma_3 \hbar \left(\frac{\partial}{\partial z} S_7 - \frac{1}{\sqrt{2}} \frac{\partial}{\partial z} S_8 \right) \right) \\
& + F_7^* \left(i \frac{P_{cv} m_0}{\sqrt{6}\hbar} S_1 + \sqrt{3}\hbar (-\gamma_2 k_y + i \gamma_3 k_x) S_2 - \hbar k_y (\gamma_1 - \gamma_2) S_7 - \sqrt{2} \gamma_2 \hbar k_y S_8 + \frac{\sqrt{3}}{2} \gamma_3 \hbar \left(\frac{\sqrt{3}}{\sqrt{2}} \frac{\partial}{\partial z} S_4 + \frac{\partial}{\partial z} S_6 \right) \right) \\
& + F_8^* \left(i \frac{P_{cv} m_0}{\sqrt{3}\hbar} S_1 - \sqrt{2} \gamma_2 \hbar k_y S_7 - \gamma_1 \hbar k_y S_8 + \sqrt{6} (-\gamma_2 \hbar k_y + i \gamma_3 \hbar k_x) S_2 + \frac{\sqrt{3}}{2} \gamma_3 \hbar \left(\frac{\sqrt{3}}{\sqrt{2}} \frac{\partial}{\partial z} S_3 - \frac{1}{\sqrt{2}} \frac{\partial}{\partial z} S_6 \right) \right) \\
& + \frac{\sqrt{3} \gamma_3 \hbar}{2} \Bigg[- \left(S_3 + \frac{1}{\sqrt{2}} S_4 \right) \frac{\partial}{\partial z} F_2^* - \left(S_2 - \frac{\sqrt{3}}{\sqrt{2}} S_8 \right) \frac{\partial}{\partial z} F_3^* + \left(\frac{\sqrt{3}}{\sqrt{2}} S_7 - \frac{1}{\sqrt{2}} S_2 \right) \frac{\partial}{\partial z} F_4^* \\
& \qquad + \left(S_7 - \frac{1}{\sqrt{2}} S_8 \right) \frac{\partial}{\partial z} F_6^* + \left(\frac{\sqrt{3}}{\sqrt{2}} S_4 + S_6 \right) \frac{\partial}{\partial z} F_7^* + \left(\frac{\sqrt{3}}{\sqrt{2}} S_3 - \frac{1}{\sqrt{2}} S_6 \right) \frac{\partial}{\partial z} F_8^* \Bigg] \Bigg\}. \qquad (14)
\end{aligned}
$$

Abstract

The topic of research is concerned with modelling and simulation of high temperature long wavelength infrared quantum photodetectors using advanced finite element methods. The aim is to devise novel designs based on quantum well structures to improve quantum efficiency, and operating temperature. These new designs rely on quantum confinement of electrons and holes inside a mixture of materials within which the energies of the carriers become discrete and differ from those observed in bulk materials. Type II GaSb / InAs superlattices is one of these meta--materials which offer a large flexibility in the design of infrared photodetectors, including the possibility to adjust the detected wavelength over a very wide range and to realize a suitable absobers' uniploar barriers to suppress dark current while maintaining a significant portion of photocurrent at high temperatures. In order to validate this interest, A set of rigorous modelling tools based on multi-band **k· p** band structure theory and Boltzmann transport theory has been developed, which provide a better understanding of the electronic structure and transport in these heterostructures. The framework takes into account in particular the effect of the intrinsic strained property of the unintentional interfaces on the electronic structure and the optical properties. Using this tools, new structures based on nBn and nBp architectures have been designed, with optimized design, which contribute to the realization of mid- and long-wave infrared photodetector based on Type-II superlattices InAs / GaSb material system as well as InAs/AlAsSb alloy mterial system. The developed model allows to study the underlying physics of these devices and to explain the factors limiting the device performances.

keywords : Superlattice, Infrared, Photodetector, T2SL, nBn, nBp, Barrier, InAs/GaSb

ملخص

يهتم موضوع البحث بنمذجة ومحاكاة أجهزة كشف الأشعة تحت الحمراء الطويلة الكمية عالية درجة الحرارة باستخدام طرق العناصر المحدودة المتقدمة. الهدف هو ابتكار تصميمات جديدة تستند إلى هياكل الآبار الكمية لتحسين الكفاءة الكمية ودرجة حرارة التشغيل. تعتمد هذه التصميمات الجديدة على الحصر الكمي للإلكترونات والثقوب الموجودة داخل خليط من المواد ، حيث تصبح طاقات الحاملات منفصلة ومختلفة عن تلك التي لوحظت في المواد السائبة. تعتبر الشبكات الفائقة InAs/GaSb من النوع الثاني إحدى هذه المواد الفوقية التي توفر مرونة كبيرة في تصميم أجهزة الكشف الضوئي بالأشعة تحت الحمراء، بما في ذلك إمكانية ضبط الطول الموجي المكتشف على نطاق واسع جدًا وتحقيق حواجز أحادية القطبية مناسبة لقمع تيار الظلام مع الحفاظ على جزء كبير من التيار الضوئي عند درجات حرارة عالية. من أجل التحقق من صحة هذا الاهتمام ، تم تطوير أدوات محاكاة دقيقة بناءً على نظرية بنية العصابات المتعدد k · p ونظرية النقل لبلتزمان والتي توفر فهمًا أفضل للبنية الإلكترونية والنقل في هذه الهياكل غير المتجانسة. يأخذ النموذج في الاعتبار على وجه الخصوص تأثير خاصية الاجهادات الذاتية للسطوح البينية غير المقصودة على البنية الإلكترونية والخصائص البصرية. باستخدام هذه الأدوات ، تم تصميم هياكل جديدة بناءً على بنية nBn و nBp مع تصميم محسّن ، مما يساهم في تحقيق كواشف ضوئية بالأشعة تحت الحمراء للموجات الطويلة والمتوسطة على أساس الشبكات الفائقة من النوع الثاني لنظام المواد InAs/GaSb ، وكذا سبائك نظام المواد InAs/AlAsSb . يسمح النموذج المطور بدراسة الفيزياء الأساسية لهذه الأجهزة وشرح العوامل التي تحد من أدائها.

كلمات مفتاحية: بنى فائقة، تحت حمراء، كاشف ضوئي ،T2SL ،nBn ،nBp ،حاجز، InAs/GaSb .

Résumé

Le sujet de recherche concerne la modélisation et la simulation de photodétecteurs quantiques infrarouges à haute température et à longue longueur d'onde à l'aide de méthodes avancées d'éléments finis. L'objectif est de concevoir de nouvelles conceptions basées sur des structures de puits quantiques pour améliorer l'efficacité quantique et la température de fonctionnement. Ces nouvelles conceptions reposent sur le confinement quantique des électrons et des trous à l'intérieur d'un mélange de matériaux dans lequel les énergies des porteurs deviennent discrètes et différentes de celles observées dans les matériaux massifs. Les super-réseaux GaSb/InAs de type II sont l'un de ces méta-matériaux qui offrent une grande flexibilité dans la conception des photodétecteurs infrarouges, y compris la possibilité d'ajuster la longueur d'onde détectée sur une très large gamme et de réaliser des barrières uniplairs appropriées pour supprimer le courant d'obscurité tout en maintenant une partie importante du photocourant à des températures élevées. Afin de valider cet intérêt, un ensemble d'outils de modélisation rigoureux basés sur la théorie de la structure des bandes **k · p** multi-bandes et la théorie du transport de Boltzmann a été développé, qui permettent de mieux comprendre la structure électronique et le transport dans ces hétérostructures. Le model prend en compte en particulier l'effet de la propriété de contrainte intrinsèque des interfaces non intentionnelles sur la structure électronique et les propriétés optiques. En utilisant ces outils, des nouvelles structures basées sur l'architecture nBn et nBp, ont été conçues avec une conception optimisée, qui contribuent à la réalisation de photodétecteurs infrarouges à ondes moyennes et longues basées sur les super-réseaux de Type II du système de matériaux GaSb/InAs ainsi que sur le système de l'alliage InAs/AlAsSb. Le modèle développé permet d'étudier la physique sous-jacente de ces dispositifs et d'expliquer les facteurs limitant leurs performances.

Mots-clés : Super-réseau, Infrarouge, Photodétecteur, T2SL, nBn, nBp, Barrière, InAs/GaSb